

CARDIFF
UNIVERSITY

PRIFYSGOL
CAERDYDD

**The Study of Polymeric and Solid-State
Luminescent Materials**

Thesis submitted for the degree of Doctor of Philosophy by:

Owaen G. Guppy

School of Chemistry

Cardiff University

October 2021

Abstract

This thesis explores the synthesis and photophysical evaluation of inorganic and organic luminescent materials in the form of doped zinc sulfides and doped-ring-opened co-polymerisation polymers.

In chapter 1, doped zinc sulfide phosphors are prepared using a high temperature (800 °C) solid state synthetic procedure under non-oxidising conditions. Copper doped zinc sulfides, within the literature, have been claimed to emit light over a wide range of wavelengths, including 450, 520, and 600 nm. Previously these transitions have been assigned to zinc vacancies, interstitial zinc, relaxation from a shallow trap state to copper, relaxation from the conduction band to copper t_2 states, and relaxation to interstitial copper defects. In this work, four emission peaks are observed: 454, 490, 520, and 600 nm, and assigned to zinc vacancies, sulfur vacancies, interstitial zinc, and interstitial zinc defects, respectively. The assignments were also supported with quasiparticle G_0W_0 calculations that showed reasonable agreement with the experimental data, with the exception of the interstitial sulfur defect. Doping with Group 2 metals was also explored. Barium and strontium were observed to form both zinc defects and sulfur vacancies, respectively. Calcium was found to not favour the formation of any defect. With the addition of a manganese co-dopant, only barium caused a substantial red shift of the emission to 620 nm, with strontium and calcium causing no alteration to the manganese emission.

Chapter 2 focuses on the preparation of small organic luminophores, 1,8-naphthalimides and 1-aminoanthraquinone, suitable for incorporation into a polymer through either post-polymerisation modification using an amine, or through direct incorporation during the polymerisation procedure using a terminal epoxide group.

In chapter 3, these small luminophores are used for the synthesis of luminescent polymers with varying concentrations of luminophores. Three small scale polymers are prepared, using 5 and 10 mol% anthraquinone dopant (by epoxide), and 100% naphthalimide as a monomer. Anthraquinone doped polymers displayed molecular weights significantly higher than predicted, while the naphthalimide based polymer exhibited a lower than expected molecular weight. Additionally, large scale (300 g) polymerisation was performed using dopant level quantities of a luminophore to prepare blue, green, and yellow emitting polymers, with colour-fast properties.

Acknowledgements

Firstly, I would like to thank my primary supervisor Dr Benjamin Ward. Who constantly supported, and motivated me during my time as a PhD student, taught me computational chemistry, and humoured my no doubt crazy ideas. I would also like to thank my secondary supervisor, Professor Simon Pope, for his support and help over the course of my PhD, especially with photophysics. In addition, I would like to thank the postdocs who have helped me through my time at Cardiff University, who are now no longer with us, having moved on to bigger and brighter futures: Dr Andrew Wood, Dr Samuel Adams, Dr Mauro Monti, and Dr Adam Day. I would also like to thank the Cardiff University technical services team for running mass spectrometry experiments. As well as Dr Thomas Davies for his help with Electron Microscopy. Of course, a huge thank you to labmates past and present, but especially to Chris, Ella, Sam, Adam, Andy, Siôn, Bria, Mark, Rob, Matt, and Taylor for keeping me sane and helping me over the course of my PhD. As well as Jordan for his help with learning Quantum Espresso. Lastly, I would like to express enormous gratitude towards my parents and family for supporting me not just during the writing of this thesis but also during my entire time at Cardiff.

Table of Contents

1	Introduction	1
1.1	Project Aims.....	2
1.2	Luminescence.....	2
1.3	Organic Luminophores.....	5
1.4	Luminescent Materials	7
1.4.1	Organic Light Emitting Diodes.....	8
1.4.2	Polymer Light Emitting Diodes	11
1.4.3	Inorganic Light Emitting Diodes.....	13
1.4.3.1	II-VI Binary Phosphors	15
1.4.3.2	Ternary Phosphors.....	17
1.4.3.2.1	Copper Indium Sulfides.....	17
1.4.3.2.2	Zinc Indium Sulfides.....	17
1.4.3.3	Perovskites.....	18
1.4.3.3.1	Lead Perovskites	19
1.4.3.3.2	Tin Perovskites	19
1.4.3.3.3	Bismuth Perovskites	20
1.5	Inorganic vs. Organic Phosphors	21
1.6	References	22
2	Synthesis and Characterisation of Zinc Sulfide Phosphors	28
2.1	Aims	29
2.2	Introduction.....	30
2.2.1	Copper, and Copper Co-Doped Zinc Sulfides	31
2.2.2	Silver Doped Zinc Sulfides.....	34
2.2.3	Manganese Doped Zinc Sulfides	34
2.2.4	Barium and Manganese Co-Doped Zinc Sulfides.....	35
2.3	Experimental and Methods	35
2.3.1	Synthetic Procedures.....	36
2.4	Results and discussion	39

Table of Contents

2.4.1	Synthesis of Zinc Sulfides	39
2.4.2	Copper and Aluminium Doped Zinc Sulfides	40
2.4.2.1	Assessment of Literature Methods	40
2.4.2.2	Aluminium Doped Zinc Sulfides	44
2.4.2.3	Copper Doped Zinc Sulfides	46
2.4.2.3.1	SEM and EDX Analysis	46
2.4.2.3.2	Luminescence Spectroscopy	48
2.4.2.3.3	Wet Impregnation	52
2.4.2.4	Computational Studies	56
2.4.2.4.1	Computational Details	57
2.4.2.4.2	Generalised Gradient Approximation Calculations	58
2.4.2.4.2.1	GGA Parameterisation	58
2.4.2.4.2.2	Supercell optimisation	59
2.4.2.4.2.3	Band Structures and Projected Density of States	61
2.4.2.4.3	Non-Self-Consistent GW calculations	65
2.4.2.4.3.1	GW Parameterisation	65
2.4.2.4.3.2	Band Structures and Density of States	66
2.4.3	Group 2 Doped Zinc Sulfides	72
2.4.3.1	SEM and EDX Analysis	72
2.4.3.2	PXRD Analysis	78
2.4.3.3	Luminescence Spectroscopy of Barium Doped Zinc Sulfides	80
2.4.3.4	Luminescence Spectroscopy of Strontium Doped Zinc Sulfides	82
2.4.3.5	Luminescence Spectroscopy of Calcium Doped Zinc Sulfides	84
2.4.4	Manganese Doped Zinc Sulfides	88
2.4.5	Group 2 and Manganese Co-Doped Zinc Sulfides	89
2.4.5.1	SEM and EDX Analysis	89
2.4.5.2	PXRD Analysis	94
2.4.5.3	Luminescence Spectroscopy of Barium and Manganese Oxide Doped Zinc Sulfides	96

Table of Contents

2.4.5.4	Luminescence Spectroscopy of Barium and Manganese Nitrate Doped Zinc Sulfides	98
2.4.5.5	Luminescence Spectroscopy of Strontium and Manganese Oxide Doped Zinc Sulfides.....	99
2.4.5.6	Luminescence Spectroscopy of Calcium and Manganese Oxide Doped Zinc Sulfides	101
2.4.6	Silica Coating of Zinc Sulfides.....	102
2.4.6.1	Uncoated Zinc Sulfide	102
2.4.6.2	Silica Coated Zinc Sulfide.....	105
2.5	Conclusion.....	110
2.5.1	Determination and Assignment of Defects Within Doped Zinc Sulfides.....	110
2.5.1.1	Experimental analysis	110
2.5.1.2	Computational analysis	111
2.5.2	Doping of Zinc Sulfides with Group 2 Metals and Manganese	112
2.5.3	Silica Coating of Zinc Sulfides.....	112
2.6	References	113
3	Luminophore Design, Synthesis, and Characterisation.....	116
3.1	Aims	117
3.2	Introduction.....	117
3.2.1	Epoxides.....	118
3.2.2	1,8-Naphthalimides.....	120
3.2.3	9,10-Anthraquinones.....	122
3.3	Results and Discussion.....	125
3.3.1	Luminophore Synthesis and characterisation.....	125
3.3.1.1	1,8-Naphthalimide Based Luminophores.....	125
3.3.1.2	Thiol functionalisation.....	126
3.3.1.3	Amine Functionalisation	128
3.3.1.4	Epoxide functionalisation of a 1,8-naphthalimide.....	129
3.3.1.5	1-Aminoanthraquinone Based Luminophores	132
	UV-Vis Absorption Spectroscopy	135

Table of Contents

3.3.2	Luminescence Spectroscopy	140
3.4	Conclusion	141
3.5	Experimental and methods	142
3.5.1	X-Ray Diffraction Data Collection and Refinement	142
3.5.2	DFT Studies	143
3.5.3	Synthetic Procedures	143
3.6	References	152
4	Design, Synthesis, and Characterisation of Luminophore Functionalised Doped-Ring Opening Co-Polymerisation Polymers	155
4.1	Aims	156
4.2	Introduction	157
4.2.1	Current Plastics	157
4.2.2	Tuning Polymer Properties	160
4.2.3	Luminescent Polymers	160
4.2.4	Sustainable Polymers	164
4.2.5	Ring Opening Co-Polymerisation (ROCOP)	165
4.2.5.1	Post-Polymerisation Modification	171
4.2.5.2	Degradation of Polyesters	171
4.3	Results and Discussion	173
4.3.1	Catalyst Synthesis	173
4.3.2	Polymer Synthesis	173
4.3.2.1	Small Scale Synthesis and Characterisation	175
4.3.2.2	Large Scale (300 g) Synthesis and Characterisation	180
4.3.3	UV-Vis Absorption Spectroscopy	186
4.3.3.1	[Al(^t Bu-salen)Cl]	186
4.3.3.2	Functionalised Polymers	187
4.3.4	Luminescence Spectroscopy	189
4.3.5	Post-Polymerisation Modification of Polymers	190
4.3.6	Polymer degradation	192

Table of Contents

4.3.7	Doped Polymers as Functionalised Materials.....	194
4.4	Conclusion.....	194
4.5	Experimental and Methods.....	195
4.6	References.....	198
5	Thesis Summary and Future Work.....	201
5.1	Summary.....	202
5.2	Future Work.....	204
5.3	References.....	206
6	Appendix.....	207
6.1	Chapter 2 Appendix.....	208
6.2	Chapter 3 Appendix.....	224
6.2.1	UV-Vis Absorption Graphs.....	224
6.2.2	TD-DFT Graphs.....	224
6.2.3	Cartesian Coordinates.....	249
6.3	Chapter 4 Appendix.....	255
6.3.1	Small Scale AAQ Doped Polymer.....	255
6.3.2	Large Scale Polymer Synthesis.....	258
6.3.3	Post-Polymerisation Modification.....	260
6.3.4	Polymer Degradation.....	261
6.3.5	Cartesian Coordinates.....	267

Table of Figures

Figure 1.1: Jablonski diagram.	3
Figure 1.2: Structures and photophysical parameters of selected chromophores with their spectra recorded in select solvents: ^a acetone, ¹⁷ ^b acetone, ^c iso-propanol, ¹⁵ ^d isopropanol. ¹⁶ ...	6
Figure 1.3: Structures and photophysical parameters of selected 1,8-naphthalimide luminophores. ^a Acetonitrile, ²⁰ ^b acetonitrile. ²¹	7
Figure 1.4: Simplified structure of an OLED device.	8
Figure 1.5: Structure of tris(8-hydroxyquinoline)aluminium.....	8
Figure 1.6: Structure of tris(8-hydroxyquinoline)aluminium derivatives.....	9
Figure 1.7: Structure of luminescent aluminium complexes with salen type ligands.	10
Figure 1.8: Structure of some imidazole coumarin derivatives.....	10
Figure 1.9: Structure of some luminescent triarylborons.....	11
Figure 1.10: Structure of a white light emitting polymer containing green and red (iridium) emitting components.	12
Figure 1.11: Structure of a white light emitting polymer without a green emitting component.	12
Figure 1.12: Structure of a white light emitting polymer containing platinum.....	13
Figure 1.13: Structure of a white light emitting polymer containing zinc.....	13
Figure 1.14: Energy diagram for nanoparticle emission tuneability (L), and dopant emission tuneability (R).....	15
Figure 1.15: Wurtzite crystal structure, where black circles represent zinc and yellow circles represent sulfur.	16
Figure 1.16: Perovskite structure, where black circles represent monovalent cations (A), red circles represent monovalent anions (X) and the blue circle represents an inorganic cation (B).....	18
Figure 2.1: Pictorial representations (clockwise) of pure zinc sulfide, zinc sulfide with a substitutional defect, zinc sulfide with a sulfur vacancy defect, and zinc sulfide with an interstitial zinc defect. Where zinc = black circles, sulfur = yellow circles, substituted ion = red circle, interstitial ion = blue circle, and dashed purple circle = vacant site.....	30
Figure 2.2: Excitation (left) ($\lambda_{em1} = 483 \text{ nm}$, $\lambda_{em2} = 456 \text{ nm}$, $\lambda_{em3} = 478 \text{ nm}$, $\lambda_{em} = 471 \text{ nm}$) and emission (right) ($\lambda_{ex} = 345 \text{ nm}$) spectra for example literature samples.	41
Figure 2.3: SEM and EDX images for aluminium sulfide doped zinc sulfide showing contributions from zinc, sulfur and oxygen.	44
Figure 2.4: Excitation (left) and emission (right) spectra of aluminium sulfide doped zinc sulfides.....	45

Table of Figures

Figure 2.5: SEM images of copper doped zinc sulfides: a) solid state CuSO_4 (6), b) solid state $\text{CuI NH}_4\text{Cl}$ (7), c) wet impregnation CuSO_4 (10), d) wet impregnation no dopant	47
Figure 2.6: SEM and EDX images of doped ZnS samples a) CuI (5), b) $\text{CuI, NH}_4\text{Cl}$ (7), c) CuSO_4 (6), and d) $\text{CuSO}_4, \text{AlNO}_3 \cdot (\text{H}_2\text{O})_9$ (4) prepared by the solid state method, showing contributions from zinc, sulfur and oxygen.	48
Figure 2.7: Excitation (left) and emission (right) spectra for doped zinc sulfides with the two excitation and emission wavelengths labelled.	49
Figure 2.8: Excitation (left) and emission (right) spectra of CuSO_4 and NH_4Cl , and NH_4Cl doped zinc sulfides method with excitation and emission wavelengths (nm) labelled.	52
Figure 2.9: Excitation (left) and emission (right) spectra for CuSO_4 (10) doped zinc sulfides.	54
Figure 2.10: Excitation (left) and emission (right) spectra of undoped zinc sulfide with excitation and emission wavelengths labelled.	55
Figure 2.11: Energy (black line, ●) and nominal band gap (red line, o) of a 64 atom zinc sulfide cell with a lattice parameter of 10.81854 Å, and the same structure with an optimised lattice parameter of 10.71451 Å; energy (blue line, ▲) and band gap (orange line, Δ) as the kinetic energy cutoff of the wavefunction (ecutwfc) is altered.	59
Figure 2.12: Band structure (left) where purple lines indicate the top and bottom of the valence and conductance bands, respectively. PDOS (right) showing the contribution of orbitals towards the filled (shaded) and empty bands for an optimised ZnS supercell of 64 atoms with no defects.	62
Figure 2.13: Band structure (left) where purple lines indicate the top and bottom of the valence and conductance bands of the bulk ZnS, respectively; and the yellow line indicates the top of the valence band caused by the sulfur defect. PDOS (right) showing the contribution of orbitals towards the filled (shaded) and empty bands for an optimised ZnS supercell of 65 atoms with an interstitial sulfur.	64
Figure 2.14: Band structure (left) where purple lines indicate the top and bottom of the valence and conductance bands respectively. DOS (right) showing the contribution of orbitals towards the filled (shaded) and empty bands for an optimised ZnS supercell of 64 atoms with no defects.	66
Figure 2.15: Band structure (left) where purple lines indicate the top and bottom of the valence and conductance bands respectively. DOS (right) showing the contribution of orbitals towards the filled (shaded) and empty bands for an optimised ZnS supercell of 64 atoms with an interstitial sulfur defect.....	70
Figure 2.16: Band structure (left) where purple lines indicate the top and bottom of the valence and conductance bands respectively. DOS (right) showing the contribution of	

Table of Figures

orbitals towards the filled (shaded) and empty bands for an optimised ZnS supercell of 64 atoms with an interstitial zinc defect.	70
Figure 2.17: Band structure (left) where purple lines indicate the top and bottom of the valence and conductance bands respectively. DOS (right) showing the contribution of orbitals towards the filled (shaded) and empty bands for an optimised ZnS supercell of 63 atoms with a zinc vacancy defect.	71
Figure 2.18: Band structure (left) where purple lines indicate the top and bottom of the valence and conductance bands respectively. DOS (right) showing the contribution of orbitals towards the filled (shaded) and empty bands for an optimised ZnS supercell of 63 atoms with a sulfur vacancy defect.	71
Figure 2.19: SEM image of 8 mol% barium (a), 8 mol% strontium (b), 8 mol% calcium (c) and 4 mol% strontium (d) doped zinc sulfides.	72
Figure 2.20: SEM and EDX images for zinc sulfide with varying barium doping levels: a) 8 mol% b) 4 mol% c) 2 mol% showing contributions from zinc, sulfur barium and oxygen.	73
Figure 2.21: SEM image of 4 mol% barium doped zinc sulfide with point analysis locations marked.	76
Figure 2.22: SEM and EDX images for 4 mol% barium doping at different accelerating voltages: a) 5 kV, b) 15 kV, c) 30 kV showing contributions from zinc, sulfur barium and oxygen.	78
Figure 2.23: PXRD pattern for varying barium doping: 8 mol% 4 mol% 2 mol%, undoped zinc sulfide, and calculated powder patterns for barium sulfide, sphalerite and wurtzite. S indicates sphalerite phase, and W the wurtzite phase.	79
Figure 2.24: Excitation (left) ($\lambda_{em} = 450$ nm) and emission (right) ($\lambda_{ex} = 372$ nm) spectra for barium doped zinc sulfides.	80
Figure 2.25: Excitation (left) ($\lambda_{em} = 518$ nm) and emission (right) ($\lambda_{ex} = 410$ nm) spectra for barium doped zinc sulfides.	81
Figure 2.26: Calculated structure of barium doped (L) and undoped (R) zinc sulfide using the PBEsol functional.	82
Figure 2.27: Excitation (left) and emission (right) spectra for strontium doped zinc sulfides.	83
Figure 2.28: Excitation (left) and emission (right) spectra for 10 mol% calcium doped zinc sulfide.	84
Figure 2.29: Excitation (left) and emission (right) spectra for 8 mol% calcium doped zinc sulfide with excitation and emission wavelengths labelled.	86
Figure 2.30: Excitation (left) and emission (right) ($\lambda_{ex} = 345$ nm) spectra of manganese nitrate hydrate and manganese oxide doped zinc sulfides.	88

Table of Figures

Figure 2.31: SEM image of 2 mol% barium with manganese oxide (a), 8 mol% barium with manganese nitrate (b), 4 mol% strontium with manganese oxide (c), and 8 mol% calcium with manganese oxide (d) doped zinc sulfides.	89
Figure 2.32: SEM and EDX images for barium sulfide and manganese oxide doped zinc sulfides a) 8 mol% Ba, b) 4 mol% Ba, c) 2 mol% Ba showing contributions from zinc, sulfur barium, oxygen, and manganese.	91
Figure 2.33: PXRD pattern for barium and manganese oxide doped zinc sulfide: 8 mol% 4 mol% 2 mol% Ba, undoped zinc sulfide, and calculated powder patterns for barium sulfide, sphalerite and wurtzite. S indicates sphalerite phase, and W the wurtzite phase.	95
Figure 2.34: PXRD pattern for barium and manganese nitrate doped zinc sulfide: 8 mol% 4 mol% 2 mol% Ba, undoped zinc sulfide, and calculated powder patterns for barium sulfide, sphalerite and wurtzite. S indicates sphalerite phase, and W the wurtzite phase.	96
Figure 2.35: Excitation spectra of the emission peaks in 8 mol% barium sulfide, and manganese oxide doped zinc sulfides.....	97
Figure 2.36: Excitation (left) ($\lambda_{em\ 8,4\ mol\%} = 620\ nm$, $\lambda_{em\ 2\ mol\%} = 587\ nm$) and emission (right) ($\lambda_{ex\ 8,4\ mol\%} = 360\ nm$, $\lambda_{ex\ 2\ mol\%} = 350\ nm$) of barium sulfide and manganese oxide doped zinc sulfides.....	97
Figure 2.37: Excitation (left) ($\lambda_{ex,\ 8,\ 4\ mol\%} = 612\ nm$, $\lambda_{ex,\ 2\ mol\%} = 580\ nm$) and emission (right) ($\lambda_{ex,\ 8,\ 4\ mol\%} = 360\ nm$, $\lambda_{ex,\ 2\ mol\%} = 350\ nm$) spectra of barium sulfide and manganese nitrate.	98
Figure 2.38: Excitation (left) ($\lambda_{em} = 584\ nm$) and emission (right) ($\lambda_{ex} = 345\ nm$) spectra for strontium sulfide, and manganese oxide doped zinc sulfides	99
Figure 2.39: Excitation ($\lambda_{em} = 515\ nm$) spectra of strontium sulfide and manganese oxide doped zinc sulfides	100
Figure 2.40: Excitation (left) ($\lambda_{em} = 581\ nm$) and emission (right) ($\lambda_{ex} = 345\ nm$) spectra of calcium sulfide (8 mol%) and manganese oxide doped zinc sulfide	101
Figure 2.41: SEM images of uncoated zinc sulfides treated with silica coating method without the addition of tetraethoxysilane exposed to different conditions: a) nitrogen at 800 °C, b) stored in vial, c) air at 800 °C.	103
Figure 2.42: SEM and EDX images of uncoated zinc sulfides treated with silica coating method without the addition of tetraethoxysilane exposed to different conditions: a) nitrogen at 800 °C, b) stored in a vial, c) air at 800 °C showing contributions from zinc, sulfur, silicon, and oxygen.	105
Figure 2.43: SEM images of silica coated zinc exposed to different conditions: a) nitrogen at 800 °C, b) stored in vial, c) air at 800 °C.	106

Table of Figures

Figure 2.44: Silica coated zinc sulfides exposed to different conditions: a) nitrogen at 800 °C, b) air at room temperature, c) air at 800 °C showing contributions from zinc, sulfur, silicon, and oxygen.	107
Figure 2.45: SEM and EDX images of silica coated zinc sulfides heat treated at 800 °C in air at difference accelerating voltages: a) 5kV, b) 15 kV, c) 30 kV showing contributions from zinc, sulfur, silicon, and oxygen.....	110
Figure 3.1: Example structures of blue emitting 1,8-naphthalimides.....	121
Figure 3.2: Example structures of 4-amino substituted 1,8-naphthalimides.	122
Figure 3.3: Examples of anthraquinone dyes, and their colours.	123
Figure 3.4: Intramolecular charge transfer observed in 1-aminoanthraquinones.	123
Figure 3.5: Example structures of substituted anthraquinones.	124
Figure 3.6: Molecular structure of 4-piperdiny-N-(propylene oxide)-naphthalimide, only one orientation is shown, H atoms omitted for clarity.	132
Figure 3.7: Crystal network and packing of 55 showing the double herringbone arrangement (top) and the rotation of the compound between layers.....	132
Figure 3.8: Molecular structure of 1-(propylene-oxide)amino)anthraquinone, only one orientation is shown, H atoms omitted for clarity.	134
Figure 3.9: Crystal network and stacking of 58 showing the slight displacement of the anthraquinone groups between layers and the orientation of the anthraquinones such that the epoxide groups form equilateral triangles within a plane. (The apparent circular arrangement of the epoxides is from two separate layers of anthraquinones)	135
Figure 3.10: UV-Vis absorption spectra for compounds 46a , 54 , and 55 , as chloroform solutions.....	135
Figure 3.11: Experimental (black line) and simulated (red line, predicted ϵ) UV-Vis spectra of 55 in chloroform using TD-DFT with the B3LYP functional and cc-PVDZ basis set	136
Figure 3.12: Calculated HOMO (bottom) and LUMO (top) and geometries of 58 using the B3LYP functional and cc-PVDZ basis set.....	138
Figure 3.13: Calculated HOMO (bottom) and LUMO (top) and geometries of 55 using the B3LYP functional and cc-PVDZ basis set.....	138
Figure 3.14: UV-Vis absorption spectra of compounds 58 , and 59 , as chloroform solutions.	139
Figure 3.15: Experimental (black line) and simulated UV-Vis spectra (red line, predicted ϵ) of 58 in chloroform performed with TD-DFT using the B3LYP functional and cc-PVDZ basis set.	140
Figure 3.16: Excitation and emission spectra for compounds 47 (black line), 55 (red line), and 59 (blue line) as chloroform solutions.....	141
Figure 4.1: Doped ring-opening co-polymerisation (D-ROCOP).	156

Table of Figures

Figure 4.2: Porphyrin catalysts for the co-polymerisation of epoxides and anhydrides.	166
Figure 4.3: Structure of β -diiminate zinc catalysts.	167
Figure 4.4: Examples of salicylaldehyde/amine based catalysts used for the co-polymerisation of epoxides and anhydrides.....	168
Figure 4.5: Structure of the polymer degraded by the Williams group. ⁶⁷	172
Figure 4.6: Example ¹ H NMR spectra of a polymerisation reaction mixture with highlighted regions showing the conversion of monomer (green region) to polymer (orange region) and the selectivity of the ester formation (blue region) vs ether formation (red region).....	175
Figure 4.7: Structure of the AAQ doped PhA-CHO co-polymer.	175
Figure 4.8: Experimental and fitted GPC data for AAQ-PhA-CHO1	176
Figure 4.9: repeat unit of PhA-Nap co-polymer, PhA-Nap	179
Figure 4.10: 2 litre reaction vessel used for large scale polymerisation reactions (AAQ-PHA-CHO3).	180
Figure 4.11: Structure of the polymer repeat unit and the luminophore dopants.....	181
Figure 4.12: Deconvoluted GPC traces of vacuum oven dried large scale polymers.	183
Figure 4.13: Solid polymer samples (L to R) PhA-CHO , AAQ-PhA-CHO3 , Nap-PhA-CHO under ambient light (Top). Eluted GPC solvent showing the emissive polymer (Nap-PhA-CHO) fractions (Bottom).....	185
Figure 4.14: UV-Vis absorption spectra for compounds 37 , and 38 as chloroform solutions.	186
Figure 4.15: Experimental (black line) and simulated (red line, predicted ϵ) UV-Vis spectra of 38 in chloroform using TD-DFT with the B3LYP functional and cc-PVDZ basis set.	187
Figure 4.16: Calculated HOMO (bottom) and LUMO (top) and geometries of the ^t Bu-Salen ligand (L) (37) and [Al(^t Bu-Salen)Cl] (R) (38) using the B3LYP functional and cc-PVDZ basis set.....	187
Figure 4.17: UV-Vis absorption spectra for the three large scale doped polymers.....	188
Figure 4.18: Structure of the PhA-CHO catalyst with the alkoxide aluminium species bound.	190
Figure 4.19: Excitation (L) (λ_{em} = 480 nm (PhA-CHO), 583 nm (AAQ-PhA-CHO3), and 510 nm (Nap-PhA-CHO)) and emission (R) (λ_{ex} = 370 nm (PhA-CHO), 490 nm (AAQ-PhA-CHO3), and 410 nm (Nap-PhA-CHO)) spectra of the large scale polymers.	189
Figure 4.20: MALDI spectrum for un-functionalised (L) and functionalised (R) co-polymers.	191
Figure 4.21: Experimental and fitted GPC data for ECH(38)-PhA	192
Figure 4.22: Example structure from acidic hydrolysis of a polyester.	193
Figure 4.23: Images of extruded polymer showing the high crystallinity and brittleness of the extruded material.	194

Table of Figures

Figure 6.1: SEM and EDX images of ZnS samples a) No dopant, b) NH ₄ Cl, c) CuSO ₄ , and d) CuSO ₄ , NH ₄ Cl prepared by wet impregnation showing contributions from zinc, sulfur, and oxygen.	208
Figure 6.2: Energy (black line, ●) and band gap (red line, o) of a 64 atom zinc sulfide cell with a lattice parameter of 20.44408 Bohr (10.81854 Å) as the kinetic energy cutoff of the charge density and potential (ecutrho) is altered.	209
Figure 6.3: Energy (black line, ●) and band gap (red line, o) of a 64 atom zinc sulfide cell with a lattice parameter of 20.24749 Bohr (10.71451 Å) as the kinetic energy cutoff of the charge density and potential (ecutrho) is altered.	209
Figure 6.4: Band structure (L) where purple lines indicate the top and bottom of the valence and conductance bands respectively. PDOS (R) showing the contribution of orbitals towards the filled (shaded) and empty bands for a fixed ZnS supercell of 64 atoms with no defects.	210
Figure 6.5: Band structure (L) where purple lines indicate the top and bottom of the valence and conductance bands of the bulk ZnS, respectively; and the yellow line indicates the bottom of the conductance band caused by the zinc defect. PDOS (R) showing the contribution of orbitals towards the filled (shaded) and empty bands for an optimised ZnS supercell of 64 atoms with an interstitial zinc.	211
Figure 6.6: Band structure (L) where purple lines indicate the top and bottom of the valence and conductance bands respectively. PDOS (R) showing the contribution of orbitals towards the filled (shaded) and empty bands for a fixed ZnS supercell of 64 atoms with a sulfur vacancy.	212
Figure 6.7: Band structure (L) where purple lines indicate the top and bottom of the valence and conductance bands respectively. PDOS (R) showing the contribution of orbitals towards the filled (shaded) and empty bands for a fixed ZnS supercell of 64 atoms with a zinc vacancy.	213
Figure 6.8: Energy of the valence and conductance bands for an optimised ZnS supercell with 64 atoms as the cutoff energy governing the number of RL vectors is changed.	214
Figure 6.9: Energy of the valence and conductance bands for an optimised ZnS supercell with 64 atoms as the cutoff energy governing the size of the dielectric matrix is changed.	214
Figure 6.10: SEM and EDX data for strontium doped zinc sulfides at varying dopant levels; a) 8 mol%, b) 4 mol%, c) 2 mol% showing contributions from zinc, sulfur, strontium, and oxygen.	215
Figure 6.11: Calculated structure of a 64 atom ZnS supercell with a strontium defect (green) using the PBEsol functional.	216
Figure 6.12: SEM and EDX data for calcium doped zinc sulfides at varying dopant levels; a) 12 mol%, b) 8 mol% showing contributions from zinc, sulfur, calcium, and oxygen.	217

Table of Figures

Figure 6.13: Calculated structure of a 64 atom ZnS supercell with a calcium defect (green) using the PBEsol functional.....	218
Figure 6.14: SEM and EDX images for barium sulfide and manganese nitrate doped zinc sulfides a) 8 mol% Ba, b) 4 mol% Ba, c) 2 mol% Ba showing contributions from zinc, sulfur, barium, oxygen, and manganese	219
Figure 6.15: X-ray spectrum for 8 mol% barium and manganese oxide doped zinc sulfide	220
Figure 6.16: SEM and EDX images for strontium sulfide and manganese oxide doped zinc sulfides a) 8 mol% Sr, b) 4 mol% Sr, c) 2 mol% Sr showing contributions from zinc, sulfur, strontium, oxygen, and manganese	221
Figure 6.17: SEM and EDX images for 8 mol% calcium sulfide and manganese sulfide doped zinc sulfides showing contributions from zinc, sulfur, calcium, oxygen, and manganese	222
Figure 6.18: SEM and EDX images of uncoated zinc sulfides heat treated at 800 °C in air at difference accelerating voltages: a) 5kV, b) 15 kV, c) 30 kV showing contributions from zinc, sulfur, silicon, and oxygen.....	223
Figure 6.19: UV-Vis absorption spectra of 50a , and 50b as chloroform solutions, with the TFA counterion omitted for clarity.....	224
Figure 6.20: Experimental (black line) and simulated UV-Vis spectra (red line, predicted ϵ) of 45b in chloroform performed with TD-DFT using the B3LYP functional and cc-PVDZ basis set.....	224
Figure 6.21: Experimental (black line) and simulated UV-Vis spectra (red line, predicted ϵ) of 54 in chloroform performed with TD-DFT using the B3LYP functional and cc-PVDZ basis set.	225
Figure 6.22: Experimental (black line) and simulated UV-Vis spectra (red line, predicted ϵ) of 58 in chloroform performed with TD-DFT using the B3LYP functional and cc-PVDZ basis set.	225
Figure 6.23: Calculated molecular structure of 4-Piperidiny-1,8-naphthalic anhydride	249
Figure 6.24: Calculated molecular structure of 4-Piperidiny-1,8-naphthalimide.....	250
Figure 6.25: Calculated molecular structure of 4-Piperidiny-1,8-naphthalimide.....	251
Figure 6.26: Calculated molecular structure of 1-((3-chloro-2-hydroxypropyl)amino)anthraquinone	253
Figure 6.27: Calculated molecular structure of 1-(propylene-oxide)amino)anthraquinone (66).	254
Figure 6.28: Experimental and fitted GPC data for AAQ-PhA-CHO2	255
Figure 6.29: Ring opened epoxide regions.....	256
Figure 6.30: Experimental and fitted GPC data for Nap-Pha	257

Table of Figures

Figure 6.31: Experimental and fitted GPC data for PhA-CHO.	258
Figure 6.32: Experimental and fitted GPC data for AAQ-PhA-CHO	258
Figure 6.33: Experimental and fitted GPC data for Nap-PhA-CHO	259
Figure 6.34: Experimental (black line) and simulated (red line, predicted ϵ) UV-Vis spectra of 36 in chloroform using TD-DFT with the B3LYP functional and cc-PVDZ basis set	260
Figure 6.35: ESI mass spectrum for acidic hydrolysis of a polyester	261
Figure 6.36: Calculated molecular structure of ^t Bu-Salen (46).	267
Figure 6.37: Calculated molecular structure of [Al(^t Bu-Salen)Cl] (47).	268

Table of Schemes

Scheme 3.1: Proposed synthetic routes for functionalised polymers; post polymerisation modification (PPM), with a thiol-ene Click example given; and the direct polymerisation of the luminophore during the polymerisation.....	117
Scheme 3.2: Pathways for the synthesis of epoxides. (i) oxidant (H_2O_2 , m-CPBA, etc); (ii) NBS, water; (iii) Base	119
Scheme 3.3: Generalised synthetic routes to substituted 1,8-naphthalimides. (i) Primary amine, EtOH, (ii) Primary or secondary amine, DMSO, or 2-methoxyethanol.....	126
Scheme 3.4: Initial synthetic pathway for 4-amino substituted naphthalimides with a thiol functional group. (i) Ethanol, 2-aminoethanthiol; (ii) DMSO, piperidine.....	126
Scheme 3.5: Second synthetic pathway for 4-amino substituted naphthalimides with a thiol functional group. (i) 2-methoxyethanol, piperidine; (ii) ethanol, aminoethanthiol.....	127
Scheme 3.6: Synthesis of naphthalimides with a protected thiol group. (i) THF, thioacetic acid, AIBN; (ii). R = Cl (a) or piperidinyl (b).....	128
Scheme 3.7: Synthesis of naphthalimides with a terminal amine. (i) BOC-NHC ₂ H ₄ NH ₂ , EtOH; (ii) DCM, TFA. Where R = morpholinyl (a), or piperidinyl (b).....	129
Scheme 3.8: Post-polymerisation modification of a chloride containing co-polymer, ECH-PhA, using an amine-terminated naphthalimide showing the luminophore component. (i) MeCN, K ₂ CO ₃	129
Scheme 3.9: Initial route for the formation of epoxide functionalised naphthalimides. Where R = Cl (a), morpholinyl (b), or piperidinyl (c). (i) DCM, or DCE, and mCPBA.	129
Scheme 3.10: Second route for the synthesis of an epoxide terminated naphthalimide where R = Cl (a), morpholine (b) or piperidine (c). (i) THF/Water and NBS; (ii) 1,4 dioxane, NaOH.	130
Scheme 3.11: Final synthetic route for the synthesis of epoxide terminated 4-piperidinyl naphthalimides.(i) NH ₃ , EtOH; (ii) Epichlorohydrin, K ₂ CO ₃	131
Scheme 3.12: Initial reaction pathway for the synthesis of epoxide functionalised 1-aminoanthraquinone. (i) Epichlorohydrin, K ₂ CO ₃	133
Scheme 3.13: Successful synthetic route for the formation of epoxide terminated 1-aminoanthraquinone. (i) Epichlorohydrin, acetic acid; (ii) 1,4 dioxane, potassium hydroxide.	133
Scheme 4.1: Glycolysis of poly(ethylene terephthalate).	159
Scheme 4.2: Example synthesis of poly(fluorenes) doped with luminophores/chromophores; (i) Pd(PPh ₃) ₄ , K ₂ CO ₃ , 1 , 2 , toluene; ³⁶ (ii) Pd(PPh ₃) ₄ , K ₂ CO ₃ , 3 , toluene. ³⁷	161
Scheme 4.3: Synthesis of the PPE co-polymer. (i) Pd(PPh ₃) ₄ , CuI, toluene, ¹ Pr ₂ NH.	162
Scheme 4.4: Synthesis of triarylborane containing polymers; (i) Styrene, AIBN, anisole. ³⁸	162

Table of Schemes

Scheme 4.5: Synthesis of co-polymers using a naphthalimide dye. (i) Styrene, DBP, N ₂ ; (ii) methyl methacrylate, DBP, N ₂ ³⁹	163
Scheme 4.6: Synthesis of fluorescent polymers via mechanoradical coupling; (i) 1 , 30 Hz milling for 30 mins. ⁴⁰	164
Scheme 4.7: Example approaches of chromophore introduction via the DyeCat process: chromophore attached to the ligand, or as the ligand (10) and as an initiator (11).....	165
Scheme 4.8: Generalised Ring Opening Co-Polymerisation (ROCOP) of a cyclic anhydride and epoxide to form a polyester.	166
Scheme 4.9: Proposed catalytic cycle for phthalic anhydride and cyclohexene oxide co-polymerisation with a PPNCI co-catalyst. Adapted from Coates and Tolman. ⁵⁵	170
Scheme 4.10: Hydroboration and thiol-ene coupling of ROCOP polymers. ⁶⁴	171
Scheme 4.11: Degradation of a polyester via methanolysis; (i) MeOH, 150 °C, 12 h. ⁶⁸	172
Scheme 4.12: Synthesis of aluminium(3,5-ditertbutyl)chloride. (i) Diethylaluminium chloride, toluene.	173
Scheme 4.13: General route for the synthesis of ROCOP polymers.....	173
Scheme 4.14: Post-polymerisation modification of ECH-PhA using an amine-terminated naphthalimide showing the luminophore component. (i) MeCN, K ₂ CO ₃	191
Scheme 4.15: Degradation of doped polyesters under acidic conditions. (i) Toluene, pTSA•H ₂ O, 60 °C.	193

Table of Tables

Table 1.1: Comparison of organic and inorganic materials for display technologies	21
Table 2.1: Literature reported emission wavelengths and their assigned transitions.....	31
Table 2.2: Reported supplier purity and impurities of zinc sulfide and the dopants used within this chapter.	38
Table 2.3: MP-AES results for copper and aluminium doped zinc sulfides prepared according to literature reports.....	40
Table 2.4: Variations in dopant and method used to investigate the effect of copper doping on the luminescent properties of zinc sulfide.....	46
Table 2.5: Lattice parameter and average Zn-S, excluding the defect, and Zn/S defect to nearest neighbour site bond lengths	61
Table 2.6: Band gaps of samples with and without defects of cells with fixed lattice parameters.....	64
Table 2.7: GW, GGA and experimental band gaps in nm for the five calculated zinc sulfide systems: Pure ZnS with no defects (None), with an interstitial zinc (I_{Zn}), interstitial sulfur (I_S), zinc vacancy (V_{Zn}), and sulfur vacancy (V_S) defect.....	68
Table 2.8: Atomic% values for barium doped zinc sulfides from EDX mapping analysis.....	74
Table 2.9: Atomic% EDX data for strontium doped zinc sulfides.....	75
Table 2.10: Atomic% EDX data for calcium doped zinc sulfides	75
Table 2.11: Atomic % EDX data for 4 mol% barium doped zinc sulfide	77
Table 2.12: Excitation and emission wavelengths for zinc sulfides doped with group 2 metals	87
Table 2.13: Atomic% data for barium sulfide and manganese oxide doped zinc sulfides....	92
Table 2.14: Atomic% EDX map data for barium sulfide and manganese nitrate doped zinc sulfides	92
Table 2.15: Atomic% data from strontium sulfide and manganese oxide doped zinc sulfides	93
Table 2.16: Atomic% data for 8 mol% calcium sulfide and manganese oxide doped zinc sulfide	94
Table 2.17: Atomic% data from EDX analysis of uncoated zinc sulfides exposed to different conditions.....	103
Table 2.18: Atomic% data for non-silica coated zinc sulfide exposed to flowing air at 800 °C at different accelerating voltages.....	104
Table 2.19: Atomic% data for silica coated zinc sulfides exposed to different conditions. .	108
Table 2.20: Atomic% data for silica coated zinc sulfides exposed to air at 800 °C at different accelerating voltages	109

Table of Tables

Table 2.21: Recommended dopants to achieve the desired emission wavelengths outlined during the aims section	112
Table 3.1: Absorbance wavelengths (λ) and molar absorptivity (ϵ) for 1,8-naphthalimides showing the influence of 4-position and imide substitution	136
Table 3.2: Fluorescence properties of synthesised luminophores suitable for polymer incorporation as chloroform solutions.....	141
Table 4.1: Structure and use cases of commonly encountered plastics.....	157
Table 4.2: Fitted GPC data for AAQ doped PhA-CHO co-polymers.....	178
Table 4.3: Fitted GPC data for PhA-CHO	180
Table 4.4: Fitted GPC data for large scale polymers.....	184
Table 4.5: Fluorescence properties of the large scale polymers as chloroform solutions..	190
Table 6.1: Crystal data and structure refinement for 55.....	226
Table 6.2: Atomic coordinates ($\times 10^4$) and equivalent isotropic displacement parameters ($\text{\AA}^2 \times 10^3$) for 55 . $U(\text{eq})$ is defined as one third of the trace of the orthogonalized U^{ij} tensor	226
Table 6.3: Bond lengths [\AA] and angles [$^\circ$] for 55.....	227
Table 6.4: Crystal data and structure refinement for 58.....	229
Table 6.5: Atomic coordinates ($\times 10^4$) and equivalent isotropic displacement parameters ($\text{\AA}^2 \times 10^3$) for 58 . $U(\text{eq})$ is defined as one third of the trace of the orthogonalized U^{ij} tensor	230
Table 6.6: Bond lengths [\AA] and angles [$^\circ$] for 58.....	230
Table 6.7: GPC fit parameters for AAQ-PhA-CHO1	255
Table 6.8: GPC fit parameters for AAQ-PhA-CHO2	256
Table 6.9: GPC fit parameters for Nap-PhA	257
Table 6.10: GPC fit parameters for large scale polymers.....	259
Table 6.11: GPC fit parameters for ECH(38)-PhA	260

Table of Equations

Equation 1.1: Determination of lifetime (τ) where k_r is the radiative rate constant and k_{nr} is the non-radiative rate constant.....	4
Equation 1.2: Determination of quantum yield (Φ) where k_r is the radiative rate constant and k_{nr} is the non-radiative rate constant.....	4
Equation 1.3: Beer-Lambert law which governs how strongly a sample will absorb light in solution. Where A = absorption, ϵ = molar absorptivity, c = concentration ($\text{mol}^{-1}\text{dm}^3$), and l = light pathlength (cm).....	5
Equation 4.1: Exponentially modified gaussian (EMG) used for fitting GPC data as defined in the Fityk program ⁷³ . Where a = Gaussian height, b = Gaussian centre, c = gaussian width, d = distortion parameter.	177
Equation 4.2: Equation used to determine the predicted molecular weight for the polymers. Where Mw_p = predicted molecular weight, and M = molecular weight of the monomer	178
Equation 4.3: Determination of dopant concentration relative to theoretical via UV-Vis spectroscopy. Where, C = concentration, A = absorbance, and ϵ = molar absorptivity. As the path length was 1 cm it has been omitted from the equation.	188

Abbreviations

BHET	Bis(2-hydroxyethyl) terephthalate
BOC	tert-Butyloxycarbonyl
CHO	Cyclohexene oxide
CPA	cyclopentane-1,2-dicarboxylic acid anhydride
CPrA	Cyclopropane-1,2-dicarboxylic acid anhydride
DCE	Dichloroethane
DCM	Dichloromethane
DFT	Density functional theory
\bar{D}	Polydispersity index of a polymer, M_w/M_n
DMAP	4-dimethylaminopyridine
DMSO	Dimethyl sulfoxide
D-ROCOP	Doped-ring-opening co-polymerisation
ECH	Epichlorohydrin
EDX	Energy dispersive x-ray
EMG	Exponentially modified gaussian
EtOH	Ethanol
FEG-SEM	Field emission gun scanning electron microscopy
FWHM	Full width half height max
GGA	Generalised gradient approximation
GPC	Gel permeation chromatography
HDPE	High density poly(ethylene)
HOMO	Highest occupied molecular orbital
ICT	Intramolecular charge transfer
IPA	Isoproanol
IR	Infrared
Kr	Radiative decay rate constant
Knr	Non-radiative decay rate constant
LCD	Liquid Crystal Display
LDPE	Low Density Poly(ethylene)
LED	Light Emitting Diode
LUMO	Lowest Unoccupied Molecular Orbital
MALDI	Matrix Assisted Laser Desorption Ionisation

Abbreviations

<i>m</i> CPBA	<i>meta</i> -Chloroperoxybenzoic acid
MeCN	Acetonitrile
M _n	Number average molecular weight
M _w	Weight average molecular weight
NBS	N-bromosuccinimide
NMR	Nuclear magnetic resonance
OLED	Organic light emitting diode
PDOS	Projected density of states
PET	Poly(ethylene terephthalate)
PhA	Phthalic anhydride
PLA	Poly(lactic acid)
PO	Propylene oxide
PP	poly(propylene)
PPA	Plasmon pole approximation
PPM	Post-polymerisation modification
PPNCI	Bis(triphenylphosphine)iminium chloride
PXRD	Powder X-ray diffraction
Φ	Quantum yield
QLED	Quantum dot light emitting diode
ROCOP	Ring-opening co-polymerisation
SA	Succinic anhydride
SCF	Self consistent field
SO	Styrene oxide
T	Lifetime
^t Bu	tert-Butyl
TD-DFT	Time-dependant density functional theory
TFA	Trifluoro acetic acid
THF	Tetrahydrofuran
TLC	Thin layer chromatography
UV	Ultraviolet
UV-Vis	Ultraviolet visible
XRD	X-Ray diffraction

1 Introduction

1.1 Project Aims

This thesis aims to explore the development, characterisation, and analysis of both inorganic and organic luminescent materials for display technologies. Zinc sulfides are a well-known material, and extensively explored throughout the literature. However, the origin of the emission is still not fully understood with a range of assignments made, many of which are in conflict with each other. Therefore, there is a desire to further investigate the emission using a range of dopants, to ascertain the nature of the emission and defect states, in the hope that this can lead to development of zinc sulfide luminophores with commercially desirable properties. Organic light emitting diodes have become increasingly popular to display technologies as they provide individual pixel control providing completely black pixels, wider viewing angles, typically resulting in a perceived improvement in picture quality. However, the fabrication of these devices requires vacuum deposition of the organic layer,¹⁻³ which adds to the cost of the final product. Polymer based luminescent materials, have a significant advantage in this regard over traditional OLEDs as the solubility of the material is rarely an issue allowing more cost effective methods of deposition such as inkjet printing to be used.⁴ The approach used in this work aims to explore the benefits of a doping method for the introduction of luminophores into a non-luminescent host polymer through a polymerisation method, the ring opening co-polymerisation of anhydrides and epoxides. Such an approach was hoped to afford a range of physical properties that could be altered independently of the luminophore, potentially allowing the use of previously unusable materials. The existence of ester bonds within these polymers creates a target for chemical depolymerisation of the polymer, potentially affording a circular economy, reducing plastic pollution. To that end these polymers are also examined as an alternative to the plastics used throughout modern society. The existence of a covalent bond between the polymer and additive would result in color fast plastics and should function as a proof of concept for the incorporation of other additives to prevent leaching⁵ and degradation of the desired properties.

1.2 Luminescence

Briefly, luminescence is the radiative relaxation of an electron from an excited state to a ground state conformation with the release of a photon equivalent to the energy gap between these two states (Figure 1.1).⁶ There are a multitude of pathways capable of exciting a molecule, such as: chemiluminescence, mechanoluminescence, and electroluminescence. This thesis focuses on photoluminescence.

Chapter 1. Introduction

As implied by the name, photoluminescence involves the absorption of a photon, of suitable energy, by a molecule, promoting an electron from the singlet ground state (S_0) to an excited state level (S_1 , S_2 , etc.). The Franck-Condon principle states that the electronic transition to the excited state occurs on a timescale shorter than that of nuclear motion, i.e., vibrations,⁷ and thus the molecule is excited to an excited vibrational state within the excited state manifold. Because room temperature is not sufficient to populate the higher excited states, absorption and emission typically occur from the lowest vibrational state. Following

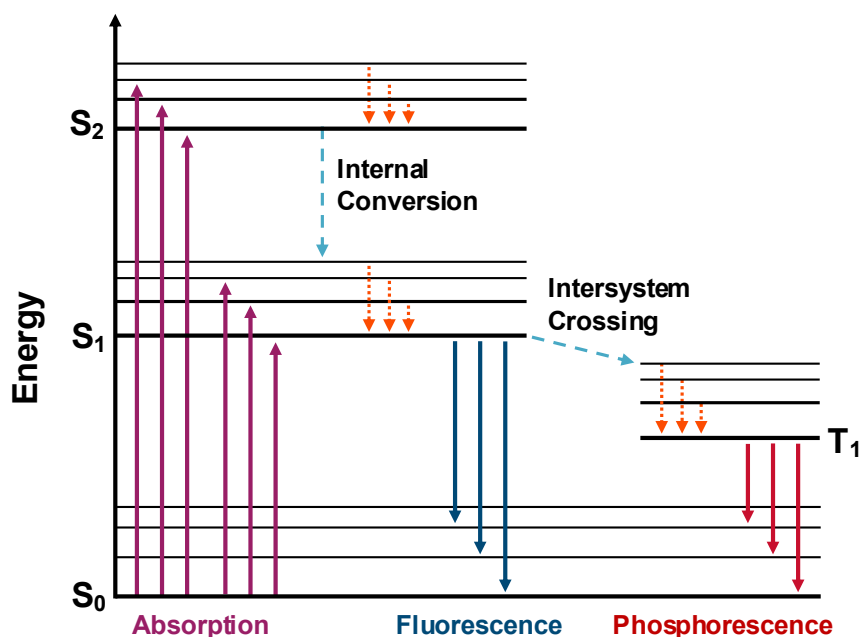


Figure 1.1: Jablonski diagram.

excitation by a photon, the molecule exists in both an excited electronic state and vibrational state. Relaxation of the molecule to the lowest vibrational level happens rapidly, within 10^{-12} s, and as fluorescence lifetimes are typically three orders of magnitude slower than relaxation, emission will occur from thermally equilibrated vibrational levels, as dictated by Kasha's rule. Therefore, this often means emission wavelength is independent of excitation, in cases such as excitation to higher electronic level (S_2), which relaxes to the lowest excited state (S_1), this is not the case. Emission from the excited state typically occurs to an excited vibrational level within the ground state, which like the excited state, rapidly relaxes back to the ground state vibrational level. This also means that emission and absorption are often mirror images of each other, since the spacing of the vibrational levels in the excited state are not significantly different from that of the ground state. The relaxation to a lower vibrational excited state causes a decrease in the energy of the transition back to the ground state, and thus the wavelength of light emitted will be of a shorter wavelength than the light absorbed, this phenomenon is called the Stokes' shift. In addition to relaxation to the ground state from a singlet state, a second pathway is relaxation from a triplet state (T_1), termed phosphorescence, and causes emission at longer wavelengths than fluorescence due to the

Chapter 1. Introduction

lower-lying T_1 state. The conversion of a singlet state to a triplet state is called intersystem crossing and is mediated by a heavy atom, such as third row transition metals. As the molecule now exists in an excited triplet state, relaxation to the singlet state is spin forbidden and occurs over relatively long time (10^{-4} to 10^2 s).

The lifetime (Equation 1.1) and quantum yield (Equation 1.2) of the luminophore are important characteristics to consider. Both of which are described in terms of decay rates, from either radiative events (k_r , light emission), or from non-radiative events (k_{nr}), such as vibrational relaxation, or quenching.

Briefly, the quantum yield is a measure of the number of photons emitted relative to the number of photons absorbed. As such, molecules with a high quantum yield, such as rhodamines,⁸ will appear very bright under photoexcitation, compared to samples with a low quantum yield. The lifetime provides a measure of how long the average molecule remains excited for, and thus defines the time available for the molecule to interact with its environment. Hence, samples with a long lifetime, such as phosphorescent molecules, are more prone to quenching via non-radiative decay.

$$\tau = \frac{1}{k_r + k_{nr}}$$

Equation 1.1: Determination of lifetime (τ) where k_r is the radiative rate constant and k_{nr} is the non-radiative rate constant

$$\Phi = \frac{k_r}{k_r + k_{nr}}$$

Equation 1.2: Determination of quantum yield (Φ) where k_r is the radiative rate constant and k_{nr} is the non-radiative rate constant

Regarding quenching, the most commonly observed pathway is luminophores in solution interacting with the surrounding solvent molecules, through methods such as collisional quenching, or static quenching. In the case of collisional quenching the excited state luminophore's non-radiative decay pathways are promoted, and in static quenching, the quencher forms a complex with the luminophore that is non-fluorescent.^{6,9} However solvent interactions can also modulate the energy of the emission (i.e. solvatochromism). For example, a molecule with an excited state that is more polar than the ground state, in a polar medium, will experience a stabilising effect and decrease in energy as the solvent sphere reorients itself following excitation. This will lead to a further decrease in energy of the transmission termed a bathochromic shift, or red shift. Similarly, if the molecule has a less polar excited state, or the solvent was nonpolar, the opposite is true, and the emission will increase in energy termed hypsochromic shift, or blue shift. The pH of the solution¹⁰ or the presence of ions or functional groups¹¹⁻¹³ can similarly influence the emission or absorption.

1.3 Organic Luminophores

Luminescent organic compounds, like their inorganic counterparts, are materials that contain filled, and unfilled orbitals with an energy gap within the visible region, which lies between ~400 and 750 nm.¹⁴ Therefore, emission and absorption wavelengths, are highly dependent upon the bonds present within the compound, intramolecular, and intermolecular interactions. Compounds that absorb light within the visible region are termed chromophores, with the efficiency of the light absorption determining how 'strong' the colour appears to the human eye. This is described by the Beer-Lambert law (Equation 1.3), where ϵ , the molar absorptivity, provides a measure of the probability a transition(s) occurs and therefore, how strongly it will absorb the light.

$$A = \epsilon cl$$

Equation 1.3: Beer-Lambert law which governs how strongly a sample will absorb light in solution. Where A = absorption, ϵ = molar absorptivity, c = concentration ($\text{mol}^{-1}\text{dm}^3$), and l = light pathlength (cm).

However, not all chromophores will be luminescent since non-radiative, quenching, pathways can dominate the relaxation processes. They also vary vastly in their structure, and functional groups, providing a range of colours, and are commonly used as dyes (Figure 1.2). Fully organic chromophores contain extended π delocalisation in the form of a linear system of alternating double bonds, such as β -carotene (**1**), polyaromatic systems (naphthalene, anthracene, etc.), a combination of the two, and some that include a donor-acceptor pair (**2**, **3**). In the case of solely π systems, the absorption will involve excitation from a filled π orbital to an anti-bonding π^* orbital. For donor-acceptor systems, intramolecular charge transfer (ICT) transitions are also observed. Regarding **2**, the donor system is comprised of both the quinoxaline and the indolyl group, and the acceptor consists of the quinoxaline and anisole group.¹⁵ In the case of the merocyanine, **3**, the amino group acts as an electron donor and the carbonyl as an acceptor. Both ICT compounds display strong solvatochromic effects, in the case of **2**, the absorption marginally red shifted (8 nm) as the solvent polarity increased, although emission was red shifted to a far greater degree (57 nm). The merocyanine absorption, however, was highly sensitive to solvent polarity: shifting from 444 nm in water to 614 in dichloromethane.¹⁶

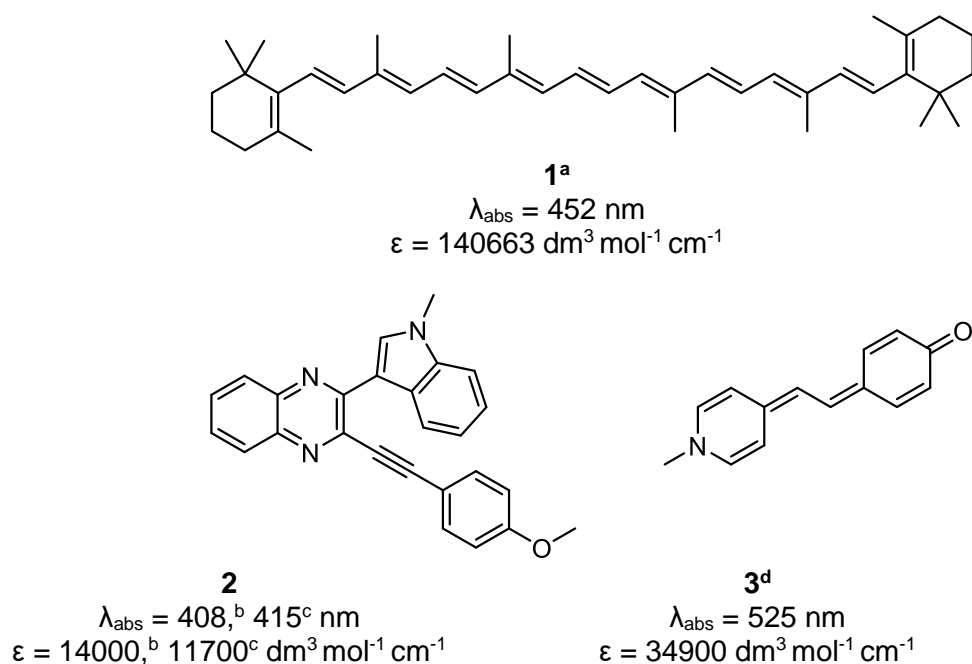


Figure 1.2: Structures and photophysical parameters of selected chromophores with their spectra recorded in select solvents: ^aacetone,¹⁷ ^bacetone, ^ciso-propanol,¹⁵ ^disopropanol.¹⁶

Expectedly, just as increasing the degree of conjugation, or incorporating donor-acceptor pairs can alter the wavelength of light absorbed by the molecule, it will also alter the wavelength of light emitted by the molecule. For example, naphthalene absorbs light at 270 nm, and emits at 320 nm.¹⁸ Fusing a third ring, increasing the conjugation, to create anthracene, shifts the absorption to 356 nm, and the emission to 396 nm.¹⁹ Similarly, 1,8-naphthalimide (**4**, Figure 1.3) absorbs within the near UV region (342 nm) and emits light at 373 nm, with a Stokes' shift of 2430 cm^{-1} . Introduction of an amine in the 4-position (**5**), however, creates a donor-acceptor pair with the carbonyl group, that lowers the energy of the absorption to 410 nm (making the material appear orange) and decreasing the energy of excited state (due to solvent effects) to 535 nm, resulting in a Stokes shift of 5699 cm^{-1} .

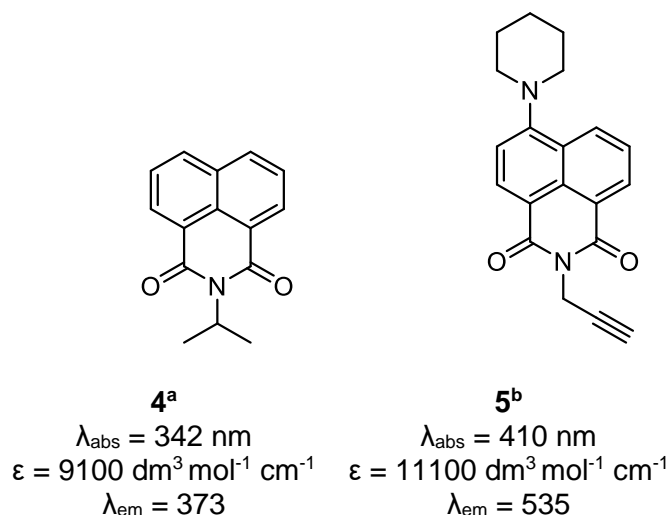


Figure 1.3: Structures and photophysical parameters of selected 1,8-naphthalimide luminophores.
^aAcetonitrile,²⁰ ^bacetonitrile.²¹

Organic luminophores have a variety of uses such as sensors^{22,23} and cell imaging agents.^{24–26} More recently, they have also been used as luminescent materials for the production of display technologies and a variety of materials have been synthesised for this purpose, such as luminescent polymers, small organic compounds, and metal complexes

1.4 Luminescent Materials

Luminescent materials have become an essential part of modern day life, allowing for the widespread adoption of indoor and outdoor lighting as well the creation of TVs, laptops, and mobile phones. Light emitting diodes (LEDs) have become the dominant source of lighting due to their low cost, brightness, long lifetime (> 15,000 h) colour tuneability, and significant cost savings due to the efficiency of an LED light source compared to incandescent bulbs. An incandescent bulb converts between 2 and 13% of the energy into light²⁷ (with the rest lost as heat) resulting in an output of only 12 lumen/watt compared to an LED bulb producing 150 lumen/watt.²⁸ In contrast, however, current LED based TV displays are not, necessarily, the most ideal choice. For example, these devices are typically edge lit along one or more edges, necessitating the use of a strong light source and attenuating films to ensure an even light distribution across the display, reducing the energy efficiency of these devices. More recently, displays using arrays of LEDs across the back of the device have been used to supply a more even distribution of light, increased brightness, and higher contrast, since these LEDs can be individually controlled.

1.4.1 Organic Light Emitting Diodes

Organic light emitting diodes (OLEDs) represent an improvement over LED displays allowing individual pixels to be turned off and on resulting in higher contrast. Samsung's PenTile AMOLED and LG's OLED displays make use of such technology.

A simplified structure of an OLED is presented in Figure 1.4, when a potential difference is

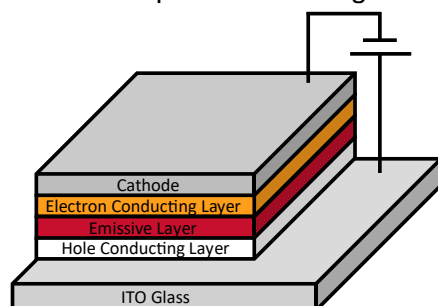


Figure 1.4: Simplified structure of an OLED device.

applied, holes and electrons migrate from the anode and cathode, respectively, and recombine in the emissive layer producing light. As the focus of this thesis is on luminescent materials, the properties of the hole conduction layers and electron conducting layers are not discussed. Many small organic compounds and complexes have been explored for use in OLED devices. One of the first examples of a metal complex for use in display applications was tris(8-hydroxyquinoline)aluminium (Figure 1.5) by Tang and Van Slyke, in which they created a device and showed electroluminescence at 550 nm.²⁹ Cölle and Brütting examined the photoluminescence of different polymorphs of **6**, and observed emission at 506 nm for the α -phase, 470 nm for the δ -phase, and 540 nm for the γ phase.³⁰ Later work by Avestissov assigned the 540 nm to an ϵ -phase instead, and observed the same trend in emission for gallium and indium variants.³¹

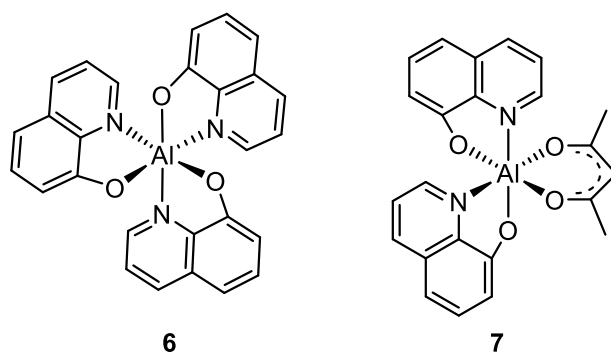


Figure 1.5: Structure of tris(8-hydroxyquinoline)aluminium.

Narasimhan and Periasamy prepared the similar aluminium complex, **7**, which showed a strong blue luminescence at 460 nm, compared to 516 for **6**.³² They ascribed this

Chapter 1. Introduction

difference to an increase in the energy of the LUMO caused by the loss of an amino group. They also reported a significant reduction in the lifetime from 16.67 (**10**) to 1.46 ns.

Anzenbacher's group synthesised a series of tris(8-hydroxyquinoline)aluminium derivatives with a range of electron donating and withdrawing groups (Figure 1.6).³³ As the electron donating ability of the Ar group increased, the emission red shifted from 490 (**8a**) to 612 nm (**8j**), although absorption wavelengths did not follow the same trend for all samples. For example, **8h**, exhibited the highest energy absorption wavelength. Presumably, this was caused by the formation of an excimer decreasing the energy of the ground excited state, resulting in a red shifted emission. Quantum yields were also observed to decrease from 0.533 to 0.008 (MeCN) as the donating ability of the aromatic group increased, likewise, lifetimes also decreased from 29.50 to 1.49 ns.

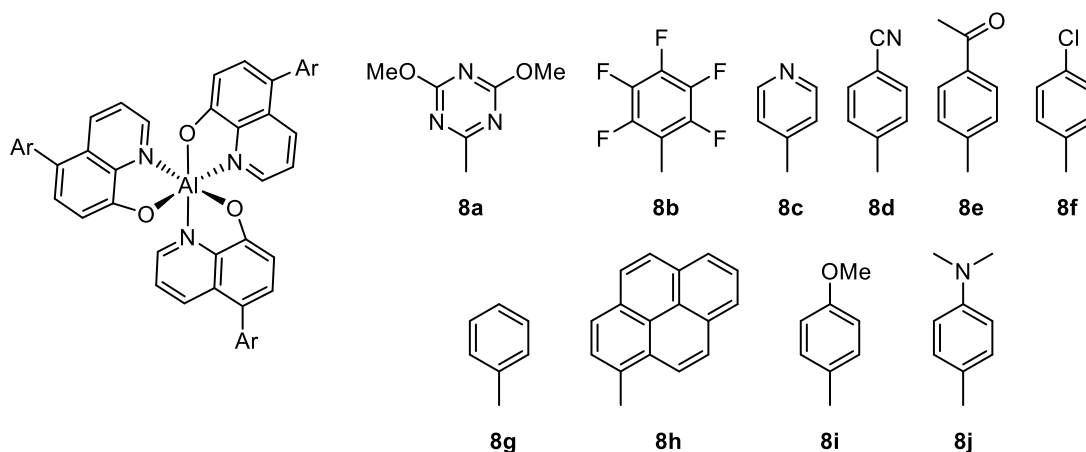


Figure 1.6: Structure of tris(8-hydroxyquinoline)aluminium derivatives.

Luminescent aluminium salen complexes (Figure 1.7) with tuneable emission have also been synthesised. Do and co-workers prepared a series of salen complexes with electron withdrawing and donating groups, **9a-f**.³⁴ Generally, as the electron donating nature of the R group increased, the emission red shifted from 458 nm, where R = H, to 599 nm, where R = NMe₂, as the energy of the HOMO increased. Absorption spectra showed a similar trend in energies, with $\pi - \pi^*$ transitions, along with partial charge transfer of the phenoxide to the imide, between 354 and 413 nm. The quantum yields ranged from less than 0.01 for **9f** and up to 0.40 for **9b** (CHCl₃). The low quantum yields for **9c** and **9f** were believed to be caused by spin orbit coupling with the bromine group to a triplet spin state, and the small HOMO-LUMO gap of **9f** facilitating non-radiative deactivation of the excited state. Zhang et.al. also demonstrated tuneability by synthesising the red emitting complex, **10**, which displayed a strong red emission at 643 nm upon excitation at 390 nm with a quantum yield of 0.49 (DMSO) and a lifetime of 4.3 ns.³⁵ Presumably, such a red shift in emission was caused by a combination of the electron donating pyrrolidine and electron

Chapter 1. Introduction

withdrawing nitrile group, allowing for an intramolecular charge transfer to occur. However, these complexes have not been explored as OLED materials except for **9b** as a hole-blocking layer.³⁶ Zinc salen complexes, however, have been used in OLED devices.³⁷

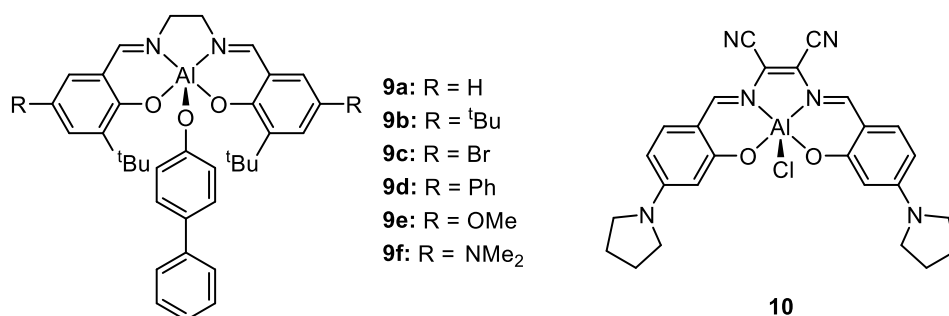


Figure 1.7: Structure of luminescent aluminium complexes with salen type ligands.

A range of other metals have also been employed for use in OLEDs such as copper,^{38,39} silver,^{40,41} zinc,^{37,42–44} tin,⁴⁵ iron,⁴⁶ nickel,^{47,48} and titanium.⁴⁹ However, many of these complexes suffer from limited emission tuneability, low quantum yields and/or brightness compared to aluminium OLEDs.

Purely organic materials have also been trailed for OLED applications. Typically, coumarin shows a weak blue emission at 430 nm,⁵⁰ however, incorporation of electron donating and withdrawing groups on the 7 and 3-positions can enhance the emission and red shift the emission through creation of a donor and acceptor pair. Zhang's group prepared functionalised coumarins with such groups, including aromatic imidazole derivatives (Figure 1.8).⁵¹ As the electron withdrawing ability of the imidazole derivative increased the emission red shifted from 479 (**11a**), to 492 (**11b**) to 519 (**11c**) with quantum yields values of 94, 97 and 98%, respectively in DCM. As solid films, however, the quantum yield values decreased significantly to 6.5, 14, and 12% due to aggregation induced quenching.

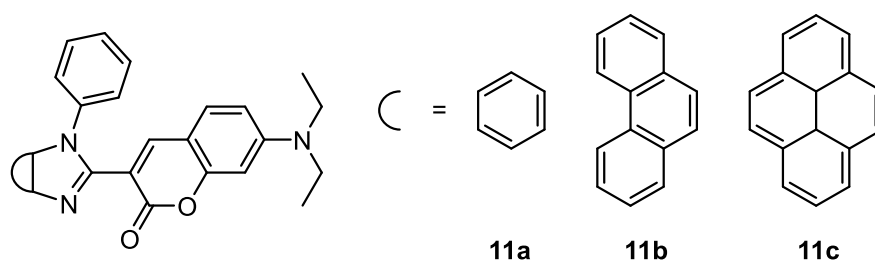


Figure 1.8: Structure of some imidazole coumarin derivatives.

Triarylborons have also been explored as small, metal free luminophores for use in OLEDs.^{52,53} Kaji and co-workers synthesised three triarylboron compounds (Figure 1.9) that exhibited promising photophysical results.⁵⁴ In solution, the compounds were found to emit at 509 (**12a**), 495 (**12b**), and 477 nm (**12c**) with quantum yields of 44, 84, and 91%, respectively, in degassed toluene. When incorporated into a host material as part of an

Chapter 1. Introduction

OLED, quantum yields were observed to, on average, increase to 92, 100, and 87%, respectively.

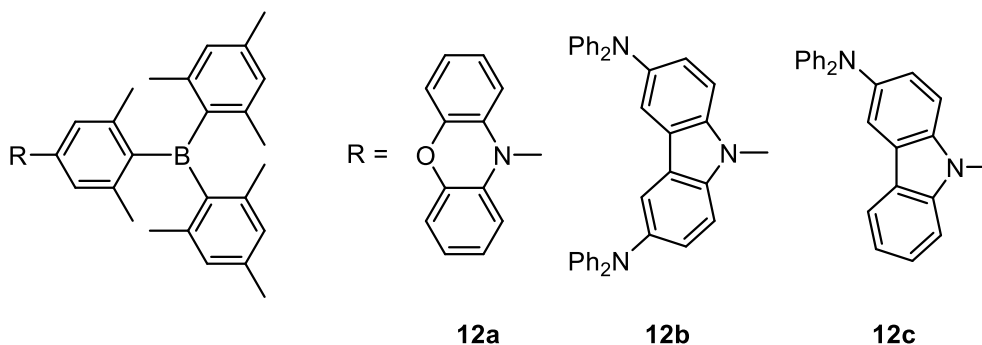


Figure 1.9: Structure of some luminescent triarylborons.

1.4.2 Polymer Light Emitting Diodes

Commercial OLED displays use vacuum deposition to deposit the emissive layer onto the substrate as this technique allows for easier control of multilayer devices and, in some cases, due to the insolubility of the emissive layer. This technique, however, is resource intensive and contributes to the cost of OLED devices.^{2,3} Polymer based light emitting diodes (PLEDs) offer an attractive alternative as the polymer can be solution processed allowing inkjet printing of the emissive layer⁴ as more cost effective production method. These devices can also be made of fewer layers as the emissive organic layer can be multifunctional, acting as both an electron donor and acceptor.⁵⁵⁻⁵⁷ Such an idea can also be used to prepared doped polymers, in which either the luminescence is wholly imparted by the dopant, or combined with an emissive polymer to create the desired photophysical properties.

One such example is the combination of blue and green emitting organic molecules with a red emitting iridium (III) phosphor to generate a broad white light emitting material. Typically, these materials are prepared via the poly-condensation of an organic halide and an organoboron compound. This was demonstrated by Qin's group, who prepared a white light emitting polymer (Figure 1.10) by combining the blue emitting poly(fluorene), the green emitting fluorenone, and a red emitting iridium complex.⁵⁸ Showing emission peaks around 425, 450, 525, and 620 nm. The intensity of the green and red emission was rather weak, being roughly 50% the intensity of the blue emission. However, electroluminescence increased the intensity of these transitions dramatically to be up to twice as strong as the blue emission. White light emission was observed with 0.05 equivalents of fluorenone and 0.1 equivalents of the iridium complex [(piq)₂Irdbm] Values lower than this were not observed to be green and red emissive under excitation.

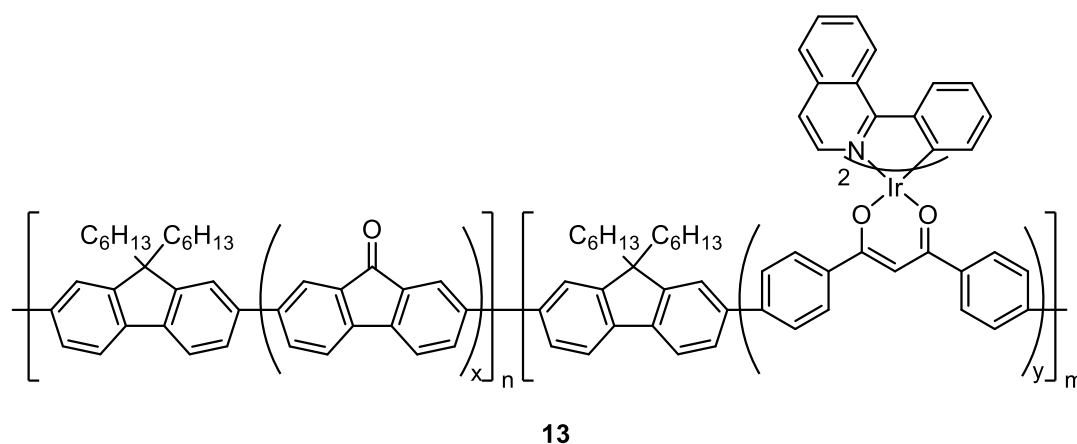


Figure 1.10: Structure of a white light emitting polymer containing green and red (iridium) emitting components.

The groups of Hwang and Shim also reported a white light emitting polymer containing iridium, but without the need for a green emitting component (Figure 1.11).⁵⁹ They note that the carbazole ligand of the iridium improved the overall stability of the molecule and was capable of donating the lone pair from the nitrogen into the iridium, increasing the energy of the HOMO, inducing a red shift in the emission. With the material showing strong emission at 453 and 642 nm of almost equal intensity with 0.96 equivalents of N-hexylcarbazole and 0.04 equivalents of [(bec)₂IrdbmBr].

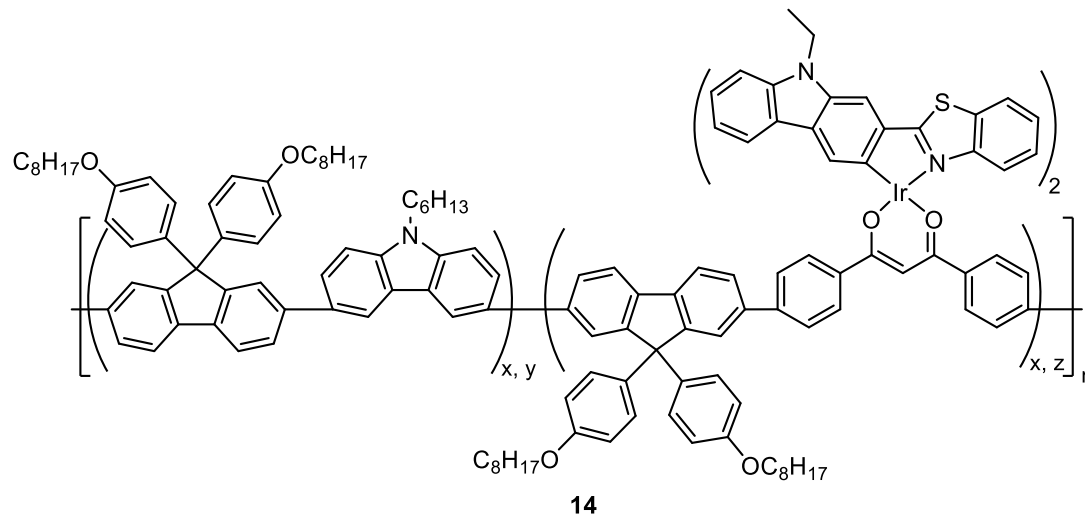


Figure 1.11: Structure of a white light emitting polymer without a green emitting component.

Other groups have also incorporated iridium as a side chain component, rather than as part of the main chain, with similar results, creating white light emission from blue, green and yellow (iridium) components.⁶⁰⁻⁶² In addition to iridium, platinum, and zinc containing luminescent polymers have also been synthesised. Wong and co-workers prepared a platinum(II) containing polymer coordinated via ethylene linkers (Figure 1.12), prepared via a

Chapter 1. Introduction

copper iodide mediated dehydrohalogenation reaction.⁶³ With emission observed at 427, 555 and 599 nm for the fluorene and platinum, respectively.

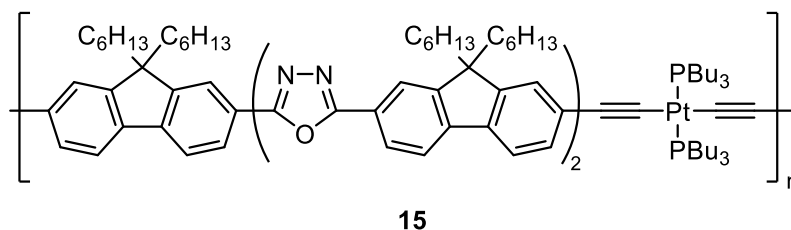


Figure 1.12: Structure of a white light emitting polymer containing platinum.

Moon's group prepared a fluorene polymer with benzothiadiazole, and porphyrin bound zinc as dopants through a Suzuki cross-coupling.⁶⁴ As with compound **15**, poly(fluorene) acts as a host and blue emitter, whilst the benzothiadiazole and metal complex act as green and red emitters, respectively. However, in solution only blue emission was observed, with a strong green (520 nm) and weak red (612 nm) emission only observed for a thin film of the polymer. Metal free luminescent polymers not based on a poly(fluorene) structure have also been prepared and are discussed in Chapter 4.

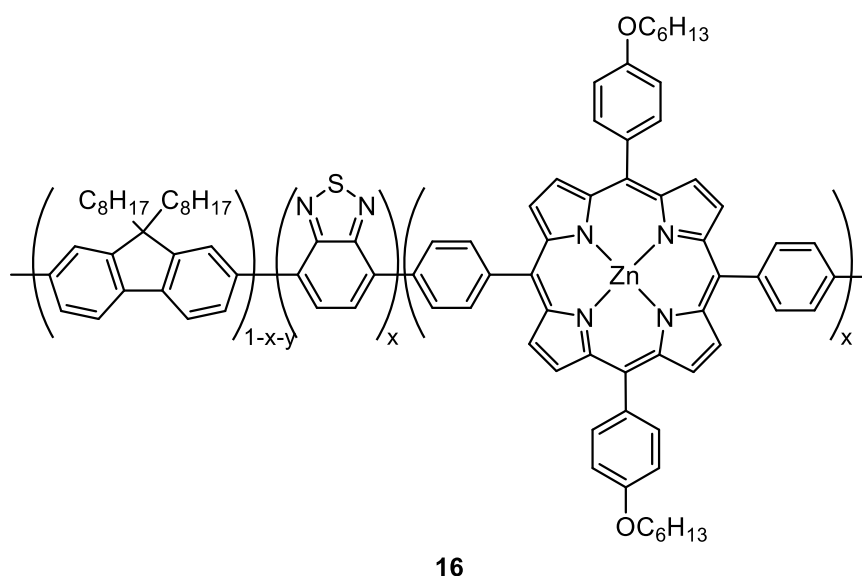


Figure 1.13: Structure of a white light emitting polymer containing zinc.

1.4.3 Inorganic Light Emitting Diodes

With regards to commercial application for large screen displays, LG, the largest manufacturer of OLED panels, used a WOLED design, consisting of RGB sub pixels with a broadband white emitter.⁶⁵ This design is required due to the low brightness of commercially relevant organic emitters, requiring a second source to create a readable display. However, this can result in washed out colours in bright scenes. While thermally activated delayed fluorescent (TADF) emitters have shown promising results through reverse intersystem

Chapter 1. Introduction

crossing – converting non-emissive triplet states into fluorescent singlet states. However, despite possessing desirable features (high brightness, longevity, or colour purity) these are rarely found in a single material.^{66,67} These materials, as of yet, have also not been incorporated into a commercial device. In contrast, inorganic particles, known as quantum dots, have recently been incorporated into flat panel displays due to their narrow bandwidth and high brightness. In the last couple of years, Samsung has produced two new types of display panel, QLED, which uses nanometre sized inorganic particles, quantum dots, as an emissive layer and micro-LED. The first, QLED, relies on the same technology as a fully array LCD TV, but uses quantum dots to increase the brightness and colour accuracy of the displays. Micro-LED replaces the organic compound in an OLED TV with an inorganic material providing all the benefits of an OLED with the brightness and colour purity obtainable with inorganic materials. It should be noted, however, that these are marketing terms, and the formation of a micro-LED displaying using quantum dots is possible.⁶⁸

Inorganic phosphors, commonly employed as light emitting diodes (LEDs), are ubiquitous in modern life, being used in all manner of displays and lighting technologies due to their power efficiency and high brightness.⁶⁹ Commercial LEDs can be divided into selective red, green, and blue (RGB) emitters, or combined to produce white light. Broad spectrum white light emitters are typically made from the blue emitting InGaN coated with the yellow emitting cerium doped $\text{Y}_3\text{Al}_5\text{O}_{12}$ (YAG:Ce³⁺) phosphor.⁷⁰ For indoor lighting, where a warmer colour is desired, an additional red emitting phosphor such as $\text{Ba}_2\text{Si}_5\text{N}_8:\text{Eu}^{2+}$,⁷¹ or $\text{CaAlSiN}_3:\text{Eu}^{2+}$,⁷² is included. Other examples of phosphors within the literature are the red emitting $\text{Ca}_2\text{ZnSi}_2\text{O}_7:\text{Eu}^{2+}$,⁷³ $\text{K}_2\text{SiF}_6:\text{Mn}^{4+}$,⁷⁴ and $(\text{Y},\text{Gd})\text{BO}_3:\text{Eu}^{2+}$,⁷⁵ and the green emitting $\text{ZnGa}_2\text{S}_4:\text{Eu}^{2+}$,⁷⁶ and $\text{SrSi}_2\text{O}_2\text{N}_2:\text{Eu}^{2+}$.⁷⁷ An alternative option for luminescent inorganic phosphors are materials that achieve tuneable emission through doping a host material, altering the size of the nanoparticle (quantum dots). Zinc sulfide is one of the most well-known examples, having previously been used in lighting and display applications,⁷⁸ and the methods of synthesis and emission tuneability are discussed in chapter 2. However, materials such as cadmium sulfide, cadmium selenide, zinc oxide, copper indium sulfide, and zinc indium sulfides, have also been explored within the literature. These materials can be divided into two broad classes: those that achieve emission tunability through altering the size of the particle, and those that introduce a dopant with an energy level within the band gap of the host material allowing for energy transfer from the host material (Figure 1.14). Extensive work has also been undertaken on perovskite materials.

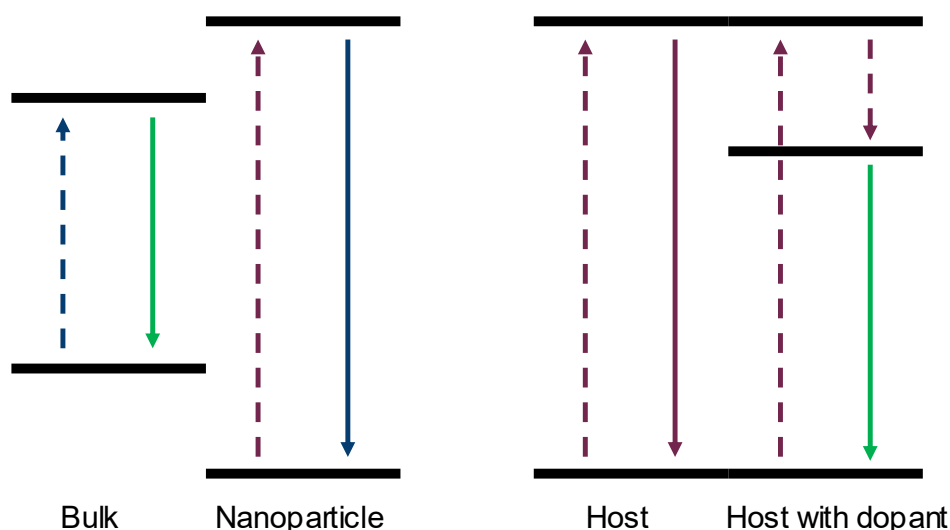


Figure 1.14: Energy diagram for nanoparticle emission tuneability (L), and dopant emission tuneability (R).

1.4.3.1 II-VI Binary Phosphors

Cadmium sulfide (CdS) crystallizes in the wurtzite form, with a tetrahedral arrangement of zinc and sulfur (Figure 1.15), and a bulk band gap of ~ 2.5 eV.⁷⁹ Because of the relatively narrow band gap, creation of luminescent materials has focused on the development of small nanoparticles, typically less than 10 nm, known as quantum dots. Weller and co-workers prepared a cadmium sulfide nanoparticles with a varying surface coverage of mercury sulfide to impart emission tuneability.⁸⁰ They note that as the mercury ion concentration was increased, the intense green emission of the cadmium sulfide was quenched, and the emergence of a new peak which red shifted from 550 to 770 nm as the mercury ion concentration increased. They attributed this change to electron transfer to the mercury sulfide, which experienced a shrinking of the band gap as the size of the mercury sulfide particles grew. Tuneable emission was also been achieved by Rosenzweig by capping the cadmium sulfide nanoparticle, and thereby altering the size of the nanoparticles, with l-cysteine (460 nm), thioglycerol (560 nm), and polyphosphate (650 nm).⁸¹

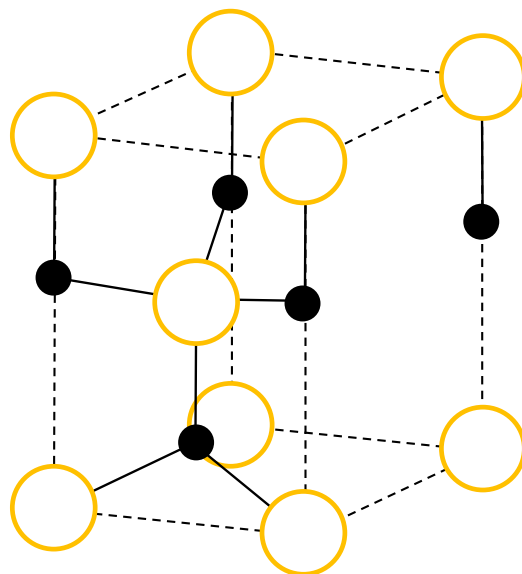


Figure 1.15: Wurtzite crystal structure, where black circles represent zinc and yellow circles represent sulfur.

Cadmium selenide (CdSe) shares the same wurtzite structure, with a significantly smaller band gap of 1.74 eV,⁸² but exhibits a similar degree of band gap tuneability as the particle size is altered.⁸³ This was exploited by Bawendi's group who prepared four different sizes of cadmium selenide nanoparticles that displayed emission at 480, 560, 600, and 625 nm with quantum yields between 0.05 and 0.15. Additionally, they demonstrated coating the nanoparticle core with zinc sulfide caused a significant increase in the quantum yield of the nanoparticles (between 30 and 50%), and a minor red shift in the emission wavelength.⁸³ Weller's group also noted a red shift in the emission of the nanoparticles as they grew in size.⁸⁴ Doping of these materials has been demonstrated, with silver doping resulting in a broad emission (200 – 300 nm FWHM) with a maxima that varied from 650 to 880 nm,⁸⁵ and copper doping exhibiting an emission centred at 705 nm with a 100 nm FWHM.⁸⁶ The highly toxic nature of cadmium,⁸⁷ however, makes cadmium based phosphors an unsuitable choice for lighting applications, despite their promising qualities.

Like the previous phosphors, zinc oxide has the wurtzite crystal structure, but a much larger band gap of 3.3 eV,⁸⁸ therefore the luminescence observed in this material is controlled by introducing a dopant, creating defects with an energy within the visible light region. Green emission, occurring around 520 nm is well known, and has been reported to be caused by a range of defects, such as: an oxide anti-site defects,⁸⁹ oxygen vacancies,^{90,91} zinc vacancies,^{92,93} and interstitial oxygen.⁹⁴ Blue emission, at 445 nm, assigned to interstitial zinc,⁹⁵ and red emission assigned to a combination of interstitial oxygen and oxygen vacancy defects have also been observed.⁹⁶ Copper doping was found to promote the formation of these defects, increasing the intensity of the transition around 550 nm.^{97,98}

Similarly, doping with aluminium and vanadium resulted in broad (150 nm FWHM) emission around 550 nm assigned to various zinc and oxygen defects.⁹⁹

1.4.3.2 Ternary Phosphors

1.4.3.2.1 Copper Indium Sulfides

Copper indium sulfide (CuInS_2) phosphors, with the chalcopyrite structure, have recently been investigated as potential phosphors that are free from toxic heavy metals. Castro and co-workers were the first to examine the photoluminescence of colloidal CuInS_2 nanoparticles.¹⁰⁰ As with cadmium nanoparticles, they observed an emission that was dependent upon the size of the nanoparticles, with sizes of 2.1 ± 0.2 nm causing emission around 650 nm, and slightly larger particles of 2.7 ± 0.3 nm caused an emission close to 700 nm. Likewise, they also note a strong surface ligand effect on the quantum yield, pyridine and trioctylphosphine (TOP) both resulted in quantum yields below 0.002, whilst hexanethiol demonstrated a significantly higher value of 0.044. Later work by Li's group observed a greater range of emission maxima, 630 to 740 nm, by altering the growth time of the particles at 240 °C, and observed similar quantum yields and FWHM values to Castro.¹⁰¹ Alloying copper indium sulfide nanoparticles with zinc sulfide was observed by Maeda's group to significantly improve the quantum yield of TOP coated particles to 0.05.¹⁰² They attributed this to migration of zinc to copper sites and prevent the formation of anti-site defects. Additionally, they showed coating of these particles with zinc sulfide almost doubled the photoluminescence intensity from the elimination of surface defects of the core zinc copper indium sulfide material. They noted the emission was tuneable between 620 and 800 nm as the ratio of zinc decreased, albeit with a reduction in quantum yield. Reiss's group further improved upon this coating procedure, generating highly luminescent materials with reasonably long lifetimes (100s ns).¹⁰³ The highest quantum yield they achieved was 60% for nanoparticles prepared in 20 minutes at 230 °C that decreased to 0.12 for nanoparticles prepared in 60 minutes. Han's group similarly observed this, producing a highly luminescent (QY = 0.61) core shell particle with an emission peak located at 561 nm.¹⁰⁴

1.4.3.2.2 Zinc Indium Sulfides

In contrast, zinc indium sulfide emission tuneability has been explored through the introduction of dopants into the host lattice. Manganese doped zinc indium sulfides, prepared by Zheng and co-workers, initially showed a weak luminescence around 610 nm.¹⁰⁵ However, by coating with a zinc sulfide shell, the quantum yield improved significantly from 0.04 to 0.56, which has been suggested to be related to the removal of surface trap states on the surface by zinc.¹⁰⁶ Lifetimes were also lengthened from 0.2 ms to 4.2 ms. For manganese doped samples, in which emission occurs from a ${}^5\text{T}_1 - {}^6\text{A}_1$ relaxation, tunability

Chapter 1. Introduction

is limited, as this can only be achieved by altering the ligand field strength which would result from replacing the ligands, and thus, changing the material itself. Dopants such as copper and silver, however, afford a wider range of emission tuneability. Chen's group initially demonstrated this, showing a silver concentration dependant emission from 480 (2.5% Ag) to 530 nm (12.5% Ag).¹⁰⁷ The strongest emission was observed for nanoparticles prepared at 200 °C, showing a quantum yield of 0.07, and a lifetime of 265 ns. The low quantum yield was attributed to structural defects, decreasing the photostability of the material. Coating with zinc sulfide, once again, resulted in an improvement of the quantum yield to 0.28. Similar results were also observed by Zheng who observed emission up to 585 nm for 15% silver doping.¹⁰⁸ Emission tuneability of copper doped zinc indium sulfides has been explored by several groups. Zhong et.al, prepared copper doped materials with varying copper, and varying Zn:In ratios.¹⁰⁹ Increasing the copper composition from 1 to 0.2, resulted in an emission shifting from 518 to 606 nm, altering the Zn:In ratio caused a more significant red shift in the emission from 450 to 710 nm. As with the silver doped samples, coating the nanoparticle increased the quantum yield from 0.63 – 0.85. Similar results have been reported by other groups within the literature.^{110–114}

1.4.3.3 Perovskites

Perovskites are perhaps most well known for their use in solar cells,¹¹⁵ but they are also an efficient inorganic luminescent material,^{116,117} due to their high quantum yields (up to 0.9),¹¹⁸ optical purity, and spectral stability. Perovskites consist of a broad range of materials with the formula ABX_3 , where A is a monovalent cation, B is an inorganic cation surrounded by an octahedral arrangement of X anions (Figure 1.16). Perovskites can be categorised into hybrid organic-inorganic structures where A is an organic cation, such as methylammonium, or fully inorganic structures where A is caesium.

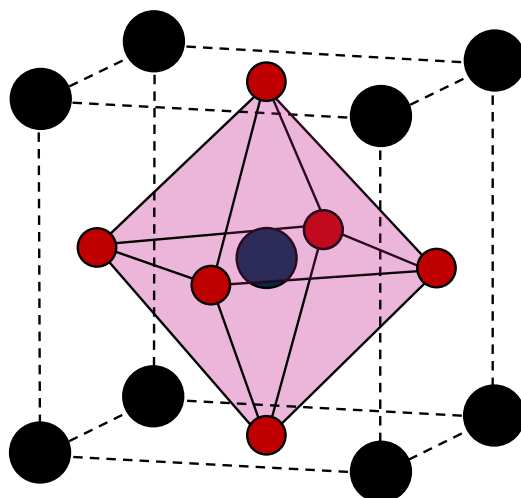


Figure 1.16: Perovskite structure, where black circles represent monovalent cations (A), red circles represent monovalent anions (X) and the blue circle represents an inorganic cation (B).

1.4.3.3.1 Lead Perovskites

Dong and co-workers reported the preparation of methylammonium (MA) lead halide perovskites at room temperature using ligand-assisted reprecipitation (LARP).¹¹⁹ By precipitating a DMF solution of the precursors, n-octylamine, and oleic acid in toluene, they were able to prepare quantum dots with an average diameter of 3.3 nm (MAPbBr₃). Emission tunability was achieved by altering the proportion of the halide during synthesis. For example, MAPbCl₃ gave an emission at 373 and 407 nm with bandwidths of 37, and 34 nm, respectively. Substituting some of the chloride for bromide, to form MAPbCl_{2.1}Br_{0.9}, shifted the emission to 446 nm with a FWHM of 17 nm. By exchanging all the halide, a green emitting (515 nm) MAPbBr₃ phosphor with a FWHM of 22 nm, and the red/near-IR emitting (734 nm) MAPbI₃ with a FWHM of 45 nm, were synthesised. They noted, however, that the materials containing iodide were very sensitive to air. Gao's group subsequently improved on this method by combining the precursors in solution without the need for the initial precipitation of an amine salt.¹²⁰ They similarly showed the highly luminescent nature of the MAPbBr₃ phosphor both in solution and as a solid state device. Caesium lead perovskites have shown a similar level of tuneability in their emission with halide exchange. Kovalenko's group prepared such compounds using a hot injection technique and demonstrated emission from 410 to 700 nm with FWHM between 10 and 40 nm, and quantum yields of 0.2 – 0.8.¹²¹ Manna's group demonstrated similar results, although they reported a more significant reduction in the quantum yield after chloride substitution.¹²² Like their methylammonium counterparts, caesium lead iodide perovskites are not stable over long periods and degrade into a non-luminescent polymorph. Further work by Kovalenko's group,¹²³ showed formamidinium (FA) perovskites, prepared via hot injection, had remarkable stability over a period of six months with no shift in the emission wavelength. FA_{0.1}Cs_{0.9}PbI₃ showed the same degree of stability with a narrow FWHM of ~ 25 nm and a quantum yield greater than 0.7. Lead perovskites have shown a high degree of emission tuneability, and narrow bandwidths, allowing them to cover a wide colour gamut (almost the entire CIE colour space). However, the toxicity of the lead component, and overall (in)stability¹²⁴ poses issues for commercial uptake of these materials.^{125–127}

1.4.3.3.2 Tin Perovskites

Böhm and co-workers prepared a series of lead-free caesium tin halide nanocrystals following a hot injection protocol in which the precursors are combined in a hot solvent (in this case 170 °C) to induce precipitation of the perovskite.¹²⁸ As with lead perovskites, descending the halogen group caused a red shift of the emission. However, the emission is also red shifted compared to their lead counterparts, with the chloride derivative exhibiting emission around 500 nm, and the iodide perovskite acting as near-IR emitter around 920

nm. Whilst the FWHM of the bromide species was similar to the lead samples (50 nm), both chloride and iodide based materials showed broader peaks, and all demonstrated incredibly low quantum yields of less than 0.0014. In contrast, Tan's group observed the iodide samples to display the highest quantum yield.¹²⁹ With value of 0.053 for CsSnI₃ which rapidly dropped to 0.001 when the iodide content decreased to 50%. However, tin(II), unlike lead(II), is not stable when exposed to air and rapidly converts to the more stable tin(IV) oxidation state, causing a significant decrease in the luminescence properties of the material.¹³⁰ Recently, Bao's group demonstrated gelatin coating of tin perovskites provided exceptional protection from degradation, with luminescence intensity only decreasing by 6.72% after 72 hours of exposure to air and 23.6% after submersion in water.¹³¹

1.4.3.3.3 Bismuth Perovskites

Bismuth derived perovskites of the form A₃B₂X₉ have also been explored as a less toxic alternative. Han's group prepared a set of caesium bismuth halide perovskites through precipitation of the metal bromides to form nanocrystals.¹³² In contrast to the tin perovskites, these samples displayed tuneable emission from 400 to 580 nm as the halide was altered. They noted that due to a fast trapping process the quantum yield was poor (0.002), however, passivation of the surface with oleic acid significantly increased the quantum yield to 0.045. Such an effect is believed to occur due to increasing the coordination number of surface ions, by increasing the steric bulk around surface sites, or by filling in vacant sites on the surface.^{133–137} Thereby reducing the rate of non-radiative relaxation and increasing the proportion of radiative relaxation, however, the precise mechanism of passivation is still uncertain.^{138,139} In addition, these materials exhibited far greater air and moisture stability than tin perovskites. Following this work, Zhao and co-workers prepared bismuth perovskites in the presence of oleic acid and an octylammonium halide.¹⁴⁰ They were able to prepare nanoparticles with emission wavelengths of 380, 411 and 526 nm, with low to high quantum yields (0.62, 0.22, and 0.023) and relatively narrow FWHMs (57, 38, and 76 nm). The enhancement in quantum yield was attributed to the surface passivation caused by a steady ligand shell created by the oleic acid and octylammonium bromide. Recently, Zeng's group were able to prepare a blue (437 nm) emitting perovskite with a remarkably high quantum yield of 0.52, using formamidinium bromide.¹⁴¹ Like their caesium counterparts, emission was only observed between 399 and 526 nm. Red emission has recently been achieved with silver bismuth and silver indium based perovskites. Gamelin's group prepared Cs₂AgBiX₆ (X= Cl, or Br) phosphors using a hot injection technique.¹⁴² Emission was observed at 738 (Cl), and 708 and 629 nm (Br) at 40 K, increasing to room temperature caused a red shift in the emission maxima, and a significant reduction in the quantum yields to ~ 0.003. They also noted that after exposure to light and air for 6 weeks, the formation of silver bromide was

observed in X-ray diffraction data. Feldmann prepared the bromide derivative and noted an emission maxima at 650, with a FWHM of roughly 200 nm.¹⁴³ Giustino's group similarly prepared the Cs₂InAgCl₆ perovskite and demonstrated emission at 608 nm with a FWHM of 120 nm.¹⁴⁴ In 2019 Jang, in collaboration with Samsung, published a paper on the formation of InP/ZnSe/ZnS quantum dots showing high brightness, external quantum efficiency, lifetime, and colour accuracy (bandwidth = 35 nm) which they claim will aid in the fabrication of next-generation quantum dot displays.¹⁴⁵ Clearly, despite 120 years of research into luminescent materials for displays, starting with zinc sulfide materials over 100 years ago,⁷⁸ there is an ever present demand for new materials which are brighter, more colour accurate, and more stable.

1.5 Inorganic vs. Organic Phosphors

Overall, there are advantages and disadvantages to each type of phosphor, and the specific choice will typically be dictated by the application of the material. In the case of inorganic materials, quantum dots offer narrow bandwidths due to the quantum confinement effect giving atom-like emission,¹⁴⁶ allowing for high colour accuracy and a wide colour gamut. Emission can also be easily tuned across the entire visible region using a single material, with high brightness and efficiency.¹⁴⁷ However, these materials are hindered by, in some cases, the use of toxic materials and non-toxic variants showing poorer photophysical properties. As well as poor lifetimes for blue emitting phosphors.¹⁴⁸ Whereas organic materials typically, have far wider bandwidths resulting in a reduced colour gamut and, therefore, less accurate reproduction of colours. However, the luminescent materials are often far less toxic than their inorganic counterparts.¹⁴⁹ Thermally activated delayed fluorescence materials have recently been explored as method to obtain greater efficiency of electroluminescence.^{150,151} However, these materials often produced wide band emission, and only recently have narrowband phosphors been produced.¹⁵² Additionally, the long lifetime of these materials, often greater than a microsecond,¹⁵² limits their use in fast switching displays. Iridium phosphors, which are commonly used as a red phosphor, while exhibiting promising photophysical properties, often take a substantial time to reach their max luminance, similarly making them less desirable choices.¹⁵³

Table 1.1: Comparison of organic and inorganic materials for display technologies

	Organic	Inorganic
Bandwidth (FWHM)	30 – 100 nm ^{154,155}	≈ 5 – 60 nm ¹⁵⁶
Quantum Yield	Up to 100%	Up 100%

Chapter 1. Introduction

Lifetime^a	Up to 12,500 for blue emitters ¹⁵⁷	Up 16,000 for blue emitters ¹⁵⁸
Emission Tunability	Often limited, requiring significantly different molecules to cover the visible spectrum	Entire visible spectrum is possible through alteration of particle size or introduction of a dopant
Nature of Elements	Metal free luminophores are readily prepared	Can use rare or hazardous elements such as: cadmium, lead, indium, gold, tellurium or selenium

^a Lifetime measured as time taken for brightness to decrease by 50%

1.6 References

- 1 X. Xing, L. Zhong, L. Zhang, Z. Chen, B. Qu, E. Chen, L. Xiao and Q. Gong, *J. Phys. Chem. C*, 2013, **117**, 25405–25408.
- 2 H. Zheng, Y. Zheng, N. Liu, N. Ai, Q. Wang, S. Wu, J. Zhou, D. Hu, S. Yu, S. Han, W. Xu, C. Luo, Y. Meng, Z. Jiang, Y. Chen, D. Li, F. Huang, J. Wang, J. Peng and Y. Cao, *Nat Commun*, 2013, **4**, 1971.
- 3 P.-A. Will and S. Reineke, in *Handbook of Organic Materials for Electronic and Photonic Devices (Second Edition)*, ed. O. Ostroverkhova, Woodhead Publishing, 2019, pp. 695–726.
- 4 J. Park, H. Yoon, G. Kim, B. Lee, S. Lee, S. Jeong, T. Kim, J. Seo, S. Chung and Y. Hong, *Advanced Functional Materials*, 2019, **29**, 1902412.
- 5 A. T. Ngoc Do, Y. Ha, H.-J. Kang, J. M. Kim and J.-H. Kwon, *Journal of Hazardous Materials*, 2022, **427**, 128144.
- 6 J. R. Lakowicz, *Principles of fluorescence spectroscopy*, Springer, New York, 3rd ed., 2006.
- 7 J. Franck and E. G. Dymond, *Trans. Faraday Soc.*, 1926, **21**, 536–542.
- 8 R. F. Kubin and A. N. Fletcher, *Journal of Luminescence*, 1982, **27**, 455–462.
- 9 K. G. Fleming, in *Encyclopedia of Spectroscopy and Spectrometry (Third Edition)*, eds. J. C. Lindon, G. E. Tranter and D. W. Koppenaal, Academic Press, Oxford, 2017, pp. 647–653.
- 10 X. Jia, J. Li and E. Wang, *Nanoscale*, 2012, **4**, 5572–5575.
- 11 A. Mokhir, A. Kiel, D.-P. Herten and R. Kraemer, *Inorg. Chem.*, 2005, **44**, 5661–5666.
- 12 W. Sun, W. Li, J. Li, J. Zhang, L. Du and M. Li, *Tetrahedron*, 2012, **68**, 5363–5367.
- 13 H. Dai and H. Xu, *Bioorganic & Medicinal Chemistry Letters*, 2011, **21**, 5141–5144.
- 14 D. H. Sliney, *Eye*, 2016, **30**, 222–229.
- 15 C. F. Gers, J. Nordmann, C. Kumru, W. Frank and T. J. J. Müller, *J. Org. Chem.*, 2014, **79**, 3296–3310.
- 16 T. Kolev, B. B. Koleva, S. Stoyanov, M. Spiteller and I. Petkov, *Spectrochimica Acta Part A: Molecular and Biomolecular Spectroscopy*, 2008, **70**, 1087–1096.
- 17 E. Biehler, F. Mayer, L. Hoffmann, E. Krause and T. Bohn, *Journal of Food Science*, 2010, **75**, C55–C61.
- 18 I. B. Berlman, in *Handbook of Fluorescence Spectra of Aromatic Molecules (Second Edition)*, ed. I. B. Berlman, Academic Press, 1971, pp. 67–95.

- 19 I. B. Berlman, in *Handbook of Fluorescence Spectra of Aromatic Molecules (Second Edition)*, ed. I. B. Berlman, Academic Press, 1971, pp. 417–459.
- 20 O. V. Prezhdo, B. V. Uspenskii, V. V. Prezhdo, W. Boszczyk and V. B. Distanov, *Dyes Pigments*, 2007, **72**, 42–46.
- 21 E. E. Langdon-Jones, D. Lloyd, A. J. Hayes, S. D. Wainwright, H. J. Mottram, S. J. Coles, P. N. Horton and S. J. A. Pope, *Inorg. Chem.*, 2015, **54**, 6606–6615.
- 22 Y. Hoon Lee, S. Jana, H. Lee, S. Uck Lee and M. Hyung Lee, *Chemical Communications*, 2018, **54**, 12069–12072.
- 23 H. Dai, Y. Yan, Y. Guo, L. Fan, Z. Che and H. Xu, *Chemistry – A European Journal*, 2012, **18**, 11188–11191.
- 24 J.-C. G. Bünzli, *Chem. Rev.*, 2010, **110**, 2729–2755.
- 25 X. Li, C. Yin, S. S. Liew, C.-S. Lee and K. Pu, *Advanced Functional Materials*, **n/a**, 2106154.
- 26 D. Lloyd, M. P. Coogan and S. J. A. Pope, in *Reviews in Fluorescence 2010*, ed. C. D. Geddes, Springer, New York, NY, 2012, pp. 15–44.
- 27 D. C. Agrawal, H. S. Leff and V. J. Menon, *American Journal of Physics*, 1996, **64**, 649–654.
- 28 P. Von Dollen, S. Pimputkar and J. S. Speck, *Angewandte Chemie International Edition*, 2014, **53**, 13978–13980.
- 29 C. W. Tang and S. A. VanSlyke, *Appl. Phys. Lett.*, 1987, **51**, 913–915.
- 30 M. Cölle, J. Gmeiner, W. Milius, H. Hillebrecht and W. Brütting, *Advanced Functional Materials*, 2003, **13**, 108–112.
- 31 R. I. Avetisov, A. A. Akkuzina, A. G. Cherednichenko, A. V. Khomyakov and I. Ch. Avetissov, *Dokl Chem*, 2014, **454**, 6–8.
- 32 P. K. Nayak, N. Agarwal, F. Ali, M. P. Patankar, K. L. Narasimhan and N. Periasamy, *J Chem Sci*, 2010, **122**, 847–855.
- 33 R. Pohl, V. A. Montes, J. Shinar and P. Anzenbacher, *J. Org. Chem.*, 2004, **69**, 1723–1725.
- 34 K. Y. Hwang, H. Kim, Y. S. Lee, M. H. Lee and Y. Do, *Chemistry – A European Journal*, 2009, **15**, 6478–6487.
- 35 J. Tang, H.-Y. Yin and J.-L. Zhang, *Chem Sci*, 2018, **9**, 1931–1939.
- 36 K. Y. Hwang, M. H. Lee, H. Jang, Y. Sung, J. S. Lee, S. H. Kim and Y. Do, *Dalton Trans.*, 2008, 1818–1820.
- 37 F. Dumur, L. Beouch, M.-A. Tehfe, E. Contal, M. Lepeltier, G. Wantz, B. Graff, F. Goubard, C. R. Mayer, J. Lalevée and D. Gigmes, *Thin Solid Films*, 2014, **564**, 351–360.
- 38 Y. Ma, C.-M. Che, H.-Y. Chao, X. Zhou, W.-H. Chan and J. Shen, *Advanced Materials*, 1999, **11**, 852–857.
- 39 F. Wu, J. Li, H. Tong, Z. Li, C. Adachi, A. Langlois, P. D. Harvey, L. Liu, W.-Y. Wong, W.-K. Wong and X. Zhu, *J. Mater. Chem. C*, 2014, **3**, 138–146.
- 40 C.-W. Hsu, C.-C. Lin, M.-W. Chung, Y. Chi, G.-H. Lee, P.-T. Chou, C.-H. Chang and P.-Y. Chen, *J. Am. Chem. Soc.*, 2011, **133**, 12085–12099.
- 41 A. Poethig and T. Strassner, *Organometallics*, 2011, **30**, 6674–6684.
- 42 T. Yu, W. Su, W. Li, Z. Hong, R. Hua and B. Li, *Thin Solid Films*, 2007, **515**, 4080–4084.
- 43 H.-P. Zeng, G.-R. Wang, G.-C. Zeng and J. Li, *Dyes and Pigments*, 2009, **83**, 155–161.
- 44 G. Cheng, G. K.-M. So, W.-P. To, Y. Chen, C.-C. Kwok, C. Ma, X. Guan, X. Chang, W.-M. Kwok and C.-M. Che, *Chem. Sci.*, 2015, **6**, 4623–4635.
- 45 Y. Fazaeli, M. M. Amini, E. Najafi, E. Mohajerani, M. Janghour, A. Jalilian and S. W. Ng, *J Fluoresc*, 2012, **22**, 1263–1270.
- 46 P. Chábera, Y. Liu, O. Prakash, E. Thyrhaug, A. E. Nahhas, A. Honarfar, S. Essén, L. A. Fredin, T. C. B. Harlang, K. S. Kjær, K. Handrup, F. Ericson, H. Tatsuno, K. Morgan, J. Schnadt, L. Häggström, T. Ericsson, A. Sobkowiak, S. Lidin, P. Huang, S. Styring, J. Uhlig, J. Bendix, R. Lomoth, V. Sundström, P. Persson and K. Wärnmark, *Nature*, 2017, **543**, 695–699.

- 47 J. Cerezo, A. Requena, J. Zúñiga, M. J. Piernas, M. D. Santana, J. Pérez and L. García, *Inorg. Chem.*, 2017, **56**, 3663–3673.
- 48 K. O. Kirlikovali, J. C. Axtell, A. Gonzalez, A. C. Phung, S. I. Khan and A. M. Spokoyny, *Chem. Sci.*, 2016, **7**, 5132–5138.
- 49 A. Erdoğan, M. Durmuş, A. L. Uğur, O. Avciata, U. Avciata and T. Nyokong, *Synthetic Metals*, 2010, **160**, 1868–1876.
- 50 T. Yu, Y. Zhao and D. Fan, *Journal of Molecular Structure*, 2006, **791**, 18–22.
- 51 Y. Wang, Y. Li, T. Yu, W. Su, H. Ma, Y. Zhao, X. Li and H. Zhang, *Dyes and Pigments*, 2020, **173**, 107958.
- 52 Y. Shiota, M. Kinoshita, T. Noda, K. Okumoto and T. Ohara, *J. Am. Chem. Soc.*, 2000, **122**, 11021–11022.
- 53 W. L. Jia, X. D. Feng, D. R. Bai, Z. H. Lu, S. Wang and G. Vamvounis, *Chem. Mater.*, 2005, **17**, 164–170.
- 54 K. Suzuki, S. Kubo, K. Shizu, T. Fukushima, A. Wakamiya, Y. Murata, C. Adachi and H. Kaji, *Angewandte Chemie International Edition*, 2015, **54**, 15231–15235.
- 55 K. Gilissen, J. Stryckers, P. Verstappen, J. Drijkoningen, G. H. L. Heintges, L. Lutsen, J. Manca, W. Maes and W. Deferme, *Organic Electronics*, 2015, **20**, 31–35.
- 56 Y. Ma, Z. Zhong, F. Peng, L. Ying, J. Xiong, J. Peng and Y. Cao, *Organic Electronics*, 2019, **68**, 103–107.
- 57 M. Y. Wong, *Journal of Elec Materi*, 2017, **46**, 6246–6281.
- 58 K. Zhang, Z. Chen, C. Yang, Y. Tao, Y. Zou, J. Qin and Y. Cao, *J. Mater. Chem.*, 2008, **18**, 291–298.
- 59 M.-J. Park, J. Kwak, J. Lee, I. H. Jung, H. Kong, C. Lee, D.-H. Hwang and H.-K. Shim, *Macromolecules*, 2010, **43**, 1379–1386.
- 60 J. X. Jiang, Y. H. Xu, W. Yang, R. Guan, Z. Q. Liu, H. Y. Zhen and Y. Cao, *Advanced Materials*, 2006, **18**, 1769–1773.
- 61 Y. Xu, R. Guan, J. Jiang, W. Yang, H. Zhen, J. Peng and Y. Cao, *Journal of Polymer Science Part A: Polymer Chemistry*, 2008, **46**, 453–463.
- 62 C. Mei, J. Ding, B. Yao, Y. Cheng, Z. Xie, Y. Geng and L. Wang, *Journal of Polymer Science Part A: Polymer Chemistry*, 2007, **45**, 1746–1757.
- 63 T. Goudreault, Z. He, Y. Guo, C.-L. Ho, H. Zhan, Q. Wang, K. Y.-F. Ho, K.-L. Wong, D. Fortin, B. Yao, Z. Xie, L. Wang, W.-M. Kwok, P. D. Harvey and W.-Y. Wong, *Macromolecules*, 2010, **43**, 7936–7949.
- 64 H. J. Song, D. H. Kim, T. H. Lee and D. K. Moon, *European Polymer Journal*, 2012, **48**, 1485–1494.
- 65 C.-W. Han, J.-S. Park, H.-S. Choi, T.-S. Kim, Y.-H. Shin, H.-J. Shin, M.-J. Lim, B.-C. Kim, H.-S. Kim, B.-S. Kim, Y.-H. Tak, C.-H. Oh, S.-Y. Cha and B.-C. Ahn, *Journal of the Society for Information Display*, 2014, **22**, 552–563.
- 66 A. Monkman, *ACS Appl. Mater. Interfaces*, DOI:10.1021/acsami.1c09189.
- 67 T. Kamata, H. Sasabe, N. Ito, Y. Sukegawa, A. Arai, T. Chiba, D. Yokoyama and J. Kido, *J. Mater. Chem. C*, 2020, **8**, 7200–7210.
- 68 T. Wu, Y.-M. Huang, J. S. Konthoujam, Z. Chen and H.-C. Kuo, in *Semiconductors and Semimetals*, eds. H. Jiang and J. Lin, Elsevier, 2021, vol. 106, pp. 173–201.
- 69 H.-M. Kim, Y.-H. Cho, H. Lee, S. I. Kim, S. R. Ryu, D. Y. Kim, T. W. Kang and K. S. Chung, *Nano Lett.*, 2004, **4**, 1059–1062.
- 70 U. Kaufmann, M. Kunzer, K. Köhler, H. Obloh, W. Pletschen, P. Schlotter, J. Wagner, A. Ellens, W. Rossner and M. Kobusch, *physica status solidi (a)*, 2002, **192**, 246–253.
- 71 H. A. Höpfe, H. Lutz, P. Morys, W. Schnick and A. Seilmeier, *Journal of Physics and Chemistry of Solids*, 2000, **61**, 2001–2006.
- 72 K. Uheda, N. Hirotsuki, Y. Yamamoto, A. Naito, T. Nakajima and H. Yamamoto, *Electrochem. Solid-State Lett.*, 2006, **9**, H22.
- 73 H. Kamioka, T. Yamaguchi, M. Hirano, T. Kamiya and H. Hosono, *Journal of Luminescence*, 2007, **122–123**, 339–341.

Chapter 1. Introduction

- 74 R. A. Osborne, N. J. Cherepy, Z. M. Seeley, S. A. Payne, A. D. Drobshoff, A. M. Srivastava, W. W. Beers, W. W. Cohen and D. L. Schlagel, *Optical Materials*, 2020, **107**, 110140.
- 75 A. Lakshmanan, R. S. Bhaskar, P. C. Thomas, R. S. Kumar, V. S. Kumar and M. T. Jose, *Materials Letters*, 2010, **64**, 1809–1812.
- 76 Y.-S. Cho and Y.-D. Huh, *Bulletin of the Korean Chemical Society*, 2017, **38**, 493–498.
- 77 X. Song, H. He, R. Fu, D. Wang, X. Zhao and Z. Pan, *J. Phys. D: Appl. Phys.*, 2009, **42**, 065409.
- 78 T. Hase, T. Kano, E. Nakazawa and H. Yamamoto, in *Advances in Electronics and Electron Physics*, ed. P. W. Hawkes, Academic Press, 1990, vol. 79, pp. 271–373.
- 79 S. Ninomiya and S. Adachi, *Journal of Applied Physics*, 1998, **78**, 1183.
- 80 A. Haesselbarth, A. Eychmueller, R. Eichberger, M. Giersig, A. Mews and H. Weller, *J. Phys. Chem.*, 1993, **97**, 5333–5340.
- 81 Y. Chen and Z. Rosenzweig, *Anal. Chem.*, 2002, **74**, 5132–5138.
- 82 S. Ninomiya and S. Adachi, *Journal of Applied Physics*, 1995, **78**, 4681–4689.
- 83 B. O. Dabbousi, J. Rodriguez-Viejo, F. V. Mikulec, J. R. Heine, H. Mattoussi, R. Ober, K. F. Jensen and M. G. Bawendi, *J. Phys. Chem. B*, 1997, **101**, 9463–9475.
- 84 D. V. Talapin, A. L. Rogach, E. V. Shevchenko, A. Kornowski, M. Haase and H. Weller, *J. Am. Chem. Soc.*, 2002, **124**, 5782–5790.
- 85 A. H. Khan, V. Pinchetti, I. Tanghe, Z. Dang, B. Martín-García, Z. Hens, D. Van Thourhout, P. Geiregat, S. Brovelli and I. Moreels, *Chem. Mater.*, 2019, **31**, 1450–1459.
- 86 A. Dutta, R. Bera, A. Ghosh and A. Patra, *J. Phys. Chem. C*, 2018, **122**, 16992–17000.
- 87 J.-M. Moulis and F. Thévenod, *Biometals*, 2010, **23**, 763–768.
- 88 V. Srikanth and D. R. Clarke, *Journal of Applied Physics*, 1998, **83**, 5447–5451.
- 89 B. Lin, Z. Fu and Y. Jia, *Appl. Phys. Lett.*, 2001, **79**, 943–945.
- 90 P. H. Kasai, *Phys. Rev.*, 1963, **130**, 989–995.
- 91 K. Vanheusden, W. L. Warren, C. H. Seager, D. R. Tallant, J. A. Voigt and B. E. Gnade, *Journal of Applied Physics*, 1996, **79**, 7983–7990.
- 92 M. Liu, A. H. Kitai and P. Mascher, *Journal of Luminescence*, 1992, **54**, 35–42.
- 93 E. G. Bylander, *Journal of Applied Physics*, 1978, **49**, 1188–1195.
- 94 L. L. Yang, Q. X. Zhao, M. Willander, J. H. Yang and I. Ivanov, *Journal of Applied Physics*, 2009, **105**, 053503.
- 95 H. Zeng, Z. Li, W. Cai and P. Liu, *Journal of Applied Physics*, 2007, **102**, 104307.
- 96 V. Kumar, H. C. Swart, O. M. Ntwaeaborwa, R. E. Kroon, J. J. Terblans, S. K. K. Shaat, A. Yousif and M. M. Duvenhage, *Materials Letters*, 2013, **101**, 57–60.
- 97 M. Sajjad, I. Ullah, M. I. Khan, J. Khan, M. Y. Khan and M. T. Qureshi, *Results in Physics*, 2018, **9**, 1301–1309.
- 98 N. Narayanan and N. K. Deepak, *Optik*, 2018, **158**, 1313–1326.
- 99 T. Elkar, N. Mzabi, M. Ben hassine, P. Gemeiner, B. Dkhil, S. Guermazi and H. Guermazi, *Superlattices and Microstructures*, 2018, **122**, 349–361.
- 100 S. L. Castro, S. G. Bailey, R. P. Raffaele, K. K. Banger and A. F. Hepp, *J. Phys. Chem. B*, 2004, **108**, 12429–12435.
- 101 H. Zhong, Y. Zhou, M. Ye, Y. He, J. Ye, C. He, C. Yang and Y. Li, *Chem. Mater.*, 2008, **20**, 6434–6443.
- 102 H. Nakamura, W. Kato, M. Uehara, K. Nose, T. Omata, S. Otsuka-Yao-Matsuo, M. Miyazaki and H. Maeda, *Chem. Mater.*, 2006, **18**, 3330–3335.
- 103 L. Li, T. J. Daou, I. Texier, T. T. Kim Chi, N. Q. Liem and P. Reiss, *Chem. Mater.*, 2009, **21**, 2422–2429.
- 104 J. Lee and C.-S. Han, *Nanoscale Res Lett*, 2014, **9**, 78.
- 105 S. Cao, J. Zhao, W. Yang, C. Li and J. Zheng, *J. Mater. Chem. C*, 2015, **3**, 8844–8851.
- 106 Y. Yang, O. Chen, A. Angerhofer and Y. C. Cao, *Chemistry – A European Journal*, 2009, **15**, 3186–3197.
- 107 Q.-H. Zhang, Y. Tian, C.-F. Wang and S. Chen, *RSC Adv.*, 2016, **6**, 47616–47622.

Chapter 1. Introduction

- 108 X. Shi, J. Zheng, M. Shang, T. Xie, J. Xie, S. Cao and W. Yang, *Journal of Materials Research*, 2017, **32**, 3585–3592.
- 109 W. Zhang, Q. Lou, W. Ji, J. Zhao and X. Zhong, *Chem. Mater.*, 2014, **26**, 1204–1212.
- 110 T. Jiang, J. Song, H. Wang, X. Ye, H. Wang, W. Zhang, M. Yang, R. Xia, L. Zhu and X. Xu, *J. Mater. Chem. B*, 2015, **3**, 2402–2410.
- 111 T. Jiang, M. Shen, P. Dai, M. Wu, X. Yu, G. Li, X. Xu and H. Zeng, *Nanotechnology*, 2017, **28**, 435702.
- 112 M. Cao, C. Yu, J. Xia, D. Jiang, S. Wang and H. Li, *Journal of the American Ceramic Society*, 2018, **101**, 5586–5595.
- 113 X. Yuan, J. Hua, R. Zeng, D. Zhu, W. Ji, P. Jing, X. Meng, J. Zhao and H. Li, *Nanotechnology*, 2014, **25**, 435202.
- 114 J. Zhu, S. Mei, W. Yang, G. Zhang, Q. Chen, W. Zhang and R. Guo, *Journal of Colloid and Interface Science*, 2017, **506**, 27–35.
- 115 H. J. Snaith, *J. Phys. Chem. Lett.*, 2013, **4**, 3623–3630.
- 116 X. Hong, T. Ishihara and A. V. Nurmikko, *Solid State Communications*, 1992, **84**, 657–661.
- 117 M. Era, S. Morimoto, T. Tsutsui and S. Saito, *Appl. Phys. Lett.*, 1994, **65**, 676–678.
- 118 L. Protesescu, S. Yakunin, M. I. Bodnarchuk, F. Krieg, R. Caputo, C. H. Hendon, R. X. Yang, A. Walsh and M. V. Kovalenko, *Nano Lett.*, 2015, **15**, 3692–3696.
- 119 F. Zhang, H. Zhong, C. Chen, X. Wu, X. Hu, H. Huang, J. Han, B. Zou and Y. Dong, *ACS Nano*, 2015, **9**, 4533–4542.
- 120 Y. Ling, Z. Yuan, Y. Tian, X. Wang, J. C. Wang, Y. Xin, K. Hanson, B. Ma and H. Gao, *Advanced Materials*, 2016, **28**, 305–311.
- 121 G. Nedelcu, L. Protesescu, S. Yakunin, M. I. Bodnarchuk, M. J. Grotevent and M. V. Kovalenko, *Nano Lett.*, 2015, **15**, 5635–5640.
- 122 Q. A. Akkerman, V. D’Innocenzo, S. Accornero, A. Scarpellini, A. Petrozza, M. Prato and L. Manna, *J. Am. Chem. Soc.*, 2015, **137**, 10276–10281.
- 123 L. Protesescu, S. Yakunin, S. Kumar, J. Bär, F. Bertolotti, N. Masciocchi, A. Guagliardi, M. Grotevent, I. Shorubalko, M. I. Bodnarchuk, C.-J. Shih and M. V. Kovalenko, *ACS Nano*, 2017, **11**, 3119–3134.
- 124 Z. Andaji-Garmaroudi, M. Abdi-Jalebi, F. U. Kosasih, T. Doherty, S. Macpherson, A. R. Bowman, G. J. Man, U. B. Cappel, H. Rensmo, C. Ducati, R. H. Friend and S. D. Stranks, *Advanced Energy Materials*, 2020, **10**, 2002676.
- 125 S. T. Williams, A. Rajagopal, C.-C. Chueh and A. K.-Y. Jen, *J. Phys. Chem. Lett.*, 2016, **7**, 811–819.
- 126 M. Grätzel, *Nature Mater*, 2014, **13**, 838–842.
- 127 B. V. Lotsch, *Angewandte Chemie International Edition*, 2014, **53**, 635–637.
- 128 T. C. Jellicoe, J. M. Richter, H. F. J. Glass, M. Tabachnyk, R. Brady, S. E. Dutton, A. Rao, R. H. Friend, D. Credgington, N. C. Greenham and M. L. Böhm, *J. Am. Chem. Soc.*, 2016, **138**, 2941–2944.
- 129 M. L. Lai, T. Y. S. Tay, A. Sadhanala, S. E. Dutton, G. Li, R. H. Friend and Z.-K. Tan, *J. Phys. Chem. Lett.*, 2016, **7**, 2653–2658.
- 130 T. Leijtens, R. Prasanna, A. Gold-Parker, M. F. Toney and M. D. McGehee, *ACS Energy Lett.*, 2017, **2**, 2159–2165.
- 131 B. Lyu, X. Guo, D. Gao, M. Kou, Y. Yu, J. Ma, S. Chen, H. Wang, Y. Zhang and X. Bao, *Journal of Hazardous Materials*, 2021, **403**, 123967.
- 132 B. Yang, J. Chen, F. Hong, X. Mao, K. Zheng, S. Yang, Y. Li, T. Pullerits, W. Deng and K. Han, *Angewandte Chemie International Edition*, 2017, **56**, 12471–12475.
- 133 Y. J. Yoon, Y. S. Shin, C. B. Park, J. G. Son, J. W. Kim, H. S. Kim, W. Lee, J. Heo, G.-H. Kim and J. Y. Kim, *Nanoscale*, 2020, **12**, 21695–21702.
- 134 X. Yang, X. Zhang, J. Deng, Z. Chu, Q. Jiang, J. Meng, P. Wang, L. Zhang, Z. Yin and J. You, *Nat Commun*, 2018, **9**, 570.
- 135 L. Wang, C. McCleese, A. Kovalsky, Y. Zhao and C. Burda, *J. Am. Chem. Soc.*, 2014, **136**, 12205–12208.
- 136 T. Zhang, N. Guo, G. Li, X. Qian and Y. Zhao, *Nano Energy*, 2016, **26**, 50–56.

Chapter 1. Introduction

- 137 V. G. V. Dutt, S. Akhil and N. Mishra, *ChemNanoMat*, 2020, **6**, 1730–1742.
- 138 N. K. Noel, A. Abate, S. D. Stranks, E. S. Parrott, V. M. Burlakov, A. Goriely and H. J. Snaith, *ACS Nano*, 2014, **8**, 9815–9821.
- 139 D. Yang, X. Li and H. Zeng, *Advanced Materials Interfaces*, 2018, **5**, 1701662.
- 140 Y. Lou, M. Fang, J. Chen and Y. Zhao, *Chem. Commun.*, 2018, **54**, 3779–3782.
- 141 Y. Shen, J. Yin, B. Cai, Z. Wang, Y. Dong, X. Xu and H. Zeng, *Nanoscale Horiz.*, 2020, **5**, 580–585.
- 142 S. E. Creutz, E. N. Crites, M. C. De Siena and D. R. Gamelin, *Nano Lett.*, 2018, **18**, 1118–1123.
- 143 A. Dey, A. F. Richter, T. Debnath, H. Huang, L. Polavarapu and J. Feldmann, *ACS Nano*, 2020, **14**, 5855–5861.
- 144 G. Volonakis, A. A. Haghighirad, R. L. Milot, W. H. Sio, M. R. Filip, B. Wenger, M. B. Johnston, L. M. Herz, H. J. Snaith and F. Giustino, *J. Phys. Chem. Lett.*, 2017, **8**, 772–778.
- 145 Y.-H. Won, O. Cho, T. Kim, D.-Y. Chung, T. Kim, H. Chung, H. Jang, J. Lee, D. Kim and E. Jang, *Nature*, 2019, **575**, 634–638.
- 146 M. A. Kastner, *Physics Today*, 1993, **46**, 24–31.
- 147 H. Shen, Q. Gao, Y. Zhang, Y. Lin, Q. Lin, Z. Li, L. Chen, Z. Zeng, X. Li, Y. Jia, S. Wang, Z. Du, L. S. Li and Z. Zhang, *Nature Photon*, 2019, **13**, 192–197.
- 148 Y. Yang, Y. Zheng, W. Cao, A. Titov, J. Hyvonen, J. R. Manders, J. Xue, P. H. Holloway and L. Qian, *Nature Photon*, 2015, **9**, 259–266.
- 149 I. Jun, S. J. Han, H.-S. Shin, J. Kim, E. K. Kim, T. Kim, S. C. Yoon and K. Y. Seo, *Sci Rep*, 2020, **10**, 11582.
- 150 J. H. Kim, J. H. Yun and J. Y. Lee, *Advanced Optical Materials*, 2018, **6**, 1800255.
- 151 M. Y. Wong and E. Zysman-Colman, *Advanced Materials*, 2017, **29**, 1605444.
- 152 J.-M. Teng, Y.-F. Wang and C.-F. Chen, *J. Mater. Chem. C*, 2020, **8**, 11340–11353.
- 153 C. E. Housecroft and E. C. Constable, *Coordination Chemistry Reviews*, 2017, **350**, 155–177.
- 154 Y. Wen, Y.-K. Wang, J.-G. Zhou, J.-Y. Li, W. He, Y.-J. Zhang, X.-Z. Zhu, L.-S. Liao and M.-K. Fung, *J. Mater. Chem. C*, 2022, **10**, 5666–5671.
- 155 B. Qu, Z. Chen, F. Xu, H. Cao, M. Huang and Q. Gong, *Materials Letters*, 2006, **60**, 1927–1930.
- 156 J. S. Steckel, J. Ho, C. Hamilton, J. Xi, C. Breen, W. Liu, P. Allen and S. Coe-Sullivan, *Journal of the Society for Information Display*, 2015, **23**, 294–305.
- 157 D. Zhang, M. Cai, Y. Zhang, D. Zhang and L. Duan, *Materials Horizons*, 2016, **3**, 145–151.
- 158 T. Kim, K.-H. Kim, S. Kim, S.-M. Choi, H. Jang, H.-K. Seo, H. Lee, D.-Y. Chung and E. Jang, *Nature*, 2020, **586**, 385–389.

2 Synthesis and Characterisation of Zinc Sulfide Phosphors

2.1 Aims

Doped zinc sulfides within the literature have been prepared through both solid state reactions and precipitation from solution, resulting in a range of emission wavelengths and different proposed assignments of these transitions. For example, both Kröger, and Bowers and Melamed report blue emission (440 nm) from zinc vacancies, while Sen claimed the transition was caused by relaxation from sulfur vacancy energy levels. Similarly, copper doping of zinc sulfides has led to a range of emission wavelengths, that are assigned to the same transition, without an explanation for the origin of the emission shift with respect to earlier literature reports. This chapter aimed to prepare a series of doped materials capable of emitting at (blue, green and red wavelengths) 460, 530, and 620 nm for use in displays and lighting technology. Based upon literature work, it was expected that silver, chloride, copper, and barium/manganese doping could afford the desired wavelengths. Secondly, this work aims to explore the nature of the defects causing the various emission wavelengths through the preparation of doped zinc sulfides using copper (I), copper (II), aluminium, and chloride dopants, along with undoped zinc sulfides. And computational analysis to provide an assignment that is consistent across the range of dopants.

2.2 Introduction

Zinc sulfide is a wide band gap ($3.50 - 3.80 \text{ eV}^{1-3}$) semiconductor comprised of tetrahedrally coordinated zinc and sulfur in a 1:1 ratio. The material is known to exist in one of two polymorphs, the cubic sphalerite form (zinc blende, Figure 2.1) and the hexagonal wurtzite form that is typically only present after heating temperatures greater than $1000 \text{ }^\circ\text{C}$.⁴ Zinc sulfide is particularly well known for the ability to be doped with a wide range of ions, generating defects, affording tunability of the electronic properties allowing use in a wide range of areas such as: field emitters⁵, UV light sensors⁶, gas sensors⁷, photovoltaics and photocatalysis.^{8,9} These defects can be classified into one of three forms: interstitial, where an ion exists in an off-site position; a vacancy, where an ion has been removed from the lattice position; or a substitutional defects (Figure 2.1), associated with the introduction of a second ion, such as a metal. Typically, the introduction of a substitutional defect will also cause one or both of the other defects, generating a range of emission wavelengths.

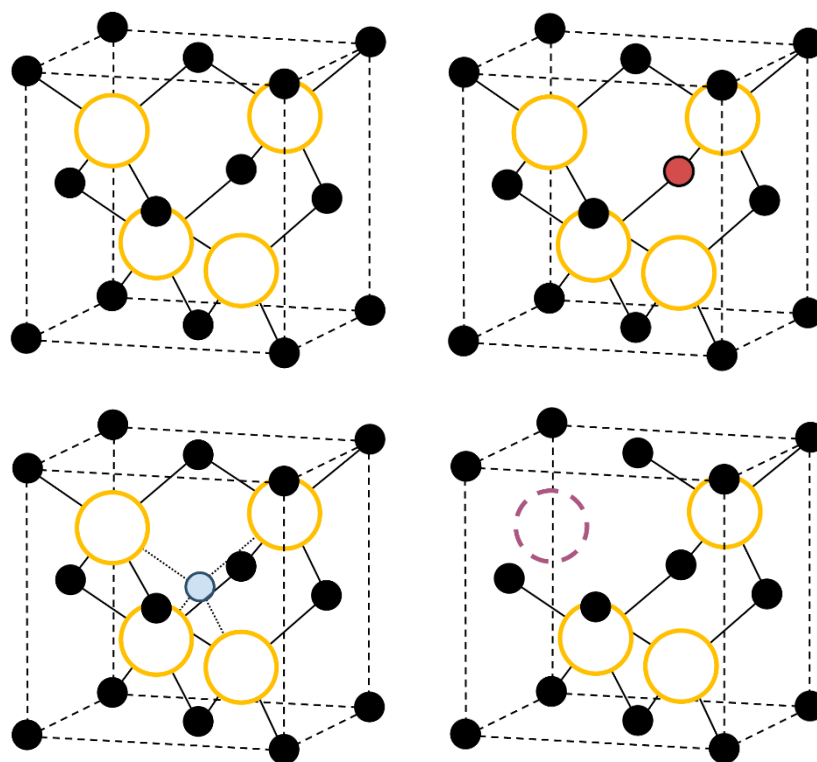


Figure 2.1: Pictorial representations (clockwise) of pure zinc sulfide, zinc sulfide with a substitutional defect, zinc sulfide with a sulfur vacancy defect, and zinc sulfide with an interstitial zinc defect. Where zinc = black circles, sulfur = yellow circles, substituted ion = red circle, interstitial ion = blue circle, and dashed purple circle = vacant site.

2.2.1 Copper, and Copper Co-Doped Zinc Sulfides

Table 2.1: Literature reported emission wavelengths and their assigned transitions.

Author	Dopant	Emission wavelength /nm	Assignment
Bowers and Melamed ¹⁰	NH ₄ Cl	440	Interstitial Zn and Zn vacancy
	Cu (0.01%)	520	Cu(I) interstitial or substitutional Cu(I)
	Cu (0.06%)	440	Cu ₂ ⁺ Cl
	Cu (0.3%)	520	Substitutional Cu(I)
	Cu	670	Interstitial Cu(I)
Meijernik ¹¹	Cu (0.123 at%)	470	Shallow donor → Cu(II)
		600	S vacancy → Cu(II)
Deshpand ¹²	Cu (0.06%)	480	Shallow donor → Cu(II)
Wang ¹³	-	411, 455	S vacancy, Zn vacancy
	Cu (0.5 mol%)	412, 446, 497	S vacancy, Zn vacancy, S vacancy → Cu(II)
	Cu (1 mol%)	411, 446, 505	S vacancy, Zn vacancy, S vacancy → Cu(II)
	Cu (2 mol%)	414, 450, 512	S vacancy, Zn vacancy, S vacancy → Cu(II)
Vatsa ¹⁴	Cu (0.5 at%)	450, 521	Interstitial Cu(I) → substitutional Cu(I), Shallow donor → Cu(I)
	Cu (1 at%)	450, 521	Interstitial Cu(I) → substitutional Cu(I), Shallow donor → Cu(I)
Zhang ¹⁵	-	440	Shallow donor → Zn vacancy
	Cu, Cl	490	Shallow donor → Cu(I)

Copper doped and co-doped zinc sulfides are probably the most studied zinc sulfide material, with emission maxima of 440 to 600 nm reported within the literature for a range of preparation procedures. In 1955, Bowers and Melamed attempted to relate the reported emission of copper activated zinc sulfides to the states of the activator and its position within the lattice.¹⁰ They prepared doped zinc sulfides through the solid state mixing of a zinc sulfide powder with copper nitrate and 3 wt% ammonium

Chapter 2. Synthesis and Characterisation of Zinc Sulfide Phosphors

chloride, which was then fired in a furnace. Four distinct emission profiles were observed depending upon the ratio of dopants, and the presence of a co-activator. Zinc sulfide doped with (ammonium) chloride produced a single emission peak with a maximum at 440 nm, and with the addition of 0.06 wt% copper, introduced a second weaker peak at 520 nm. Reducing the copper loading to 0.01 wt% or increasing it to 0.4 wt% resulted in a strong green emission at 520 nm, with a very minor blue (440 nm) component for 0.01 wt% doping. Without the presence of a chloride co-activator, a dual 440 and 670 nm emission was observed. The blue emission was assigned to a zinc vacancy and agreed with the earlier work by Kröger.¹⁶ Green emission, however, was less clear, since incorporation of Cu^+ into a Zn^{2+} site would require the incorporation of second additive, such as Cl^- , Br^- , or Al^{3+} or a sulfur vacancy. They concluded that since the emission arising from the above defects was the same; the green emission must be caused by copper in a substitutional site. Red emission was similarly assigned to copper, but from an interstitial location, that caused the formation of zinc vacancies giving rise to the blue emission that was also observed.

Meijernik's group observed similar blue and red emission for copper-doped zinc sulfide nanocrystals prepared via co-precipitation of zinc and copper with sodium sulfide.¹¹ However, the red emission was located at 600 nm, which they assigned to a transition between a localised donor, such as a sulfur vacancy, and the copper impurity. They also note an emission at 470 nm at 4 K, which shifts to higher energies as the temperature increases reaching ~440 nm at room temperature. In this case, however, the emission was assigned to the relaxation from a shallow donor state to the t_2 levels of the copper dopant. Deshpande, however, observed emission at 480 nm with room temperature measurements of copper doped zinc sulfides, which they similarly assigned to relaxation from a shallow state to the t_2 levels.¹² Wang's group similarly explored the photoluminescence of copper (0%, 0.5%, 1%, and 2% molar ratio to zinc) doped nanoparticles prepared by precipitation with sodium sulfide.¹³ Unlike the prior examples, a single component emission was not observed at any copper concentration. For undoped zinc sulfide, they reported a composite peak made of two emissions at 411 and 455 nm, with addition of copper a third peak emerged, around 512 nm and increased in intensity as the copper loading was increased. Like Bowers and Melamed, they assigned the emission at 455 to zinc vacancy defect, the green emission to a relaxation from a sulfur vacancy to the t_2 level of copper, and a sulfur vacancy to the highest energy

Chapter 2. Synthesis and Characterisation of Zinc Sulfide Phosphors

transition at 411 nm. Interestingly, they did not observe the red emission reported in other literature sources. Vatsa's group prepared copper doped zinc sulfides without a co-activator using the solid state method. Likewise, they reported no red emission from this doping procedure. However, at both copper concentrations trialled, 0.5 and 1%, a dual blue green emission was observed at 450, and 521 nm respectively. They assigned the 450 nm emission to a donor acceptor pair of interstitial copper and substitutional copper, and the green to relaxation from shallow donors to copper.¹⁴ Recent work from Zhang's group explored the photophysics of copper doped zinc sulfides prepared using microwave irradiation. The emission was found to red shift from 500 to 595 nm with increasing irradiation time up to 120 minutes. They claimed that the longer reactions times increased the proportion of copper dopant which is able to interact with sulfur vacancies, altering the level of the donor state.¹⁷

Sharma and co-workers prepared copper doped zinc sulfides using bromide and aluminium co-activators. Specifically, they found a 3:1:3 ratio of incorporated copper, aluminium, and bromide was able to achieve a bright green emission at 530 nm.¹⁸ Zhang explored the effect of copper concentration on the emission wavelength of copper and chloride co-precipitated nanoparticles.¹⁵ Interestingly, they note that no emission was observed without the reflux of the solution for an hour, with the intensity exhibiting a significant improvement when the samples were heated at reflux with excess zinc. For undoped particles they reported an emission at 440 nm, which shifted to 464 nm with the addition of 0.2% copper, which shifted again to 487 nm, following the addition of 3% copper, as was observed by Zhang's group, but to a lesser degree. In this case they assigned a transition at 490 nm to a relaxation from an electron trap state to the copper state, and a blue emission at 440 nm to relaxation from the same trap state to a hole trap caused by zinc vacancy surrounded by three sulfide ions and a chloride. Regarding copper doping, it is clear a range of emission profiles and energies are observed, with little agreement on the energy of the copper associated transition. However, most of the literature is in agreement that a relaxation from a shallow defect, such as a sulfur vacancy, to the copper bands causes the emission between 480 and 595 nm. A red emission has also been observed in a few literature reports which agreed on an assignment to a sulfur vacancy associated with interstitial copper.

2.2.2 Silver Doped Zinc Sulfides

The group of Sen prepared silver doped nanoparticles via a combined hydrothermal and high temperature (750, and 950 °C) solid state method.¹⁹ They noted an increase in the intensity of the emission and a slight shift from 445 to 454 nm upon annealing at 950 °C, similar to Zhang, and a corresponding increase in the intensity of peak at 337 nm for the excitation spectrum. No shift in emission was observed following the addition of silver and annealing at 750 °C, however, increasing the temperature to 950 °C caused a single emission at 533 nm, and a new peak in the excitation spectra at 370 nm. The difference between the two silver doped samples was ascribed to the melting of silver sulfide at 950 °C allowing for a greater proportion of silver to be incorporated within the zinc sulfide lattice. The blue emission from an undoped zinc sulfide was assigned to relaxation from a sulfur vacancy state. For the doped samples, relaxation from the conduction band to silver energy levels was assigned to the blue emission, whilst green emission was claimed to originate from relaxation from the sulfur vacancy down to the silver energy levels. Shen's group also prepared silver doped zinc sulfides using a precipitation method in alkaline solution.²⁰ With similar emission maxima reported, around 450 nm, with introduction of silver causing a red shift to 515 nm, which increased in intensity as the silver dopant concentration increased. These transitions were assigned in the same manner Sen's group.

2.2.3 Manganese Doped Zinc Sulfides

Bhargava and Gallagher were among the first to report a high luminescence efficiency and short lifetime for manganese doped zinc sulfides in 1993.²¹ They prepared manganese doped bulk zinc sulfide through solid state mixing, and a nanocrystalline form through a chemical precipitation in toluene. For both of these materials, only a single emission peak was observed at 584 and 590 nm, with band gaps of 332 and 265 nm, respectively. This yellow emission was assigned to the ${}^4T_1 - {}^6A_1$ transition of the substituted manganese ion. While such transitions are usually forbidden, perturbation by the zinc sulfide crystal field was claimed to partially allow the transition through the mixing of opposite spin states. They also claim the broad bandwidth of the yellow emission was caused by inhomogeneous broadening and phonon assisted transitions.²² Prakash's group also prepared manganese doped zinc sulfides through precipitation affording an emission at 589 nm. However, they also observed an additional four transition at 417, 446, 480, and 520 nm which they assigned to interstitial sulfur, and zinc; and sulfur, and zinc vacancies, respectively,

with the yellow emission assigned to the same ${}^4T_1 - {}^6A_1$ transition as before. This work represents one of the few total assignments of the possible transitions from native defects in a zinc sulfide material. Combined with the literature work so far, it presents an issue of accurate assignment to the observed emissions, with multiple sources reporting the same emission wavelength assigned to different transitions and vice versa. Of course, while it is possible for the defects to have the same transition, it indicates that careful consideration of the expected structural defects will play a significant role in assignment of the emissions observed in this work.

2.2.4 Barium and Manganese Co-Doped Zinc Sulfides

Work by Rao and co-workers prepared a red emitting manganese and barium co-doped zinc sulfide using a carbothermal reduction approach.²³ The degree of red shift from the typical manganese emission was observed to be dependent on the barium concentration, reaching an emission of 620 nm with 10% equivalent of barium added during the preparation. Powder X-ray diffractions showed a largely sphalerite phase with a minor component of Ba_2ZnS_3 . The shift in emission was claimed to be caused by two factors: the large size of the barium ion the crystal field stabilisation was expected to be large, which they argue will cause the manganese transition to shift to lower wavelengths. Secondly, they suggest the manganese ion leads to increased phonon coupling due to the large size of the barium ion. However, no precise assignment for the cause of the red shift was made.

2.3 Experimental and Methods

Powder X-ray Diffraction analysis was performed between 20° and 80° using a pro PAN Analytical powder diffractometer using a Cu $K\alpha$ radiation source operation at 40 KeV and 40 mA. Analysis of the diffraction pattern was carried out using Profex software. Microscopy was performed on a Tescan Maia3 field emission gun scanning electron microscope (FEGSEM) operating at 5, 15, and 30 kV. Images were acquired using the secondary electron and backscattered electron detectors. Samples were dispersed as a powder onto adhesive carbon Leit discs mounted onto aluminium stubs. Samples were analysed after coating in 7 nm (14 nm for silica coated samples) 80:20 Au:Pd using a Quorum 150T ES sputter coater. Energy-dispersive X-ray (EDX) analysis and mapping were performed using an Oxford Instruments X-Max^N80 detector, and the data was analysed using the Aztec software. Photophysical data was obtained on a JobinYvon-Horiba Fluorolog spectrometer fitted with a JY TBX picosecond photodetection module as solid

Chapter 2. Synthesis and Characterisation of Zinc Sulfide Phosphors

powders. Emission spectra were uncorrected and excitation spectra were instrument corrected.

2.3.1 Synthetic Procedures

All reactions were performed using a Carbolite-Gero tube furnace equipped with a mulite tube and programable temperature control unit. All reagents used were of high purity (ZnS: 99.99% pure by metal basis, dopants: > 99% pure by metal basis), purchased from commercial suppliers and used without further purification. Water used during the wet impregnation method was collected from a Barnstead EASYpure II RF ultrapure water system with a resistivity of 18.2 MΩcm⁻¹.

General Furnace Synthesis of Doped Zinc Sulfides: Zinc sulfide was mixed with the dopant(s) in an agate mortar and pestle for 10 minutes and decanted into a porcelain firing boat and placed in a furnace. Then purged with nitrogen for 10 minutes and heated to 800 °C with a temperature ramp of 3 °C/min and held at 800 °C for one hour before being allowed to cool passively under a flow of nitrogen.

Copper and Aluminium Doped Literature Samples: Prepared following the general scheme using zinc sulfide (1.00 g, 10.25 mmol) with copper sulfate pentahydrate (0.7 mg, 2.83 μmol [1, 3, 4], 3.9 mg, 15.74 μmol [2]) and aluminium nitrate nonahydrate (2.5 mg, 6.67 μmol [1], 7.0 mg, 18.53 μmol [2], 1.1 mg, 2.97 μmol [3, 4]) and potassium bromide (100 mg, 0.84 mmol [2]) ammonium bromide (50 mg, 0.51 mmol) as dopants.

Aluminium Doped: Prepared following the general scheme using zinc sulfide (1.00 g, 10.25 mmol) aluminium sulfide (5.0 mg, 33 μmol) as the dopant.

Copper Iodide Doped (5): Prepared following the general scheme using zinc sulfide (1.00 g, 10.25 mmol) with copper iodide (1.2 mg, 6.30 μmol) as the dopant.

Copper Sulfate Doped (6): Prepared following the general scheme using zinc sulfide (1.00 g, 10.25 mmol) with copper sulfate pentahydrate (1.5 mg, 6.01 μmol) as the dopant.

Copper Iodide and Ammonium Chloride (7): Prepared following the general scheme using copper iodide (1.2 mg, 6.30 μmol) and ammonium chloride (10.0 mg, 186.95 μmol)

Chapter 2. Synthesis and Characterisation of Zinc Sulfide Phosphors

Barium Doped: Following the general procedure using zinc sulfide (1.00 g, 10.25 mmol) with barium sulfide (140 mg, 0.83 mmol (8 mol%); 70 mg, 0.42 mmol (4 mol%); or 35 mg, 0.21 mmol (2 mol%)) added as the dopant.

Strontium Doped: Following the general procedure using zinc sulfide (1.00 g, 10.25 mmol) with strontium sulfide (99 mg, 0.83 mmol (8 mol%); 55 mg, 0.42 mmol (4 mol%); 27.5 mg, 0.21 mmol (2 mol%)) added as the dopant.

Calcium Doped: Following the general procedure using zinc sulfide (1.00 g, 10.25 mmol) with calcium sulfide (72 mg, 1 mmol (10 mol%); 60 mg, 8.3 mmol (8 mol%)) added as the dopant.

Barium and Manganese Oxide Doped: Following the general procedure using zinc sulfide (1.00 g, 10.25 mmol) with barium sulfide (140 mg, 0.83 mmol (8 mol%); 70 mg, 0.42 mmol (4 mol%); or 35 mg, 0.21 mmol (2 mol%)) added as the dopant with manganese oxide (7.1 mg, 0.1 mmol) added as a co-dopant to all samples

Barium and Manganese Nitrate: Following the general procedure using zinc sulfide (1.00 g, 10.25 mmol) with barium sulfide (140 mg, 0.83 mmol (8 mol%); 70 mg, 0.42 mmol (4 mol%); or 35 mg, 0.21 mmol (2 mol%)) with manganese nitrate tetrahydrate (25 mg, 0.1 mmol) added as a co-dopant.

Strontium And Manganese Doped: Following the general procedure using zinc sulfide (1.00 g, 10.25 mmol) with strontium sulfide (99 mg, 0.83 mmol (8 mol%); 55 mg, 0.42 mmol (4 mol%); 27.5 mg, 0.21 mmol (2 mol%)) added as the dopant with manganese oxide (7.1 mg, 0.1 mmol) added as a co-dopant to all samples

Calcium And Manganese Doped: Following the general procedure using zinc sulfide (1.00 g, 10.25 mmol) with calcium sulfide (60 mg, 8.3 mmol (8 mol%) and manganese oxide (7.1 mg, 0.1 mmol) added as dopants.

Wet Impregnation Method: Zinc sulfide was added to water (20 mL) along with dopants and heated to 90 °C and the water allowed to evaporate. The sample was then added to a furnace in a porcelain boat, purged under nitrogen for 10 minutes and heated to 800 °C with a ramp of 3 °C/min, held for one hour and allowed to cool passively under a flow of nitrogen.

Ammonium Chloride Doped (8): Following the wet impregnation procedure using zinc sulfide (1.00 g, 10.25 mmol) with ammonium chloride (10 mg, 186.95 µmol) as the dopant.

Chapter 2. Synthesis and Characterisation of Zinc Sulfide Phosphors

Copper Doped (9): Following the wet impregnation procedure using zinc sulfide (1.00g, 10.25 mmol) using copper sulfate pentahydrate (1.5 mg, 6.01 μ mol) as the dopant.

Copper and Chloride Doped (10): Following the wet impregnation procedure using zinc sulfide (1.00 g, 10.25 mmol) using ammonium chloride (10 mg) and copper sulfate pentahydrate (1.5 mg, 6.01 μ mol) as the dopants.

Silica Coating: Zinc sulfide (1.00 g) was dispersed in a mixture of water (50 mL), methanol (50 mL) and ammonia solution (5 mL, 35%) with TEOS (1 mL) and stirred overnight. The Mixture was filtered and the solid washed with water and dried under reduced pressure. The sample was then divided into three portions and subjected to three sets of conditions. One sample was fired in the same manner outlined in the general procedure: placed into a porcelain boat, purged with nitrogen for 10 minutes and heated to 800 °C with a temperature ramp of 3 °C/min and held at 800 °C for one hour before being allowed to cool passively under a flow of nitrogen. A second sample was exposed to the same conditions but fired under a flow of air. The third sample was stored in a vial under ambient conditions.

Uncoated Zinc sulfide treatment: Zinc sulfide (1.00 g) was dispersed in a mixture of water (50 mL), methanol (50 mL) and ammonia solution (5 mL, 35%) and stirred overnight. The Mixture was filtered and the solid washed with water and dried under reduced pressure. The sample was then divided into three portions and subjected to three sets of conditions. One sample was fired in the same manner outlined in the general procedure: placed into a porcelain boat, purged with nitrogen for 10 minutes and heated to 800 °C with a temperature ramp of 3 °C/min and held at 800 °C for one hour before being allowed to cool passively under a flow of nitrogen. A second sample was exposed to the same conditions but fired under a flow of air. The third sample was stored in a vial under ambient conditions.

Table 2.2: Reported supplier purity and impurities of zinc sulfide and the dopants used within this chapter.

Chemical	Reported Purity	Reported Impurities (ppm)
Zinc Sulfide	$\geq 99.99\%$	Not specified by supplier
Barium Sulfide	$\geq 99.7\%$	Cd (< 4), Cr (<1), Pb (<4), Si (<100), Sr (63)

Chapter 2. Synthesis and Characterisation of Zinc Sulfide Phosphors

Calcium Sulfide	99.9%	Ba (70), Fe (20), K (200), Mg (70), Na (200), Pb (10), Sr (700)
Strontium Sulfide	99.9%	Not available
Copper Sulfate	≥99.999%	Sn (2), Fe (1)
Copper Iodide	≥99.995%	Not specified by supplier
Aluminium Sulfide	≥99%	Ca (6), Cu (3), Fe (444), Mg (14), Si (54), Ti(139), V(47)
Manganese Oxide	99.997%	Not specified by supplier

2.4 Results and discussion

2.4.1 Synthesis of Zinc Sulfides

In this work, a solid state synthesis method was employed to prepare the doped zinc sulfide materials. This method provides an increased substrate scope, because certain dopants will not be readily soluble, or else the generated dopant sulfide can be significantly less soluble than zinc sulfide, thus disrupting dopant incorporation. This is particularly important for copper doped zinc sulfides. Typically, this involved combining the zinc sulfide and a dopant(s) in a mortar and pestle and grinding together to ensure thorough mixing of the materials. The powder was then transferred to a crucible and placed in a tube furnace with flowing nitrogen for 20 minutes before being heated to 800 °C and held for an hour (a process called firing). Because oxidation of these materials was a concern, the furnace, and sample, were allowed to cool overnight under a positive pressure of nitrogen. The majority of the fired materials retained the white colour of the host (zinc sulfide) material; however, copper doping caused a greying of the solid during mixing and resulted in a yellow tinged material after firing. Group 2 metals were used as sulfide salts, aluminium was used as either the sulfide or nitrate salt, and manganese was either the oxide or nitrate form. Copper was used in both oxidation states: copper(I) iodide or copper(II) sulfate. The second method of synthesis, wet impregnation, followed the same firing procedure, but mixed the host and dopant in water, which was then evaporated, to produce zinc sulfide with the dopant on the surface of the material which is then incorporated during the firing procedure. Analysis of the material morphology was carried out using scanning electron microscopy (SEM) using either

Chapter 2. Synthesis and Characterisation of Zinc Sulfide Phosphors

secondary or backscattered electrons, combined with energy dispersive X-ray (EDX) to analyse the composition of the material.

2.4.2 Copper and Aluminium Doped Zinc Sulfides

2.4.2.1 Assessment of Literature Methods

A range of copper and aluminium dopings were selected and synthesised based upon earlier work within the literature. All samples, **1** – **4**, (Table 2.3) were prepared following the same general procedure outlined in the experimental, using copper (II) sulfate and aluminium nitrate as the dopant sources with no modification made to the heating or grinding procedure. In the case of sample **2**, a minor modification was made to incorporate potassium bromide (10 wt%) and ammonium bromide (5 wt%) during the grinding process to replicate the process within the literature source.¹⁸

Table 2.3: MP-AES results for copper and aluminium doped zinc sulfides prepared according to literature reports.

Sample	Element	% Mass of dopant	
		Observed	Expected
1 ²⁴	Copper	0.017±0.001	0.018
	Aluminium	0.019±0.001	0.018
2 ¹⁸	Copper	0.087±0.003	0.1
	Aluminium	0.049±0.003	0.05
3 ²⁴	Copper	0.020±0.0006	0.018
	Aluminium	0.011±0.0006	0.008
4 ²⁴	Copper	0.016±0.0005	0.018
	Aluminium	0.008±0.002	0.008

Immediately it was observed that obtaining unity doping with respect to the expected incorporation was unreliable, with all but one sample differing from the desired values, and with a high potential for variance between samples, e.g. compare samples **3** and **4**. The variance in dopant incorporation was ascribed to two reasons: firstly, inaccuracies in measuring volumes or masses when preparing the dopants and then subsequent transfer of material, which is compounded with the small quantities used. Secondly, incomplete incorporation of the dopant during the reaction, with the (non-incorporated) excess removed in the washing step. Incomplete incorporation could potentially be overcome by increasing the reaction temperature or the reaction time however, altering either of these can adversely affect the luminescent properties.²⁵

Chapter 2. Synthesis and Characterisation of Zinc Sulfide Phosphors

Combined with the variance between samples **3** and **4**, where the same mass of dopants was used but the mass of the incorporated aluminium and copper in **4** was almost half of the observed values in sample **3** suggested issues with measuring such small volumes being the overarching cause of the differences.

Despite the variations in the incorporated dopant concentration, and the addition of excess bromide in sample **2**, the excitation spectra (Figure 2.2) of the samples were remarkably similar. All the samples exhibited a peak around 345 nm, which corresponds with literature reports of the zinc sulfide band gap,^{19,21,26,27} and assigned as such and within the range of reported values of 326 – 354 nm for bulk zinc sulfide.¹⁻³ A small peak was also observed at 280 nm which is rarely reported in the literature; it has previously been assigned to the band gap for nanocrystalline materials. However, particles small enough to cause a blue shift of the band gap would sinter at the temperatures used in the preparation reported in this thesis. As the band gap of bulk ZnS is 326 – 354 nm, transitions of a higher energy (shorter wavelength) will involve states that exist amongst the valence or conductance band of the bulk material. Therefore the 280 nm band was presumed to be a feature within the conductance band continuum. There was, however, a slight variance in the λ_{\max} of the third peak, which shifted from 368 nm to 375 nm as ratio of copper to aluminium was increased, although all four samples exhibited similar intensities above 375 nm. As the band gap appeared to be consistent throughout the samples, this change could not be due to the size of the particles causing a quantum confinement effect as discussed in Chapter 1, but instead caused by the different dopant concentrations, and the addition of excess bromide, as is the case of sample **2**.

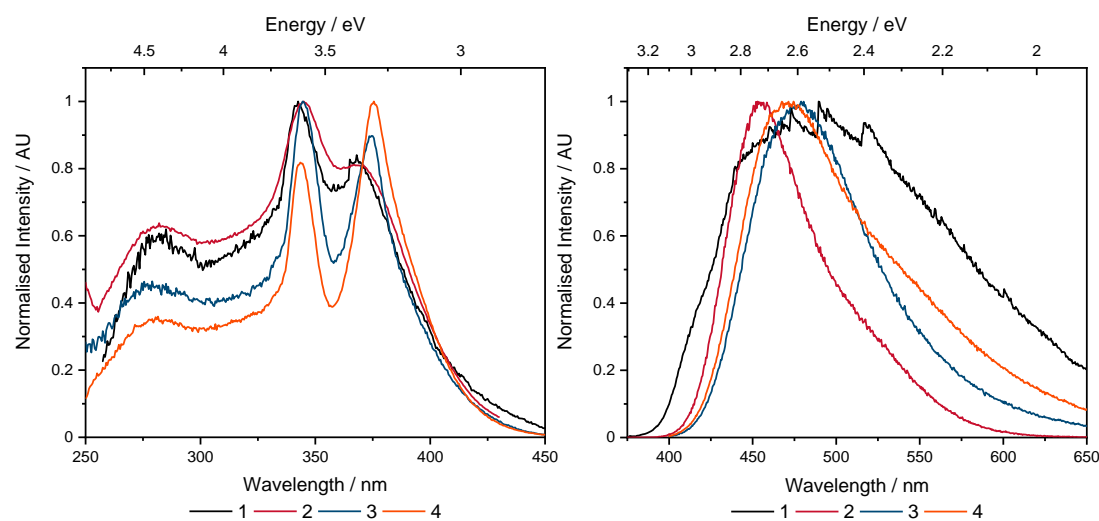


Figure 2.2: Excitation (left) ($\lambda_{\text{em}1} = 483 \text{ nm}$, $\lambda_{\text{em}2} = 456 \text{ nm}$, $\lambda_{\text{em}3} = 478 \text{ nm}$, $\lambda_{\text{em}} = 471 \text{ nm}$) and emission (right) ($\lambda_{\text{ex}} = 345 \text{ nm}$) spectra for example literature samples.

Chapter 2. Synthesis and Characterisation of Zinc Sulfide Phosphors

In contrast, the emission spectra showed large differences between each sample. Sample **2** was dominated by a strong blue-emitting peak at 455 nm, likely caused by the excess bromide introducing a larger number of defect states than are generated by the comparatively minor copper and aluminium dopants used (discussed below). Samples **3** and **4** both showed a slight difference in λ_{max} , shifting from 470 nm to 478 nm, assuming that the change in absolute concentration of the dopant would not cause a shift in the maxima,¹³ this difference must have been due to ratio of copper and aluminium increasing, thereby forming an emission that was more representative of copper-caused emission. Surprisingly, however, this lower ratio appeared to cause a greater contribution in the green region of the spectrum. A broad emission with a FWHM of roughly 200 nm was observed upon decreasing the ratio of copper and aluminium to 1:1; since no previous literature data supports a single emissive state causing such a large broad emission, it was likely that this was caused by at least two defects, caused by both copper and aluminium.

Doping zinc sulfide with ions of a different charge to those being replaced (i.e., dopant ions without a ± 2 charge) was envisaged to cause an imbalance within the lattice, creating a charged system that required either the ejection of zinc or sulfur to balance the overall charge, or the introduction of second dopant ion that could counteract the imbalance. For example, copper(I) doping would generate a substituted zinc site that is deficient in positive charge creating an overall net negative charge. This discrepancy, in the absence of a second dopant, will lead to formation of sulfide vacancies and presumably interstitial sulfide from these vacancies. Since each sulfide vacancy can account for the incorporation of two copper ions, it could be expected that these two copper sites will differ in their local environment, i.e., one will be four coordinate – surrounded by four sulfides – whereas the second will be three coordinate, thus a slight difference in energies of these two states are expected and a commensurate change in emission would be observed. Or the sulfide vacancy will not be spatially associated with either copper ion, forming a sulfide vacancy surrounded by four zinc ions.

If, however, a co-dopant was added that accounted for the charge discrepancy, such as aluminium or a halide, the emission profile should change significantly. Specifically, literature reports suggest that an introduced halide would sit within a sulfide vacancy¹⁰, while aluminium would prevent the formation of sulfide vacancies in the first place but could also generate interstitial zinc due to substitution from zinc, if the substituted ion was unable to be reincorporated at a second location within the

Chapter 2. Synthesis and Characterisation of Zinc Sulfide Phosphors

system. Of course, this implied that the introduction of copper and aluminium in a 1:1 ratio should only generate one defect (interstitial zinc) and two emissions, from the interstitial zinc and copper states. However, as previously discussed this was not the case: sample **1**, a sample with a 1:1 ratio of Cu:Al shows a broad emission arising from several defects, without an obvious green emission. The likely explanation for this, was the source of copper used in these preparations, copper(II) sulfate, was reduced to copper(I) when exposed to the zinc sulfide; this was evident by the discoloration of the zinc sulfide immediately after addition of the copper. Coupled with the mixing of the sample, it was possible that the initial reduction created either elemental sulfur by reducing two copper ions, or two singly reduced sulfur ions, both of which generate a charge imbalance, which would be corrected by the creation of additional zinc defects (both interstitial and vacancy). Sample **3** with a 2:1 ratio of copper to aluminium displayed a sharper peak, likely caused by fewer green emitting states, presumably due to the lower concentration of aluminium which resulted in fewer zinc vacancies and interstitial zinc ions. With the addition of excess potassium and ammonium bromide in sample **2**, the formation of a large number of zinc and sulfur defects was anticipated. The emission spectrum exhibited a marked change in profile, with a single defect dominating the emissive relaxation pathway; this was expected to be a zinc related defect. From the prior discussion of charge imbalance, interstitial sulfur and zinc, along with zinc and sulfur vacancies, were the defects considered in these materials, however, due to the range of potential defects in a single sample it was not possible to unambiguously assign the transitions to a defect based upon these data alone.

2.4.2.2 Aluminium Doped Zinc Sulfides

To deconvolute the effects of the defect states observed in the copper and aluminium doped materials, the two dopants were used individually, and the corresponding materials analysed. There was no clear alteration in the morphology of the aluminium doped zinc sulfide compared to pure ZnS, although this was expected as a small concentration of dopant was used. The EDX mapping (Figure 2.3) showed a largely homogenous sample throughout, with only a couple of areas that were devoid of sulfur and zinc, that was presumed to be caused by occlusion of this site by the surrounding particles lowering the signal intensity at the detector. The aluminium map data was excluded due to the aforementioned low dopant quantity being below the limits of the detector.

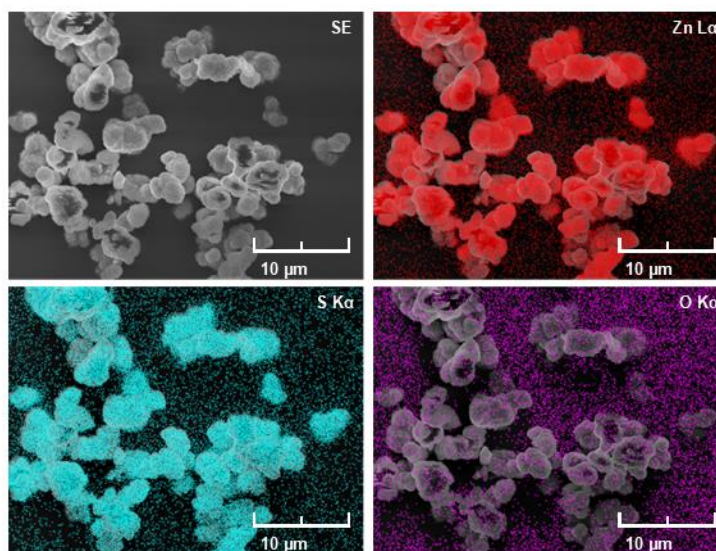


Figure 2.3: SEM and EDX images for aluminium sulfide doped zinc sulfide showing contributions from zinc, sulfur and oxygen.

Considering the photophysical properties (Figure 2.4), upon doping with only aluminium a single sharp peak located at 337 nm was observed in the excitation spectrum, showing a slight blue shift from the copper and aluminium doped samples that displayed a peak at 345 nm. Such a shift in the band gap upon removing copper was unexpected, and perhaps indicated a significant change in either the valence band or conduction band. It was possible that aluminium caused an alteration in the band gap, owing to structural variations (defects) arising from the substitution of zinc with a smaller aluminium cation, resulting in a distortion of the surrounding tetrahedra,²⁸ which in turn alters the energy of these zinc and sulfur bands. Surprisingly, the excitation spectra of the blue peak around 450 nm, did not exhibit a strong contribution at 370 nm as seen in the prior samples, which indicated a relatively low proportion of these defect states given the intensity of the band gap

Chapter 2. Synthesis and Characterisation of Zinc Sulfide Phosphors

for this excitation. However, the excitation spectra of the green peak centred around 520 nm, showed a new broad, symmetric peak with a λ_{max} of 400 nm.

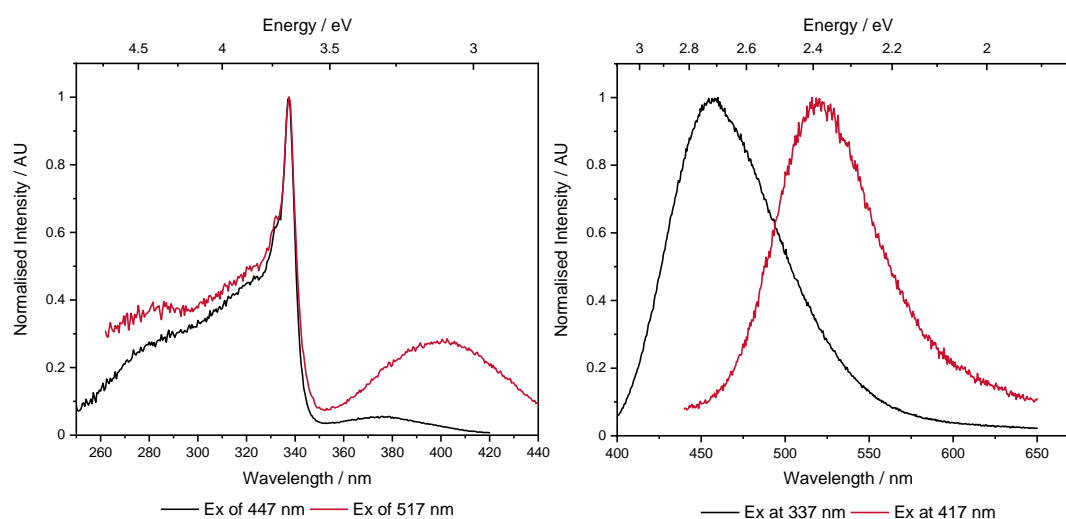


Figure 2.4: Excitation (left) and emission (right) spectra of aluminium sulfide doped zinc sulfides.

The emission spectra showed two peaks: one with a λ_{max} of 447 nm and the second with a λ_{max} 520 nm. The blue peak was almost identical to that seen in sample 2, with a λ_{max} of 456 nm, however, the peak was broader suggesting contributions in the 400 to 420 nm region as well as beyond 475 nm. It was believed that the second emission peak with a λ_{max} of 520 nm was responsible for the observed tail that extends into the green region. Given that both states showed the same transition at 337 nm in their excitation spectra, but the intensity of the emission was much weaker for the green emitting defect state, some conclusions may be drawn about the effect of doping with aluminium sulfide assuming that relaxation from the green emissive state was not disfavoured relative to relaxation via the blue pathway. Introducing a +3 metal such as Al(III) without a second monovalent anion dopant (such as a chloride) is expected to cause an overabundance of positive charge within the lattice due to substitution of a +2 zinc ion with a +3 aluminium ion,¹⁵ which can only be balanced by the ejection of zinc, presumably into an interstitial site, in a 2:1 aluminium:zinc ratio. Hence two defect states would be expected: interstitial zinc and zinc vacancies. Bands associated with interstitial zinc would correspond to a defect state bands within the band gap, while vacancies would only influence the bands of the surrounding sites, perturbing the energy of the valence and conduction bands. Because of conflicting assignments within the literature, it is difficult to assign the observed transitions. The lack of copper doping¹ in these samples means

¹ Cu concentration in AIS is 3 ppm. Combined with the mass of AIS used in aluminium doping (5 mg), the expected amount of copper is 15 ng or 0.0000015 wt%.

Chapter 2. Synthesis and Characterisation of Zinc Sulfide Phosphors

any assignment of the transitions to copper are not applicable to these samples and the defects are likely to be zinc related. However, conflicting arguments of the energy level of the interstitial and vacancy defects would make any assignment ambiguous.

2.4.2.3 Copper Doped Zinc Sulfides

2.4.2.3.1 SEM and EDX Analysis

Unlike the aluminium doped samples, the copper doped samples were prepared using two sources of copper with different oxidation states: copper(I) iodide (**5**), and copper(II) sulfate (**6**), as well as a copper iodide(I) sample prepared with the addition of ammonium chloride (**7**), to investigate the influence of a chloride co-activator. All samples were prepared following the same solid state method as the literature samples, and aluminium doped sample discussed above (Figure 2.5). Additionally, the effect of ammonium chloride (**8**), copper(II) sulfate (**10**), and a co-doped sample using copper(II) sulfate and ammonium chloride (**9**) was examined using a wet impregnation approach and is discussed below (see sections 2.4.2.3.3 and 2.3.1 for details). (Appendix Figure 6.1).

Table 2.4: Variations in dopant and method used to investigate the effect of copper doping on the luminescent properties of zinc sulfide

Method	Sample	Dopant	Co-Dopant
Solid State	5	CuI (0.04 wt% Cu)	-
	6	CuSO ₄ (0.04 wt% Cu)	-
	7	CuI (0.04 wt% Cu)	NH ₄ Cl (1 wt%)
Wet Impregnation	8	NH ₄ Cl (1 wt%)	-
	9	CuSO ₄ (0.04 wt% Cu)	NH ₄ Cl (1 wt%)
	10	CuSO ₄ (0.04 wt%)	-

Despite the variation in the oxidation state of the copper source, the presence of ammonium chloride, or the method used to produce the sample pre-firing, no significant difference was observed between each sample, nor when compared to the aluminium doped sample prepared earlier. Presumably, any differences relating to the pre-treatment were homogenised when the sample was fired, resulting in the same morphology. The samples themselves, were comprised of larger aggregated particles that varied in size from 1.6 × 2.1 μm up to 4.8 × 4.1 μm with most particles

Chapter 2. Synthesis and Characterisation of Zinc Sulfide Phosphors

being vaguely oval in shape and 2.5 μm along the longest edge. These larger particles were comprised of smaller particles that exhibited a high degree of variation in size. With the smaller particles being less than 100 nm along the longest edge, and the large particles being greater than 200 \times 200 nm.

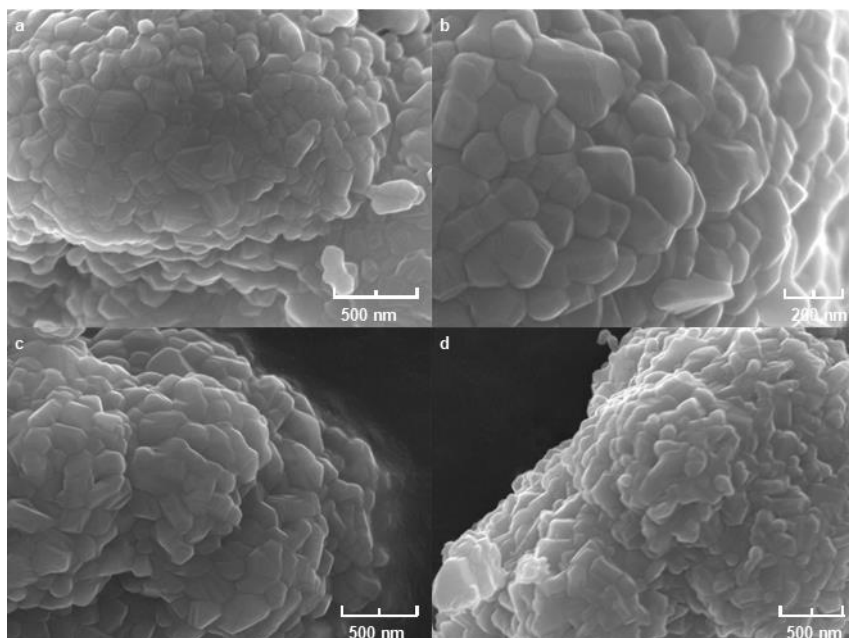


Figure 2.5: SEM images of copper doped zinc sulfides: a) solid state CuSO_4 (6), b) solid state $\text{CuI NH}_4\text{Cl}$ (7), c) wet impregnation CuSO_4 (10), d) wet impregnation no dopant

Across all samples zinc EDX data (Figure 2.6) appeared homogenous excluding a few small areas that were devoid of any significant elemental contribution; matching the background noise. However, as these areas of low concentration also occur within the sulfur maps, it was likely related to the angle of the detector relative to the sample which occluded the signal. Expectedly, the solid state samples showed no areas of high oxygen concentration, with only background oxygen signal observed, as they were not exposed to oxidising conditions. Interestingly, the lack of oxidation was mirrored in the wet impregnation samples that were exposed to hot water (Appendix Figure 6.1), which is known to react with zinc sulfide forming zinc oxide and hydrogen sulfide. Point analysis showed no significant difference in the zinc and sulfur ratio. Although, the effect of the water treatment may only be visible in the photophysical properties of the materials.

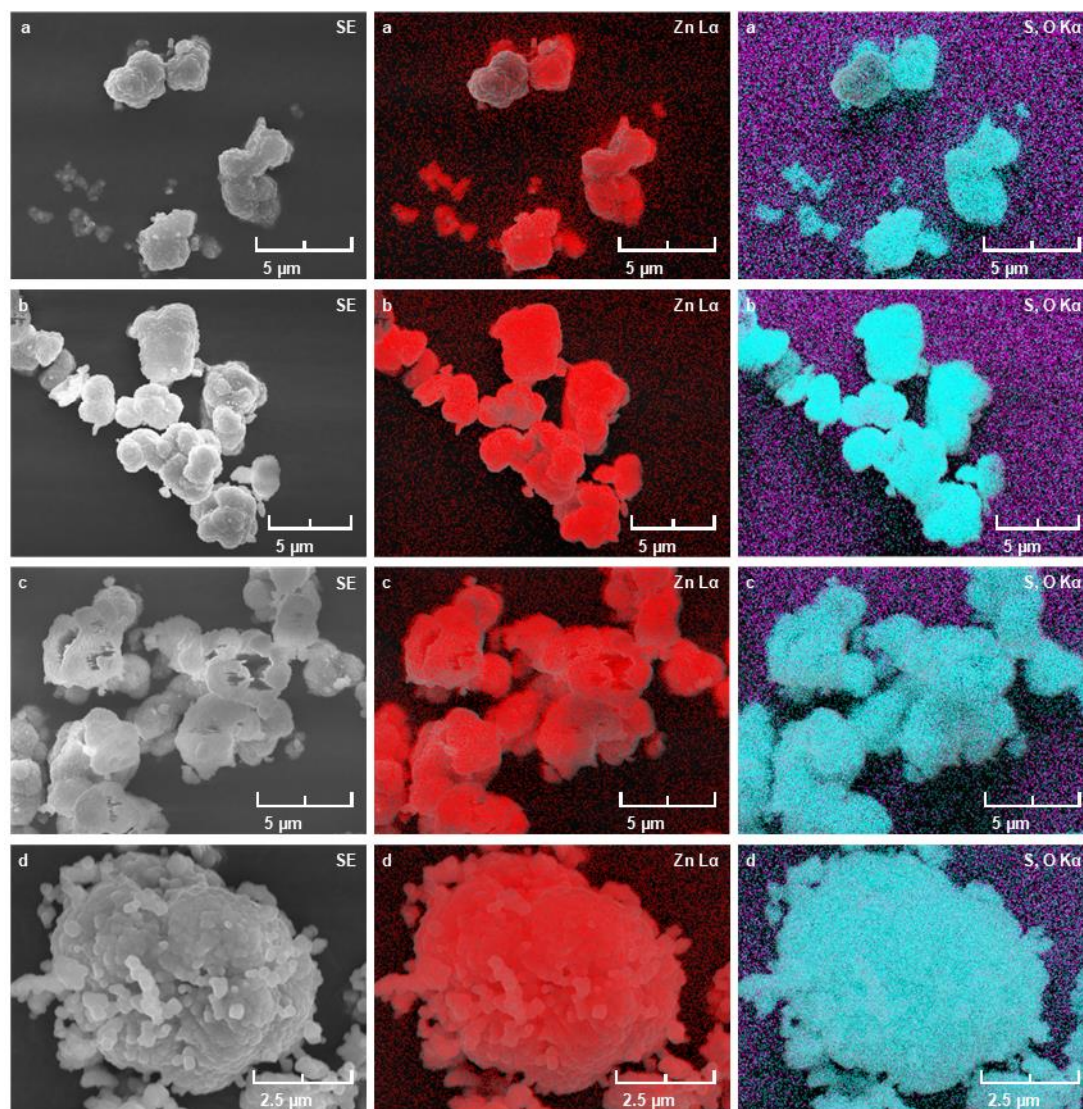


Figure 2.6: SEM and EDX images of doped ZnS samples a) CuI (**5**), b) CuI, NH₄Cl (**7**), c) CuSO₄ (**6**), and d) CuSO₄, AlNO₃•(H₂O)₉ (**4**) prepared by the solid state method, showing contributions from zinc, sulfur and oxygen.

2.4.2.3.2 Luminescence Spectroscopy

All the copper doped samples prepared via the solid state method (**5** – **7**), regardless of the source of copper, or the presence of the ammonium chloride co-dopant (**7**) showed a strong excitation peak with a λ_{\max} of 373 nm (Figure 2.7), the same as the aluminium sample discussed above, which suggested the origins of these peaks were likely to be the same. Interestingly, the sample doped with copper(II) sulfate did not appear to have a band gap peak in the expected region. It is unlikely that the band gap of the sample has changed so dramatically as to overlap with the defect peak at 373 nm. Instead, it was more likely the loss of the band gap contribution was caused either by a large number of defects corresponding to this particular state, or a defect that was not accessible via excitation of the band gap. Copper(I) iodide, unlike copper (II) sulfate, was not

Chapter 2. Synthesis and Characterisation of Zinc Sulfide Phosphors

expected to be reduced by the zinc sulfide and was therefore anticipated to have fewer types of defects. Indeed, the presence of a strong band gap excitation would support such a premise. Addition of excess ammonium chloride broadened the defect peaks into the 400 – 450 nm region, which, as with aluminium doping, were likely to be zinc defects; this is consistent with the additional broadening observed for the excitation of the peak located at 525 nm.

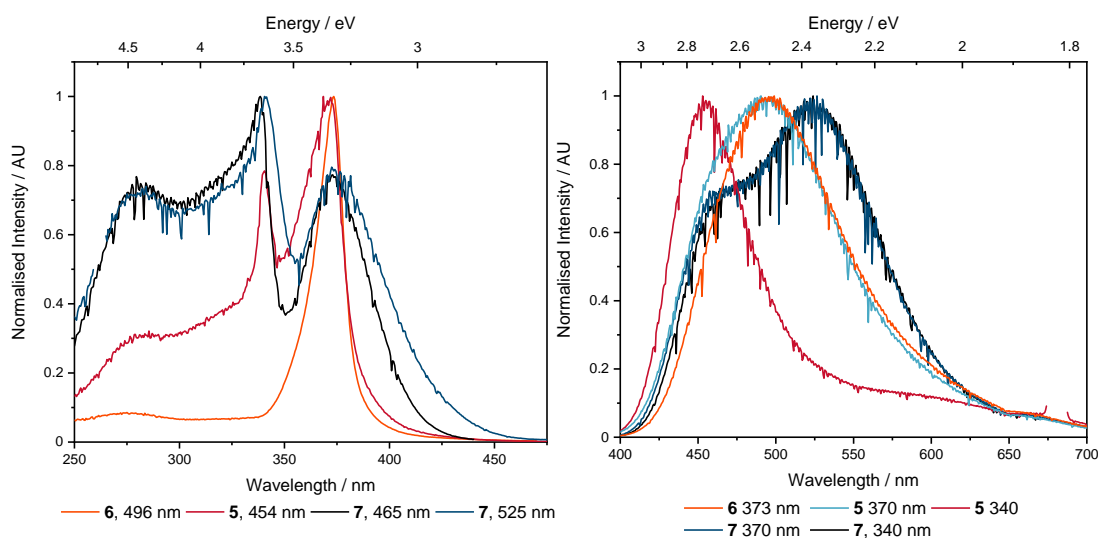


Figure 2.7: Excitation (left) and emission (right) spectra for doped zinc sulfides with the two excitation and emission wavelengths labelled.

The emission spectrum for copper(II) sulfate doped zinc sulfide (**6**) displayed a single broad peak with a λ_{\max} of 494 nm. The broad nature of this peak suggested it could be a composite of multiple separate emission events, due to the strong similarity to materials prepared with different dopants. Copper(I) iodide (**5**) doping exhibited a similarly broad peak when excited at 370 nm, and an almost identical peak maximum, showing a slight blue shift to accompany the broader peak towards the 400 nm region. However, exciting at the band gap generated a significantly altered peak shape and shifted the λ_{\max} to 454 nm. Such a significant change was unexpected as, in previous samples, a defect peak located at 370 nm also corresponded to an emission with a λ_{\max} of 454 nm. It therefore seems reasonable to infer, that one or more additional defect states were present. Likewise, addition of excess ammonium chloride (**7**) altered the emission profile once again, forming a new green peak with a λ_{\max} of 525 nm and a shoulder that corresponded to the blue emission previously discussed. As the only difference to the previous samples was the addition of chloride, the green peak must be related to a defect caused by the introduction of this anion.

Chapter 2. Synthesis and Characterisation of Zinc Sulfide Phosphors

In the case of copper(II) sulfate doped zinc sulfide (**6**), the defect states are believed to be related to the incorporation of the copper ion, as the emission wavelength observed (≈ 450 nm) has been reported for literature samples prepared without a sulfate counterion^{10,13,24,29}. Reduction of the copper(II) species could generate additional sulfur vacancies via oxidation of the sulfur¹⁵, and as before, due to mixing during the preparation of the material, these sulfur defects were not expected to all be in nearest neighbour sites to the incorporated copper. Incorporation of the mismatched copper(I) would cause the ejection of a sulfide anion in a 2:1 ratio forming both sulfur vacancies and interstitial sulfur, and zinc. Therefore, four defect states were considered: interstitial zinc and sulfur, and zinc and sulfur vacancies. Interstitial zinc was expected to cause the same excitation and emission spectra observed with aluminium doped samples. As only a single defect appeared to be present in the excitation spectrum it was not possible to assign a defect, the same was true of the emission spectra: due to the range of potential defects, and the broadness of the peak all fine detail pertaining to the defect states was obscured. Previous reports of a sharp blue emission within the literature have been assigned to chloride caused zinc interstitial and vacancy defects,¹⁰ copper caused zinc vacancies,¹³ and natural zinc vacancy defects.¹⁵ However, more recent reports claim zinc vacancies cause a green emission with the observed ≈ 450 nm blue emission assigned to interstitial zinc³⁰ or sulfur defects.¹⁴ Based upon the number of reports that agree with a zinc vacancy defect as the origin of the blue emission, this is believed to be the most likely cause and such an assignment would also agree with luminescence data of aluminium doped zinc sulfide.

In contrast, copper(I) iodide (**5**) which was not expected to be reduced during mixing with zinc sulfide – as shown by previous work within the literature examining both magnetic susceptibility¹⁰ and EPR^{15,24} of copper doped zinc sulfides - was expected to elucidate the origin of the defects. However, the iodide counterion provided a second dopant that could be incorporated into the lattice, although the size of the anion may have reduced the chance of this to occur. Iodide, and other halides, as with copper(I), cause a shift from the neutral charge of a zinc sulfide: the resulting system will have a net positive charge requiring the ejection of zinc from lattice, forming both zinc vacancies and interstitial sites. Combined with the sulfur defects caused by incorporation of copper, a broad emission was to be expected. However, sulfur and zinc vacancies can also be filled by copper and iodide

Chapter 2. Synthesis and Characterisation of Zinc Sulfide Phosphors

respectively, generating fewer defects than anticipated. Similar shifts in emission wavelength have also been observed within the literature when copper doping is carried out in conjunction with a halide anion. The red shift in emission observed in these samples is weaker than shown within the literature, along with a larger FWHM of the emission peak.^{10,24} It should be noted, however, that in both literature reports they note that the ratio of copper and the halide counterion will influence the emission observed. For example, Bowers and Melamed reported a blue emission at 440 nm with 0.06% doping of copper with excess chloride, while both 0.01 and 0.3% copper doping produced a green emission at 520 nm assigned to interstitial or substitutional copper.¹⁰ Similarly, Wang's group reported a copper concentration dependent shift from 497 nm (0.5 mol% Cu) to 512 nm (2 mol% Cu) assigned to a S vacancy → Cu transition.¹³ As discussed earlier, the defect peak located at 370 nm produced a different emission profile than either sample **6**, or the aluminium doped sample. However, the broad emission suggested the same 454 nm transition was present, and that two defects have the similar energy levels with respect to the band gap and valence band, but upon relaxation produce two states of different energies resulting in the same excitation wavelength producing different emission wavelengths. Thus, it is likely the broad curve observed for sample **5** is a combination of vacancy and interstitial defects and the involvement of a copper related transition cannot be excluded.

To further explore the impact of the halogen co-dopant, an excess of a halide was added, in this case ammonium chloride (**7**), to explore the defects related to the halide source incorporation. Since the method of incorporation and the source of copper was kept consistent, any changes compared to the copper(I) iodide sample could only be caused by the incorporation of chloride anions or ammonium cations. Zinc related defects were expected to predominate in this sample due to the balancing of charge from incorporating the anion and cation, along with presence of interstitial sulfur ions from halide substitution. The strongest peak, located around 523 nm, is often reported within the literature as a copper associated transition, being assigned as a shallow donor → substitutional copper transition.^{10,14} While other reports state the transition does not involve copper energy levels and relates to zinc vacancies^{14,30} in contrast to prior literature claims that such a transition caused a blue emission. The emergence of this second distinct peak must be caused by the ammonium chloride, however, as has been discussed earlier, the ratio of the copper and co-dopant will influence the emission wavelength obtained.

Chapter 2. Synthesis and Characterisation of Zinc Sulfide Phosphors

Therefore, the emergence of this new peak cannot be solely assigned to the presence of zinc defects caused by the introduction of chloride nor to sulfur defects caused by the incorporation of +1 cations such as the ammonium or copper dopants. The second, higher energy, peak would appear to align with the emission observed in both aluminium and copper sulfate doped samples and is likely to have the same origin. The tail observed in the excitation spectra only for sample **7**, also bares similarity with regards to the region in which it occurs (400 – 450 nm) and the existence of a green emission. Again, suggesting the defects present in these two samples are similar. Whilst copper cannot be ruled out as the assignment for the transition, the assignment to interstitial zinc and zinc vacancies is believed to be more consistent with the assignments within the literature and the results observed in this work.

2.4.2.3.3 Wet Impregnation

Wet impregnation was also trialled for doping zinc sulfides. In this method, the zinc sulfide was mixed with the dopant(s) in hot water and the water evaporated to leave a dry powder with the dopants attached to the surface, and the fired in a furnace to facilitate incorporation into the lattice. Excitation spectra (Figure 2.8) for copper(II) sulfate and ammonium chloride co-doped (**9**), and ammonium chloride (**8**) doped samples were almost identical to the solid state method. Exhibiting two different excitation peaks depending on the wavelength of interest: 342 nm corresponded to excitation of the green emission, and 338 nm for the blue emission. Whilst in these samples such a shift could be ascribed to the introduction of water altering the band gap it would not explain it for the earlier samples, nor would it resolve the influence upon the energy levels zinc defects nor the magnitude of the band gap.

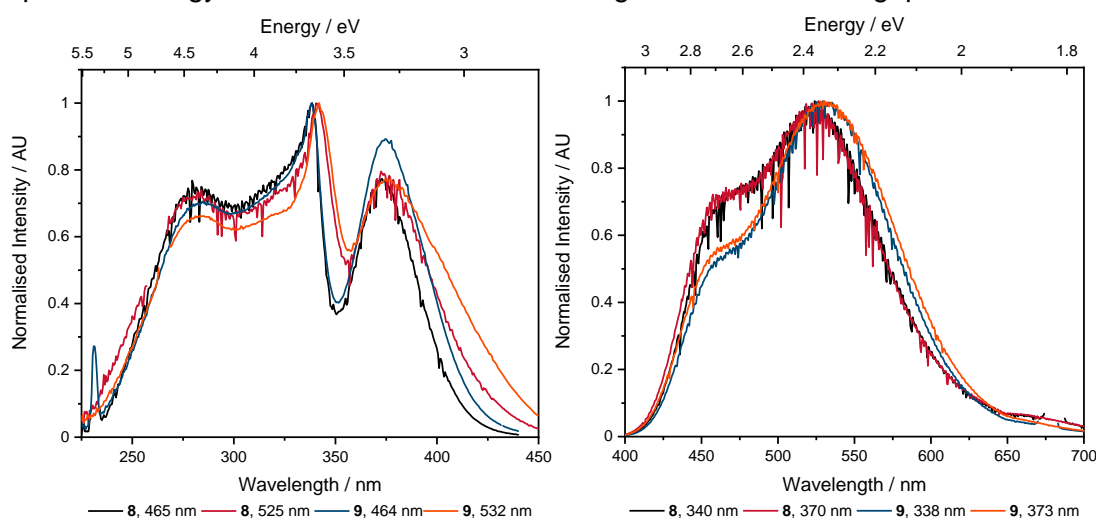


Figure 2.8: Excitation (left) and emission (right) spectra of CuSO_4 and NH_4Cl , and NH_4Cl doped zinc sulfides method with excitation and emission wavelengths (nm) labelled.

Chapter 2. Synthesis and Characterisation of Zinc Sulfide Phosphors

Interestingly, however, the emission spectra were where differences between the two methods arose. Doping with a high concentration of ammonium chloride resulted in a profile that was very similar to the copper iodide and ammonium chloride prepared via the solid-state milling route, with a clear green emission and a shoulder that was presumed to include both a zinc defect and potentially an unknown sulfur defect. With the addition of copper(II) sulfate, the ratio of the green emission compared to the blue emission increased and caused a red shift of the green emission by five nanometres to 530 nm. If an additional defect state of a lower energy were the cause of this shift, a change in the shape of the curve would be expected, with either an additional shoulder or a broadened peak, both resulting in increased intensity within the tail of the curve. Given the absence of these features, additional defects in this area were ruled out.

Due to the similarity of the emission and excitation spectra, the defects present in these two samples were highly likely to be the same. Indeed, this was to be expected as the copper dopant was used in extremely low concentrations, potentially to the point where the spectra were dominated by chloride defects, and defects introduced during the preparation. In the case of ammonium chloride, the charge mismatch caused by the halide, should form interstitial zinc and zinc vacancies – as with samples prepared through the milling technique. Certainly, it would be expected that aluminium and chloride doping could result in different energy levels as these defects are expected to occur in nearest neighbour sites, and in the case of chloride the interstitial zinc could be spatially associated, slightly altering the energy of the defect state. As the chloride anion is only slightly smaller (3 pm) than sulfur, the resultant stabilisation due to decreased strain is unlikely to be significant enough to account for a shift in the zinc defect state. Hence as with the milled samples it was likely an additional defect state was present, which could also account for the increased intensity ratio of the excitation for this defect compared to the aluminium doped sample.

With the addition of copper(II) sulfate the ratio of 370 nm defect peak and the band gap increased once again, while the intensity of the blue emission peak relative to the green emission decreased. This suggested either a greater degree of energy transfer from this higher energy state to the lower energy states increasing the relative intensity of the green peak, or sulfur defect states caused by the incorporation of copper, overlap with a zinc defect, or lastly, this peak was related to a sulfur defect. Whilst the broadened tail could signify the presence of additional

Chapter 2. Synthesis and Characterisation of Zinc Sulfide Phosphors

defects states that were not present in the non-copper doped sample, there was a slight shift in wavelength across the entire emission spectrum, with no additional shoulders or peaks observed. Therefore, it seemed that the addition of copper had not introduced new defects but influenced the incorporation of the chloride anion. The reaction of water and zinc sulfide is well known, producing zinc oxide and hydrogen sulfide, the lack of any significant alteration to the peaks present, i.e. no additional peaks have been formed when compared to the previous method, suggested that if any reaction did occur with water it either caused minimal degradation of the sample and/or the furnace treatment allows rearrangement of the sample to remove the defects formed by the addition of water.

The excitation and emission spectra for doping copper(II) sulfate without ammonium chloride (**10**) (Figure 2.9) using the wet impregnation method appeared identical to the milled preparation. A single large peak dominated the excitation spectrum with a λ_{max} of 373 nm. The lack of any other features in the spectrum suggested only one type of defect was present. As both zinc defects have previously been observed together, this suggested that zinc defects were absent, and the cause of the emission. Thus, sulfur defects were expected to be the only states present. Emission data similarly exhibited a single peak, although the broad and unsymmetrical shape suggested the presence of a second (obscured) peak.

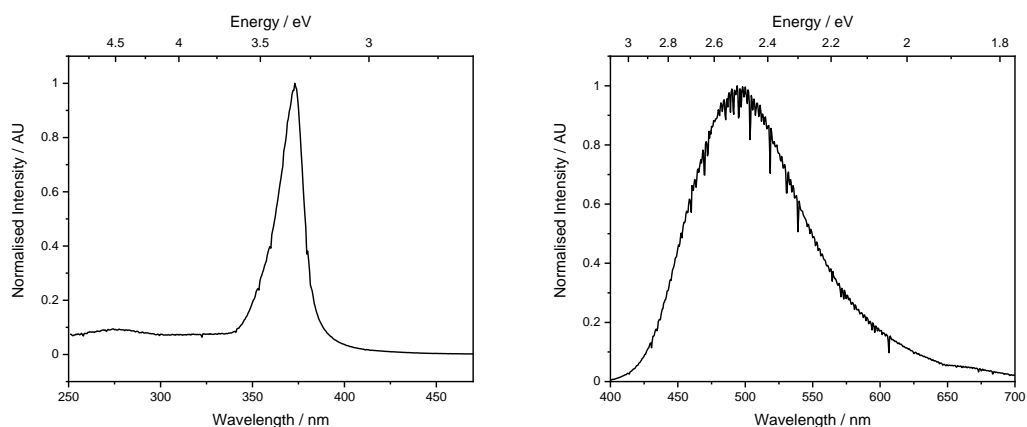


Figure 2.9: Excitation (left) and emission (right) spectra for CuSO_4 (**10**) doped zinc sulfides.

As before, copper(II) is expected to be reduced to copper(I) prior to incorporation into the lattice, generating sulfur vacancies and presumably interstitial sulfur. However, just as with the milled sample, the broadness of the peak did not allow empirical deduction of the constituent parts, if indeed there were any. Earlier literature work determined both sulfur defects to correspond to emission above 400 nm. Specifically, interstitial sulfur has been reported at 417 and vacancies at 480,³⁰ and 454 nm^{19,20}. As these literature samples were nanoparticles, a shift to longer

Chapter 2. Synthesis and Characterisation of Zinc Sulfide Phosphors

wavelengths is expected with the larger particles prepared in this work. However, as only a single peak was observed, it was not possible to more accurately determine the origin of the emission at 495 nm beyond being related to sulfur, and potentially a copper related defect.¹⁵

The excitation spectra for a non-doped zinc sulfide prepared via the wet impregnation method showed three different excitation profiles (Figure 2.10). As observed with copper(II) sulfate doping, a large peak at 370 nm was present with an identical line shape which implied the same defect was likely to be present in both samples. Excitation of the peak located at 602 nm resulted in the same defect peak at 370 nm, and three additional peaks. The first, with a λ_{max} of 280 nm is present in all the zinc sulfide samples was assigned to a feature within the band structure. The second peak was assigned to the band gap at 344 nm, showing a slight shift to previous samples. Lastly, a large broad excitation was seen stretching from 370 nm to beyond 500 nm with a distinct peak located at 465 nm –lower in energy than any defect observed so far. The broadness is believed to be caused by an additional defect(s) between 465 and 370 nm.

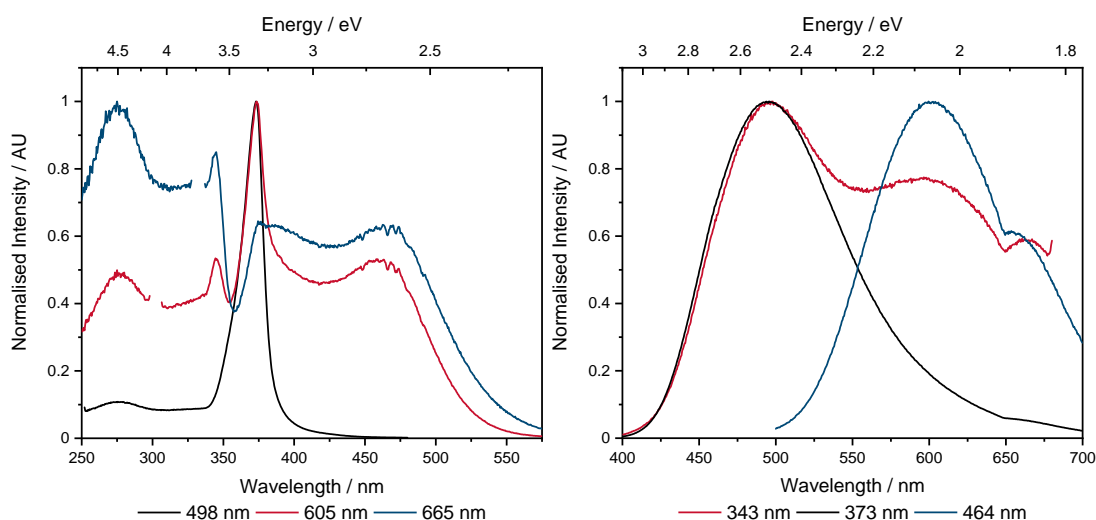


Figure 2.10: Excitation (left) and emission (right) spectra of undoped zinc sulfide with excitation and emission wavelengths labelled.

Excitation at 370 nm showed a similar emission as seen for copper(II) sulfate doped samples, which, as this sample had only been ‘doped’ with water, were not expected to be zinc related defects, as oxidation of the sample would create zinc oxide. Excitation at the band gap expectedly showed all the emissive states present, however, the intensity of the two emissions was unexpectedly similar. Excitation at 370 nm resulted in a strong emission at 490 nm that is over eight times more intense than exciting at the band gap.

Chapter 2. Synthesis and Characterisation of Zinc Sulfide Phosphors

The second emission at 600 nm was much lower in energy than any of the other doped materials prepared thus far and no samples contained any obvious contribution of this state in either emission or excitation spectra. Although, this may have been due to the transition being weak and obscured by rest of the data. Changing the excitation wavelength to 464 nm afforded a moderate increase in emission intensity (1.7 times greater) of the peak at 600 nm. The origin of these emission and excitation peaks, have previously, within the literature, been assigned to copper related defects. With a low energy peak at 600 nm or lower assigned to an interstitial copper related transition.^{10,11} However, the absence of copper in the preparation of the material rules this out and suggests either sulfur or oxygen defects were the cause.

Because the majority of peaks observed in doped zinc sulfides so far have been excited by both the band gap and their respective defect peak, it is reasonable to assume that the source of the defect must also differ from the other defects. Specifically, excitation with energy equal to the band gap involves the movement of an electron from the valence band into the conductance band, which can then relax to a lower energy defect and cause the associated emission. If, however, the energy of the defect state was close to the energy of valence band, but higher in energy than the lowest energy excited state of the material, relaxation to this defect state would not be possible. Hence the absence of a band gap contribution from this state. Unfortunately, however, it was not possible to unambiguously assign the specific origin of these transitions on this information alone.

2.4.2.4 Computational Studies

Following comparison of the experimental work and literature samples, it is clear multiple assignments are possible. For example, a blue emission found around 450 nm has previously been assigned to interstitial and vacancy defects of both zinc and sulfur or to copper related transitions. As it is highly unlikely all these assignments are correct, additional work must be conducted to further explore these defects. In an ideal scenario, a specific defect could be created in the material without the presence of any other defect and the energy of the transitions measured and an accurate assignment could be made. The isolation of these defects experimentally, however, is a non-trivial task. In these cases, a computational assessment of the material can be performed, as this allows the introduction of a single defect and the energy levels of the various states within the material determined and in conjunction with the experimental data should aid in removing the ambiguity present in the

assignment of the transitions observed within the experimental work carried out above.

Two software packages were used in this computational study: Quantum Espresso^{31–33}, and Yambo^{34,35}. Quantum Espresso was used to perform structural relaxation of the zinc sulfide cell resulting in the lowest energy conformation of the structure and is used in all subsequent calculations. Following this, two additional calculations were performed: self-consistent field (SCF) and non-self-consistent (NSCF) field. These calculations form the basis for the density of states (DOS) and band structure calculations in both Quantum Espresso and Yambo, from which the assignments of the defect transitions are possible. The density of states calculates the number of states that are available for electrons to occupy at a given energy level and provides an easy reference for where the filled and unfilled band lie. Within the Quantum Espresso package, a projected density of states (PDOS) calculation is performed, which determines the orbital contribution to the DOS for each atom, aiding in the assessment of additional bands that may appear due to a defect. Band structure calculations determine the energy of the orbitals of the material for a given position (or more commonly, path) in reciprocal space. Such a calculation enables determination of the band gap and the nature of the band gap, indirect vs direct, with direct band gap materials typically having better emissive properties as the radiative relaxation would not involve a crystal vibration to conserve momentum.³⁶ However, generalized gradient approximations functionals, such as the PBE-sol used in the Quantum Espresso calculations, have been noted to severely underpredict the energy of the band gap of zinc sulfides with values of 1.7 eV lower than experimental results being reported within in the literature.^{37,38} Therefore, the Yambo software package was used using the GW approximation which has been reported to provide calculated zinc sulfide band gaps much closer to the experimental results, typically within 0.4 eV.^{39,40}

2.4.2.4.1 Computational Details

Due to the demanding nature of these calculations, especially the GW calculations, it was not possible to use a unit cell that would match the experimental defect concentration – which could require up to 2500 atoms. Earlier examination of this (not included in this thesis) showed that a 3×3×3 supercell of 216 atoms was not feasible due to both the time and computational resources required. Therefore, a 2×2×2 supercell of 64 atoms was utilised using the sphalerite form of zinc sulfide. In this work four defects are considered: interstitial zinc (I_{Zn}) and sulfur (I_S) and

vacancies of zinc (V_{Zn}) and sulfur (V_S). The interstitial defects were modelled as an additional atom placed into the supercell totalling 65 atoms while vacancies were modelled with an atom removed totalling 63 atoms. Optimized norm-conserving Vanderbilt pseudopotentials⁴¹ were acquired from PseudoDojo,⁴² using the revised Perdew-Burke-Ernzerhof (PBE-sol) generalised gradient approximation (GGA) exchange correlation functional.⁴³ A single, non-shifted, automatically generated, Monkhorst-Pack⁴⁴ k-point grid of $3 \times 3 \times 3$ was used for most calculations, whilst a K-path of $\Gamma-X-U-K-\Gamma-L-W-X$ ⁴⁵ was used for band structure calculations. Quasiparticle calculations were performed within the YAMBO package using a G_0W_0 , plasmon pole approximation method.

2.4.2.4.2 Generalised Gradient Approximation Calculations

2.4.2.4.2.1 GGA Parameterisation

The first step in obtaining the band structures and density of states required parameterisation of the kinetic energy cutoff of the wavefunction ($ecutwfc$), as well as the charge density and potential ($ecutrho$). Initially, this was performed on a fixed cell with a lattice parameter of 10.81854 Å using a $2 \times 2 \times 2$ zinc sulfide supercell with 64 atoms and was based on the zinc sulfide unit cell which had an experimentally determined lattice parameter of 5.40930 Å, and bond lengths of 2.342 Å.³⁹ Figure 2.11 showed, expectedly, that as the cut-off is increased, the band gap converged to 1.96 eV, with a cut-off of 80 Ry, while the energy showed slight fluctuations even up to 120 Ry, however, as the difference in energy of the supercell between 80 and 120 Ry was 0.0018 Ry, a value of 80 Ry was taken as a converged system. Using an $ecutwfc$ value of 80 Ry, the charge density and potential was further parametrised (Appendix Figure 6.2). As with $ecutwfc$, the band gap reached convergence first with a value of 1.96 eV using an $ecutrho$ value of 300 Ry, whilst the energy of the system showed noise up to 400 Ry. Since both 300 and 320 Ry resulted in the same energy of the system and there was a 0.00006 Ry difference between the next lowest value, an $ecutrho$ of 320 Ry (4x the $ecutwfc$) was chosen.

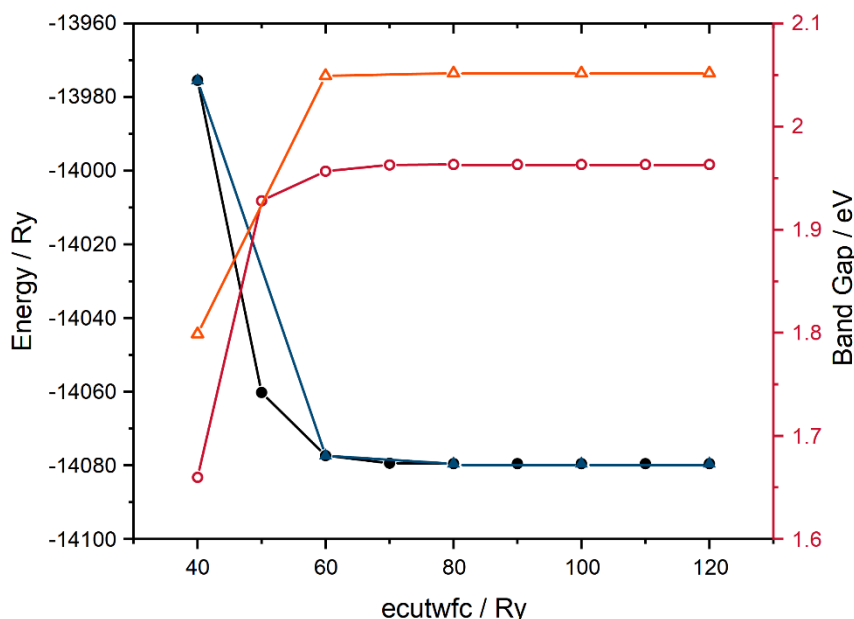


Figure 2.11: Energy (black line, ●) and nominal band gap (red line, ○) of a 64 atom zinc sulfide cell with a lattice parameter of 10.81854 Å, and the same structure with an optimised lattice parameter of 10.71451 Å; energy (blue line, ▲) and band gap (orange line, Δ) as the kinetic energy cutoff of the wavefunction (ecutwfc) is altered.

With these values in hand, the lattice parameters of the zinc sulfide supercell were optimised, which resulted in a slight reduction of lattice parameter and a very minor decrease in zinc sulfur bond lengths to 10.7145 Å (-0.1040 Å) and 2.3198 Å, (-0.0222 Å), respectively, and showed close agreement with computational work within the literature.^{40,46} Ecutwfc (Figure 2.11) and ecutrho (Appendix Figure 6.3) were similarly checked for convergence, and demonstrated the same values for convergence with values of 80 and 320 Ry, respectively. These values were used for all further calculations on ‘fixed’ and relaxed supercells.

2.4.2.4.2.2 Supercell optimisation

The defects expected in the doped zinc sulfides: interstitial zinc (I_{Zn}) and sulfur (I_S), and sulfur (V_S) and zinc (V_{Zn}) vacancies, were modelled in three ways: a charged system (e.g., a zinc vacancy results in a system with an overall -2 charge) with a fixed lattice parameter of 10.8185 Å, a charged system with variable lattice parameters, and a non-charged system with variable lattice parameters. The supercells with a fixed lattice parameter, expectedly, showed a smaller distribution in the average bond length between the different defects than the variable cells due to the lack of flexibility in the lattice parameter (Table 2.5). Introduction of an interstitial sulfur caused additional repulsion in the lattice, resulting in the zinc ‘cage’ around the sulfur expanding, with bonds lengths reaching ca. 2.52 Å. Which in turn caused a compression of these nearest neighbour zinc ions and their sulfur

Chapter 2. Synthesis and Characterisation of Zinc Sulfide Phosphors

tetrahedron bond lengths to around 2.25 – 2.26 Å. Predictably, the ZnS bond lengths between the defect and surrounding zinc ions were among the smallest in the material. An interstitial zinc defect, however, resulted in a much narrower distribution of bond lengths with 63% of bond lengths occurring between 2.30 and 2.35 Å, and rising to 89% if bond lengths up to 2.45 Å are included. Since the zinc ion is much smaller than a sulfur defect, the narrower distribution of bonds was expected. The vacancies followed a similar trend: the loss of additional strain exerted by the large sulfur ion compared to zinc resulted in a shorter average bond length than the pure sample, while the zinc vacancy showed a very minor increase of 0.0038 Å. Interestingly, both vacancies resulted in a similar degree of bond length distribution as their interstitial counterparts.

In the case of the neutral system, the introduction of a sulfur vacancy caused an incredibly minor reduction in the lattice parameter by 0.07 Å, and a within error change to the average bond length (+0.0009 Å). Likewise, a zinc vacancy caused minor shrinking of the lattice parameter by 0.036 Å and average bond lengths by 0.0035 Å. An interstitial zinc defect caused a significant reduction in the lattice parameter by 0.131 Å and shortened the average bond length by 0.0213 Å, with the interstitial zinc bond lengths being the longest in the structure. However, an interstitial sulfur defect caused a minor increase in the lattice parameter to 10.7838 Å (+0.0693 Å), with an expansion around the interstitial defect to account for the additional electron repulsion created by the sulfur. Interestingly, the surrounding zinc ions did not experience a notable decrease in their average bond length to the interstitial sulfur as was observed with the fixed unit cell.

With respect to the charged cells with optimised lattice parameters, an interstitial sulfur expectedly increased the lattice parameter 10.9709 Å (+0.256 Å) and increased the average zinc sulfur bond length 2.4044 Å (0.085 Å). Interestingly however, interstitial zinc decreased the lattice parameter to 10.5841 Å (-0.130 Å), along with a minor reduction in the average bond length to 2.2986 Å (-0.0212 Å), resulting in dimensions similar to the neutral cell. The vacancy defects showed the opposite trend: a zinc defect resulted in a lattice parameter longer than that of the optimised supercell at 10.8682 Å (+0.154 Å), and a marginally longer average bond length of 2.3560 Å (+0.036 Å). Whilst the sulfur vacancy decreased the lattice parameter by a similar magnitude to interstitial zinc 10.5916 Å (-0.123 Å) but increased the average bond length to 2.3493 Å (+0.0295 Å). The results obtained for the zinc defects were surprising, as it was initially believed these defects would

Chapter 2. Synthesis and Characterisation of Zinc Sulfide Phosphors

follow the same trend as the sulfur defects. i.e., loss of an ion would shrink the supercell, whilst addition of an ion would increase lattice parameter.

Table 2.5: Lattice parameter and average Zn-S, excluding the defect, and Zn/S defect to nearest neighbour site bond lengths

		Lattice Parameter (Å)	Zn-S bond length (Å)	Zn/S defect bond length (Å)
Charged Variable Cell	I _S	10.9709	2.4044	2.285
	I _{Zn}	10.5841	2.2986	2.605
	V _S	10.5916	2.3493	-
	V _{Zn}	10.8682	2.3560	-
Charged Fixed Cell	I _S	10.8185	2.3533	2.2650
	I _{Zn}	10.8185	2.3494	2.6533
	V _S	10.8185	2.3310	-
	V _{Zn}	10.8185	2.3458	-
Neutral Variable Cell	I _S	10.7838	2.3425	2.3495
	I _{Zn}	10.5835	2.2985	2.6060
	V _S	10.6440	2.3207	-
	V _{Zn}	10.6787	2.3163	-

Examination of the band gaps obtained from self-consistent field (SCF) calculations showed the neutral cells were a poor representation of the experimental systems. For example, the zinc defects reported an overlap of the highest and lowest occupied orbitals, indicating the system was metallic. Whilst the sulfur defects displayed band gaps similar to the charged cells, the lack of consistency throughout the samples indicated the neutral cell did not accurately describe the experimental systems. Thus, further calculations were not performed on these systems.

2.4.2.4.2.3 Band Structures and Projected Density of States

Band structure and projected density of state (PDOS) calculations were performed on each of the charged cells with fixed, and optimised lattice parameters. Figure 2.12 shows the band structure and PDOS for a zinc sulfide supercell with optimised lattice parameters and no defects. The magnitude of the direct band gap at the Γ position, 2.09 eV (Table 2.6), was in close agreement with other literature reports using GGA functionals,^{38,47} however, it was lower than the experimental band gap of 3.50 – 3.80 eV.¹⁻³ The PDOS also agreed with previous literature work showing the

Chapter 2. Synthesis and Characterisation of Zinc Sulfide Phosphors

valence bands were dominated by the sulfur 3p states, while the conduction band was comprised of a combination of zinc 4s and sulfur 3p states. The pseudopotentials used in these calculations did not include the zinc 4p shell, therefore, the contribution from these states could not be determined. However, the unaccounted density is expected to be from the zinc 4p states, as reported in earlier literature work.^{47,48} The fixed supercell exhibited the same results with the only difference being a reduced band gap to 1.96 eV (Appendix Figure 6.4).

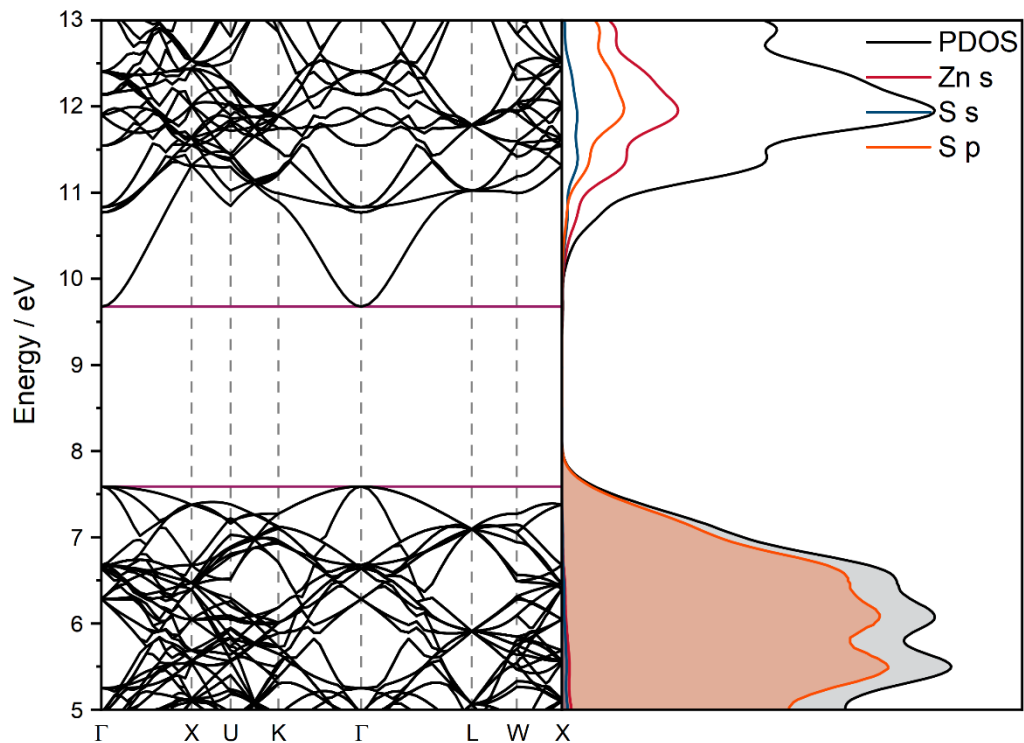


Figure 2.12: Band structure (left) where purple lines indicate the top and bottom of the valence and conduction bands, respectively. PDOS (right) showing the contribution of orbitals towards the filled (shaded) and empty bands for an optimised ZnS supercell of 64 atoms with no defects.

Introduction of an interstitial defect, such as sulfur (Figure 2.13), formed a second energy level within the band gap, consisting of 3p states from both the interstitial defect, and the surrounding sulfur ions. Unlike the bulk zinc sulfide however, the highest energy level of the defect bands did not occur at the Γ position, but at the X position instead, creating an indirect band gap as the crystal lattice position of the maxima and minima of the defect and conduction bands are in different positions within the Brillouin zone.⁴⁹ Since $\Delta K \neq 0$, the radiative recombination back to the ground state of the defect is forbidden, and requires the generation of a phonon to conserve the momentum, allowing recombination.⁵⁰ Thus emission lifetimes are often long lived⁵¹ and recombination of the electron and hole would be dominated by non-radiative events. However, as the difference between the direct and indirect

Chapter 2. Synthesis and Characterisation of Zinc Sulfide Phosphors

position is reasonably small – 0.0996 eV – the absorption spectra would show both defect related band gaps, with the onset of absorption occurring from the indirect and the absorption maxima occurring for the direct band gap.⁵² Although the PDOS suggested overlap of the interstitial defect and bulk ZnS, this was likely caused by the broadening used in creation of the PDOS, since the band structure did not suggest any overlap of these two states. An interstitial zinc defect (Appendix Figure 6.5), however, did not exhibit a shift in the position of the valence band maxima. With the band following a similar shape to the bulk ZnS valence band and positioned further away from the valence band (0.8165 eV difference) than the interstitial sulfur bands were from the conductance band (0.7492 eV). Similar to the interstitial sulfur defect, the band was comprised of 4s character from both the interstitial zinc and the neighbouring zinc sites. Unlike the sulfur defect however, the band gap of the zinc sulfide material exhibited an increase in energy of 0.3430 eV. Vacancy defects expectedly did not introduce new bands within the band gap but altered the energy of the conductance band relative to the valence band. Specifically, the zinc vacancy (Appendix Figure 6.7) influenced the shape the conductance band substantially, with the top conductance band becoming closer in energy to the surrounding k-points, and the rest of the bands showing a marked change in their path. The bottom of the valence band exhibited a significant reduction by 0.2983 eV, but otherwise appeared very similar to the pure zinc sulfide.

The sulfur vacancy showed a very minor increase in the band gap by 0.0164 eV, with the bottom of the valence band experiencing the most significant change: becoming shallower, as presumably, a band had moved from within the valence band to become the lowest unoccupied state. The lack of density accounted for in the PDOS suggested this was related to a zinc 4p state. Surprisingly, the band gap of this material was larger than that of the interstitial equivalent. The fixed supercells showed a similar trend as the optimised cells (Table 2.6). Both interstitial and vacancy zinc defects showed an expansion and compression of the band gap respectively. Although the sulfur vacancy band gap was smaller than the pure material, the difference was, like the optimised cell, rather small, being less than 0.05 eV.

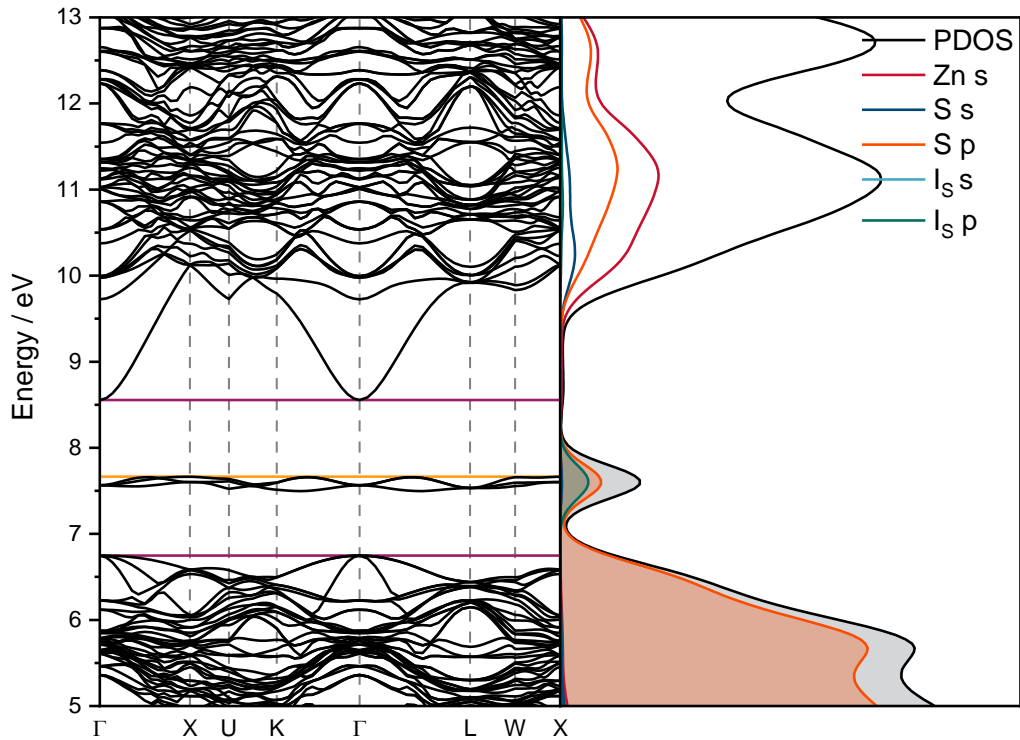


Figure 2.13: Band structure (left) where purple lines indicate the top and bottom of the valence and conduction bands of the bulk ZnS, respectively; and the yellow line indicates the top of the valence band caused by the sulfur defect. PDOS (right) showing the contribution of orbitals towards the filled (shaded) and empty bands for an optimised ZnS supercell of 65 atoms with an interstitial sulfur.

Table 2.6: Band gaps of samples with and without defects of cells with fixed lattice parameters

Defect	Band gap / eV	Defect Gap / eV	Band gap / nm
None	2.0867		594
I _{Zn}	2.4297	1.6132	510, 769
V _{Zn}	1.7884		693
I _S	1.8075	0.9903 (0.8907) ^a	686, 1252
V _S	2.1031		590

^a Indirect band gap

Table 2.6 demonstrates the limitations of the GGA approach towards calculating the zinc sulfide band gap, with and without defects, for the optimised supercells. Most notably, the band gap for the sulfur vacancy system (and the bulk band gap for an interstitial zinc defect system) was predicted to be higher in energy than the pure undoped material, which was not observed in either the experimental work carried out earlier, nor within the literature. The interstitial sulfur system was also poorly modelled, resulting in a predicted defect state almost three to two times lower in energy than the closest experimental result. Interestingly, the trend predicted by

GGA calculations indicated that the interstitial defects should correspond to the lower energy absorptions. These results agree with some of assignments reported within the literature¹⁰ and it would be reasonable to expect interstitial bands to occur at a higher energy than their onsite equivalents, resulting in lower energy transitions. Since the optimised supercells should represent the minimum energy state of each system, and therefore, are more representative of the experimental samples, these supercells were further examined within the GW approximation framework.

2.4.2.4.3 Non-Self-Consistent GW calculations

2.4.2.4.3.1 GW Parameterisation

As with the Quantum Espresso calculations, parameterisation of variables was performed to ensure convergence of the band gap. The first parameter, the exchange self-energy (Hartree-Fock energy), (Appendix Figure 6.8) showed convergence of the conductance band was rapidly achieved at 100 Ry, with no difference in the energy of the band at higher cut-off energies. The valence band, however, required a higher cut-off energy of 140 Ry to reach convergence, with a band gap of 9.3779 eV at this value. The next step was the convergence of the correlation self-energy, and quasiparticle energies, with the direction of the electric field fixed to a non-specific value of 1,1,1 for all calculations. Altering the size of the dielectric matrix (Appendix Figure 6.9), showed convergence of the conductance band was achieved more easily than the valence band with cut-off energies greater than 13 Ry showing no changes. The valence band, however, did not show convergence even at 15 Ry, however, as the difference between 13 Ry and 15 Ry was only 0.0002 eV, and computational resource demand rapidly increased as the size of the matrix was increase, a value of 13 Ry was selected as a suitable trade-off between time and convergence, resulting in a predicted band gap of 3.47 eV. The number of polarisation function bands were set to equal the maximum number of bands for each system, i.e., 832 bands for pure zinc sulfide and 814 for a zinc vacancy, since earlier calculations on a fixed supercell had shown suitable convergence could not be achieved without including all the bands. Similarly, sum over state summation required all the bands to achieve suitable convergence. All other values corresponding to the damping of Green's function (0.1 eV), the plasmon pole imaginary energy (27.2114 eV), number of G vectors for expanding the wavefunction, and the number of G vectors used for evaluating the density of the matrix element, were left at their default values. With these optimised values in

hand, the band structures and density of states (DOS) were calculated for the four defects and the pure zinc sulfide using 20 bands surrounding the band gap.

2.4.2.4.3.2 Band Structures and Density of States

Pleasingly, the GW approximation showed a significant improvement over the GGA method, resulting in an increased band gap of 3.37 eV (Figure 2.14), much closer to the experimental results, and similar to values reported within the literature of 3.19 – 3.98 eV^{38,53–57}. The energy of the X position was predicted to be much higher in energy than the GGA calculation, and almost equal to the Γ position. Although, as the energy of the conductance band at this point was 1.02 eV higher than the Γ position, this would not correlate to a second band gap transition.

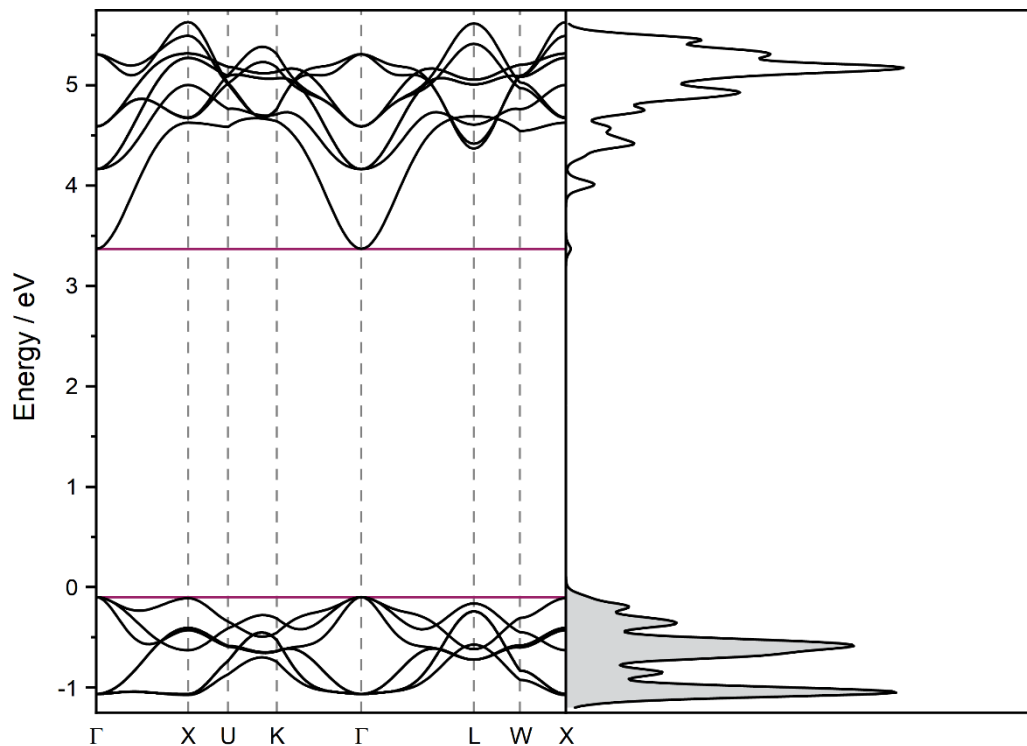


Figure 2.14: Band structure (left) where purple lines indicate the top and bottom of the valence and conductance bands respectively. DOS (right) showing the contribution of orbitals towards the filled (shaded) and empty bands for an optimised ZnS supercell of 64 atoms with no defects.

The filled bands for an interstitial sulfur defect calculated with the plasmon pole approximation (PPA) (Figure 2.15) showed remarkable agreement with the GGA method, insofar as the energy difference between the bulk ZnS and the defect bands. Whilst the unfilled bands experienced a significant increase in energy relative to the defect sulfur bands of 2.18 eV. As with the GGA calculation, the maxima of the defect bands did not occur in the Γ position but at the X position. The shape of the conductance bands was also very similar to the GGA calculation with

Chapter 2. Synthesis and Characterisation of Zinc Sulfide Phosphors

slight differences observed between the X and U positions, and at the L position. However, these were only minor alterations and did not alter the conclusions drawn from the GGA band structure calculations. The interstitial zinc defect supercell (Figure 2.16) also showed a similar result, with the defect and the conductance bands exhibiting a similar energy difference as in the GGA calculations but displayed a significantly increased band gap of 3.00 eV. The shape of the bands also showed a greater degree of variation than the GGA calculation. The energy difference of the Γ position bands being minimal to the point of overlap unlike the GGA calculations which showed a reasonable gap between bands at these positions. With regards to the vacancy defects, the sulfur vacancy (Figure 2.18) expectedly showed a reduction in the energy of the valence band compared to the pure zinc sulfide, but still showed a larger band gap than the GGA calculation of 3.16 eV. Additionally, the energy between the bottom of the conductance band and the second lowest band showed a minor increase from 0.22 eV (GGA) to 0.26 eV (PPA). As with all the calculations so far, the energy of the X position was very similar to the Γ position but the energy difference of the valence band at these positions had been significantly reduced and corresponded to a transition of 3.56 eV. The zinc vacancy (Figure 2.17) followed the same trend as the earlier results, with a larger band gap of 3.15 eV, and showed similarities in the band shape to the GGA calculations, most notably the difference in energy of the bottom two valence bands. Unlike the sulfur vacancy, however, whilst the energy differences across the k path of the conductance band were shallower, the valence band exhibited the same sharp decrease in energy at the Γ and did not reasonably afford a second low energy transition.

The GW calculations provided a more accurate description of the zinc sulfide band gap, being only slightly lower in energy than the experimentally determined values, and significantly better than the GGA sample (Table 2.7). Additionally, the zinc sulfide band gap was correctly calculated to be the highest energy transition instead of a sulfur vacancy. Regarding the experimental results, the GW calculations showed reasonable agreement with experimental transitions, the only exception was the interstitial sulfur defect with predicted band gap much larger than any transition observed in the experimental spectra, however, it was significantly better than the GGA calculations.

Like the GGA calculations the interstitial defects are predicted to be the lowest energy states, in contrast, however, the vacancy defects were determined to

Chapter 2. Synthesis and Characterisation of Zinc Sulfide Phosphors

occur at very similar values to each other. Although there were differences between predicted bands gaps and experimental values, a clear trend was observed and supported assignment of the peaks to each defect. Interstitial zinc defects were assigned to an excitation peak at 400 nm and an emission around 520 nm. Zinc vacancies were assigned to an excitation peak at 370 nm and an emission at 454. Similarly, interstitial sulfur defects were assigned to an excitation peak at 470 nm, and an emission peak at 600 nm, and sulfur vacancies were assigned to an excitation at 370 nm and an emission at 490 nm.

Table 2.7: GW, GGA and experimental band gaps in nm for the five calculated zinc sulfide systems: Pure ZnS with no defects (None), with an interstitial zinc (I_{Zn}), interstitial sulfur (I_S), zinc vacancy (V_{Zn}), and sulfur vacancy (V_S) defect.

Defect	Band Gap / nm			
	GGA	GW with BG	GW	Experimental ^a
None	594	351	367	326 – 354
I_{Zn}	768	408	413	400
I_S	1252	660	568	470
V_{Zn}	693	387	393	370
V_S	589	429	392	370

^a Values ordered to show closest agreement between experimental and calculated results.

Band gaps were also determined using the Bruneval-Gonze method.⁵⁸ Interestingly, this caused a slight increase in the energy of the zinc defects and zinc sulfide, but a more significant decrease in the energy of the sulfur defects. The cause of this is unknown as this method was created to speed up convergence with respect to the number of empty bands.⁵⁸ However, the significant difference between calculations with and without this term, and the disparity in the results obtained for the defects, suggested this method may not accurately account for these systems.

Unfortunately, the version of yambo used in this work (version 4.5) does not support self-consistent GW calculations, which may be the cause of the poorly predicted interstitial sulfur band gap. Additionally, due to computational requirements it was not feasible to perform the calculations on larger supercells, which are expected to provide a more accurate description of the experimental systems.

In conclusion, copper doping with and without a co-dopant did not appear to be the direct cause of the green emission, i.e., copper related bands were not involved in the relaxation process that gave rise to the green emission that has been reported within the literature. Instead, introduction of either copper or a co-dopant

Chapter 2. Synthesis and Characterisation of Zinc Sulfide Phosphors

caused a range of defects depending on the nature of the dopant. In the case of copper(II), a greenish blue emission at 493 nm is observed and assigned to be predominately caused by a sulfur vacancy defect. While addition of a copper(I) source, such as copper iodide, generated two defects: the aforementioned 493 nm, and a strong blue emission at 455 nm assigned to a zinc vacancy. With the addition of ammonium chloride, two convoluted peaks were observed, with λ_{\max} values of 520 nm that was assigned to an interstitial zinc defect and a weaker peak around 455 that was presumed to be caused by a zinc vacancy defect. Doping with aluminium generated two distinct emission peaks with λ_{\max} of, and 520 nm due to interstitial zinc and zinc vacancies respectively. In the absence of a dopant, the wet impregnation method generated two emission peaks, around 490 and 600 nm, which are assigned to sulfur vacancy and interstitial defects, respectively.

The assignment of these transitions was supported with computational calculations using a 64-atom supercell with charged defects using the PBE-sol functional. Initial optimisation of the lattice parameters was carried out and showed, expectedly, expansion and contraction around interstitial and vacancy sulfur defects, respectively. Zinc defects, however, presented the opposite trend, i.e., interstitial zinc was observed to decrease the lattice parameter by a similar magnitude to a sulfur defect, while a zinc vacancy increased the lattice parameter, but not to the same degree as the interstitial defect. Band structures and projected density of states calculations were performed using a GGA functional and showed band gap values below the experimental values and showed a sulfur vacancy defect as having the largest band gap which was not supported by experimental results. To improve upon these values, non-self-consistent GW calculations were performed. Pleasingly, the predicted band gap of zinc sulfide, 3.38 eV, showed reasonable agreement with literature values of 3.5 to 3.8 eV. Additionally, the trends observed in these calculations mirrored those of the experimental results, with both vacancy defects being predicted to have band gaps equal to each other. Unfortunately, however, the interstitial sulfur defect was predicted poorly, with a value of 2.18 eV, compared to the experimentally determined value of 2.68 eV. This difference was presumed to be caused by the non-self-consistent nature of the GW calculations employed in this work.

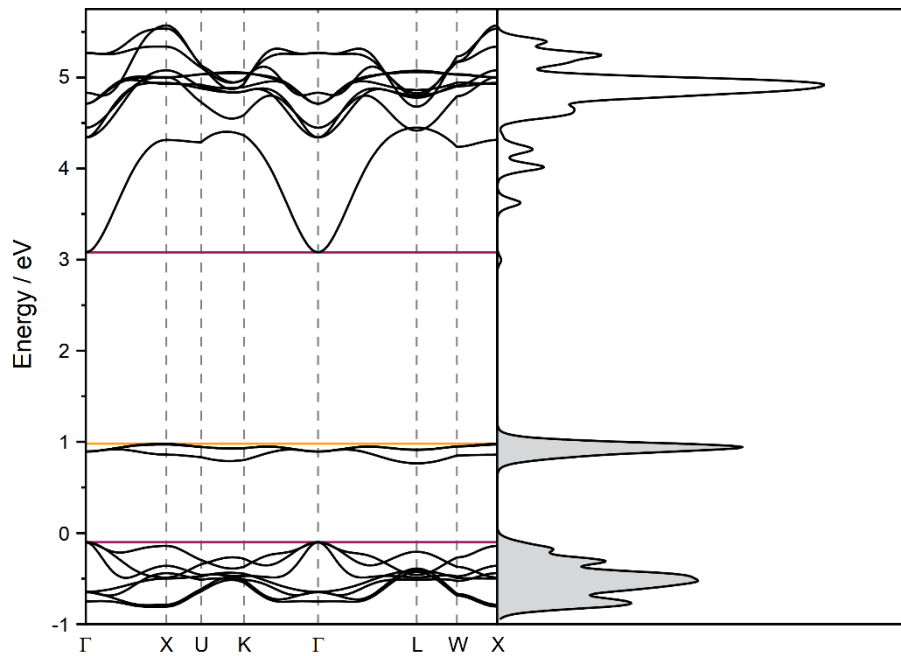


Figure 2.15: Band structure (left) where purple lines indicate the top and bottom of the valence and conduction bands respectively. DOS (right) showing the contribution of orbitals towards the filled (shaded) and empty bands for an optimised ZnS supercell of 64 atoms with an interstitial sulfur defect.

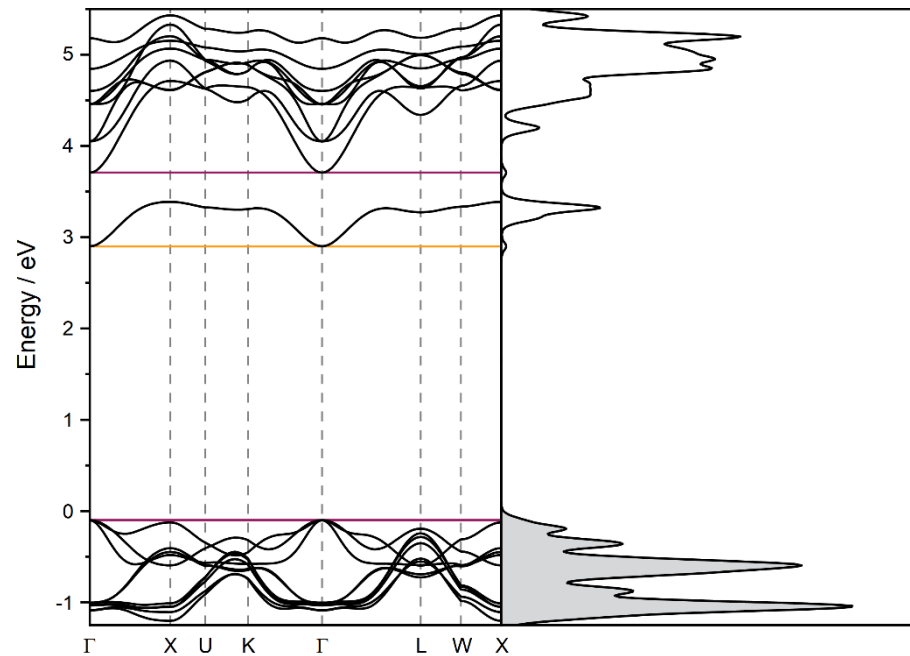


Figure 2.16: Band structure (left) where purple lines indicate the top and bottom of the valence and conduction bands respectively. DOS (right) showing the contribution of orbitals towards the filled (shaded) and empty bands for an optimised ZnS supercell of 64 atoms with an interstitial zinc defect.

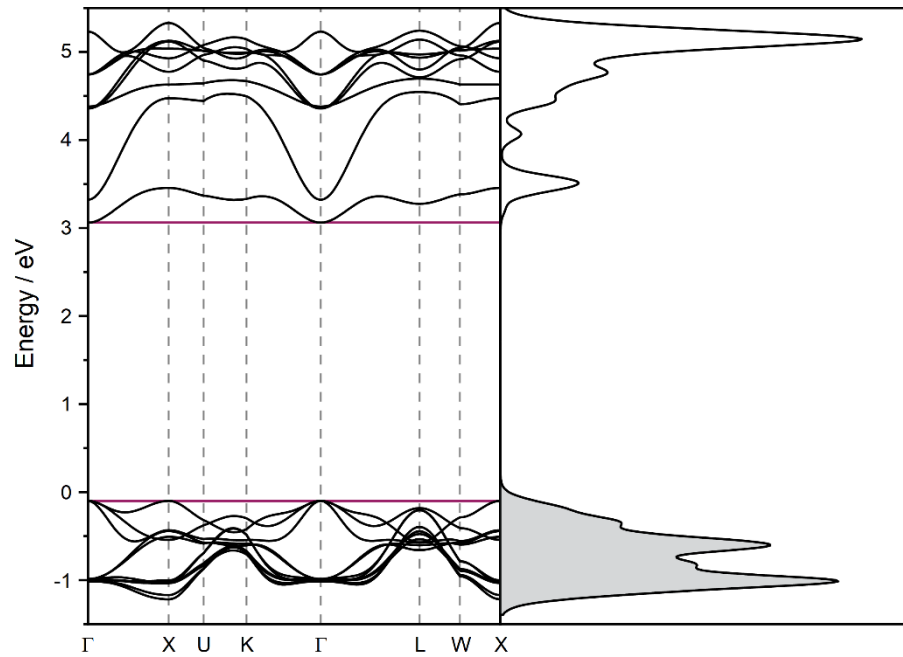


Figure 2.18: Band structure (left) where purple lines indicate the top and bottom of the valence and conduction bands respectively. DOS (right) showing the contribution of orbitals towards the filled (shaded) and empty bands for an optimised ZnS supercell of 63 atoms with a sulfur vacancy defect.

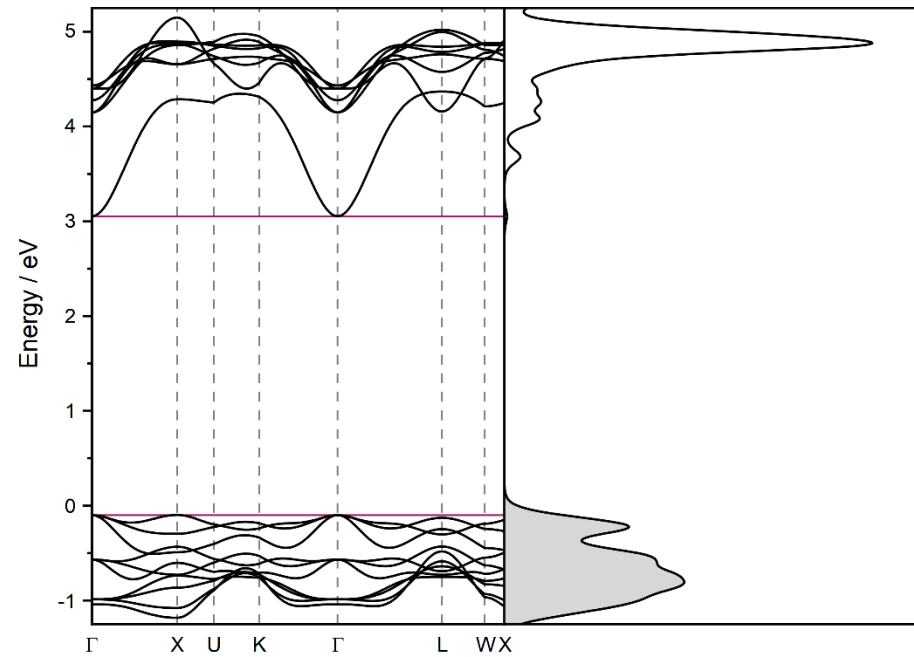


Figure 2.17: Band structure (left) where purple lines indicate the top and bottom of the valence and conduction bands respectively. DOS (right) showing the contribution of orbitals towards the filled (shaded) and empty bands for an optimised ZnS supercell of 63 atoms with a zinc vacancy defect.

2.4.3 Group 2 Doped Zinc Sulfides

2.4.3.1 SEM and EDX Analysis

Doping with Group 2 metals displayed a similar degree of aggregation and large particle sizes as seen with copper and aluminium doped zinc sulfides. The larger particles shared a similar degree of variance in their sizes as before, however, the range of sizes changed depending on the dopant metal. Barium doped samples exhibited particles around $4.0 \times 4.0 \mu\text{m}$ with few particles ranging to greater than $5.0 \mu\text{m}$ and smaller than $3.0 \mu\text{m}$. Strontium doping resulted in smaller particles, typically around $2.5 \mu\text{m}$, although smaller particles of $1.4 \mu\text{m}$ and larger particles of $3.5 \mu\text{m}$ along the longest edge were observed. Calcium doping, however, generated a range of sizes from 4.0×3.0 down to $1.0 \times 1.5 \mu\text{m}$. Whilst differences were observed between the different dopants, the sample size is reasonably small and did not necessarily suggest the dopant had influenced the growth of the particles. The range of sizes were also observed as the concentration of each metal dopant was changed with no significant trends observed in the size of the particles nor the range of sizes. As with the previous samples, these large particles were comprised of smaller fused particles (Figure 2.19) of a similar size to copper, and aluminium doping.

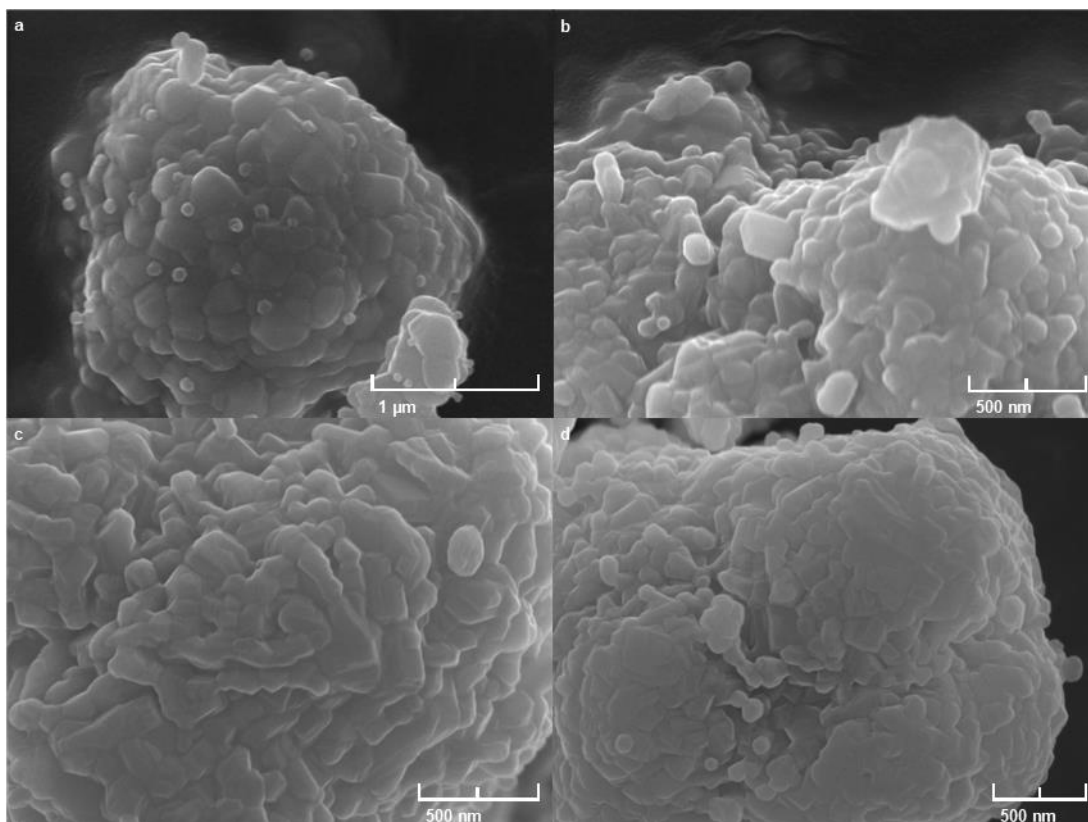


Figure 2.19: SEM image of 8 mol% barium (a), 8 mol% strontium (b), 8 mol% calcium (c) and 4 mol% strontium (d) doped zinc sulfides.

Chapter 2. Synthesis and Characterisation of Zinc Sulfide Phosphors

The majority of these particles appeared as rounded cubes or cuboids, ranging in size from 250 nm along the longest edge to 100 nm. Surprisingly, calcium doped samples exhibited a change in the morphology of the particles to a more cuboid shape, with some reaching up to 400 nm along the longest edge, and with a greater degree of diversity in the size and form of these small particles.

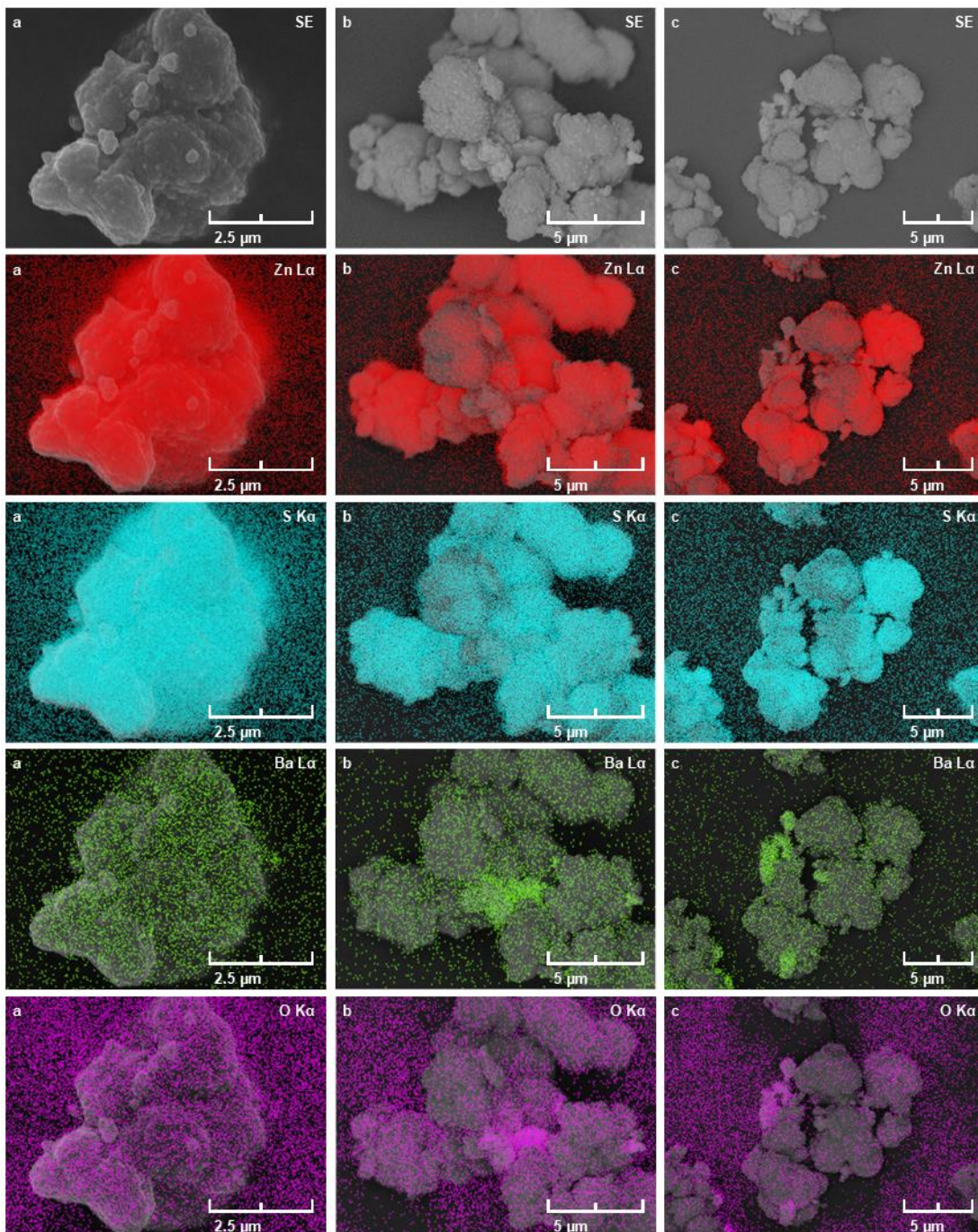


Figure 2.20: SEM and EDX images for zinc sulfide with varying barium doping levels: a) 8 mol% b) 4 mol% c) 2 mol% showing contributions from zinc, sulfur barium and oxygen.

Analysis of the EDX data, however, showed the materials were not as homogenous as first thought. With regards to 8 mol% barium doping (Figure 2.20), whilst the sample appeared homogenous with no areas devoid of zinc or sulfur, the barium

map shows a low concentration of barium, significantly below the expected value (Table 2.8). The high oxygen concentration was not believed to be from the particle, as substantial amounts of zinc oxide would be evident from the oxygen and sulfur maps, instead this was believed to be background data. Unlike the 8 mol%, both 4 mol% and 2 mol% showed areas of high barium concentration which aligned with areas of high oxygen concentration, and a corresponding decrease in both zinc and sulfur concentrations. 4 mol% doping similarly showed a slightly lower than expected value for barium concentration. Whilst 2 mol% exhibited a higher concentration, over 3.5 times greater, than expected; the highest barium concentration of all the samples.

Table 2.8: Atomic% values for barium doped zinc sulfides from EDX mapping analysis.

Element	8 mol%	4 mol%	2 mol%
Zinc	40.3	38.1	20.1
Sulfur	40.0	35.7	25.8
Oxygen	19.3	24.8	52.1
Barium	0.4	1.2	1.9

Strontium doping displayed a similar story. Zinc appeared homogenous for two of the samples with only 4 mol% containing a particle that was obviously deficient in zinc (Appendix Figure 6.10). Strontium mapping showed that all three samples contained areas of localisation that aligned with areas of lower zinc concentration, although lower than expected (Table 2.9). Analysis at specific sites agreed with the assumptions from the mapping: strontium was highly localised to these specific areas, with very little incorporated into the bulk material. Site 1 showed an excess of sulfur for 4 mol% and slightly deficient for 2 mol% doping which was presumed to be indicative of strontium sulfide and strontium oxide being present in these samples. Whilst oxygen concentration was greater in these strontium rich sites it was beyond the amount expected for strontium oxide and even for strontium hydroxide. If these materials were present, it would imply the particles contained an amount of free unbound sulfur which was not expected to exist as a stable material at the reaction temperatures used, since sulfur has a boiling point of less than 450 °C.

Chapter 2. Synthesis and Characterisation of Zinc Sulfide Phosphors

Table 2.9: Atomic% EDX data for strontium doped zinc sulfides

Element	8 mol%		4 mol%		2 mol%		
	Map	Map	Site 1	Site 2	Map	Site 1	Site 2
Zinc	36.3	39.4	3.5	46.6	35.6	12.9	45.5
Sulfur	34.9	37.9	18.6	43.4	35.1	23.4	46.3
Oxygen	28.3	21.4	66.2	9.7	28.6	47.3	7.8
Strontium	0.4	1.2	11.8	0.2	0.7	16.4	0.4

Similarly, calcium doping showed localisation of the dopant with little evidence of distribution throughout the material (Appendix Figure 6.12). As before areas that were deficient in zinc correlated with calcium sites. However, unlike barium and strontium doped samples, a high concentration of oxygen was not observed anywhere on these samples demonstrating the sample is comprised of zinc sulfide, and either calcium sulfide or a combined zinc and calcium sulfide. Atomic% data for the mapping (Table 2.10) of 10 mol% shows calcium was less than half of the expected value, along with a lower-than-expected sulfur concentration, sites 1 and 2 similarly displayed this sulfur deficiency with respect to the metal concentration. 8 mol% doping shows the same sulfur deficiency; however, the calcium rich site contained a greater proportion of zinc than calcium but was still clearly localised within this area and not distributed throughout the material. The lack of oxygen localisation for the calcium doped samples was unexpected, as both previous metals have shown a high degree of colocalization, and the standard enthalpies of formation would suggest calcium experiences a greater degree of stabilisation than strontium or barium upon forming the oxide.

Table 2.10: Atomic% EDX data for calcium doped zinc sulfides

Element	10 mol%			8 mol%		
	Map	Site 1	Site 2	Map	Site 1	Site 2
Zinc	24.8	7.9	47.3	33.8	21.4	46.7
Sulfur	22.7	32.7	46.8	32.0	29.0	44.3
Oxygen	51.5	30.9	5.8	33.8	30.5	8.8
Calcium	1.0	28.4	0.1	0.5	19.0	0.2

Chapter 2. Synthesis and Characterisation of Zinc Sulfide Phosphors

Point analysis and mapping, combined with three different accelerating voltages (5, 15 and 30 kV) was utilised to further explore these areas of localisation, using barium doped zinc sulfides as a representative sample. If the barium was not incorporated throughout the material, and only upon the surface, it would be reasonable to expect that as the accelerating voltage was increased, the barium concentration would decrease as the proportion of bulk zinc sulfide being analysed increases.

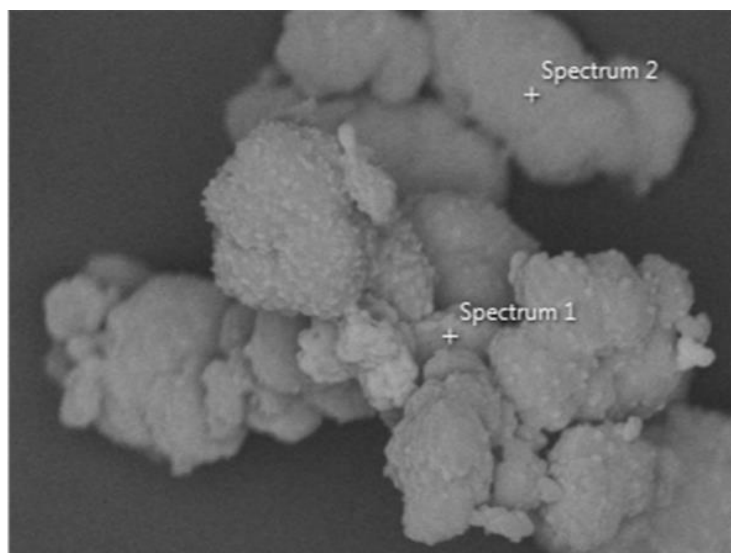


Figure 2.21: SEM image of 4 mol% barium doped zinc sulfide with point analysis locations marked

Figure 2.21 shows a slight difference in the morphology of the two areas of analysis. The barium rich area of the sample appeared to consist of flaky layers while the rest of the sample was aggregated particles with fewer visible layers. Table 2.11 displays the atomic contribution to the material across the entire sample, and at two sites, one of which was barium rich, and the second that was chosen in conjunction with the EDX mapping to represent the average of particle. Unfortunately, the lowest chosen accelerating voltage, 5kV, was below the minimum threshold to enable analysis of barium distribution which was observed in the map showing only noise. However, the barium concentration was inferred by comparing the ratios of the remaining elements along with trends seen for the two remaining accelerating voltages. The most obvious difference was the incredibly low contribution of zinc towards site 1 but a greater proportion of sulfur and oxygen. As both barium and zinc form 1:1 compounds with the chalcogenides, the expected distribution of the metals and non-metals is 1:1, but as barium was excluded in these readings the weighting will lie towards the non-metals appearing in excess. Given this, site 1 could be a mix of both barium oxide and barium sulfide. Site 2 was expectedly different, with zinc and sulfur comprising the majority of the sample.

Chapter 2. Synthesis and Characterisation of Zinc Sulfide Phosphors

Table 2.11: Atomic % EDX data for 4 mol% barium doped zinc sulfide

Element	5 kV			15 kV			30 kV		
	Map	Site 1	Site 2	Map	Site 1	Site 2	Map	Site 1	Site 2
Zinc	38.4	4.8	46.5	38.1	12.5	48.4	28.9	19.4	32.6
Sulfur	44.1	34.9	49.2	35.7	21.7	47.0	36.6	29.5	43.9
Oxygen	17.5	60.3	4.2	24.8	55.5	3.8	33.7	49.4	23.3
Barium	-	-	-	1.2	10.3	0.3	0.8	1.7	0.2

Increasing the accelerating voltage to 15 kV, caused an increase in the zinc composition at site 1, along with data for barium doping showing a significant contribution: more than 11 times the expected values. Combined, the zinc and barium were roughly equal to sulfur, which was surprising given the oxygen observed in EDX images (Figure 2.22) would suggest barium oxide is present in reasonably high concentrations. As before, site 2 showed a composition typical of zinc sulfide, with only a small proportion of barium present; significantly lower than was expected. Increasing the accelerating voltage further, to 30 kV, showed an increase in the zinc present at site 1 and a corresponding decrease for barium, suggesting localisation on the surface was the case, as a higher accelerating voltage should detect more of the bulk material shifting the overall composition. Although once again, the zinc to sulfur ratio displayed a large deviation from the ideal. Surprisingly, site 2 also showed a disparity between the ratio of zinc and sulfur, and a dramatic increase in the proportion of oxygen which cannot be accounted for by the zinc sulfide particle.

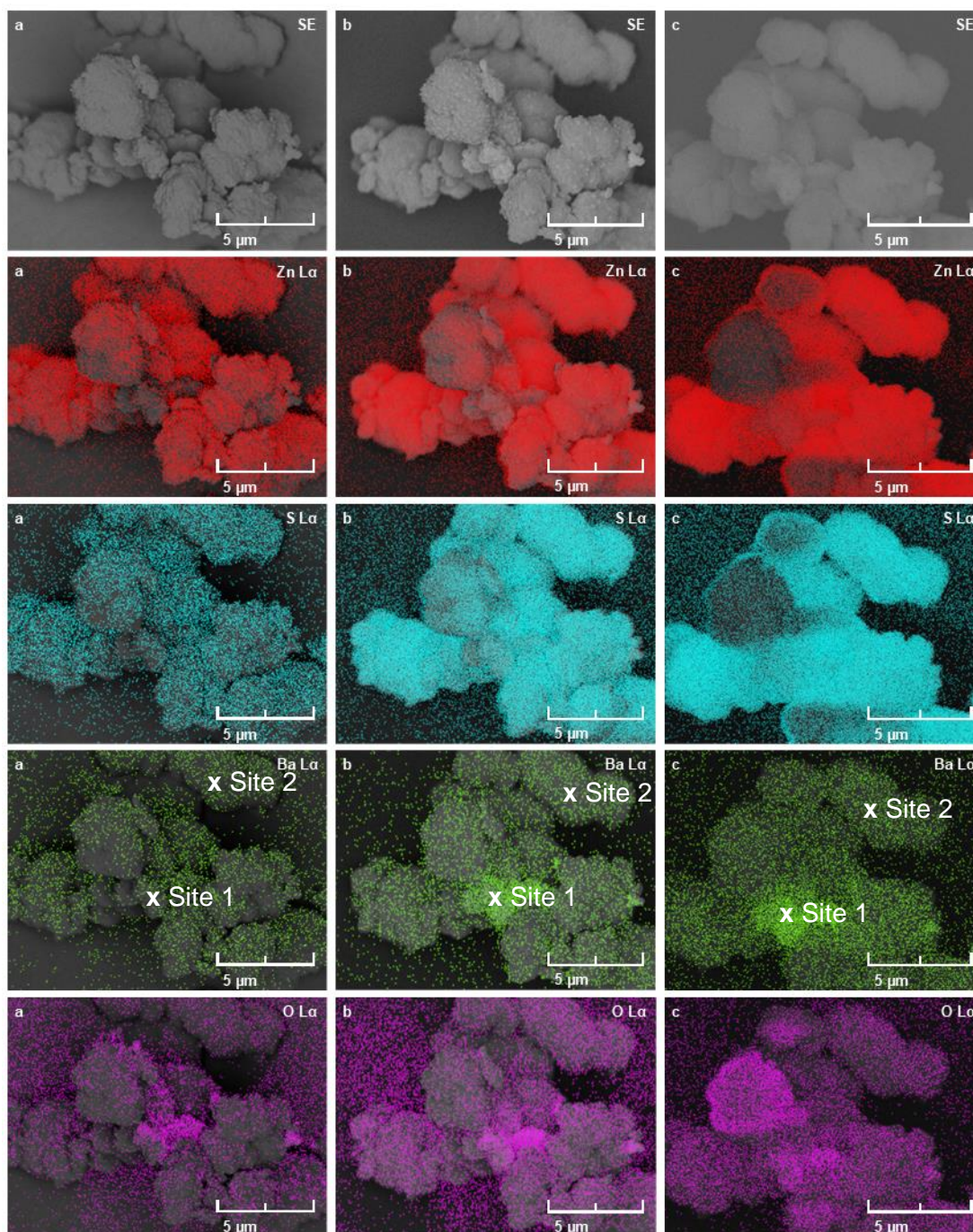


Figure 2.22: SEM and EDX images for 4 mol% barium doping at different accelerating voltages: a) 5 kV, b) 15 kV, c) 30 kV showing contributions from zinc, sulfur barium and oxygen.

2.4.3.2 PXRD Analysis

Unincorporated barium sulfide should be detected through the corresponding halite peaks via powder X-ray diffraction (PXRD). All three samples, regardless of the mass of barium sulfide added during the preparation, displayed the same peaks (Figure 2.23), with some varying in intensity proportional to the amount of barium added. None of the observed peaks corresponded to a halite phase, or if it was present, the intensity was too weak to be detected. Therefore, it was believed that

Chapter 2. Synthesis and Characterisation of Zinc Sulfide Phosphors

these samples did not have a significant halite phase. In addition to the expected sphalerite phase, a wurtzite phase was also present with an intensity that was proportional to the mass of barium added during the synthesis.

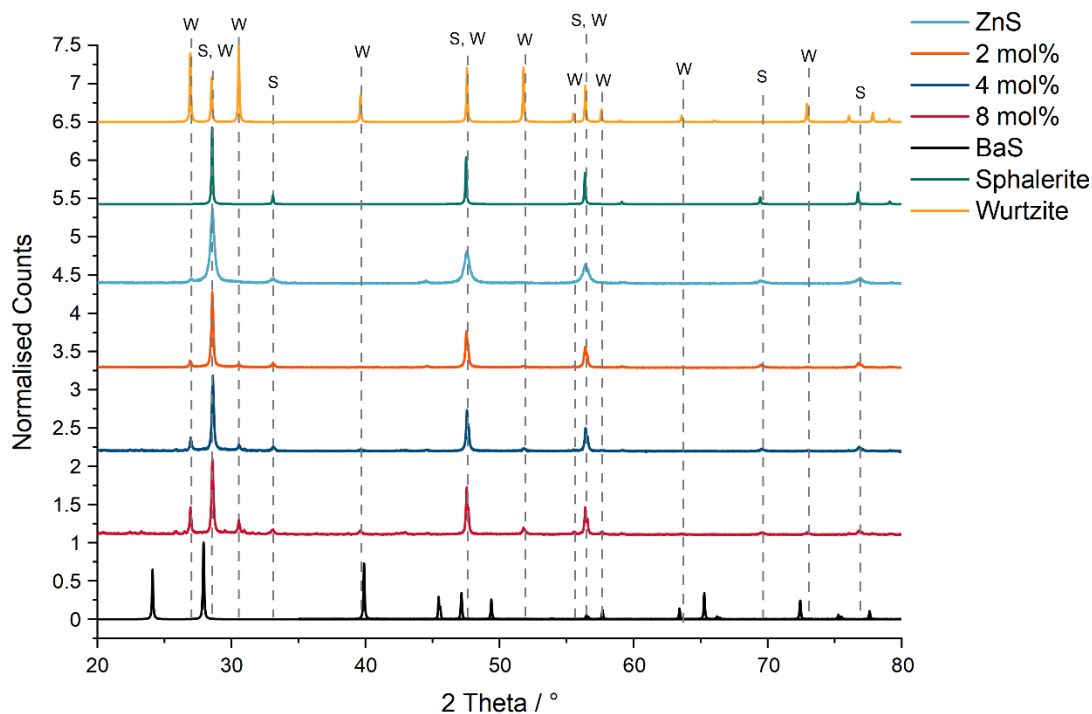


Figure 2.23: PXRD pattern for varying barium doping: 8 mol% 4 mol% 2 mol%, undoped zinc sulfide, and calculated powder patterns for barium sulfide, sphalerite and wurtzite. S indicates sphalerite phase, and W the wurtzite phase.

Typically, the wurtzite phase is only observed when zinc sulfide is exposed to temperatures in excess of 1020 °C;^{59,60} greater than the 800 °C used in the preparation of these materials. Although it has been previously shown that a smaller grain size will allow the phase transition to occur at lower temperatures of 1000 °C,⁶¹ this was still significantly higher than these samples were subjected to. Following the slow cooling of these samples, which should cause a shift back towards the more stable sphalerite phase, the generation of a wurtzite phase was not considered to be directly caused by the method used to synthesise these materials. Instead, it was likely that the addition of barium caused this change. Comparing the volume of each unit cell, it is unlikely that the shift to a wurtzite phase occurred to allow the incorporation of barium, since the sphalerite unit cell has a greater volume per atom. Earlier literature preparations regarding the incorporation of barium into zinc sulfide have shown the formation of a Ba_2ZnS_3 phase.⁶² Analysis of 8 mol% doping, suggested the presence of this phase, albeit with a rather low intensity. Unfortunately, due to this low signal to noise ratio of the corresponding peaks, a quantitative assessment of these phases was not possible.

Thus, in the absence of electron backscatter diffraction it was not possible to obtain a full assessment of the material.

2.4.3.3 Luminescence Spectroscopy of Barium Doped Zinc Sulfides

Barium doping, like aluminium, and ammonium chloride (copper(II) sulfate), generated two emissive states: a blue peak around 450 nm, and a green peak around 518 nm (Figure 2.24). The excitation of the blue peak showed a strong symmetric peak at 372 nm, and a band gap peak at 337 nm for 8 mol% doping. Given the peak at 372 nm has been assigned to a zinc vacancy, the loss of an excitation contribution for the band gap for both 4 and 2 mol% doping was unexpected. Addition of barium during the firing process did not appear to have influenced the band gap in a meaningful way, showing the same peak position as the aluminium doped zinc sulfide. The presence of the band gap in only one sample was not considered to be related to the wurtzite phase shown in the PXRD data, as the band gap for this phase has been reported to be 3.91 eV (317 nm);⁶³ higher in energy than this peak. Similarly, this was not assigned as a defect peak from the wurtzite phase as additional, or broadened peaks were expected to be observed in the emission spectra.

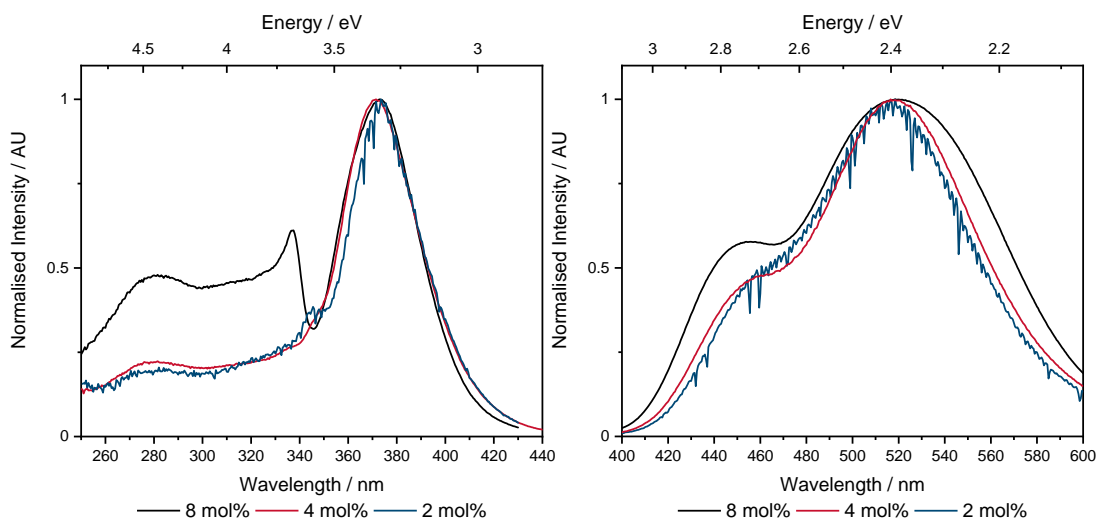


Figure 2.24: Excitation (left) ($\lambda_{em} = 450$ nm) and emission (right) ($\lambda_{ex} = 372$ nm) spectra for barium doped zinc sulfides.

The emission spectra showed two key differences as the barium concentration decreased: the relative intensity of the blue peak increased, and the FWHM of both peaks also decreased. The change in intensity of the peak located around 450 nm was presumed to be caused by a decrease in the number of defect sites that gave rise to this emission. All samples, regardless of the barium doping concentration, showed a significant green emission centred around 518 nm. Because the peak broadening was particularly apparent at the highest doping, it was presumed this

could be caused by ions/defects in slightly different strain environments combining to form a broad emission. Caused either, by an increase in the number of defects, such that some are spatially associated with each other, or for barium to be in a nearby site causing increased strain.

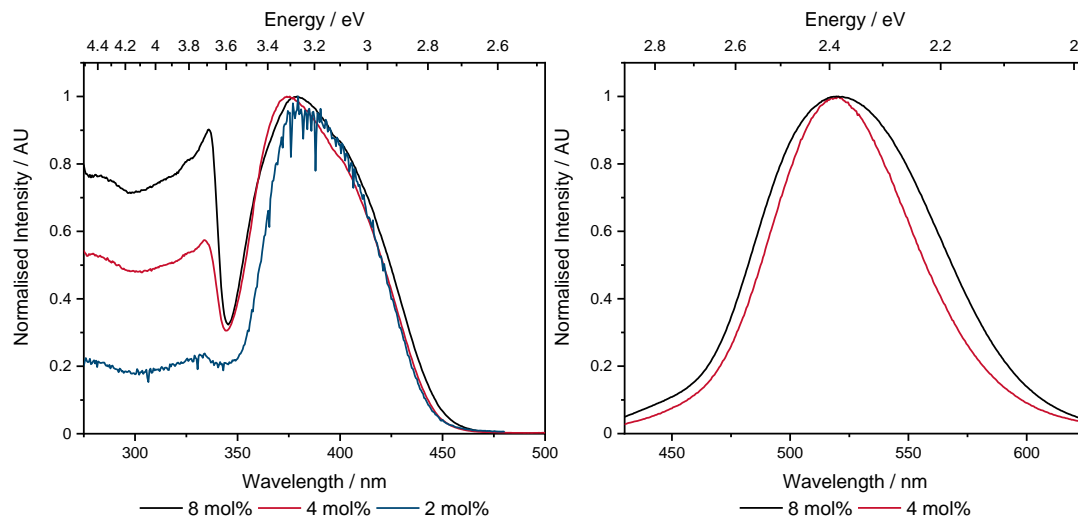


Figure 2.25: Excitation (left) ($\lambda_{em} = 518$ nm) and emission (right) ($\lambda_{ex} = 410$ nm) spectra for barium doped zinc sulfides.

Excitation of the green peak, unlike the blue peak, exhibited a band gap excitation for all three barium doped samples at 337 nm, with an intensity proportional to the barium added during preparation. As with copper(II) sulfate doping, energy transfer between the blue defect and the green defect was apparent from the strong contribution of the defect state at 372 nm to the green emission. Since the two defect peaks overlapped with the aluminium doped samples the defects were presumed likely to be the same. As discussed for 372 nm excitation, the broadening of the 8 mol% barium doping after excitation at 410 nm was believed to be related to slight variations in the defect environment across the material.

Barium, being a fully oxidised group 2 metal, has no valence electrons to contribute within the band gap and the empty orbitals are not expected to lie within the band gap and contribute any additional defect states. Instead, due to the large disparity in ionic radii of barium and zinc ions, 135 pm and 74 pm respectively, it was anticipated that any incorporation of barium within the crystal structure will impart a large degree of strain upon the lattice. However, given the large size of the barium ion, incorporation within the lattice was expected to be relatively minor, which would be supported based upon the EDX data. Initially, it was believed barium incorporation would result in the generation of sulfur defects to reduce the strain upon the rest of the lattice. Based upon emission data it would seem this was not the case, and zinc, not sulfur, was ejected from the lattice to reduce the strain.

Further insight into the structure was obtained by through a cell relaxation using Quantum Espresso on a barium doped zinc sulfide supercell using the same optimised parameters discussed in Section 2.4.2.4. With barium incorporated into the structure, the lattice parameter increased to 10.8041 Å (+0.08955 Å) and an expansion around the barium centre, with calculated average barium sulfur bond lengths of 2.8544 Å and average zinc sulfur bond lengths of 2.3267 Å, and a lattice parameter of 10.8041 Å (+0.08959 Å). Surprisingly, the average bond length only increased by a minor 0.0069 Å, which suggested the impact of the barium ion was largely limited to an expansion around the defect. However, it cannot be said whether such a small difference would cause the formation of zinc defects. Barium may be considered a suitable choice for the generation of a green emitting zinc sulfide as the green emission dominated emission at each excitation wavelength. With a selective green emission obtained via excitation at 410 nm and a FWHM similar to aluminium doping for both 4 mol% and 2 mol% barium samples.

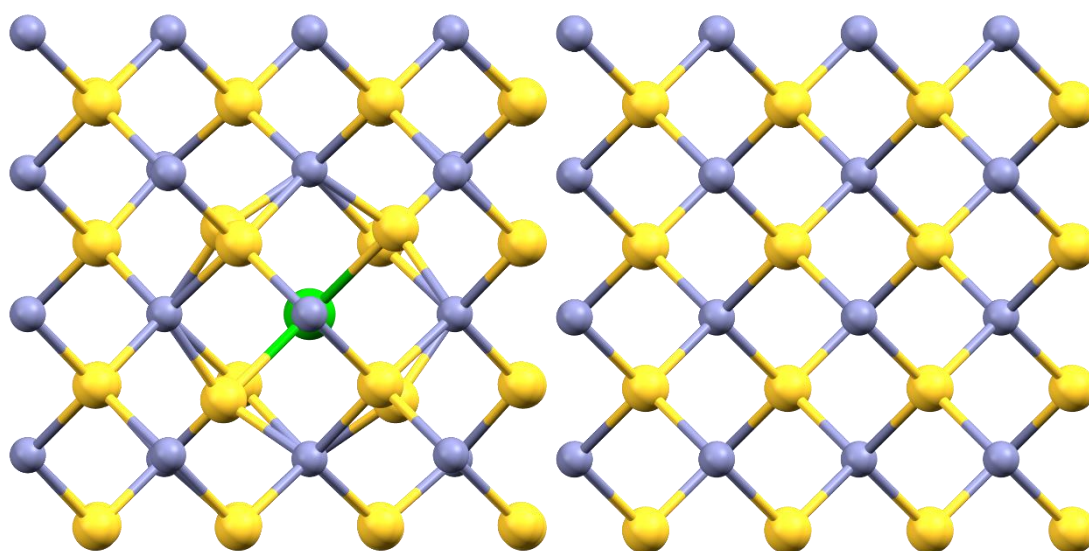


Figure 2.26: Calculated structure of barium doped (L) and undoped (R) zinc sulfide using the PBEsol functional.

2.4.3.4 Luminescence Spectroscopy of Strontium Doped Zinc Sulfides

Unlike barium doped zinc sulfides, strontium doping only exhibited a single peak in the excitation spectra at 373 nm. Which was identical to copper(II) sulfate doped zinc sulfides and showed very little difference as the amount of dopant varied. In fact, the only difference was the presence of a small weak peak around 430 nm observed for the lowest strontium doping which was presumed to be a defect caused by the preparation of the doped zinc sulfide and not caused by the strontium ion. The similarity to copper(II) sulfate doped samples implied that sulfur vacancies were formed by the incorporation of the strontium ion. The emission spectra showed a single peak of λ_{\max} 494 nm and no change in the FWHM was observed as the

Chapter 2. Synthesis and Characterisation of Zinc Sulfide Phosphors

strontium doping was altered; showing the same broad emission as observed with copper(II) sulfate doped samples.

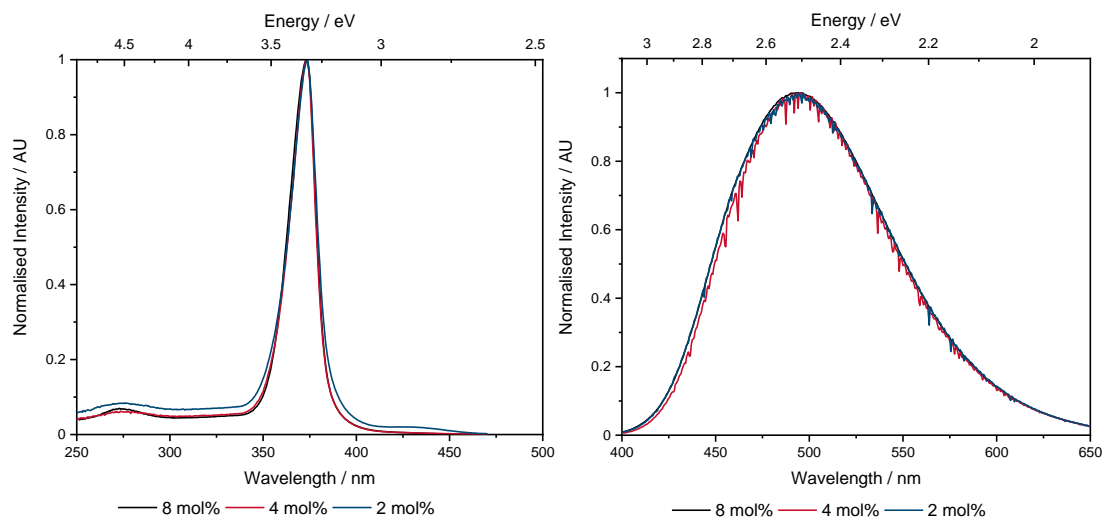


Figure 2.27: Excitation (left) and emission (right) spectra for strontium doped zinc sulfides.

Strontium being in a stable +2 oxidation state would not be reduced by the zinc sulfide, and with no darkening of the zinc sulfide observed upon addition strontium sulfide, unlike copper(II) sources, reduction was not the cause of this defect. The lack of reduction will also not require the loss of sulfur to counteract the mismatched charge, thus the defect must be related to the size of strontium ion, as with barium doping. Strontium with an ionic radius of 118 pm is significantly larger than zinc, therefore, the same defects observed in barium doped samples were expected. While strontium is smaller than barium the difference is relatively small (17 pm) and EDX data did not suggest incorporation of strontium was greater than that of the barium doped samples. As with barium, the increased strain on the lattice introduced by the large ion requires the ejection of a zinc or sulfur from the lattice. Strontium being smaller than barium exerts less force on the sulfur ions that in turn places less strain on the surrounding zinc ions and instead of a zinc ion being displaced from the lattice, a sulfide is removed to relieve strain in the system. As with the barium doped sample, relaxation of the structure was performed, and showed a similar increase of the lattice parameter to 10.7879 (+0.0734 Å) and a minor increase in the average zinc sulfur bond length to 2.3249 Å (+0.0051 Å), with strontium sulfur bond lengths of 2.7245 Å. Expectedly, the expansion around strontium was lower than the barium doped sample with a very minor decrease in the displacement of the zinc ions in the second shell surrounding the defect (Appendix Figure 6.11).

2.4.3.5 Luminescence Spectroscopy of Calcium Doped Zinc Sulfides

Regarding calcium, 10 mol% doping bared little similarity to any of the previously prepared samples (Figure 2.28). A strong peak at 373 nm was present, as it has been for all dopants thus far, indicating sulfur or zinc vacancy defects were present in the material. However, the signal was also broadened towards 475 nm, suggesting the presence of other defects as well. Closer analysis of the excitation spectrum for 580 nm emission showed a second peak around 420 nm. Both excitation spectra exhibited an unusually prominent peak at 250 nm – significantly lower in energy than the peak observed at 280 nm in these materials so far. The origin of this peak is unknown, as such a high energy transition would involve states deep within the band gap. This has not observed in previous samples nor within the literature thus an accurate assignment cannot be made. Both excitation spectra showed a peak at 342 nm which was within the expected region for the band gap of sphalerite zinc sulfide. The excitation of the 520 nm peak, however, showed a second peak at 327 nm, this peak is too low in energy to be assigned as a wurtzite phase transition, but also too high in energy to be typically considered from the sphalerite phase: the size of the particles observed via SEM are too large to cause quantum confinement effects that would increase the energy of the band gap. The reported band gap for calcium sulfide covers a wide range of 3.4 – 4.4 eV⁶⁴ because of this, and the unknown crystal structure, assignment to calcium sulfide would be ambiguous.

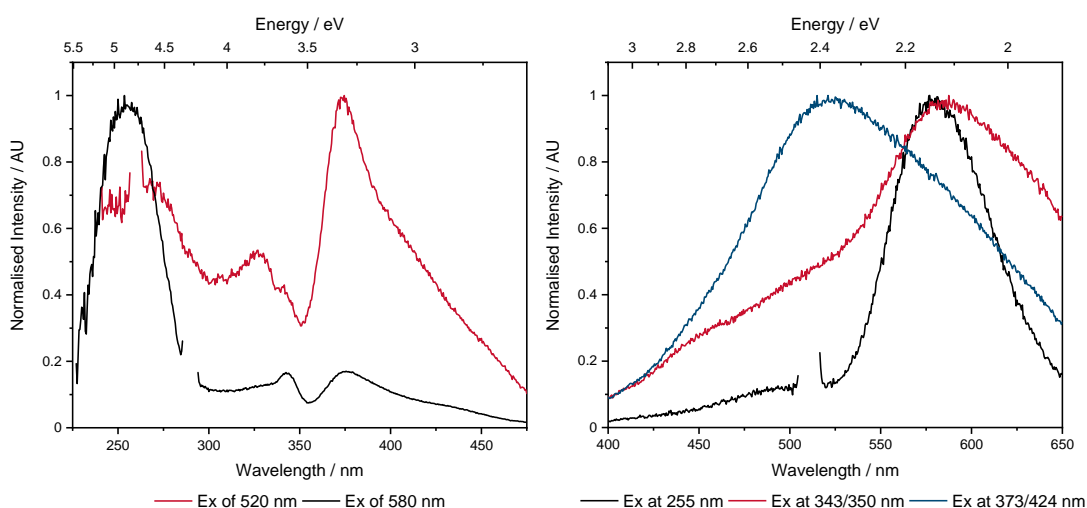


Figure 2.28: Excitation (left) and emission (right) spectra for 10 mol% calcium doped zinc sulfide.

Emission spectra showed three distinct peaks: a broad peak centred around 510 nm, a peak at 580 nm, and a third broad emission that appeared to combine both defects. Excitation at 255 nm generated an emission with a λ_{\max} 580 nm, along with a small contribution around 500 nm which was initially believed to be caused by a

sulfur vacancy based upon the peak position and the broad nature of the peak. The emission at 580 nm has so far not been observed to be caused by zinc or sulfur defects, in fact, this emission is usually only observed in manganese doped zinc sulfides. Any manganese present in these materials could only be derived from the calcium sulfide but given the purity of the calcium sulfide, manganese can at most only be 0.008 wt%. Combined with an excitation spectrum that did not match a manganese doped zinc sulfide species,⁶⁵ it seemed unlikely that manganese was the origin of the emission.

Decreasing the excitation energy to either 343 or 350 nm resulted in an emission with a greater intensity and increased the relative intensity of the peak around 520 nm. Further decreasing the excitation energy to 373 or 424 nm shifted the emission to 510 nm, although the broadness of the peak indicated there was still a significant contribution of yellow emission due to excitation of this unknown defect. An emission at 510 nm has previously been assigned to an interstitial zinc defect and was also likely to be present in this material when combined with the excitation spectra. Based upon the emission maxima obtained from excitation at 373 nm the presence of sulfur vacancies was considered less likely than zinc vacancies, and thus it was believed that the broadening seen at higher energies is caused primarily by zinc vacancies. The additional shoulder observed at energies lower than 580 nm has only been observed from the wet impregnation method of zinc sulfide doping corresponding to an interstitial sulfur defect. However, the lack of a distinct peak in the excitation spectra corresponding to this emission, and the less prominent peak when excited at lower energies suggested this may not be a correct assignment for this material. Whilst the origin of the emission centred around 580 nm is still ambiguous.

Decreasing the dopant concentration to 8 mol% generated additional peaks in both the excitation and emission spectra with a high degree of similarity in the excitation spectra (Figure 2.29). As with 10 mol% calcium doping, a peak was observed at 374 nm relating to either sulfur or zinc vacancies, with shoulders at lower energies that were anticipated to be caused by interstitial zinc, which is particularly evident in the excitation for the 500 nm emission seen around 420 nm. As before, two band gaps appeared to be present, found at the same wavelengths as before: 344 and 327 nm. The emission spectra (Figure 2.29), showed a range of peaks with λ_{\max} values of 426, 450, 495, 520, and 585 nm. Excitation at the band gap of 340 nm, generated two of these peaks: 450 and 585 nm, the first of which was assigned to a zinc vacancy due to the similarity of the excitation and emission spectra with previous samples. Excitation of the peak located at 520 nm, exhibited a high energy transition at 328 nm, without the presence of the band gap peak shared by the other excitation spectra. The excitation of the emission at 580 nm shared an identical profile to the zinc vacancy but with a slightly broadened defect peak.

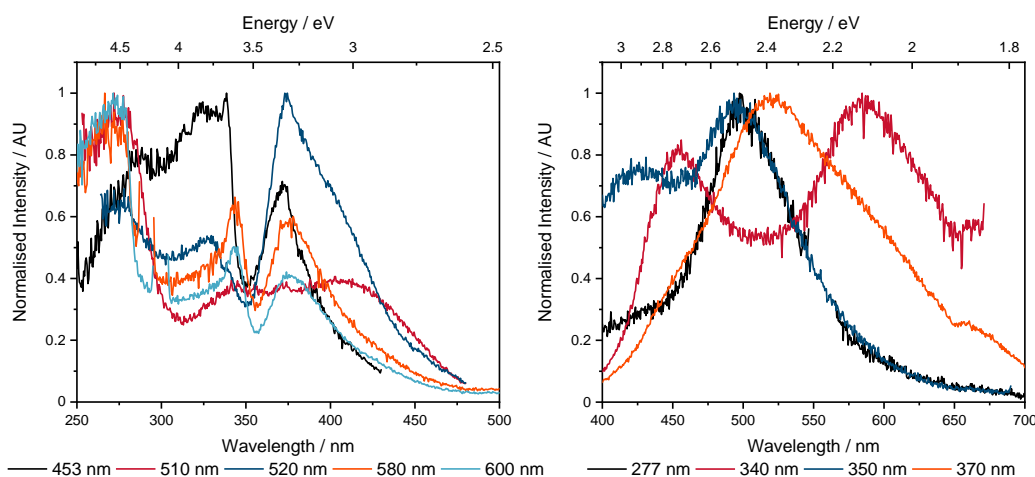


Figure 2.29 Excitation (left) and emission (right) spectra for 8 mol% calcium doped zinc sulfide with excitation and emission wavelengths labelled.

The broad emission peak with a λ_{\max} of 520 nm was expected to be the combination of multiple peaks, with the majority of the intensity caused by interstitial zinc defect, as with barium doped samples. Similarly, the emission peak centred around 495 nm was believed to be caused by sulfur vacancy defects. The highest energy emission peak, 425 nm, was only observed by excitation at 350 nm and weakly at 277 nm. Again, an emission this high in energy has not been demonstrated in either of the previous group 2 metal doping, nor by copper or aluminium doping. The broad excitation of this peak centred at 350 nm was not typically observed for zinc sulfide band gaps and was too high in energy to be considered a zinc sulfide defect. The number of emissive states and the range of excitations possible, suggested these

Chapter 2. Synthesis and Characterisation of Zinc Sulfide Phosphors

defects were natural defects caused by the doping procedure and not specially related to calcium.

Computational structural analysis displayed the same trends as observed with the previous Group 2 metals. The lattice parameter increased to 10.7670 (+0.0525 Å), as did the average zinc sulfur bond length to 2.3228 Å (+0.0030 Å) due to an expansion caused by the larger calcium ion, albeit to a lesser degree (Figure 6.13). Analysis of the calculated bond length distributions showed a reduced spread of bond lengths with 68% of bond lengths occurring within 0.005 Å of each other. Both strontium and barium structures showed a much broader distribution of bond lengths and modal bond length becoming longer and decreasing in frequency. The reduced distribution of bond lengths suggested the calcium defect imparted less strain on the surrounding ions, therefore a reduced propensity to form defects is expected.

Table 2.12: Excitation and emission wavelengths for zinc sulfides doped with group 2 metals

Dopant	Mol% added	Excitation / nm	Emission / nm
Ba	8	372	450, 518
	4	372	450, 518
	2	337, 372	450, 518
Sr	8	372	494
	4	372	494
	2	372	494
Ca	10	342, 373	510, 580
	2	344, 374	426, 450, 495, 520, 585

In conclusion, the incorporation of suitably large ions such as barium or strontium exerted a high degree of strain within the lattice causing the ejection of either a zinc or a sulfide ion depending on the metal (Table 2.12). Barium, the largest ion, favoured the formation of zinc vacancies and interstitial zinc, with an emission profile dominated by emission from interstitial zinc defects with a λ_{\max} of 520 nm. However, 8 mol% doping resulted in a broader emission when exciting at both 337 nm, and 410 nm compared to 4 mol% 337 nm, and 410 nm. Whilst doping with strontium only caused the formation of sulfur vacancy defects that maintained the same bandwidth seen in previous examples, and regardless of the dopant concentration with a λ_{\max} of 490 nm. The smallest of the group 2 metals, calcium, did not favour the formation of either zinc or sulfur defects. However, the formation of

two new peaks centred around 425, and 580 nm was observed, however their origin was not known.

2.4.4 Manganese Doped Zinc Sulfides

The excitation spectra of manganese-doped zinc sulfide materials (Figure 2.30) exhibited band gaps dependant on the dopant: one at 349 nm in manganese nitrate doped, and two at 343 and 341 nm caused by manganese oxide doped samples. Both nitrate and oxide sources showed the same peaks between 370 and 550 nm and were assigned to manganese d-d transitions.^{51,66} Demonstrating the source of manganese did not influence the environment of the substituted manganese. Doping with an oxide counterion however, introduced a second defect state with an excitation centred around 380 nm which did not match any previous zinc or sulfur defect thus far, and suggested an oxide defect caused. Excitation at 345 nm for manganese nitrate doped zinc sulfide exhibited the expected emission with a λ_{max} of 584 nm in good agreement with the literature²¹ for bulk particles, whilst manganese oxide doping showed a slight blue shift to 580 nm. Both transitions were assigned to the manganese relaxation^{21,30,67}. The oxide source generated a second, smaller,

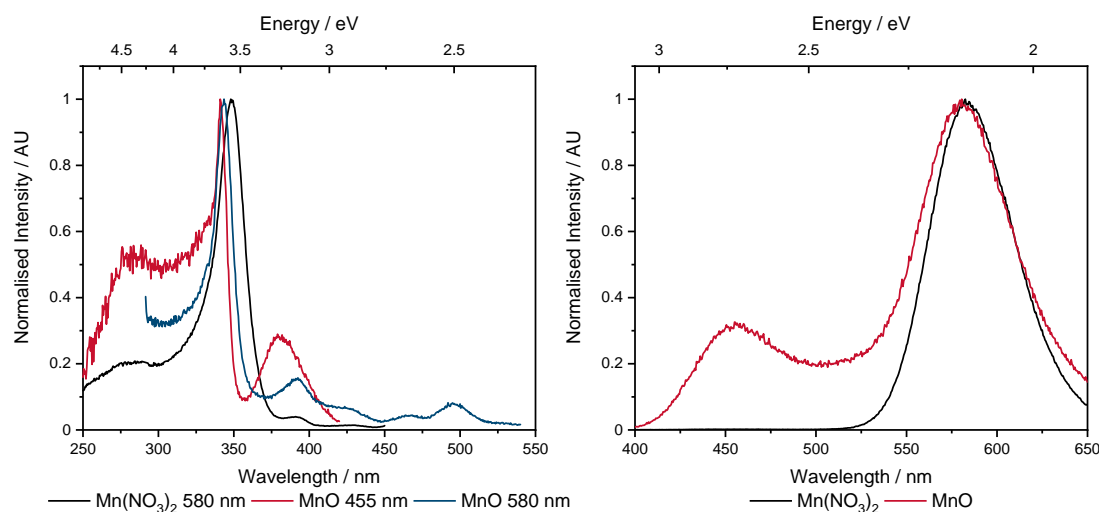


Figure 2.30: Excitation (left) and emission (right) ($\lambda_{\text{ex}} = 345$ nm) spectra of manganese nitrate hydrate and manganese oxide doped zinc sulfides

peak at 455 nm – the same as a zinc vacancy. However, the intensity around 500 nm suggested additional defects were present, i.e., sulfur vacancies or interstitial zinc. As this second defect was only observed with the addition of oxide it was expected be related to this anion, as either a substitutional oxygen or interstitial sulfur. Interstitial sulfur can be ruled out, as it does not agree with data from the samples discussed earlier. Although the similarity of the emission and excitation spectra suggests a zinc vacancy defect, the formation of such a defect has typically required the introduction of a large metal or an ion with a charge greater than +2.

Because both these features are absent, the transition can reasonably be assigned to an oxygen defect.

2.4.5 Group 2 and Manganese Co-Doped Zinc Sulfides

2.4.5.1 SEM and EDX Analysis

Addition of manganese along with a Group 2 metal displayed the same amount of aggregation, and dispersity in sizes that has observed in all the other zinc sulfides prepared so far. Barium doped samples exhibited large particles around 4-5 μm along the longest edge, with smaller particles of 3.4 \times 3.4, and 4.0 \times 2.8 μm also

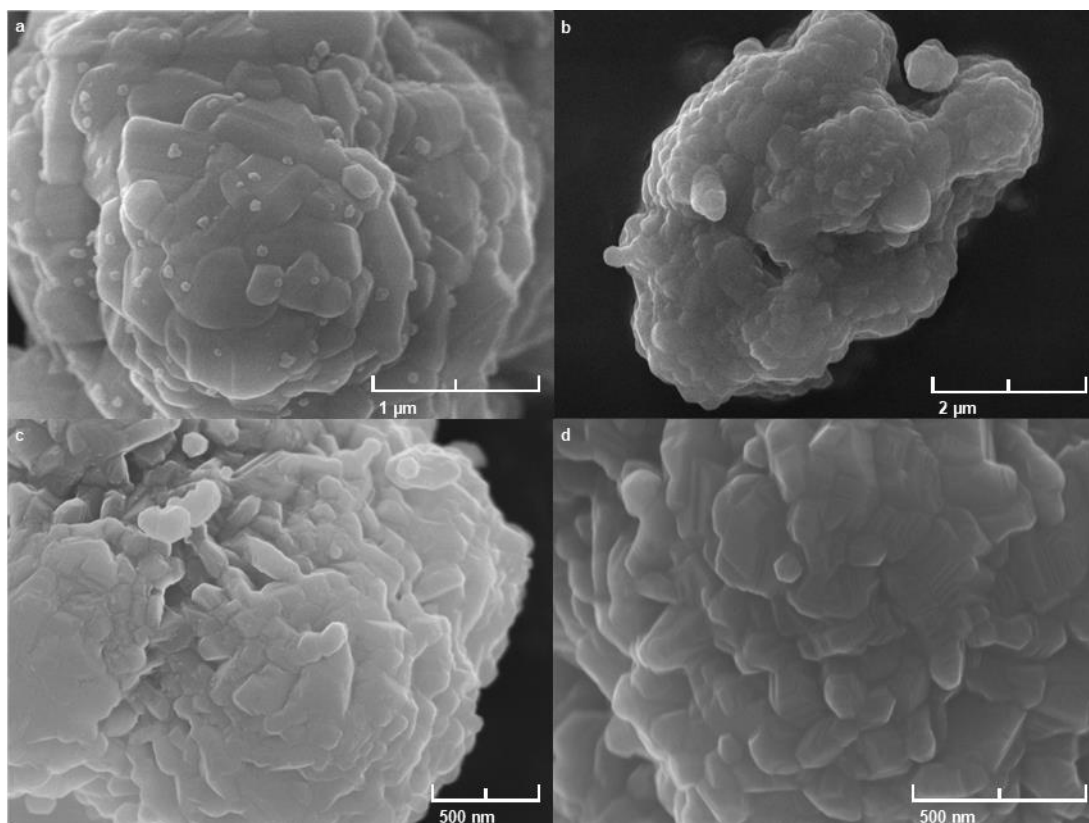


Figure 2.31: SEM image of 2 mol% barium with manganese oxide (a), 8 mol% barium with manganese nitrate (b), 4 mol% strontium with manganese oxide (c), and 8 mol% calcium with manganese oxide (d) doped zinc sulfides.

observed. Replacing the manganese oxide with manganese nitrate did not cause significant deviation from these sizes with particles as small as 2.0 \times 1.8 μm , and as large as 5.8 \times 4.2 μm observed. As before, strontium doping typically caused smaller particles, with most showing dimensions ca. 2.9 \times 2.5 μm , however, some larger 5.6 \times 4.0 μm particles were also present. Calcium doping exhibited a similar range of particle sizes from 1.9 \times 2.1 μm up to 5.6 \times 4.5 μm . Since all the Group 2 dopants showed a similar range of aggregated particles, it was unlikely the nature of the dopant had considerable influence upon the aggregation. Expectedly, the large aggregates were formed of smaller fused particles (Figure 2.31). Interestingly, all

the barium doped samples appeared to consist of the large particles greater than 500 nm along the shortest edge, with a few smaller particles around 200 nm. Strontium and calcium doped samples, in contrast, contained smaller fused particles, typically around 120 and 80 nm along the longest edge.

EDX mapping of barium and manganese oxide samples (Figure 2.32) showed areas deficient in zinc for all three doping concentrations, while sulfur was more consistent across the entire sample, with just a few areas that were visibly devoid of sulfur. Predictably, 8 mol% doping showed a high degree of localisation suggesting an entire particle was barium sulfide rather than just surface bound. Both 4 and 2 mol% doping showed localisation of barium, but to a lesser degree; 4 mol% contained the lowest concentration of barium. Oxygen, as before, occurred in the same regions as barium, although to a lesser degree than observed in samples without a manganese co-dopant. Because of the low manganese concentration, it was not possible to accurately measure the distribution with EDX as the signal to noise ratio was too low (Appendix Figure 6.15). The EDX mapping data of 8 mol% (Table 2.13) indicated a deficiency of sulfur with respect to zinc and barium, as well as a two times excess of barium. Site 1 showed the same sulfur deficiency, but a higher concentration of barium, which again, suggested some barium oxide was present within these materials. Site 2, however, exhibited a sulfur metal ratio that was within experimental error to the predicted values. 2 mol% displayed a similar trend as 8 mol% and 4 mol% showed a similar level of metal and sulfide concentration with a slightly lower than expected barium concentration. Overall, the EDX analysis demonstrated that barium was not homogeneously incorporated under the experimental conditions.

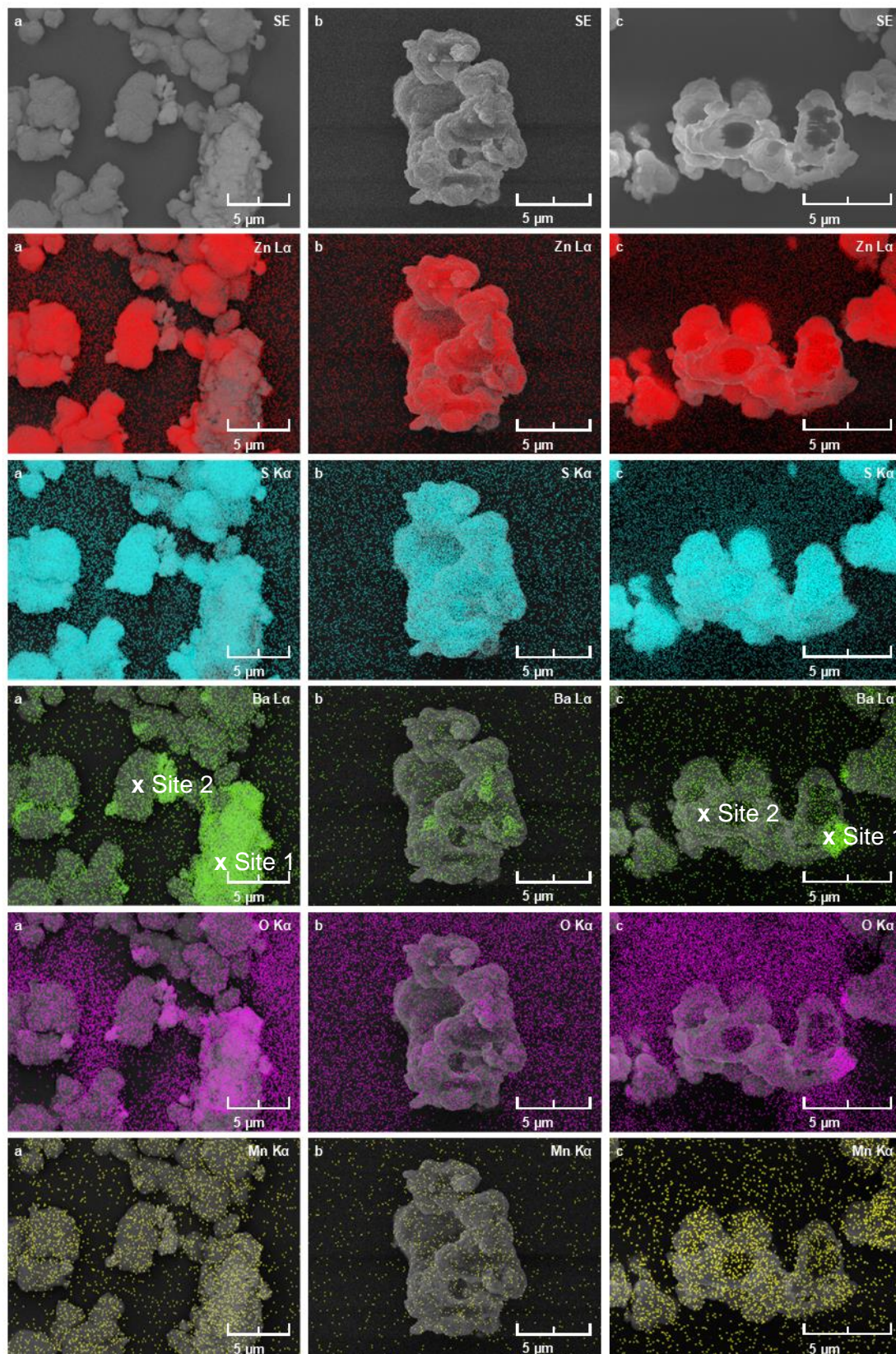


Figure 2.32: SEM and EDX images for barium sulfide and manganese oxide doped zinc sulfides a) 8 mol% Ba, b) 4 mol% Ba, c) 2 mol% Ba showing contributions from zinc, sulfur barium, oxygen, and manganese.

Chapter 2. Synthesis and Characterisation of Zinc Sulfide Phosphors

Table 2.13: Atomic% data for barium sulfide and manganese oxide doped zinc sulfides

Element	8 mol%			4 mol%		2 mol%	
	Map	Site 1	Site 2	Map	Map	Site 1	Site 2
Zinc	32.6	8.4	46.1	30.8	35.4	13.3	45.9
Sulfur	34.4	32.9	47.5	29.3	35.4	24.2	45.6
Oxygen	27.2	31.6	5.5	38.9	28.7	46.4	8.3
Barium	5.8	27.1	0.9	1.0	0.6	16.1	0.2

Doping with manganese nitrate instead of manganese oxide, showed no perceptible change in the morphology. EDX mapping (Appendix Figure 6.14) indicated zinc was homogeneously dispersed across both 8 and 4 mol% samples while 2 mol% contained sites that are clearly deficient in zinc. Sulfur maps showed a similar trend, although to a lesser degree, as any barium localisation is expected to occur with a sulfide counterion. Both 8 and 4 mol% displayed a low concentration of barium present within the zinc sulfides, potentially only showing background noise. The lowest doping, 2 mol%, showed a higher degree of localisation and aligned with the zinc deficient sites. Expectedly, oxygen concentration spiked in the same area as barium. Atomic% data (Table 2.14), confirms the EDX mapping with zinc and sulfur near unity in all samples, and all but the 2 mol% sample showing barium concentrations below the expected values.

Table 2.14: Atomic% EDX map data for barium sulfide and manganese nitrate doped zinc sulfides

Element	8 mol%	4 mol%	2 mol%
Zinc	27.9	36.3	37.7
Sulfur	27.2	35.1	37.2
Oxygen	44.5	28.3	23.7
Barium	0.4	0.2	0.8

EDX mapping data for 8 mol% strontium, and manganese oxide doped zinc sulfides (Appendix Figure 6.16), similarly, displayed areas that were zinc and sulfur deficient, with 4 mol% showing a similar result but to a lesser degree, with only one particle clearly deficient in zinc. For 2 mol% any differences in concentration were too small to identify. However, the concentration of sulfur in these sites was expectedly greater than that of zinc, since a sulfide source was used for strontium doping. Strontium showed a high degree of localisation that expectedly aligned with the deficient zinc sites, and for 8 mol% also occurred in areas with a slightly

Chapter 2. Synthesis and Characterisation of Zinc Sulfide Phosphors

different morphology. Reducing the strontium loading to 4 mol% retained the localisation but did not exhibit a difference in morphology at this site. 2 mol% similarly showed the co-localisation of strontium and oxygen but only on a very small particle. As with the barium samples, both 8 and 4 mol% demonstrated a lower degree of co-localisation compared to the samples doped without manganese oxide. Either addition of manganese oxide influenced the propensity for the group 2 oxide to form, or it was random chance that the particles examined happened to display this composition. Manganese was, as in previous samples, too low in concentration to reliably detect in EDX against the background noise. Atomic% data (Table 2.15) for EDX mapping of 4 and 2 mol% showed sulfur and metals within experimental error of unity, whilst 8 mol% showed a minor excess of the metals. Analysis of strontium rich sites (Site 1) suggested most of the strontium was present as the sulfide form with only 1 or 2% existing as the oxide. The majority of the oxygen present was believed to be bound atmospheric oxygen, since otherwise would indicate a high proportion of free sulfur/sulfide. In the case of 2 mol% a significant contribution from the background was present due to the small size of the particle being analysed. Zinc rich sites showed only a small proportion of strontium present, and similar proportion of zinc and sulfur.

Table 2.15: Atomic% data from strontium sulfide and manganese oxide doped zinc sulfides

Element	8 mol%			4 mol%			2 mol%		
	Map	Site 1	Site 2	Map	Site 1	Site 2	Map	Site 1	Site 2
Zinc	36.4	5.8	46.5	25.6	5.1	44.5	30.6	8.2	48.5
Sulfur	38.7	25.6	44.7	25.4	29.3	45.2	30.5	15.2	46.5
Oxygen	20.5	45.4	7.5	47.9	39.9	9.3	38.9	67.7	5.1
Strontium	4.4	23.2	1.3	1.0	25.7	1.0	0.0	8.9	0.0

Regarding the calcium and manganese doped zinc sulfides (Appendix Figure 6.17), zinc and sulfur maps were homogenous; only a few sites devoid of both elements that did not align with any other element being present. Calcium appeared to be localised in two areas with no clear morphological differences; aligned with zinc deficiencies. Oxygen, as with non-manganese doped samples showed little to no colocalization with calcium. Atomic% map data (Table 2.16) displayed a significantly lower concentration for calcium than expected, demonstrating again that the Group 2 dopant had not been homogeneously incorporated within the zinc sulfide host. The calcium rich site (Site 1) showed a greater proportion of zinc than calcium, potentially due to the spot size of the site analysis including nearby zinc sulfide. The

combination of the two metals was greater than sulfur proportion; suggesting calcium oxide was present (up to half of the calcium at this site).

Table 2.16: Atomic% data for 8 mol% calcium sulfide and manganese oxide doped zinc sulfide

Element	Map	Site 1	Site 2
Zinc	29.4	21.1	45.0
Sulfur	28.5	30.5	43.9
Oxygen	41.7	30.2	10.9
Calcium	0.4	18.2	0.1

2.4.5.2 PXRD Analysis

As previously mentioned, any unincorporated barium sulfide should be evident in the PXRD pattern via the presence of halite peaks (Figure 2.33). However, just as with samples doped without manganese, no peaks that match the halite phase were present. Whilst the wurtzite phase was still observed in these samples, and more intense than the starting material, it was weaker than for samples only doped with barium; the differences between each dopant concentration were also greatly reduced. Therefore, this may indicate that manganese oxide perturbed the formation of the wurtzite phase, or the combination of manganese oxide and barium sulfide create a second phase, but as no obvious peaks were present, this was deemed unlikely. Consequently, it seemed reasonable to deduce that without the presence of any broad amorphous peaks, the samples consisted of two phases. A sphalerite phase accounting for the majority of the sample, and a wurtzite phase representing a minor component.

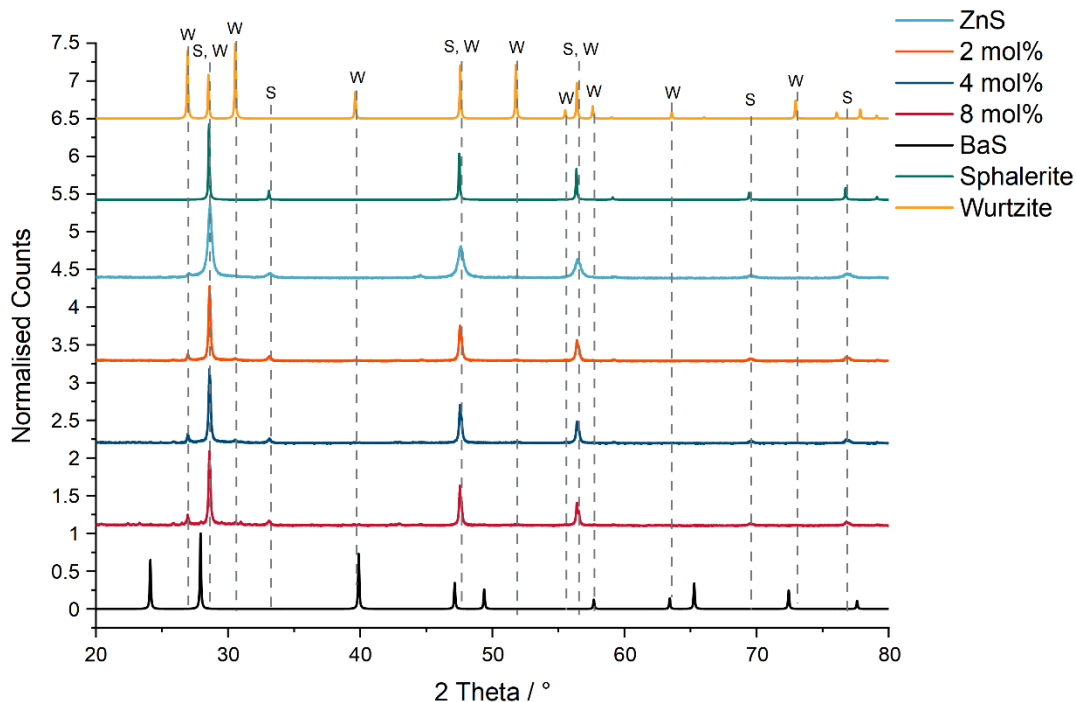


Figure 2.33: PXRD pattern for barium and manganese oxide doped zinc sulfide: 8 mol% 4 mol% 2 mol% Ba, undoped zinc sulfide, and calculated powder patterns for barium sulfide, sphalerite and wurtzite. S indicates sphalerite phase, and W the wurtzite phase.

Unlike manganese oxide doped samples, manganese nitrate did not suppress the formation of the secondary wurtzite phase (Figure 2.34) which, as with the non-manganese doped samples, was proportional to the concentration of barium added. The absence of the halite phase suggested that all the barium sulfide had been incorporated either into the zinc sulfide host framework or into a new crystal structure. A third phase of Ba_2ZnS_3 was observed, however, the signal was very weak and only reliably identified for the 8 mol% barium doping. The existence of the wurtzite phase was unusual given the temperature of the furnace used in the preparation of these materials. It was possible, given the intensity of these peaks was proportional to the barium concentration, that the wurtzite phase acted as a transition between the zinc rich sphalerite phase and the barium rich Ba_2ZnS_3 phase. Rietveld refinement calculated wurtzite composition as 41.17, 34.25, and 17.80 wt%, and Ba_2ZnS_3 composition as 9.15, 3.19, and 0.86 wt% for 8, 4, and 2 mol% barium doping respectively. The lack of a trend between the wurtzite and Ba_2ZnS_3 phases suggested the existence of additional factors. Unfortunately, the residual data for each sample after fitting and refinement was a reasonably high proportion of the data (> 12%).

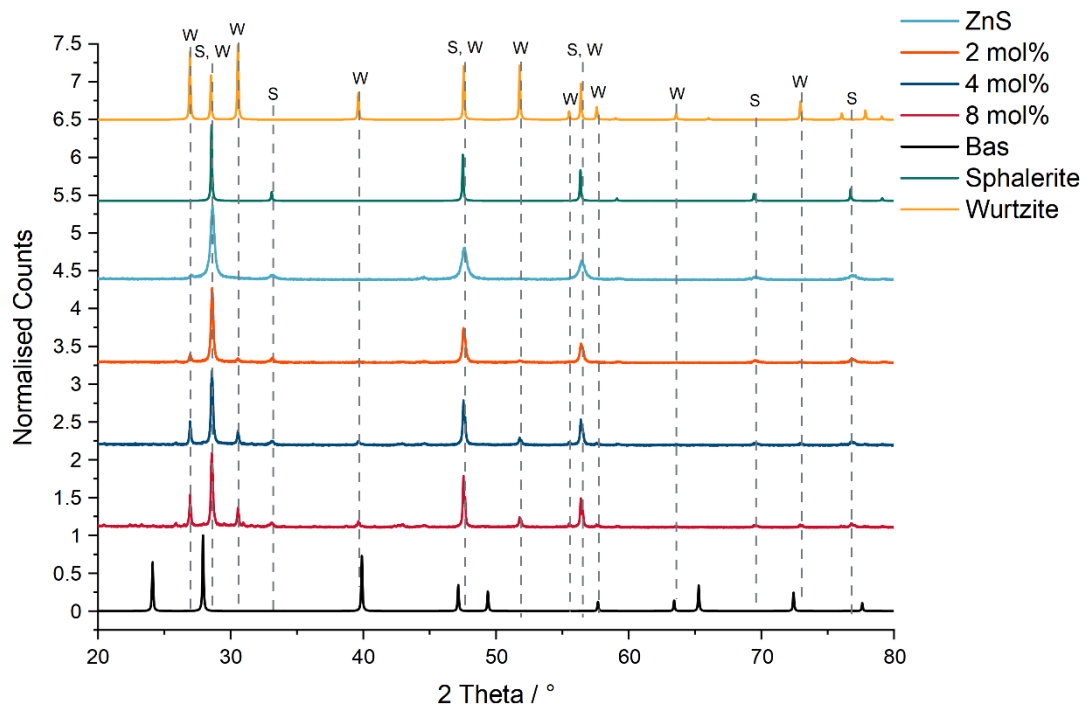


Figure 2.34: PXRD pattern for barium and manganese nitrate doped zinc sulfide: 8 mol% 4 mol% 2 mol% Ba, undoped zinc sulfide, and calculated powder patterns for barium sulfide, sphalerite and wurtzite. S indicates sphalerite phase, and W the wurtzite phase.

2.4.5.3 Luminescence Spectroscopy of Barium and Manganese Oxide Doped Zinc Sulfides

Excitation of the dominant emission peaks of barium and manganese co-doped zinc sulfides showed two distinct band gaps (Figure 2.36): the first at 348 nm, occurred in the 2 mol% barium doped sample, and the second at 361 nm for both 8 and 4 mol% doping. All three samples showed no shift in the transitions associated with the manganese d-d transitions, which suggested either, there had been no alteration of the manganese environment, or only a small proportion of the manganese was in this new environment. The emission spectra displayed the same trend as the excitation spectra: 8 and 4 mol% show similar emission spectra with a slight decrease in the emission maxima from 620 nm for 8 mol% down to 615 nm for 4 mol% and then a large blue shift to 587 nm for 2 mol% barium doped zinc sulfide. However, it was clear that barium still altered the emission as the bandwidth for this emission was greater than that of barium free samples, with 4 mol% showing a similar, although weaker, broadening of the dominant emission. All three samples showed evidence of additional defects in the 520 and 450 nm regions which were assigned as zinc interstitial and vacancy defects, respectively, caused by addition of barium.

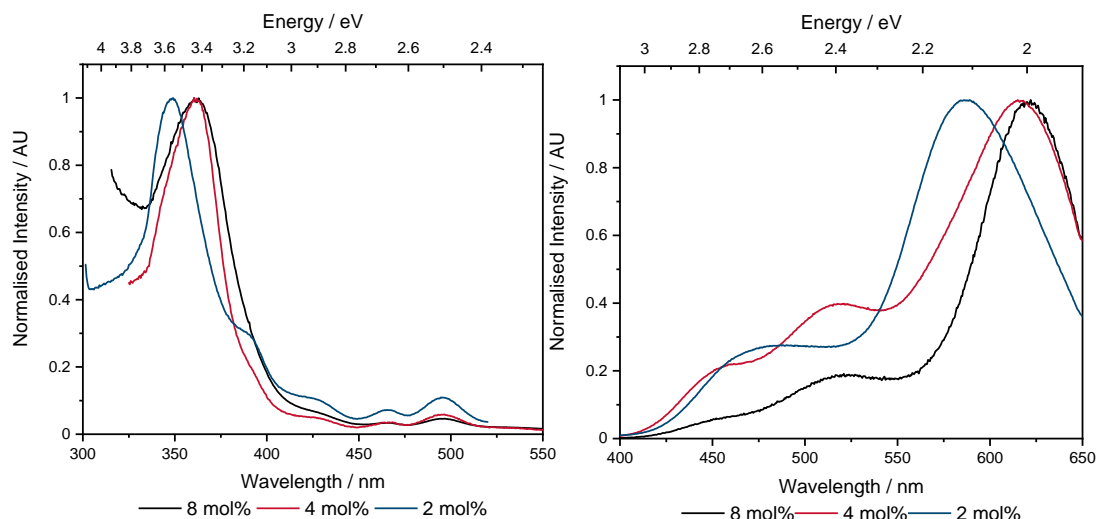


Figure 2.36: Excitation (left) ($\lambda_{em, 8.4 \text{ mol}\%} = 620 \text{ nm}$, $\lambda_{em, 2 \text{ mol}\%} = 587 \text{ nm}$) and emission (right) ($\lambda_{ex, 8.4 \text{ mol}\%} = 360 \text{ nm}$, $\lambda_{ex, 2 \text{ mol}\%} = 350 \text{ nm}$) of barium sulfide and manganese oxide doped zinc sulfides.

Interestingly, the excitation spectra (Figure 2.35) of these zinc defects only exhibited a band gap (333 nm) for excitation of the 520 nm emission. The defect peak positions and shapes showed no significant alterations to the barium doped samples discussed earlier. With a band gap of 360 nm, the presence of Ba_2ZnS_3 originated red emission was a strong possibility.⁶⁶ Assuming the formation of Ba_2ZnS_3 did occur, it was a surprise to see an emission profile that was dominated by the red emission, since the bulk of the material was still zinc sulfide. Likewise, as the d-d manganese transitions had not shifted from the non-barium doped samples, it suggested most of the manganese was still within a zinc sulfide host. Expectedly, decreasing the barium concentration increased the proportion of emission from a manganese doped zinc sulfide material; observed by the increased bandwidth.

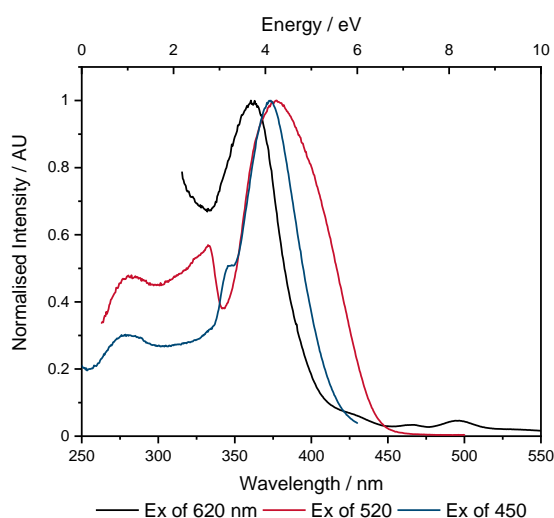


Figure 2.35: Excitation spectra of the emission peaks in 8 mol% barium sulfide, and manganese oxide doped zinc sulfides.

2.4.5.4 Luminescence Spectroscopy of Barium and Manganese Nitrate Doped Zinc Sulfides

Excitation spectra of manganese nitrate doped samples (Figure 2.37), showed a significant shift from the oxide doped samples. Only the 2 mol% barium doped sample displayed a profile that resembled the earlier manganese doped samples with a band gap at 351 nm. 4 mol% showed two peaks at energies higher than 400 nm: 388, 366 nm, and a broad continuum that stretched below 300 nm. The peak at 366 nm was assigned to the band gap transition of Ba_2ZnS_3 , and 388 nm and beyond to manganese d-d transitions. 8 mol% demonstrated none of the fine detail observed in the previous two samples and showed only a slight indication of additional peaks. However, a peak was observed at 344 nm, that agreed with previous values of the band gap in manganese doped zinc sulfides. The strong contribution from zinc sulfide suggested a smaller proportion of Ba_2ZnS_3 activated manganese had been formed, compared to the manganese oxide samples, and the excitation spectrum was a composite of both these materials which resulted in the broad relatively featureless spectrum. All samples regardless of the barium concentration or emission wavelength exhibited the same manganese d-d transitions with no notable shifts.

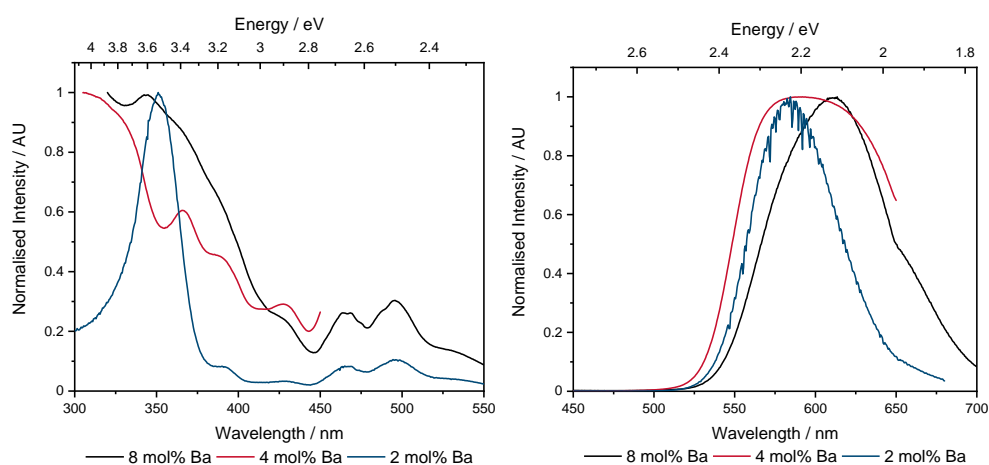


Figure 2.37: Excitation (left) ($\lambda_{ex, 8, 4 \text{ mol}\%} = 612 \text{ nm}$, $\lambda_{ex, 2 \text{ mol}\%} = 580 \text{ nm}$) and emission (right) ($\lambda_{ex, 8, 4 \text{ mol}\%} = 360 \text{ nm}$, $\lambda_{ex, 2 \text{ mol}\%} = 350 \text{ nm}$) spectra of barium sulfide and manganese nitrate.

The emission spectra, like the manganese oxide doped samples, displayed a barium dependant red shift of the emission spectra proportional to the concentration of the barium. The 8 mol% barium doped sample displayed a slight blue shift compared to previous example with an emission maximum located at 616 nm, and also showed a broadened signal towards the higher energies indicating a greater proportion of manganese doped zinc sulfide was present. Reducing the barium loading to 4 mol% generated a broad curve comprised of roughly equal contributions of both manganese doped zinc sulfide and manganese doped

Ba_2ZnS_3 . Decreasing the barium concentration further to 2 mol% exhibited a single peak at 584 nm, with a similar bandwidth to manganese doped zinc sulfide.

Surprisingly, no zinc defects related to the incorporation of barium were observed in these materials. The addition of a large molar quantity of barium resulted in the formation of Ba_2ZnS_3 that acts as an efficient luminophore when doped with manganese. Or as an effective sink for manganese creating a preferential environment for the substitution of zinc and generated an emission that is red shifted from 584 nm in zinc sulfide to 620 nm. Although the source of the manganese used would seem to play a significant role, as the oxide counterion demonstrated a greater proportion of red emission of incorporation but also did not prevent the formation of zinc related defects.

2.4.5.5 Luminescence Spectroscopy of Strontium and Manganese Oxide Doped Zinc Sulfides

Doping with both strontium sulfide and manganese oxide afforded a single strong peak in the excitation spectra (Figure 2.38), located at 346 nm: similar to manganese nitrate doped samples. No shift in the peak position nor FWHM was observed as the strontium concentration decreased. The emission spectra, however, did show a slight change as the dopant concentration was altered. Although no trend was observed, 4 mol% strontium doping exhibited a small blue shift to 581 nm and no secondary emission was generated. 8 and 2 mol% strontium doped samples on the other hand were dominated by an emission at 587 nm that was broadened compared to both 4 mol% and doping without strontium.

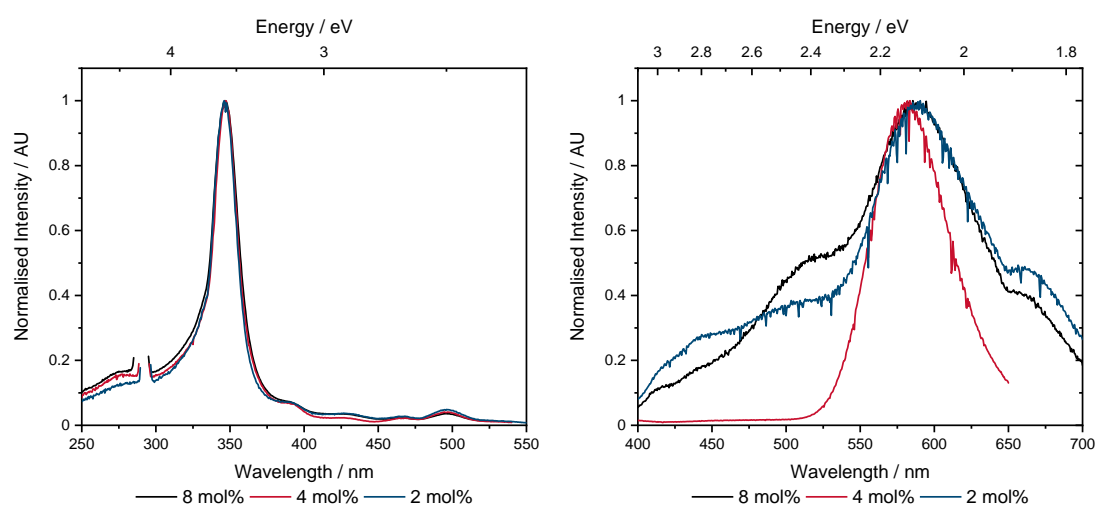


Figure 2.38: Excitation (left) ($\lambda_{em} = 584$ nm) and emission (right) ($\lambda_{ex} = 345$ nm) spectra for strontium sulfide, and manganese oxide doped zinc sulfides

Additional defects were present, with emission demonstrated around 520 and 450 nm. The blue emission was found to be relatively stronger for the 2 mol% strontium doping, which was believed to be a combination of the weaker emission from the strontium derived defects and the blue emission caused by manganese oxide. Previously, samples doped with strontium resulted in a single defect centred around 490 nm. However, in all these samples, the emission was either absent, or red shifted by ~25 nm and more closely resembled an interstitial zinc defect. Excitation of this wavelength (515 nm) (Figure 2.39) generated a range of peaks with a strong zinc vacancy defect associated transition at 373 nm. A second broad peak was observed at lower energies and within the region that has been assigned to interstitial zinc and was similarly believed to cause the green emission. A second band gap like transition at 331 nm was observed for all species and was the only transition in this area observed for 4 mol% doping. Presumably, this peak corresponded to a band gap. Although whether it was associated with zinc sulfide is unknown, as this would be higher in energy than has been observed for any other material prepared thus far. However, the existence of two separate band gaps both relating to the same material seems unlikely. It was possible that some amount of strontium zinc sulfide (Sr_2ZnS_3) had formed, however, in the absence of both EBSD and PXRD it was not possible to determine if such a phase existed. Unlike the barium samples a significant red shift of the manganese emission was not observed. Potentially this was caused by the lack of the formation of strontium zinc sulfide, or the environment was so similar to zinc sulfide that a large shift was not seen, or the manganese ions did not favour the new host material to the same degree as they did for Ba_2ZnS_3 , or manganese was not emissive in the potential Sr_2ZnS_3 material.

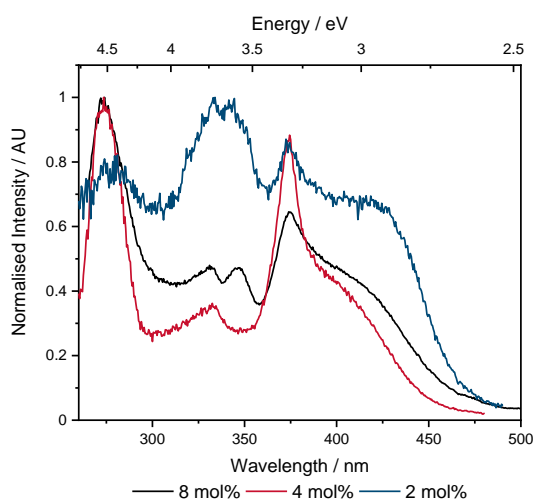


Figure 2.39: Excitation ($\lambda_{em} = 515$ nm) spectra of strontium sulfide and manganese oxide doped zinc sulfides

2.4.5.6 Luminescence Spectroscopy of Calcium and Manganese Oxide Doped Zinc Sulfides

The excitation spectra of calcium sulfide and manganese co-doped zinc sulfides was, like strontium co-doped samples, dominated by a single strong peak at 345 nm assigned to the band gap transition. Excitation at this wavelength generated two peaks, the first at 456 nm was assigned to a zinc vacancy, and the second at 581 nm to manganese emission. Such data showed that calcium was unable to affect the photophysics of the material.

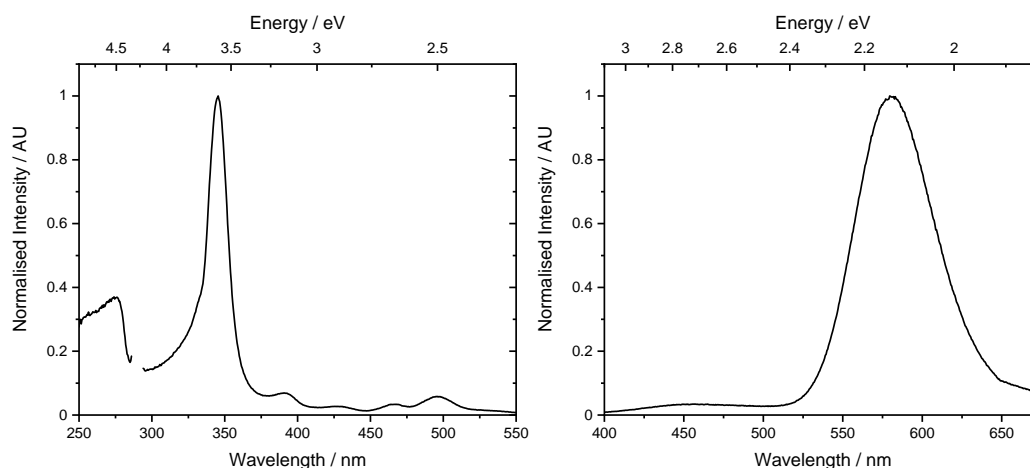


Figure 2.40: Excitation (left) ($\lambda_{em} = 581$ nm) and emission (right) ($\lambda_{ex} = 345$ nm) spectra of calcium sulfide (8 mol%) and manganese oxide doped zinc sulfide

In conclusion, of the group 2 metals co-doped with manganese oxide, only barium doped samples were observed to cause a red shift of the emission spectra (by 40 nm), generating a red emission (620 nm) that dominated the spectrum caused by the formation of a second crystal phase, Ba_2ZnS_3 . Further analysis showed that manganese was also incorporated into the zinc sulfide host resulting in the expected emission around 584 nm. However, this was exclusively observed after excitation of the manganese d-d transitions, suggesting the emissive relaxation pathway is favoured to a greater degree in Ba_2ZnS_3 . The presence of this second crystal structure was unexpected, as typically, this material is synthesised from metal precursors and not from premade zinc and barium sulfide.^{62,68} The source of the manganese was also observed to influence the proportion of red emitting manganese that formed. Manganese oxide displayed few yellow emissive states at 8 mol%, whilst manganese nitrate contained a significantly greater number of yellow emitting states at all barium loadings. Altering the group 2 metal to either strontium or calcium did not appear to generate a second crystal lattice that caused the red shift of the manganese emission. However, due to the lack of PXRD data it was not possible to determine if the second crystal structure had indeed formed.

2.4.6 Silica Coating of Zinc Sulfides

A potential issue for zinc sulfide luminophores is the oxidation of the material over time into zinc oxide. Small scale oxidation would likely introduce additional defects, while large scale oxidation may even prevent the material from being luminescent. One such method to prevent, or minimize oxidation, is a surface coating with silica. This work aimed to explore the impact of oxidation on the morphology of undoped zinc sulfide with and without a silica shell. Two batches of materials were prepared by dispersing zinc sulfide in a mixture of water, methanol and ammonia, and tetraethoxysilane (if silica coated was desired) overnight. The resulting materials were washed and dried and then a sample was taken and exposed to three different conditions: fired at 800 °C in a flowing nitrogen atmosphere, at 800 °C in a flowing air atmosphere, and a sample that was analysed without further processing.

2.4.6.1 Uncoated Zinc Sulfide

Zinc sulfide that was not subjected to grinding in a mortar and pestle displayed a range of aggregated particles sizes from approximately spherical and 1 µm in diameter, to larger clumps up to 2.5 × 5 µm. As with previous examples, smaller fused particles were present, however, their morphology changed depending on the conditions the zinc sulfide was exposed to (Figure 2.41). Without the addition of any heat treatment steps, the fused particle appeared as short chains of triangular particles (100 × 50 nm), and smaller spherical particles with a diameter of 30 nm. Treatment at 800 °C under a flowing nitrogen atmosphere caused sintering of the particles, and a shift in the morphology of the fused particles to be smoother and more rectangular in appearance. In contrast, exposing the particles to 800 °C in flowing air, caused the small particles to become more rounded in appearance with a few spherical and elongated ovoid particles observed as well.

EDX mapping (Figure 2.42) expectedly showed a homogenous zinc distribution across all three conditions. Sulfur however, while distributed evenly for the samples that were not exposed to an oxidising atmosphere, sample **c** (exposed to flowing air at 800 °C) was only background noise; showing the material had been fully oxidised to zinc oxide. This was similarly observed in the oxygen map, that showed a background oxygen signal for the nitrogen (**a**) and vial (**b**) samples. Atomic% data (Table 2.17) confirmed the initial analysis, as non-oxidised samples displayed similar levels of zinc and sulfur. Whilst the oxidised sample showed a nominal amount of sulfur.

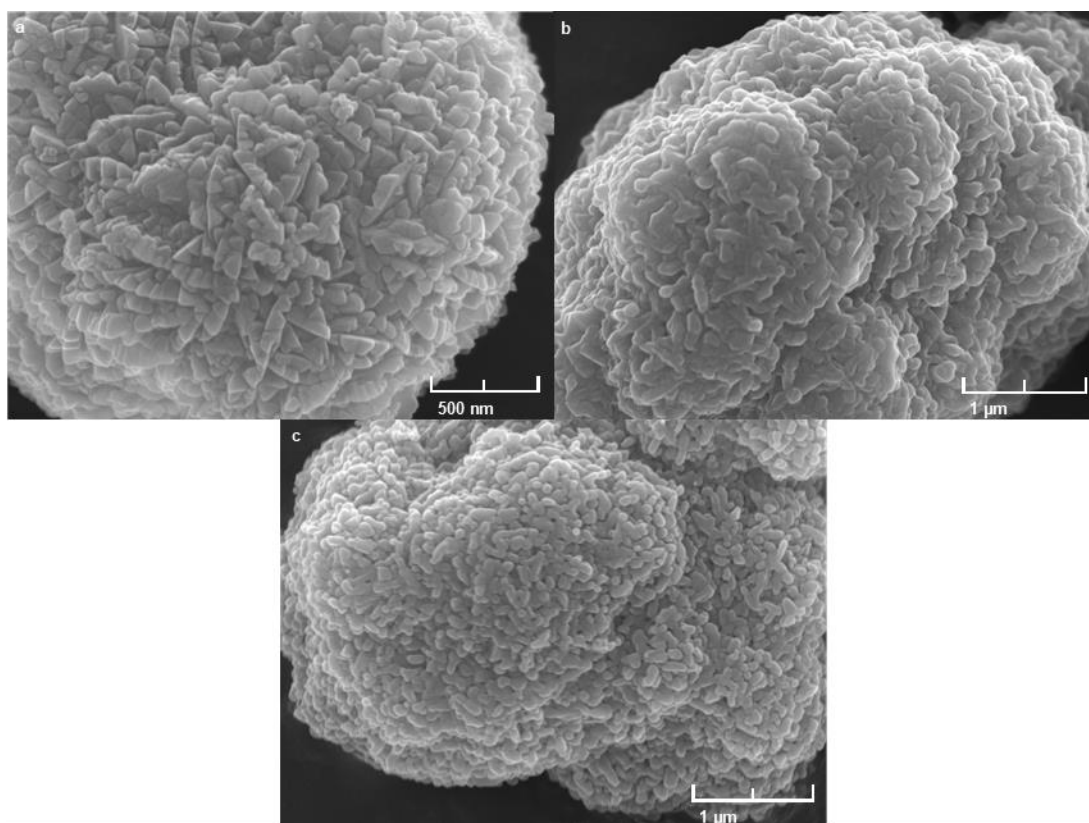


Figure 2.41: SEM images of uncoated zinc sulfides treated with silica coating method without the addition of tetraethoxysilane exposed to different conditions: a) nitrogen at 800 °C, b) stored in vial, c) air at 800 °C.

Table 2.17: Atomic% data from EDX analysis of uncoated zinc sulfides exposed to different conditions.

Element	Nitrogen at 800 °C			Air at 25 °C	Air at 800 °C
	Map	Site 1	Site 2	Map	Map
Zinc	38.1	46.7	47.4	43.7	38.2
Sulfur	36.9	50.1	45.2	42.7	1.9
Oxygen	24.6	3.0	7.0	13.3	59.6
Silicon	0.4	0.2	0.3	0.3	0.4

Altering the accelerating voltage of the electron beam gave insight into the extent of the zinc sulfide oxidation. Both EDX mapping (Appendix Figure 6.18) and atomic% data (Table 2.18) confirmed the complete conversion of the zinc sulfide. EDX sulfur maps showed only noise, with no degree of sulfur localisation on the particle at any of the accelerating voltages used. Atomic% data displayed a consistently low concentration of sulfur, and only showed a minor increase at 30 kV. However, as this also occurred with a decrease in the zinc concentration, it was believed to be noise as more of the carbon disc background is probed.

Chapter 2. Synthesis and Characterisation of Zinc Sulfide Phosphors

Table 2.18: Atomic% data for non-silica coated zinc sulfide exposed to flowing air at 800 °C at different accelerating voltages.

Element	5 kV	15 kV	30 kV
Zinc	47.1	45.2	28.0
Sulfur	1.0	0.7	1.7
Oxygen	51.1	53.9	70.0
Silicon	0.8	0.2	0.4

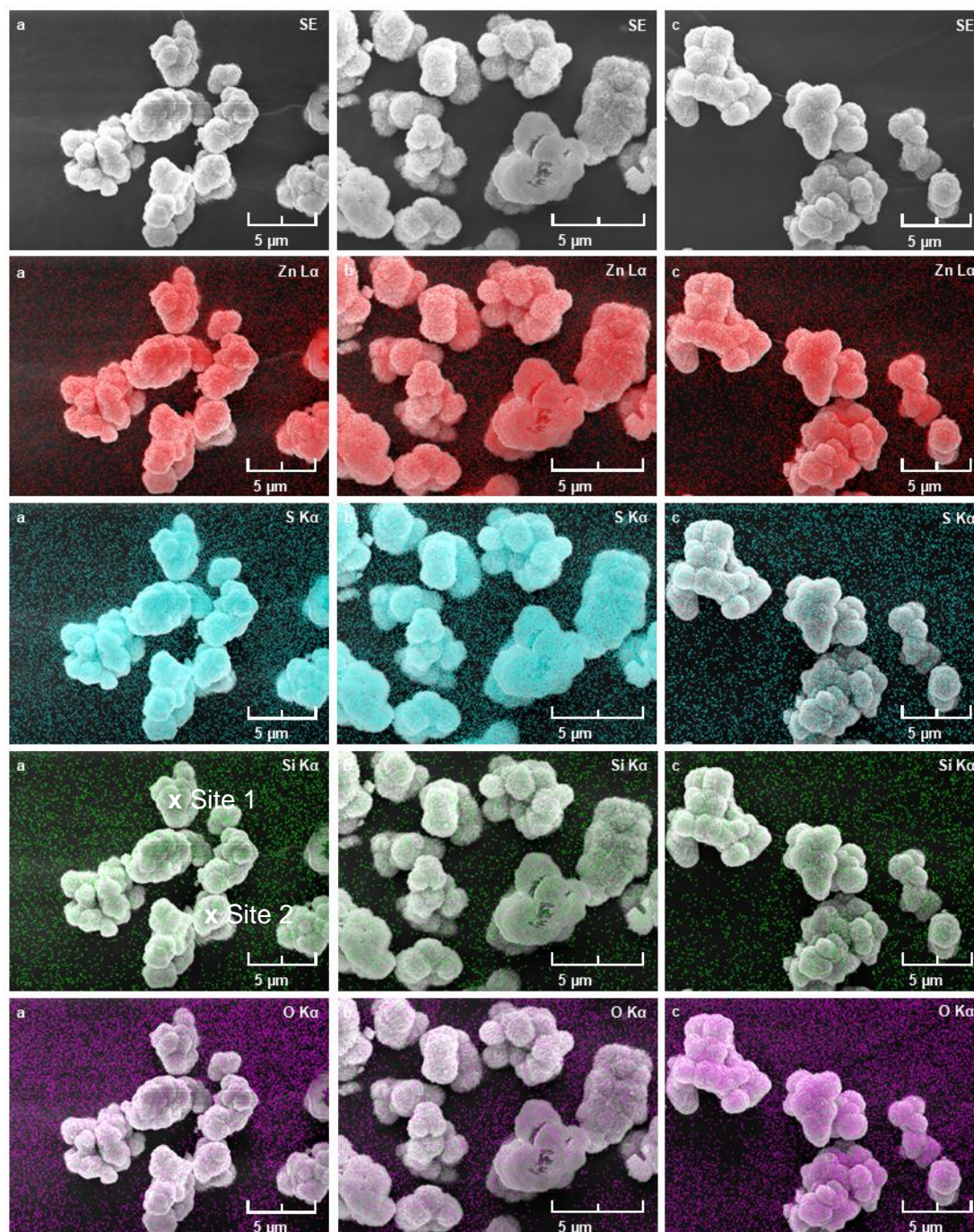


Figure 2.42: SEM and EDX images of uncoated zinc sulfides treated with silica coating method without the addition of tetraethoxysilane exposed to different conditions: a) nitrogen at 800 °C, b) stored in a vial, c) air at 800 °C showing contributions from zinc, sulfur, silicon, and oxygen.

2.4.6.2 Silica Coated Zinc Sulfide

The morphology of silica coated zinc sulfides was expectedly different to the non-coated samples exposed to the same conditions (Figure 2.43). Whilst the large, aggregated particles had not meaningfully changed in shape or size and ranged from $2 \times 2 \mu\text{m}$ to $5 \times 5 \mu\text{m}$, the smaller fused particles had, becoming rounded cubes of 150×150 and ovoids of 200×100 nm. Pleasingly, the sample prepared

Chapter 2. Synthesis and Characterisation of Zinc Sulfide Phosphors

without exposure to the furnace did not have a meaningful change in morphology compared to the heat-treated samples, unlike the non-coated samples. Because the only difference between these samples and the uncoated zinc sulfides was the addition of tetraethoxysilane it seemed reasonable to ascribe the differences to the formation of a passivating silica shell upon the surface of the particles. In addition to coating the zinc sulfides, spheres of silica that varied from 100 nm in diameter up to 700 nm were also present across the surface of the particles.

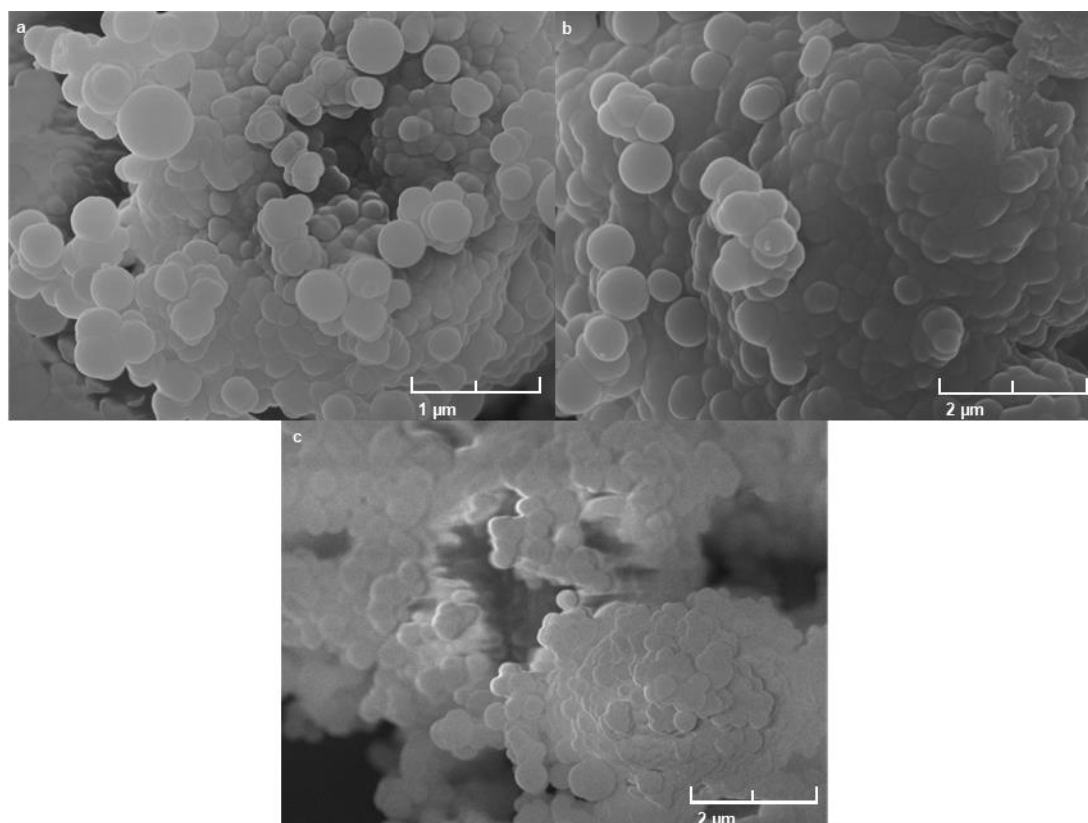


Figure 2.43: SEM images of silica coated zinc exposed to different conditions: a) nitrogen at 800 °C, b) stored in vial, c) air at 800 °C.

EDX mapping (Figure 2.44) showed, for all samples, zinc and sulfur localisation towards the interior of the particle, with the outside edges being devoid of these elements, with no areas of deficiency observed across the particle (except for the oxidised sample). Silicon, however, was present across the entirety of the particle, and was particularly strong for the room temperature sample. The nitrogen sample displayed an increased concentration of silicon towards the outer edges of the sample, which suggested the silica coverage had either been reduced by the temperature, due to rupturing of the silica, or was just poorer in this area. Oxygen expectedly aligned with silicon, although once again weaker than zinc and sulfur for the nitrogen sample. The room temperature sample exhibited oxygen across the entire particle, in a similar concentration as both sulfur and zinc. The oxidised sample displayed poor quality data, displaying areas that were unaccounted for by

Chapter 2. Synthesis and Characterisation of Zinc Sulfide Phosphors

any element, which persisted across all areas examined and upon analysing a new sample. However, the same trends were clear, with silicon and oxygen extending to the edges of the sample while zinc and sulfur were present in high concentrations towards the centre of the particle.

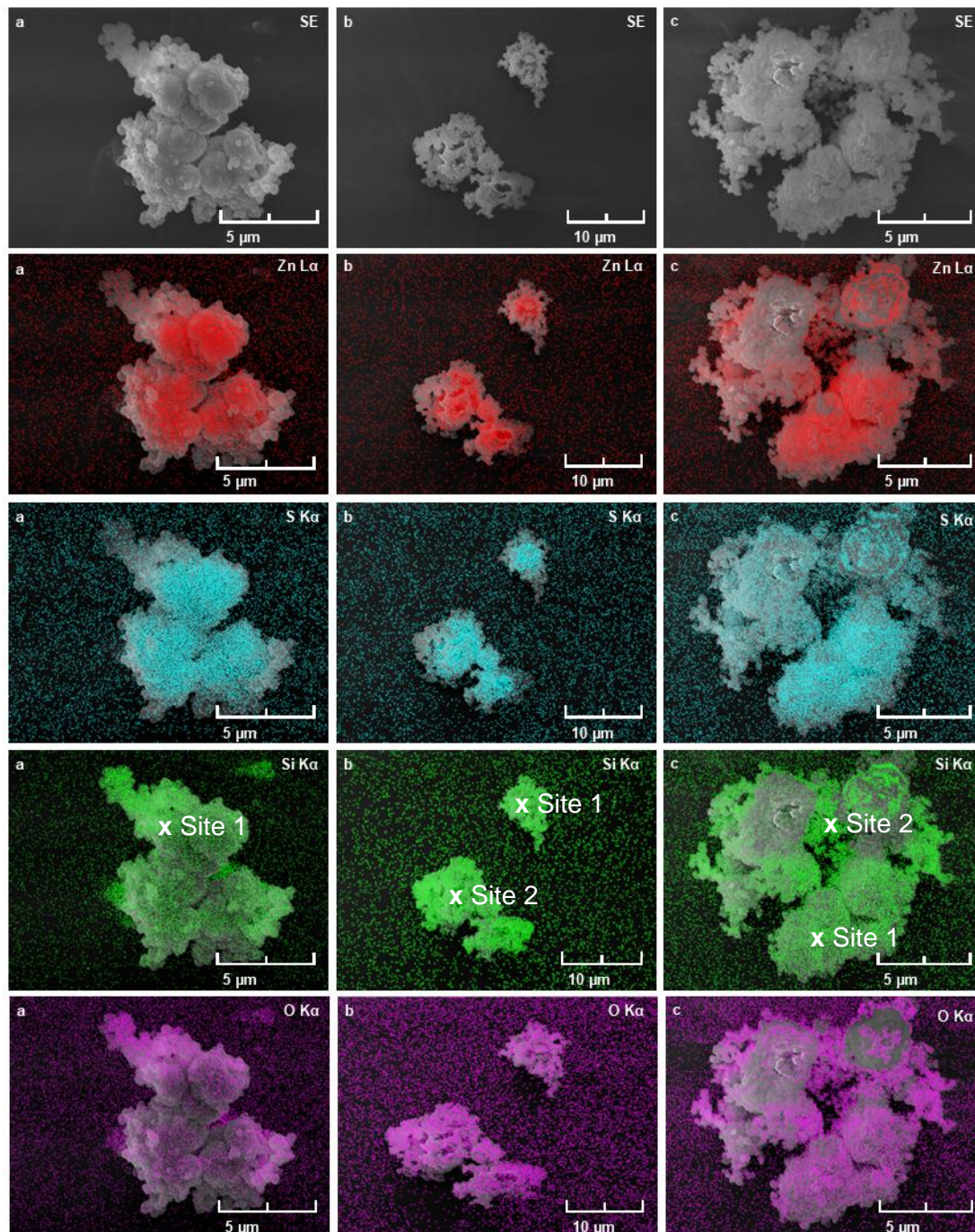


Figure 2.44: Silica coated zinc sulfides exposed to different conditions: a) nitrogen at 800 °C, b) air at room temperature, c) air at 800 °C showing contributions from zinc, sulfur, silicon, and oxygen.

Atomic% data (Table 2.19) of the EDX maps for the non-oxidising conditions showed similar relative concentrations of both zinc and sulfur. However, a difference was observed for the sample fired in air and suggested some oxidation of the

Chapter 2. Synthesis and Characterisation of Zinc Sulfide Phosphors

sample had occurred. All point analysis locations chosen displayed a deficiency of sulfur with respect to zinc, which suggested some degree of oxidation had occurred for all the samples. However, as samples prepared in an analogous manner without the addition of TEOS, and zinc sulfides prepared without exposure to water, and ammonia displayed similar results this may be random chance as mapping data did not support oxidation of all samples. Interestingly the silicon concentration for all three samples showed only slight differences with respect to zinc concentration and suggested the different treatments methods had little effect on the silica shells. Point analysis confirmed the concentration of silica is lower towards the centre of the particle, as Site 1 for the nitrogen sample exhibited a doubling of zinc and sulfur and a decrease in the silicon concentration, with similar results observed for the room temperature sample. In contrast to the uncoated sample, an oxidising atmosphere caused a minor reduction in the ratio of zinc and sulfur indicating only minor oxidation of the sample had occurred.

Table 2.19: Atomic% data for silica coated zinc sulfides exposed to different conditions.

Element	Nitrogen at 800 °C		Air at 25 °C			Air at 800 °C		
	Map	Site 1	Map	Site 1	Site 2	Map	Site 1	Site 2
Zinc	13.1	27.7	9.5	4.7	23.0	13.9	28.6	24.0
Sulfur	13.2	23.8	8.6	2.3	27.7	10.3	22.3	20.2
Oxygen	60.0	39.6	71.9	68.2	36.9	64.6	40.4	46.8
Silicon	13.7	9.0	10.0	24.8	12.4	11.1	8.7	9.1

To further explore the impact of the silica coating, three accelerating voltages were used to probe the depth of oxidation. Because 5 kV (a) should only provide surface information it was expected that silicon and oxygen would dominate the map with minor contributions from zinc and sulfur. Gratifyingly, this was observed (Figure 2.45), with only minor differences in the zinc and sulfur ratio that showed close agreement with zinc sulfides prepared under non-oxidising conditions. With silicon and oxygen present in much higher concentrations with no obvious areas of localisation. Atomic% data (Table 2.20) showed, as expected, zinc and sulfur accounted for only a small proportion of the particle with silica comprising most of the particle at this depth. The relatively large difference between zinc and sulfur, suggested the presence of zinc oxide at this depth. Point analysis (Site 1), however, indicated that the oxidation may not have been consistent across the sample, presumably due to differences in the extent of the silica collating. Increasing the accelerating voltage to 15 kV, increased both the zinc and sulfur contribution to the maps and decreased the silica contribution. As before, both sites exhibited an

Chapter 2. Synthesis and Characterisation of Zinc Sulfide Phosphors

excess of zinc which was presumed to oxidation. At an accelerating voltage of 30 kV, the map data displayed a significant decrease in the sulfur concentration, while the point analysis sites showed zinc and sulfur in similar concentrations. Therefore, the surface of the zinc sulfide particle was determined to be overwhelmingly silica with a core of zinc sulfide that had experienced little to no oxidation in contrast to the non-coated particle that was completely converted to zinc oxide with no discernible zinc sulfide even at 30 kV.

Table 2.20: Atomic% data for silica coated zinc sulfides exposed to air at 800 °C at different accelerating voltages

Element	5 kV			15 kV			30 kV		
	Map	Site 1	Site 2	Map	Site 1	Site 2	Map	Site 1	Site 2
Zinc	7.9	13.2	1.5	13.9	28.6	24.0	15.3	20.2	16.1
Sulfur	3.5	10.0	0.7	10.3	22.3	20.2	4.5	21.1	19.6
Oxygen	66.1	51.9	70.8	64.6	40.4	46.8	67.2	51.1	55.3
Silicon	22.5	24.9	27.0	11.1	8.7	9.1	12.9	8.6	9.1

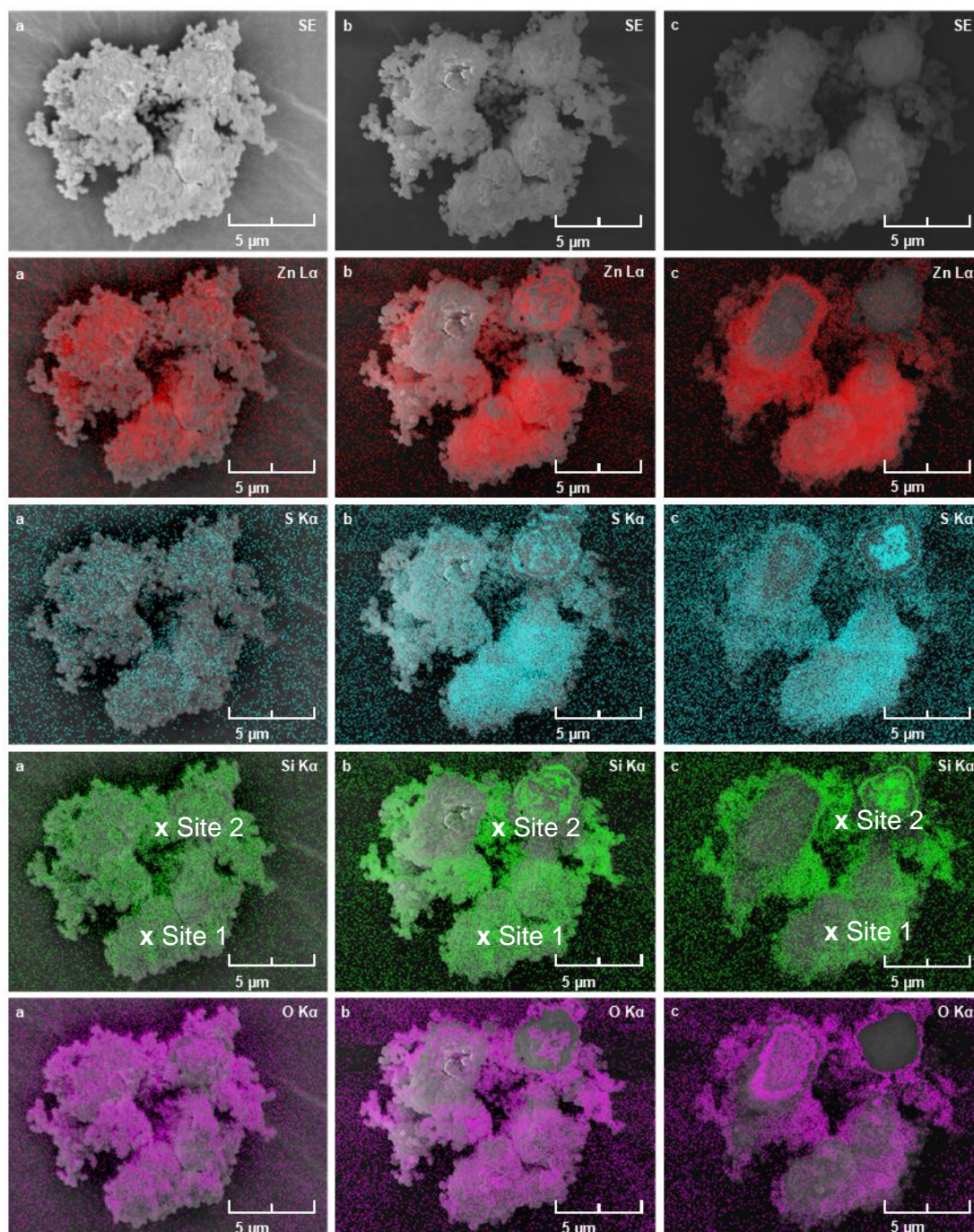


Figure 2.45: SEM and EDX images of silica coated zinc sulfides heat treated at 800 °C in air at difference accelerating voltages: a) 5kV, b) 15 kV, c) 30 kV showing contributions from zinc, sulfur, silicon, and oxygen.

2.5 Conclusion

2.5.1 Determination and Assignment of Defects Within Doped Zinc Sulfides

2.5.1.1 Experimental analysis

A series of doped zinc sulfides have been prepared with varying dopants and conditions to explore and elucidate the origins of the most commonly observed

emission within the literature. Aluminium doped samples displayed emission at 458 and 520 nm, with selective emission at 520 nm achieved by excitation at 410 nm. The origins of the emissions were assigned to zinc vacancies and interstitial defects respectively. Copper(II) sulfate doping produced a single broad emission at 493 nm. Whereas copper(I) iodide generated two defects with emission at 455 and the aforementioned 493 nm emission. Addition of ammonium chloride along with copper(I) iodide produced a single emission profile with peaks at 470 and 520 nm. Modifying the procedure with a wet impregnation technique caused no discernible differences in the emission spectra for samples doped with a metal or halide. However, performing the same procedure without a dopant resulted in defects with emission at 495 and 600 nm. These emissions were assigned to sulfur vacancies and interstitial defects, respectively. Surprisingly, the long-lived emission – visible to the naked eye – often noted for copper doped zinc sulfides was not observed.

2.5.1.2 Computational analysis

The assignment of these transitions was supported through computational periodic calculations using the Quantum Espresso and Yambo packages. Optimisation of the undoped 64 atom zinc sulfide supercell using a variable cell relaxation procedure and the PBEsol functional, showed a reduction in the lattice parameter compared to experimental determination. Similarly, structure optimisation was performed on 65 and 63 atom supercells for interstitial and vacancy defects respectively. Interstitial sulfur and vacancy defects exhibited an increase and reduction in the lattice parameters, respectively, while the equivalent zinc defects exhibited the opposite trend. Initial band structure and density of states calculations were performed using the general gradient approach but were found to significantly underestimate the band gaps of all the samples. Further analysis using non-self-consistent GW calculations was performed with and without the Bruneval-Gonze (BG) approach. Calculations using the BG method resulted in a zinc sulfide band gap of 3.53 eV that agreed with previous literature reports for both computational and experimental results. Applying this method to the defects resulted in both zinc defects showing band gaps similar to experimentally derived values while the sulfur defects were underpredicted. Calculations without the BG method followed the same trend but generated band gaps of lower energies. Further work could be carried out using larger supercells to more accurately model the experimental systems as well as using a self-consistent GW method or a full frequency approach to achieve band gaps closer to experimental values at convergence.

2.5.2 Doping of Zinc Sulfides with Group 2 Metals and Manganese

Doping of zinc sulfides was also performed with the Group 2 metals barium, strontium, and calcium. Introduction of barium caused the formation of zinc defects with emission at 450 and 518 nm. As with the aluminium doped sample, selective green emission could be achieved by exciting at energies lower than 410 nm. Strontium exhibited a single emission at 493 nm due to the presence of sulfur vacancies. Calcium however, produced a range of emissions that were believed to be caused by a range of zinc and sulfur defects across most of the visible region. Co-doping of these metals with manganese in zinc sulfides was also explored. Depending upon the source of manganese used, the proportion of phases present in the material was observed to change. Manganese nitrate resulted in a system that was determined to contain a significant wurtzite phase, whereas an oxide source showed a significant reduction in the wurtzite phase. The wurtzite phase was also found to be dependent upon the amount of barium dopant added. In addition to the zinc sulfide phases, a third Ba_2ZnS_3 phase was also observed. This new phase gave rise to the red shifted manganese emission to 620 nm, that blue shifted as the barium concentration decreased, due to the stronger contribution from manganese doped zinc sulfide. Strontium co-doping did not exhibit a red shift in the emission, and only some broadening of the emission was observed, along with blue and green emission that was assigned to zinc defects. Calcium doping only showed a yellow emission at 584 nm that was assigned to the manganese emission within a zinc sulfide host.

2.5.3 Silica Coating of Zinc Sulfides

Silica coating of zinc sulfides was also performed and was shown to significantly reduce the oxidation of the zinc sulfide, at 800 °C in flowing air, to zinc oxide. Such that only the surface of the particle was observed to undergo moderate oxidation, with the bulk of the particle remaining as zinc sulfide.

Table 2.21: Recommended dopants to achieve the desired emission wavelengths outlined during the aims section

Desired Emission Wavelength (nm)	Achieved Emission Wavelength (nm)	Dopant(s)
460	454	1.15 mg CuI
530	518	70 mg BaS
620	620	140 mg BaS, 7.1 mg MnO

2.6 References

- 1 A. Abounadi, M. Di Blasio, D. Bouchara, J. Calas, M. Averous, O. Briot, N. Briot, T. Cloitre, R. L. Aulombard and B. Gil, *Phys. Rev. B*, 1994, **50**, 11677–11683.
- 2 B. Y. Geng, X. W. Liu, Q. B. Du, X. W. Wei and L. D. Zhang, *Appl. Phys. Lett.*, 2006, **88**, 163104.
- 3 D. Theis, *Journal of Physics and Chemistry of Solids*, 1977, **38**, 1125–1129.
- 4 S. D. Scott and H. L. Barnes, *Geochimica et Cosmochimica Acta*, 1972, **36**, 1275–1295.
- 5 Z.-G. Chen, L. Cheng, H.-Y. Xu, J.-Z. Liu, J. Zou, T. Sekiguchi, G. Q. (Max) Lu and H.-M. Cheng, *Advanced Materials*, 2010, **22**, 2376–2380.
- 6 Y. Liang, H. Liang, X. Xiao and S. Hark, *J. Mater. Chem.*, 2011, **22**, 1199–1205.
- 7 S. Park, S. An, H. Ko, S. Lee and C. Lee, *Sensors and Actuators B: Chemical*, 2013, **188**, 1270–1276.
- 8 A. K. Kole, C. S. Tiwary and P. Kumbhakar, *J. Mater. Chem. C*, 2014, **2**, 4338–4346.
- 9 S. S. Boxi and S. Paria, *RSC Adv.*, 2014, **4**, 37752–37760.
- 10 R. Bowers and N. T. Melamed, *Phys. Rev.*, 1955, **99**, 1781–1787.
- 11 A. A. Bol, J. Ferwerda, J. A. Bergwerff and A. Meijerink, *Journal of Luminescence*, 2002, **99**, 325–334.
- 12 A. A. Khosravi, M. Kundu, L. Jatwa, S. K. Deshpande, U. A. Bhagwat, M. Sastry and S. K. Kulkarni, *Appl. Phys. Lett.*, 1995, **67**, 2702–2704.
- 13 W. Q. Peng, G. W. Cong, S. C. Qu and Z. G. Wang, *Optical Materials*, 2006, **29**, 313–317.
- 14 Ch. S. Kamal, R. K. Mishra, D. K. Patel, K. R. Rao, V. Sudarsan and R. K. Vatsa, *Materials Research Bulletin*, 2016, **81**, 127–133.
- 15 C. Corrado, Y. Jiang, F. Oba, M. Kozina, F. Bridges and J. Z. Zhang, *J. Phys. Chem. A*, 2009, **113**, 3830–3839.
- 16 F. A. Kröger and H. J. Vink, *J. Chem. Phys.*, 1954, **22**, 250–252.
- 17 L. He, L. Yang, B. Liu, J. Zhang, C. Zhang, S. Liu, S. Chen, J. A. Zapien, K. A. Alamry, A. M. Asiri, K. Zhang and S. Wang, *Journal of Alloys and Compounds*, 2019, **787**, 537–542.
- 18 H. Chander, V. Shanker, D. Haranath, S. Dudeja and P. Sharma, *Materials Research Bulletin*, 2003, **38**, 279–288.
- 19 M. Sharma, S. Sen, J. Gupta, M. Ghosh, S. Pitale, V. Gupta and S. C. Gadkari, *Journal of Materials Research*, 2018, **33**, 3963–3970.
- 20 E. Hao, Y. Sun, B. Yang, X. Zhang, J. Liu and J. Shen, *Journal of Colloid and Interface Science*, 1998, **204**, 369–373.
- 21 R. N. Bhargava, D. Gallagher, X. Hong and A. Nurmikko, *Phys. Rev. Lett.*, 1994, **72**, 416–419.
- 22 H.-E. Gumlich, *Journal of Luminescence*, 1981, **23**, 73–99.
- 23 P. Thiyagarajan, M. Kottaisamy, K. Sethupathi and M. S. R. Rao, *Displays*, 2009, **30**, 202–204.
- 24 Y. Y. Chen, J. G. Duh, B. S. Chiou and C. G. Peng, *Thin Solid Films*, 2001, **392**, 50–55.
- 25 D. Son, D.-R. Jung, J. Kim, T. Moon, C. Kim and B. Park, *Appl. Phys. Lett.*, 2007, **90**, 101910.
- 26 W. Chamorro, T. S. Shyju, P. Boulet, S. Migot, J. Ghanbaja, P. Miska, P. Kuppusami and J. F. Pierson, *RSC Adv.*, 2016, **6**, 43480–43488.
- 27 J. Z. Liu, P. X. Yan, G. H. Yue, J. B. Chang, D. M. Qu and R. F. Zhuo, *J. Phys. D: Appl. Phys.*, 2006, **39**, 2352–2356.
- 28 X. Zeng, S. Yan, J. Cui, H. Liu, J. Dong, W. Xia, M. Zhou and H. Chen, *J Nanopart Res.*, DOI:10.1007/s11051-015-3000-y.

- 29 M. Wang, L. Sun, X. Fu, C. Liao and C. Yan, *Solid State Communications*, 2000, **115**, 493–496.
- 30 R. Kripal, A. K. Gupta, S. K. Mishra, R. K. Srivastava, A. C. Pandey and S. G. Prakash, *Spectrochimica Acta Part A: Molecular and Biomolecular Spectroscopy*, 2010, **76**, 523–530.
- 31 P. Giannozzi, S. Baroni, N. Bonini, M. Calandra, R. Car, C. Cavazzoni, D. Ceresoli, G. L. Chiarotti, M. Cococcioni, I. Dabo, A. D. Corso, S. de Gironcoli, S. Fabris, G. Fratesi, R. Gebauer, U. Gerstmann, C. Gougoussis, A. Kokalj, M. Lazzeri, L. Martin-Samos, N. Marzari, F. Mauri, R. Mazzarello, S. Paolini, A. Pasquarello, L. Paulatto, C. Sbraccia, S. Scandolo, G. Sclauzero, A. P. Seitsonen, A. Smogunov, P. Umari and R. M. Wentzcovitch, *J. Phys.: Condens. Matter*, 2009, **21**, 395502.
- 32 P. Giannozzi, O. Baseggio, P. Bonfà, D. Brunato, R. Car, I. Carnimeo, C. Cavazzoni, S. de Gironcoli, P. Delugas, F. Ferrari Ruffino, A. Ferretti, N. Marzari, I. Timrov, A. Urru and S. Baroni, *J. Chem. Phys.*, 2020, **152**, 154105.
- 33 P. Giannozzi, O. Andreussi, T. Brumme, O. Bunau, M. B. Nardelli, M. Calandra, R. Car, C. Cavazzoni, D. Ceresoli, M. Cococcioni, N. Colonna, I. Carnimeo, A. D. Corso, S. de Gironcoli, P. Delugas, R. A. DiStasio, A. Ferretti, A. Floris, G. Fratesi, G. Fugallo, R. Gebauer, U. Gerstmann, F. Giustino, T. Gorni, J. Jia, M. Kawamura, H.-Y. Ko, A. Kokalj, E. Küçükbenli, M. Lazzeri, M. Marsili, N. Marzari, F. Mauri, N. L. Nguyen, H.-V. Nguyen, A. Otero-de-la-Roza, L. Paulatto, S. Poncé, D. Rocca, R. Sabatini, B. Santra, M. Schlipf, A. P. Seitsonen, A. Smogunov, I. Timrov, T. Thonhauser, P. Umari, N. Vast, X. Wu and S. Baroni, *J. Phys.: Condens. Matter*, 2017, **29**, 465901.
- 34 D. Sangalli, A. Ferretti, H. Miranda, C. Attaccalite, I. Marri, E. Cannuccia, P. Melo, M. Marsili, F. Paleari, A. Marrazzo, G. Prandini, P. Bonfà, M. O. Atambo, F. Affinito, M. Palumbo, A. Molina-Sánchez, C. Hogan, M. Grüning, D. Varsano and A. Marini, *J. Phys.: Condens. Matter*, 2019, **31**, 325902.
- 35 A. Marini, C. Hogan, M. Grüning and D. Varsano, *Computer Physics Communications*, 2009, **180**, 1392–1403.
- 36 L.-D. Yuan, H.-X. Deng, S.-S. Li, S.-H. Wei and J.-W. Luo, *Phys. Rev. B*, 2018, **98**, 245203.
- 37 M. Rohlfing, P. Krüger and J. Pollmann, *Phys. Rev. B*, 1998, **57**, 6485–6492.
- 38 W. Luo, S. Ismail-Beigi, M. L. Cohen and S. G. Louie, *Phys. Rev. B*, 2002, **66**, 195215.
- 39 Brain. J. Skinner, *Am. Mineral.*, 1961, **46**, 1399–1411.
- 40 B. K. Agrawal, P. S. Yadav and S. Agrawal, *Phys. Rev. B*, 1994, **50**, 14881–14887.
- 41 D. R. Hamann, *Phys. Rev. B*, 2013, **88**, 085117.
- 42 M. J. van Setten, M. Giantomassi, E. Bousquet, M. J. Verstraete, D. R. Hamann, X. Gonze and G.-M. Rignanese, *Computer Physics Communications*, 2018, **226**, 39–54.
- 43 J. P. Perdew, A. Ruzsinszky, G. I. Csonka, O. A. Vydrov, G. E. Scuseria, L. A. Constantin, X. Zhou and K. Burke, *Phys. Rev. Lett.*, 2008, **100**, 136406.
- 44 H. J. Monkhorst and J. D. Pack, *Phys. Rev. B*, 1976, **13**, 5188–5192.
- 45 Y. Hinuma, G. Pizzi, Y. Kumagai, F. Oba and I. Tanaka, *Computational Materials Science*, 2017, **128**, 140–184.
- 46 P. Li, S. Deng, L. Zhang, G. Liu and J. Yu, *Chemical Physics Letters*, 2012, **531**, 75–79.
- 47 A. Torabi and V. N. Staroverov, *J. Phys. Chem. Lett.*, 2015, **6**, 2075–2080.
- 48 B. Khamala, L. Franklin, Y. Malozovsky, A. Stewart, H. Saleem and D. Bagayoko, *Computational Condensed Matter*, 2016, **6**, 18–23.
- 49 D.-K. Seo and R. Hoffmann, *Theoretical Chemistry Accounts: Theory, Computation, and Modeling (Theoretica Chimica Acta)*, 1999, **102**, 23–32.

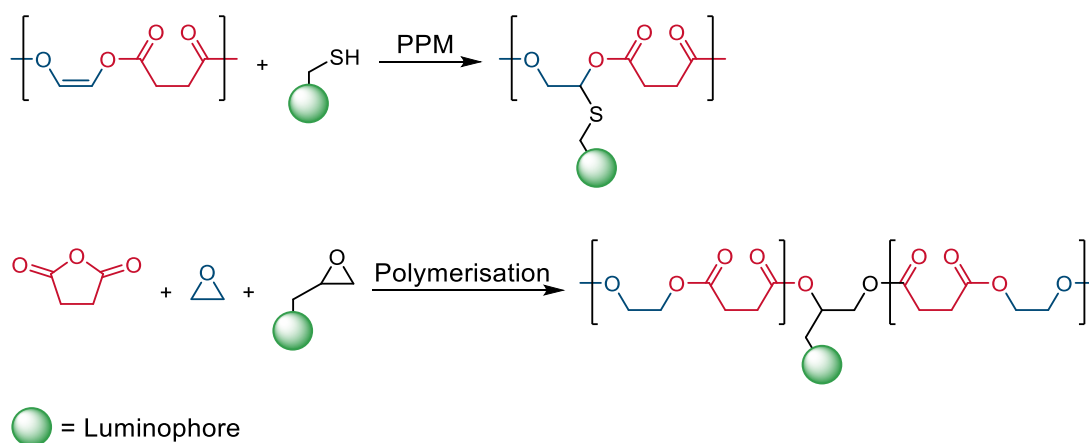
- 50 J. M. E. Fernández and A. M. Abietar, *Procedia Computer Science*, 2011, **7**, 231–232.
- 51 W. Chen, G. McLendon, A. Marchetti, J. M. Rehm, M. I. Freedhoff and C. Myers, *J. Am. Chem. Soc.*, 1994, **116**, 1585–1586.
- 52 A. R. Zanatta, *Sci Rep*, 2019, **9**, 11225.
- 53 A. Fleszar and W. Hanke, *Phys. Rev. B*, 2005, **71**, 045207.
- 54 H. Dixit, R. Saniz, D. Lamoén and B. Partoens, *J. Phys.: Condens. Matter*, 2010, **22**, 125505.
- 55 O. Zakharov, A. Rubio, X. Blase, M. L. Cohen and S. G. Louie, *Phys. Rev. B*, 1994, **50**, 10780–10787.
- 56 M. Shishkin and G. Kresse, *Phys. Rev. B*, 2007, **75**, 235102.
- 57 T. Kotani and M. van Schilfgaarde, *Solid State Communications*, 2002, **121**, 461–465.
- 58 F. Bruneval and X. Gonze, *Phys. Rev. B*, 2008, **78**, 085125.
- 59 L. A. Xue and R. Raj, *Journal of the American Ceramic Society*, 1989, **72**, 1792–1796.
- 60 M. T. Sebastian and P. Krishna, *Pramana - J Phys*, 1984, **23**, 395–403.
- 61 Y. Li, W. Tan and Y. Wu, *Journal of the European Ceramic Society*, 2020, **40**, 2130–2140.
- 62 P. Thiyagarajan, M. Kottaisamy and M. S. R. Rao, *J. Phys. D: Appl. Phys.*, 2006, **39**, 2701–2706.
- 63 J. Wang and M. Isshiki, in *Springer Handbook of Electronic and Photonic Materials*, eds. S. Kasap and P. Capper, Springer US, Boston, MA, 2006, pp. 325–342.
- 64 C. W. Raubach, A. F. Gouveia, Y. V. B. de Santana, J. A. Varela, M. M. Ferrer, M. S. Li and E. Longo, *J. Mater. Chem. C*, 2014, **2**, 2743–2750.
- 65 W. Chen, R. Sammynaiken, Y. Huang, J.-O. Malm, R. Wallenberg, J.-O. Bovin, V. Zwiller and N. A. Kotov, *Journal of Applied Physics*, 2001, **89**, 1120–1129.
- 66 C. J. Duan, A. C. A. Delsing and H. T. Hintzen, *Chem. Mater.*, 2009, **21**, 1010–1016.
- 67 D. M. Sousa, L. C. Alves, A. Marques, G. Gaspar, J. C. Lima and I. Ferreira, *Scientific Reports*, 2018, **8**, 15992.
- 68 Y.-F. Lin, Y.-H. Chang, Y.-S. Chang, B.-S. Tsai and Y.-C. Li, *Journal of Alloys and Compounds*, 2006, **421**, 268–272.

3 Luminophore Design, Synthesis, and Characterisation

Chapter 3. Luminophore Design, Synthesis, and Characterisation

3.1 Aims

This research described in this chapter demonstrates the synthesis and describes the photophysical properties of a set of luminophores or chromophores, that were suitably functionalised to enable incorporation within a polymer system to serve as a proof of concept for the creation of polymer LEDs. Therefore, it was vital these functional groups were amenable to either post-polymerisation modification (PPM), eg. a thiol-ene Click reaction, or addition to a ROCOP reaction through an epoxide group (Scheme 3.1). The method of incorporation imposes constraints upon the structure of the luminophore or chromophore, beyond that of the functional group required for the incorporation of the dopant. For example, if co-polymerisation of the dopant is desired, then the luminophore/chromophore should, ideally, not contain hydroxy or carboxylic groups as these can act as initiators for the polymerisation – producing polymer chains of lower molecular weights than desired and lowering the number of dopants per polymer chain. Similarly, the luminophore should not be able to strongly bind to the catalyst such that it severely limits the rate of polymerisation, nor displaces the pre-existing ligands of the catalyst. However, in the case of the catalyst used within this work, such an issue is mitigated by using a tetradentate salen ligand (Chapter 4). Secondly, the introduction of the functional group required for the incorporation of the dopant should not significantly alter the desired photophysical properties of the luminophore, such as shifting the absorption and emission wavelengths, or lowering the quantum yield.



Scheme 3.1: Proposed synthetic routes for functionalised polymers; post polymerisation modification (PPM), with a thiol-ene Click example given; and the direct polymerisation of the luminophore during the polymerisation.

3.2 Introduction

Coloured plastics are a constant part of modern day life; being used in packaging, toys, decorative objects, and clothing.¹ In order to ensure the longevity of the

Chapter 3. Luminophore Design, Synthesis, and Characterisation

product it is desirable that the chromophore has colour fast properties, thereby retaining the original colour throughout the lifetime of the product. With regard to the majority of plastics encountered in everyday life: poly(propylene), poly(ethylene), poly(ethylene terephthalate), poly(vinyl chloride), etc. the chromophore cannot typically be chemically bonded with the polymer substrate as is the case for many natural fibres, e.g., cotton. Thus, the chromophore is used as an additive and not chemically bound to the material. Although some dyes are soluble within the polymer and less likely to migrate towards the surface of the material, many are insoluble in the polymer,² resulting in the additive leaching into the environment.³ However, if the chromophore was directly incorporated within the polymer, i.e., chemically bound, the chromophore would be unable to leach into the environment and the material would retain its colour in perpetuity. Whilst the direct incorporation of a chromophore into conventional plastics has been demonstrated within the literature,⁴ these plastics are difficult to recycle in an efficient manner,⁵ whereas, poly(esters), such as poly(ethylene terephthalate), are readily recyclable.^{6,7} Therefore, a polymerisation technique that produces esters and allows a straightforward synthetic pathway to prepare monomers capable of polymerisation is ideal. Ring-opening co-polymerisation of epoxides and anhydrides is one such example. Modification of these polymers to incorporate additional functionality has been demonstrated within the literature using post-polymerisation techniques, such as the thiol-ene click reaction.⁸ However, direct incorporation using an epoxide functionalised chromophore has, so far, not been explored within the literature.

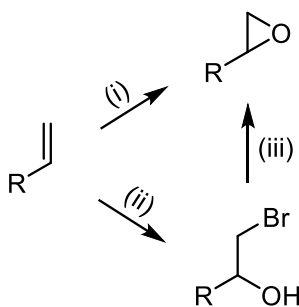
3.2.1 Epoxides

Epoxides are three-membered cyclic ethers comprising one oxygen and two carbon atoms. Epoxides have a wide variety of uses, from chemical intermediates,⁹ to epoxy resins,¹⁰ and polymers through the ring-opening co-polymerisation of anhydrides and epoxides (ROCOP).¹¹ It is this specific application, the synthesis of monomers for ROCOP, that is the focus of this chapter. Whilst a vast library of work exists on ROCOP polymers (Chapter 4), no current literature report exists on the creation of functionalised copolymers through the introduction of a dopant amount of a third monomer, in effect creating a terpolymer that has almost identical characteristics to the parent copolymer other than the specific property introduced by the dopant. Specifically, luminophores and/or chromophores are of particular interest for two reasons. Firstly, incorporation of chromophore monomers is easily demonstrated through both a colour change and luminescence spectroscopy, showing a proof-of-concept design. Secondly, the formation of coloured materials is

Chapter 3. Luminophore Design, Synthesis, and Characterisation

essential for the further application of ROCOP polymers as replacements for the plastics currently used throughout the world. Current recycling technologies are unable to completely separate the colourant additive from the bulk polymer, causing contamination of products made with recycled polymer.¹² In the case of black plastics, which usually use carbon black as a pigment, are undetectable by the automated systems, increasing waste.^{12,13} Additionally, since the dopant is directly incorporated into the polymer backbone, leaching of the functionalising component(s), that has been reported for traditional additive incorporation,^{3,14} would not be an issue, improving stability and safety of the material.

Epoxides are commonly synthesised in one of two ways (Scheme 3.2): either direct oxidation (i), or through formation of a halohydrin (ii), followed by a ring closure in the presence of a base e.g., potassium hydroxide (iii).



Scheme 3.2: Pathways for the synthesis of epoxides. (i) oxidant (H₂O₂, m-CPBA, etc); (ii) NBS, water; (iii) Base

The luminophores/chromophores selected for epoxide functionalisation require a set of key features. Foremost is the ability to be functionalised without adversely influence the photophysical properties, such that the material no longer functions as the desired luminophore/chromophore. Secondly, the dopant cannot have functional groups that will degrade the catalyst, or act as a catalyst itself, resulting in a less predictable range of polymer molecular weights. For that reason, metal complexes are undesirable choices, as are pendant hydroxy, other acidic groups, and amines. Ease of functionalisation is also a desirable property. In addition to doping of the polymerisation, post-polymerisation modification (PPM) is an alternative pathway to functionalised materials. As the name implies, modification occurs after the production of the polymer, and therefore, affords a greater degree of flexibility in the dopant. Whilst such a route would allow the incorporation of luminophores/chromophores with functional groups that are not tolerated during the polymerisation, it generates a burden upon the polymerisation. i.e. the monomers used must contain functional groups that can be used for further reactivity, or be themselves, doped into the polymerisation. Once such example of this is the thiol-

Chapter 3. Luminophore Design, Synthesis, and Characterisation

ene reaction, that combines a thiol and an alkene in a thiol-ene Click reaction.¹⁵ Earlier work within the group has shown epoxide variations are incorporated much more readily than anhydrides, thus novel anhydrides will not be discussed in this chapter.

3.2.2 1,8-Naphthalimides

A SciFinder search, reports over 18,800 compounds based upon the 1,8-naphthalimide framework, including biological imaging agents, chemical sensors, and dyes, with a range of functionalisation. They are also well known for their emission tuneability across the entire visible light spectrum and allowing functionalisation without altering their photophysical properties. The simplest 1,8-naphthalimide derivatives present no functionalisation of the aromatic system (**1** – **5**, Figure 3.1), presenting an emissive state with $\pi - \pi^*$ character. Whilst these compounds are straightforward to prepare in high yields from the parent anhydride, they tend to have small Stokes' shift (ca. 1300 – 2212 cm^{-1}) and quantum yield. Although Distanov reported compound **5** with a quantum yield of 0.31 in MeCN (due to intramolecular hydrogen bonding), all the other species prepared showed Φ_F of less than 0.1, with most of the solvents examined causing Φ values of less than 0.01. Notably, the range of emission wavelengths for these compounds showed a maximum difference of only 9 nm, although 1-2 nm was far more common across the range of solvents.¹⁶ Low fluorescence quantum yields, coupled with small Stokes shifts, and a restricted emission tuneability, limits the application of these materials. By introducing functional groups in the 4-position of the aromatic system, however, these limitations can be overcome.

4-hydroxy substituted naphthalimides, such as compound **6**, that afford an intramolecular charge transfer (ICT), are one such example. Offering a high quantum yield of 0.85 (compared to 0.03 for the non-substituted naphthalimide) and a Stokes' shift that was more than twice that of the unsubstituted samples (4897 cm^{-1}), thus shifting the emission maxima to 440 nm.¹⁷ Unfortunately, not all polymerisation methods can tolerate alcohols, therefore, using an ether functional group may be more suitable. Work by Iyer's group examined the influence of the aromatic substituent on both the emission and quantum yield in DMF. Compound **7**, like **6**, exhibited an increased quantum yield over the non-substituted variant, with a Φ_F of 0.13. Through incorporation of additional substituents on the phenyl ring, Φ_F values of 0.77, and 0.66 were obtained for compound **8**, and **9**, respectively.¹⁸ Replacing the phenyl group with an aliphatic chain (**11** – **13**) has been similarly investigated by Bojinov. No significant alterations were observed in the Stokes shift,

Chapter 3. Luminophore Design, Synthesis, and Characterisation

with quantum yields of 0.63, 0.61, and 0.58 as the length of the carbon chain increases. Replacing the aliphatic chain with the allyl group, results in a slight red shift on the emission, and a decrease in the quantum yield – which is reported to be caused by a reduction in co-planarity.¹⁹ Iyer also examined 4-phenyl substituted 1,8-naphthalimides without a bridging oxygen (**14** – **19**). As with the hydroxy substituted compounds, the quantum yield showed an improvement over the unsubstituted sample. Further derivatisation of this phenyl ring demonstrated substantial improvements in the quantum yield. Most notably, **17** resulted in a Φ_F of 0.796, with **18**, **19** and **15** all showing quantum yields of around 0.5 or higher. However, an aldehyde group, **16**, caused a significant decrease of the quantum yield to 0.028. Whilst all the compounds thus far have reported emission values between 420 and 430 for substituted naphthalimides, due to the extended conjugation of the π system offered by the phenyl group. Compound **15**, with an electron donating *para* methoxy phenyl group, was claimed to afford a favourable donor-acceptor, intramolecular charge transfer, giving rise to a remarkable red shift of the emission to 491 nm.

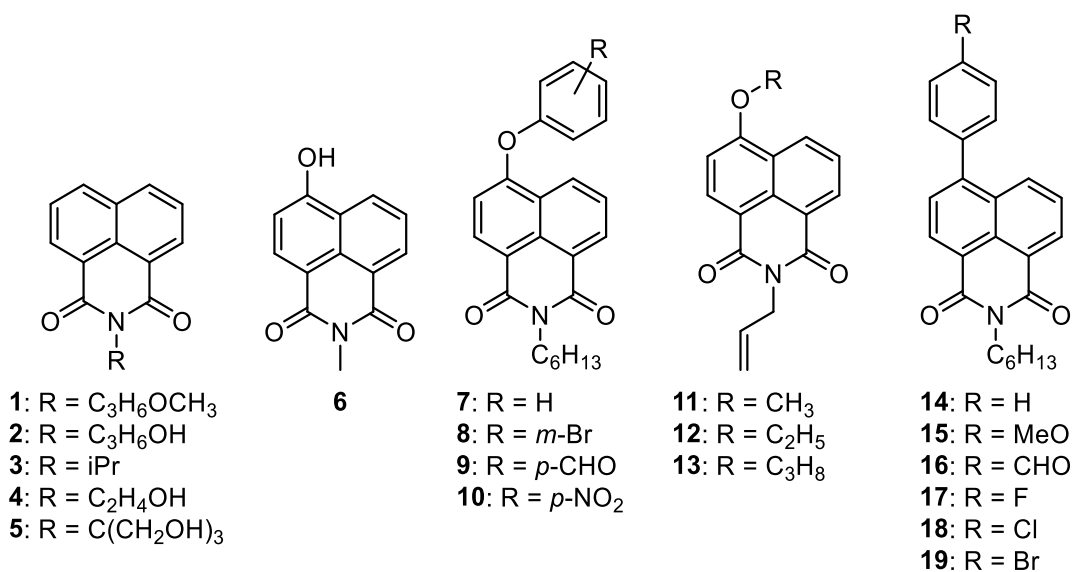


Figure 3.1: Example structures of blue emitting 1,8-naphthalimides.

This push/pull charge transfer phenomenon can be further exploited through the incorporation of an amino group in the 4-position. Work by the Pope group demonstrated this versatility in the naphthalimide framework, by creating a series of gold(I) targeted ligands (**20** – **25**, Figure 3.2) with a propargyl group and varying the amine in the 4-position, to afford tuneability of the complex's lipophilicity. The least electron rich amines, **20**, and **21**, exhibited emission maxima at 514, and 515 nm, respectively. This emission was found to red shift as the electron density of the amine increased from ligands **22** – **25**, with lifetimes of the emission followed the

Chapter 3. Luminophore Design, Synthesis, and Characterisation

same trend. Notably, **20**, and **21**, displayed the smallest stokes shift of 3947 cm^{-1} , whilst **23** demonstrated a far greater value of 6324 cm^{-1} . They do, however, note a significant reduction of the quantum yield after complexation, suggesting that further modulation of the photophysical properties is possible through the imide group.²⁰ Expanding upon this, the group synthesised various naphthalimides with N-heterocyclic carbene in the 4-position, and varied the imide group (**26** – **29**). The emission maxima showed no significant alterations as the R group was changed, and only slight deviations were observed after complexation. Interestingly, **27**, showed the highest quantum yield, 0.31, of the ligands with the other luminophores all exhibiting values of 0.04, although, after complexation these values dropped significantly.²¹ Such a result is not surprising as the electron donating ability of the amine not altered throughout the materials, so the energy level of the HOMO and LUMO remain unchanged as the imide group substituted. Introducing diphenylamine into the 4-position of the 1,8-naphthalimide (**30**, Figure 3.2), demonstrated a substantial red shift of the emission to 611 nm in DCM, along with a decrease in the quantum yield to 0.25. The authors claim this is caused by a strong donor acceptor interaction,²² presumably the diphenyl groups stabilise the aminium ion, lowering the energy of LUMO. Overall, naphthalimides have been demonstrated to possess a broad range of applications, due to their ease of functionalisation and extensive tuneability of the photophysical properties. Such properties make naphthalimides a promising candidate for incorporation into a polymer.

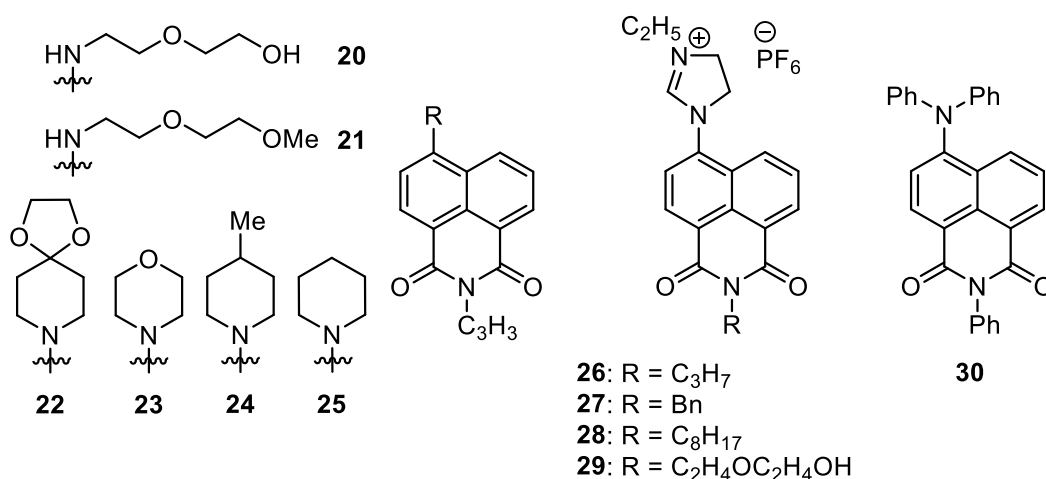


Figure 3.2: Example structures of 4-amino substituted 1,8-naphthalimides.

3.2.3 9,10-Anthraquinones

9,10-Anthraquinones have long been used as dyes for fabrics, and other textiles,²³ making them an obvious starting point for the development of deeply coloured

Chapter 3. Luminophore Design, Synthesis, and Characterisation

polymers. Like the naphthalimide species, the position and identity of the groups attached to the aromatic system influence the photophysical properties, with the literature covering a wide range of coloured dyes (Figure 3.5). Amino, and hydroxy substituents afford the greatest degree of flexibility for further functionalisation and are the most studied derivatives.

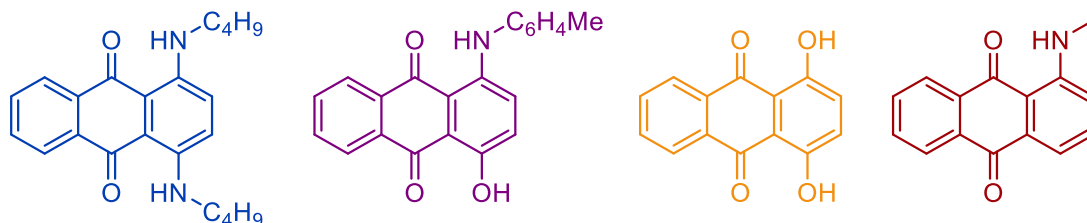


Figure 3.3: Examples of anthraquinone dyes, and their colours.

As anthraquinones derivatives are typically excited to a state with either a dominant intramolecular charge transfer (ICT) character (Figure 3.4), in the case of amino groups, or an intramolecular proton transfer or proton transfer tautomerisation for 1-hydroxy groups. Therefore, it is not surprising the influence these groups can have depending on both their position, and the substituents attached to them.

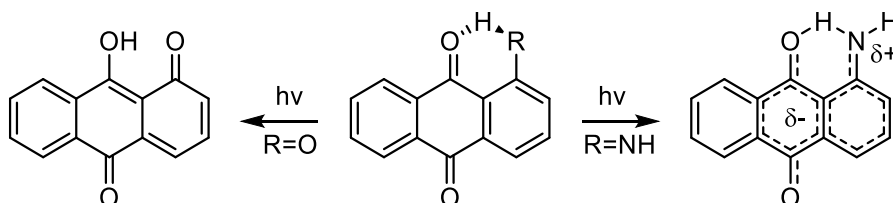


Figure 3.4: Intramolecular charge transfer observed in 1-aminoanthraquinones.

Pal's group has examined the influence of both the position and solvent effects on the absorption, and emission properties of some of these compounds (**31** – **34**^{24–26}, Figure 3.5). The 1-amino substituent (**31**) shows an absorption and emission that ranges from 452 – 467 nm, and 543 – 590 nm as the polarity of the solvent increases, with a quantum yield that follows an inverse relationship (0.066 – 0.022). Addition of a second amino group in the 4-position (**32**) results in a significantly shifted absorption (536 – 546 nm) and emission (601 – 617) spectra, and a decrease in quantum yield that is more prominent in non-polar solvents. A similar, though less pronounced, decrease in energy is observed with the addition of a hydroxy group in the 4-position (**33**). Replacing both the amines with a hydroxy group (**34**) resulted in a lower energy absorption than the mono amine as solvent polarity increased (484 – 477 nm), but an emission that showed a minor change (564 – 567). Presumably, due to the lack of protic solvents studied. Mckellar²⁷ has also examined the effect of solvent on aminoanthraquinones (**31**, **32**, and **35**),

Chapter 3. Luminophore Design, Synthesis, and Characterisation

including the use of the protic solvent isopropanol. As before, the increasing polarity of the solvent resulted in a decrease in the energy of emission. Because the excited state is more polar than the ground state, this causes the LUMO to be stabilised to a greater extent than the HOMO, and therefore, reduces the energy of the transition. Interestingly, the 1,4 diamino species, **34**, proved to more resistant to the influence of the solvent polarity, which the authors suggest is caused by the first excited state showing greater molecular rigidity than the other species. In the presence of IPA, however, the quantum yield of all three compounds dropped dramatically, due to the additional hydrogen bonding providing an additional non-radiative relaxation pathway via hydrogen bond vibrations. With compound **38**, exhibiting no discernible emission.

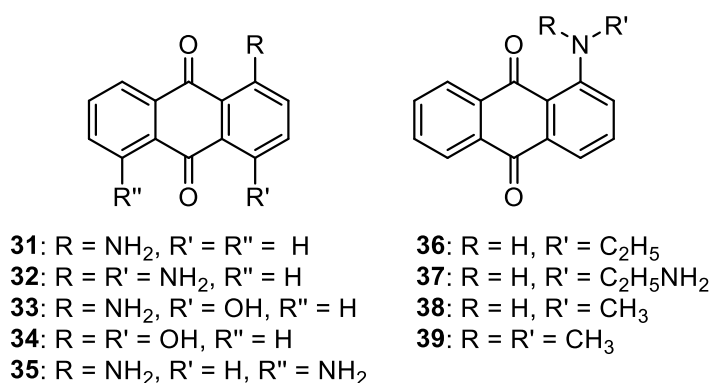


Figure 3.5: Example structures of substituted anthraquinones.

Liu and Pal's groups have also examined the effect of alkyl groups on the amino substituent, by synthesising compounds **36** and **37**,²⁸ and **38** and **39**,²⁶ respectively. The addition of the electron donating ethyl group in **36**, and **37**, caused a substantial lowering of the absorption energy from 464 to 510 nm for both compounds. Interestingly, the fluorescence maxima are different for the two compounds: **36** exhibits a red shifted emission to 608 nm compared to 558 nm without an alkyl group, while **37** shows a blue shift to 535 nm. In both cases the quantum yield was observed to decrease significantly. A similar trend was observed with a methyl substituent: absorbance and emission shifted to 488 and 563 nm, respectively accompanied by a decrease in the quantum yield. Introducing a second methyl group, **39**, showed similar absorbance and emission values in non-polar solvents but a weaker influence of polar solvents on the red shift of the emission. They also note the emission with tertiary amines is incredibly weak, preventing any measurement of the quantum yield. The decrease in quantum yield for secondary amines is believed to occur due to an enhancement of the non-radiative vibrational modes of the hydrogen bond through the amine and carbonyl moieties.²⁹ In the case

Chapter 3. Luminophore Design, Synthesis, and Characterisation

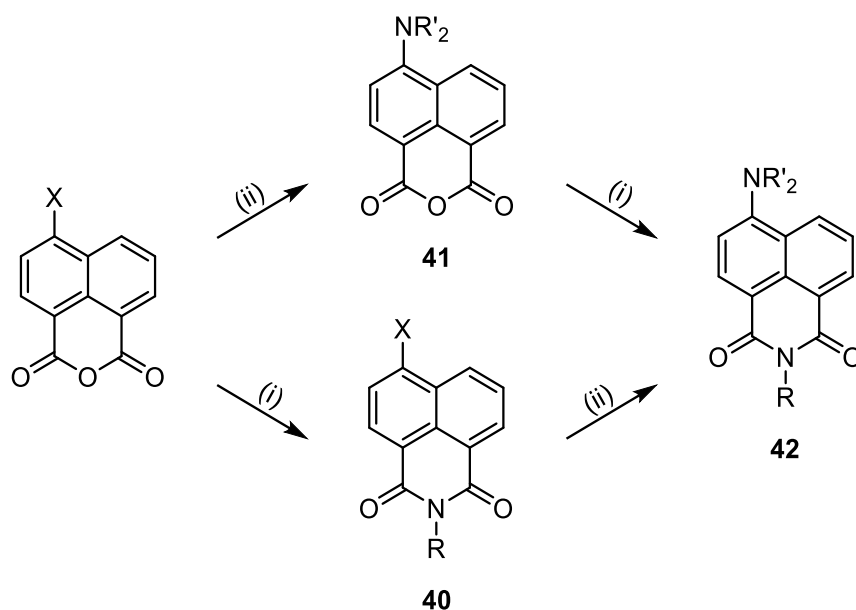
of the tertiary amine, Pal, suggests this could be caused by a twist in the geometry to accommodate the larger methyl group, leading to poorer overlap of the amine lone pair and π orbitals of the anthraquinone. The 1-aminoanthraquinone was selected as a proof-of-concept design as it was the most amenable towards epoxide development.

3.3 Results and Discussion

3.3.1 Luminophore Synthesis and characterisation

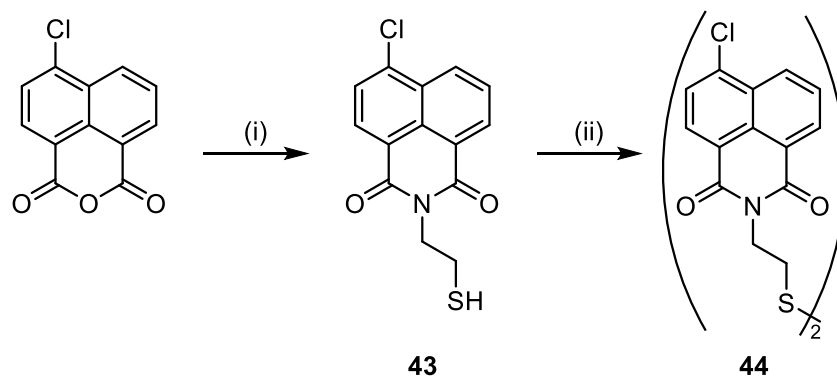
3.3.1.1 1,8-Naphthalimide Based Luminophores

4-amino, 4-chloro substituted and non-substituted 1,8-naphthalimides were typically synthesised in a one or two step process from (4-chloro)-1,8-naphthalic anhydride (Scheme 3.3). The first route involved formation of the imide via a reaction with a primary amine in ethanol (**40**) and then a further reaction with a secondary amine (**42**, piperidine or morpholine) in 2-methoxyethanol³⁰ if the 4-amino derivative was desired (DMSO has also been used for this transformation²⁰). The second route is the preparation of the 4-amino-1,8-naphthalic anhydride (**41**), and then the formation of the imide (**50**) as the last step – which is required if reactive groups, such as epoxides, are desired in the imide position. Both routes resulted in similarly high yields, typically greater than 80%. Formation of the 4-amino substituted compounds can be followed by conversion of the pale-yellow solution to dark orange as the starting material is consumed. The reaction can also be followed by thin layer chromatography (1:1 ethyl acetate:hexane), which is particularly important if the 4-amino derivative is formed first, as any slight colour changes typically observed upon formation of the imide are obscured due to the deep colour of the 4-amino compound. After purification, the synthesised compounds were analysed via ^1H , and $^{13}\text{C}\{^1\text{H}\}$ NMR analysis, UV-Vis, luminescence FTIR, and mass spectrometry, exhibiting m/z peaks as either their molecular ion (M^+), or their protonated form (M-H^+).



Scheme 3.3: Generalised synthetic routes to substituted 1,8-naphthalimides. (i) Primary amine, EtOH, (ii) Primary or secondary amine, DMSO, or 2-methoxyethanol.

3.3.1.2 Thiol functionalisation

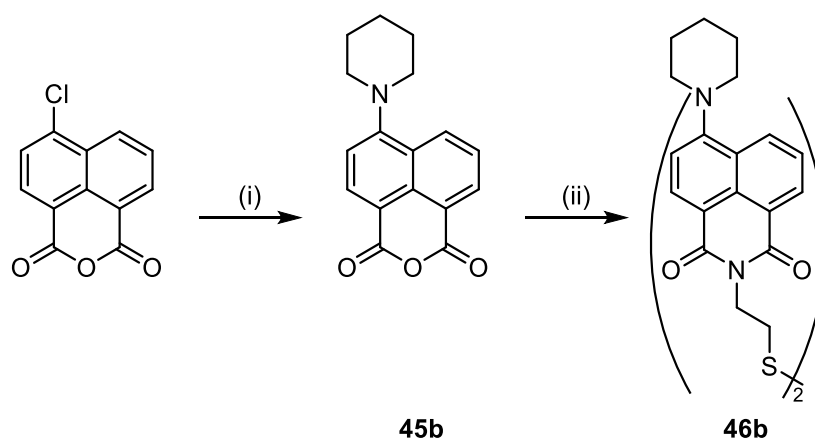


Scheme 3.4: Initial synthetic pathway for 4-amino substituted naphthalimides with a thiol functional group. (i) Ethanol, 2-aminoethanethiol; (ii) DMSO, piperidine.

As mentioned earlier, one such method of polymer functionalisation is post polymerisation modification (PPM). The thiol-ene reaction has been extensively studied and employed in PPM reactions to impart additional functionality to polymers.^{8,31–34} Therefore, the synthesis of thiol functionalised 1,8-naphthalimides was carried out following the pathway outlined in Scheme 3.4. Formation of the thiol-functionalised 4-chloro 1,8-naphthalimide (**43**) was monitored by the precipitation of a slightly yellow solid and three additional ¹H NMR signals at 4.37, 2.89, and 1.52 ppm corresponding to the two CH₂ groups and the thiol proton, respectively. A second set of signals were also observed with a downfield shift to 4.56 and 3.13 ppm and were assigned to the ethyl chain of the disulfide species (**44**), which was also observed with electrospray mass spectrometry. Further reactions to form the 4-amino-1,8-naphthalimide, regardless of the solvent used

Chapter 3. Luminophore Design, Synthesis, and Characterisation

(DMSO or DMF), all resulted in an insoluble yellow solid that was presumed to be **44**. Therefore, the second pathway for the synthesis of thiol substituted naphthalimides was attempted – forming the 4-piperidiny-1,8-naphthalic anhydride, **45b**, (Scheme 3.5) first. Formation of this species can be easily monitored using ^1H NMR spectroscopy through presence of three signals at 3.28, 1.88, and 1.73 ppm for the piperidiny group and as well as a shift in the aromatic signals of the naphthalic moiety. Conversion to the imide, follows the same conditions as the 4-chloronaphthalimide: using 2-aminoethanethiol and ethanol – with ^1H NMR spectroscopy showing the expected signals. However, in this case, the disulfide **46b** was found to be the major component (85:15) unlike the 4-chloro derivative.



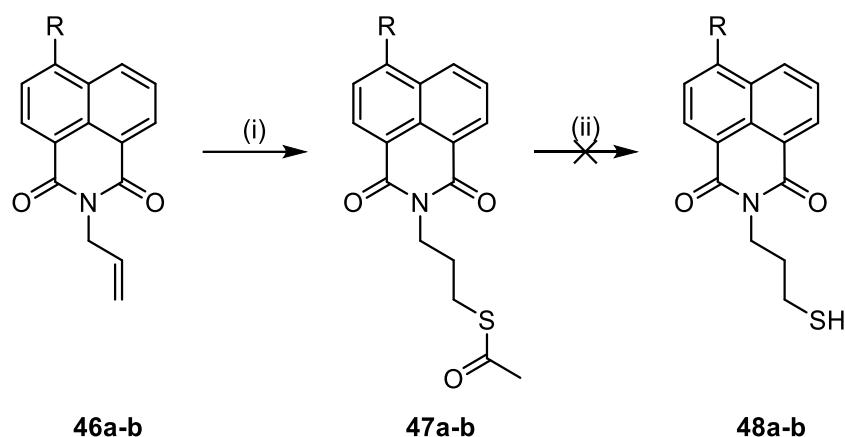
Scheme 3.5: Second synthetic pathway for 4-amino substituted naphthalimides with a thiol functional group. (i) 2-methoxyethanol, piperidine; (ii) ethanol, aminoethanethiol.

Since the disulfide form of the naphthalimide is unable to participate in thiol-ene click reactions, it cannot be used for post-polymerisation modification. Unfortunately, passing a DCM solution of the disulfide species through a sodium borohydride layer did not appear to convert the disulfide to thiol (as determined by ^1H NMR analysis).

An alternative route for thiol functionalised naphthalimides was developed and used thioacetate as a protecting group which is then deprotected (Scheme 3.6). The synthesis of these compounds used a thiol-ene click reaction with the allyl group of a naphthalimide (**46**) using standard conditions of THF, AIBN³⁵ and thioacetic acid, forming the desired protected thiol terminated naphthalimide, **47**, after an aqueous work up. ^1H NMR spectroscopy showed conversion through a significant upfield shift of the (now) alkyl protons of the imide R group and the presence of an additional signal corresponding to the three protons of the thioacetate's methyl group. Additionally, $^{13}\text{C}\{^1\text{H}\}$ NMR spectroscopy indicated the presence of the thioacetate carbonyl group around 195 ppm for both compounds. Removal of the protecting group (**48**) has been reported to occur with relative ease

Chapter 3. Luminophore Design, Synthesis, and Characterisation

following the addition of aqueous ammonia³⁶ or HCl in methanol.³⁷ Surprisingly, neither of these methods proved to deprotect the thiol, with the aqueous ammonia reaction showing no change after 16 hours of reaction time.

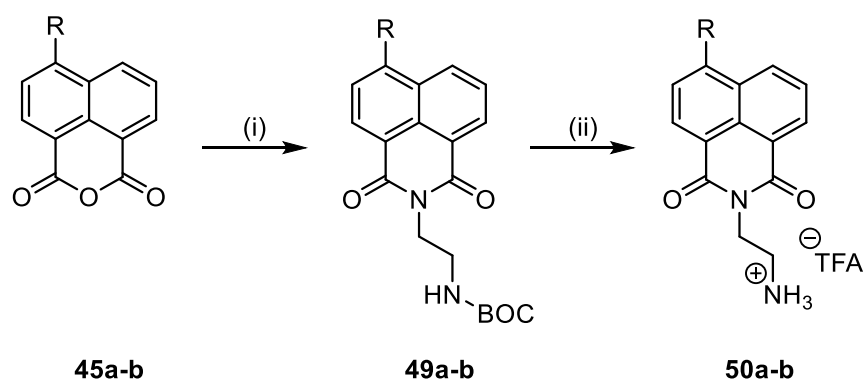


Scheme 3.6: Synthesis of naphthalimides with a protected thiol group. (i) THF, thioacetic acid, AIBN; (ii). R = Cl (a) or piperidinyl (b).

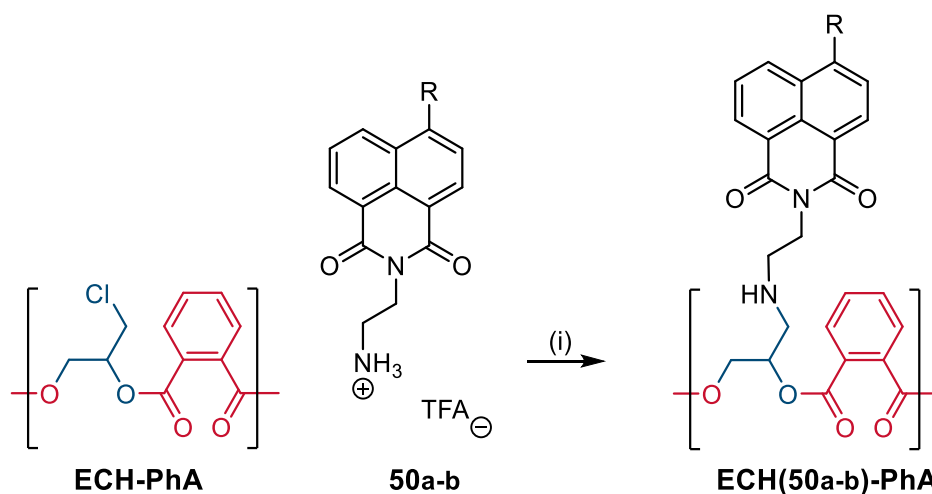
3.3.1.3 Amine Functionalisation

As an alternative to thiol-derived systems, for incorporation into a polymer via post-polymerisation modification, an amine functionalised 1,8-naphthalimide was synthesised (**50**, Scheme 3.7). Such a species was proposed to be amenable to an S_N2 reaction with the pendant chlorides of a co-polymer prepared with epichlorohydrin (Scheme 3.8). Since the morpholine (**45a**) and piperidine (**45b**) substituted 1,8-naphthalic anhydride derivatives were already prepared in a reasonable quantity, these compounds were used as the starting material for the preparation of mono-BOC protected ethylene diamine functionalised naphthalimides (**49**). Formation of these compounds was observed via the appearance of three additional signals in the ^1H NMR spectrum at 4.35 and 3.51 ppm corresponding to the diamine, and a singlet at 1.30 ppm from the tertiary-butyl group's nine protons. Deprotection of the BOC group (**50**) was accomplished through the addition of trifluoroacetic acid to a DCM solution of the naphthalimide, with TLC used to monitor the reaction. Successful synthesis was evident via ^1H NMR analysis showing the loss of a proton environment associated with the tertiary butyl peaks around 1.30 ppm.

Chapter 3. Luminophore Design, Synthesis, and Characterisation

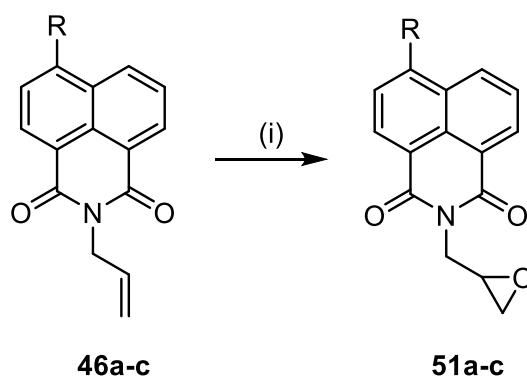


Scheme 3.7: Synthesis of naphthalimides with a terminal amine. (i) BOC-NHC₂H₄NH₂, EtOH; (ii) DCM, TFA. Where R = morpholinyl (a), or piperidinyl (b).



Scheme 3.8: Post-polymerisation modification of a chloride containing co-polymer, ECH-PhA, using an amine-terminated naphthalimide showing the luminophore component. (i) MeCN, K₂CO₃.

3.3.1.4 Epoxide functionalisation of a 1,8-naphthalimide

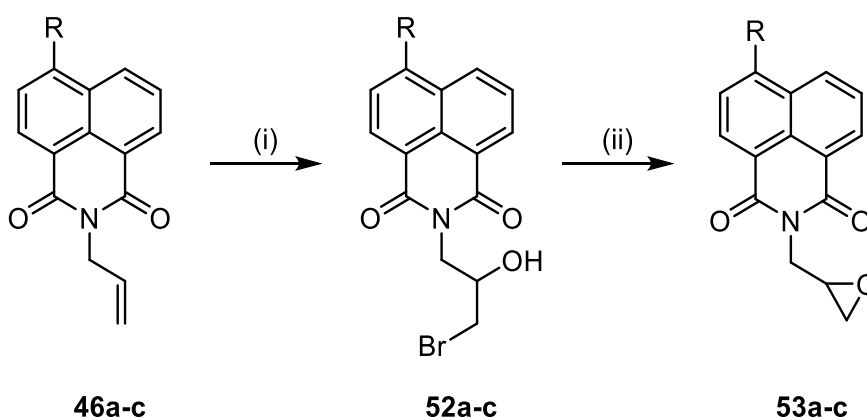


Scheme 3.9: Initial route for the formation of epoxide functionalised naphthalimides. Where R = Cl (a), morpholinyl (b), or piperidinyl (c). (i) DCM, or DCE, and *m*CPBA.

The first synthetic pathway selected for the synthesis of an epoxide functionalised 1,8-naphthalimide (**51**, Scheme 3.9) involved the use of 4-chloro-N-allyl-naphthalimide (**46a**) with *meta*-chloroperoxybenzoic acid (*m*-CPBA) in DCM.

Chapter 3. Luminophore Design, Synthesis, and Characterisation

Formation of the epoxide was monitored by a reduction in intensity of the CH proton signal of the allyl group at 5.98 ppm and by the upfield shift of the alkene protons. Whilst conversion of the alkene was observed, the rate of reaction appeared to be quite slow with only *ca.* 50% conversion achieved after 24 hours. However, the reaction was shown to work forming **51a**, and therefore the same method was applied to the 4-piperindyl substituted derivative. Surprisingly, after being allowed to stir for 24 hours no reaction was observed – evident from the lack of additional signals in the alkyl region of the ^1H NMR spectrum. The same method was repeated using the 4-morpholinyl derivative, changing the solvent to dichloroethane and conducting the reaction at reflux. However, this also showed no conversion to the desired epoxide. Thus, a second route was devised using *n*-bromosuccinimide (NBS) in a THF/water mix with the alkene containing naphthalimides (**46**) to form a bromohydrin (**52**) that could then undergo a ring closing reaction in the presence of a strong base such as sodium hydroxide (**53**, Scheme 3.10).

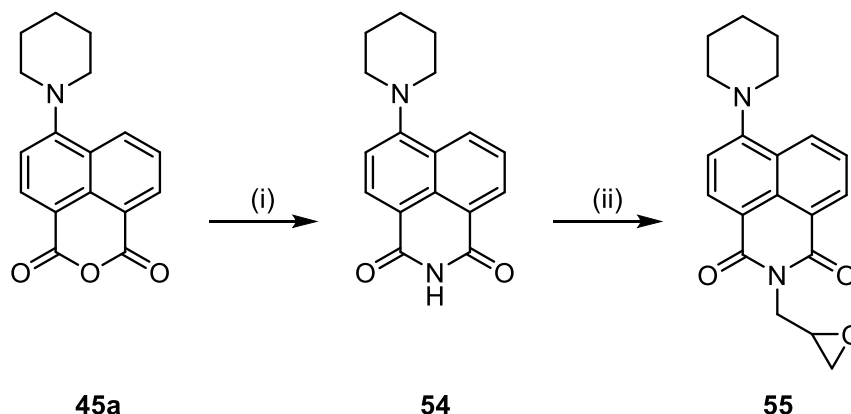


Scheme 3.10: Second route for the synthesis of an epoxide terminated naphthalimide where R = Cl (a), morpholine (b) or piperidine (c). (i) THF/Water and NBS; (ii) 1,4 dioxane, NaOH.

Allowing the reaction to proceed at room temperature overnight forms the desired bromohydrin in quantitative yield for the 4-chloro derivative (**52a**). Substituting the 4-chloro for the 4-morpholinyl (**46b**) or 4-piperidyl (**46c**) variants was also attempted. Upon addition of a portion of NBS, the orange solution of the 4-amino-1,8-naphthalimides immediately became a deep dark orange/black solution, taking 30 minutes to return to the original colour. Further portions of NBS similarly darkened the solution with no change in the time taken for the solution to return to the initial orange colour. Following an aqueous work up, ^1H NMR analysis showed no, or very little, conversion to the halohydrin product. Strangely, the integration of the protons for the allyl environment increased relative to the piperidine environment, and a shift was observed in the aromatic protons after the reaction, however, no product could

Chapter 3. Luminophore Design, Synthesis, and Characterisation

be deduced. Therefore, this method was similarly believed to be an ineffective route to the desired compounds.



Scheme 3.11: Final synthetic route for the synthesis of epoxide terminated 4-piperidinyl naphthalimides. (i) NH_3 , EtOH; (ii) Epichlorohydrin, K_2CO_3 .

In the final attempt to synthesise a naphthalimide with an epoxide functional group the reaction of a naphthalimide with a primary alkyl halide containing an epoxide – epichlorohydrin – was exploited, using an adapted reaction for the related phthalimide.³⁸ Specifically, after obtaining the 4-piperidinyl substituted material outlined in Scheme 3.5, the luminophore was reacted with aqueous ammonia in ethanol to form 4-piperidinyl-1,8-naphthalimide (**54**, Scheme 3.11) that can then readily undergo reactions with primary alkyl halides. The formation of the epoxide functionalised naphthalimide, **55**, was achieved in neat epichlorohydrin in the presence of potassium carbonate to remove the hydrobromic acid by product. ^1H NMR analysis showed complete consumption of the starting naphthalimide and formation of the desired epoxide in $\geq 95\%$ purity, with the epoxide protons observed at 4.45, 4.19, and 2.72 ppm. The impurity was presumed to be polyether oligomers of the epichlorohydrin and naphthalimide that formed during the reaction and were not removed after recrystallisation. The structure of **55**, was confirmed by growing Suitable crystals for X-ray crystallography by the slow diffusion of hexanes layered onto a solution of **55** in DCM and was found to crystallise in the orthorhombic space group, *Pbca*. The structure was solved and refined by Dr Benjamin Ward (Figure 3.6). It was observed that the pedant epoxide group caused two different orientations to crystallise in a 79:21 ratio. The greater crystal network of **55** was observed to arrange in a parallel rotated displaced double herringbone face-to-face manner through π stacking interactions with a C12-C12 distance of 3.840 Å (Figure 3.7 top). The piperidinyl group was seen to adopt the chair conformation with the C6-N2 bond undergoing an out of plane (C1-N1-C2-C3-C12-C11) bend and twisting creating a dihedral angle (C7-C6-N2-C13) of 61.19°. Due to the steric demand of

Chapter 3. Luminophore Design, Synthesis, and Characterisation

the piperidiny group the two naphthalene rings also experienced an out of plane bending in the opposite direction to the piperidiny group with only the C6 carbon lying below the rest of the ring atoms. The stacking arrangement of the naphthalimide shows a rotation between planes of approximately 136° (Figure 3.7 bottom) as this arrangement minimises electron – electron repulsion interactions.

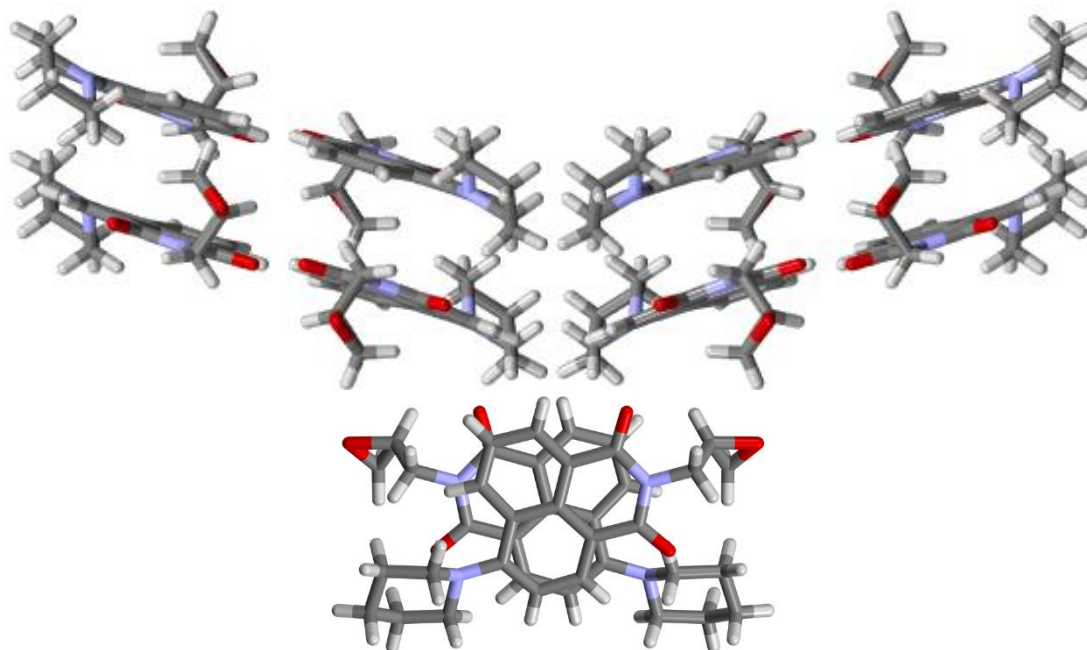


Figure 3.7: Crystal network and packing of **55** showing the double herringbone arrangement (top) and the rotation of the compound between layers.

3.3.1.5 1-Aminoanthraquinone Based Luminophores

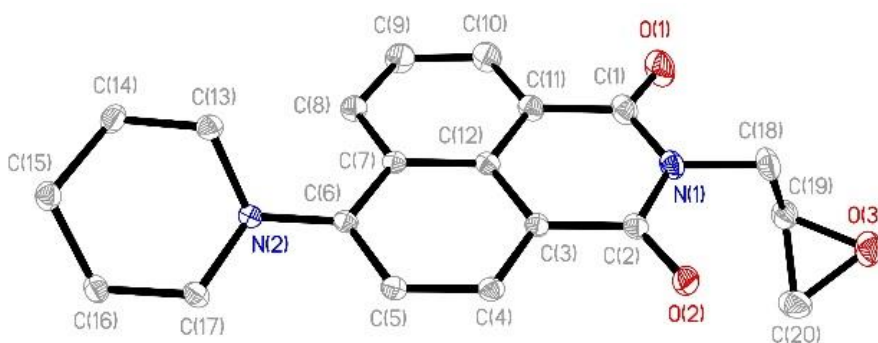
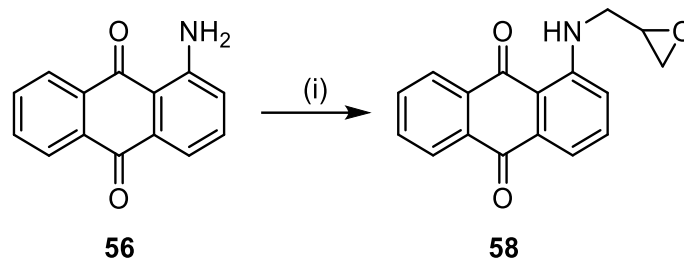


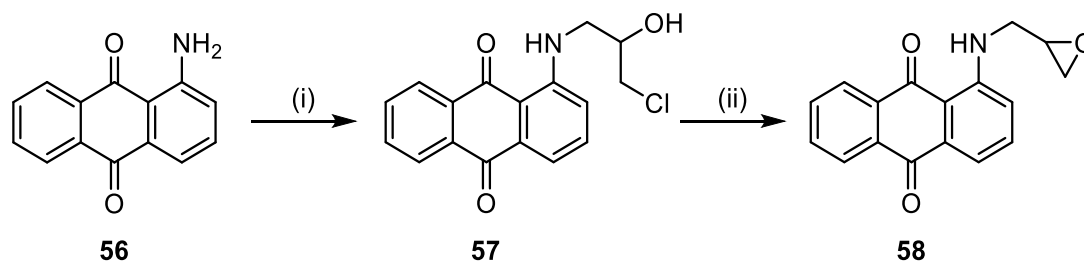
Figure 3.6: Molecular structure of 4-piperidiny-N-(propylene oxide)-naphthalimide, only one orientation is shown, H atoms omitted for clarity.

Chapter 3. Luminophore Design, Synthesis, and Characterisation



Scheme 3.12: Initial reaction pathway for the synthesis of epoxide functionalised 1-aminoanthraquinone. (i) Epichlorohydrin, K₂CO₃.

Following the successful synthesis of an epoxide containing naphthalimide, the same approach was applied to the creation of a prospective yellow/orange emitting luminophore (**58**, Scheme 3.12) using 1-aminoanthraquinone (**56**). Due to the less reactive nature of an amine group, TLC showed low conversion of the starting material after the initial five hours. Monitoring the reaction via TLC for five days showed almost complete consumption of the starting material, but also displayed a significant proportion of poly(epoxide), with the desired epoxide, **58**, existing as a minor component throughout the reaction. Therefore, a second route was employed that replaces the potassium carbonate with acetic acid, that activates the epoxide to nucleophilic attack by the amine forming the ring opened product (**57**, Scheme 3.13).³⁹



Scheme 3.13: Successful synthetic route for the formation of epoxide terminated 1-aminoanthraquinone. (i) Epichlorohydrin, acetic acid; (ii) 1,4 dioxane, potassium hydroxide.

Formation of the intermediate chlorohydrin product, **57**, was observed through a shift in proton environments of the anthraquinone, specifically the amine to 9.95 ppm, and the introduction of additional peaks at 4.22, 3.77, 3.72, 3.62, 3.63, and 2.67 ppm. A colour change was also seen from the light red solution of the starting material to a deep purple/burgundy as the intermediate formed. Conversion to the desired epoxide, **58**, was easily and quickly achieved by a ring closing of the chlorohydrin at room temperature in two hours following addition of a strong base (KOH). Similarly, conversion was observed by another shift in proton environments of the amine from 9.95 to 9.86 ppm and the alkyl protons from 4.22, 3.77, 3.72, 3.62, 3.63 ppm to 3.75, 3.54, 3.28, 2.88, and 2.75 ppm, loss of the hydroxyl proton

Chapter 3. Luminophore Design, Synthesis, and Characterisation

signal. Additionally, an upfield shift is observed from 70.11 to 50.92 ppm as the alcohol is converted to the epoxide, as well as a colour change to bright red. Similarly, the protonated molecule was observed from mass spectrometry for both molecules. The structure of **58**, was confirmed by growing Suitable crystals for X-ray crystallography by the slow diffusion of hexanes layered onto a solution of **58** in DCM and was found to crystallise in the trigonal space group, $R\bar{3}$. The structure was solved and refined by Dr Benjamin Ward (Figure 3.8). It was also observed that the pedant epoxide group caused two different orientations to crystallise in a 45:55 ratio. The greater crystal network of **58** was observed to arrange in a parallel displaced face-to-face manner through π stacking interactions with an interplanar distance of 3.362 Å (Figure 3.9). Additionally, the pendant epoxide oxygens (O3) formed equilateral triangles with neighbouring epoxide group oxygens in the same plane with interaction distances of 3.026 Å. As observed in literature reports of 1-aminoanthraquinones a hydrogen bonding interaction was observed between O2 and N1 with a O2 – N1(H) bond distance of 1.945 Å. Similarly, the bond length of this hydrogen bonding carbonyl, C16 – O2, was found to be longer at 1.244(3) Å compared to the non-hydrogen bonding carbonyl C9 – O3 bond length of 1.225(3) Å, implying a greater degree of single bond character for the C16 – O2 bond. Interestingly, this carbonyl bond length is also the longest observed for 1-aminoanthraquinones amongst those reported within the CCDC. A slight out of plane shift was also observed for the C4-C17 ring relative to the central quinoid structure by 3°.

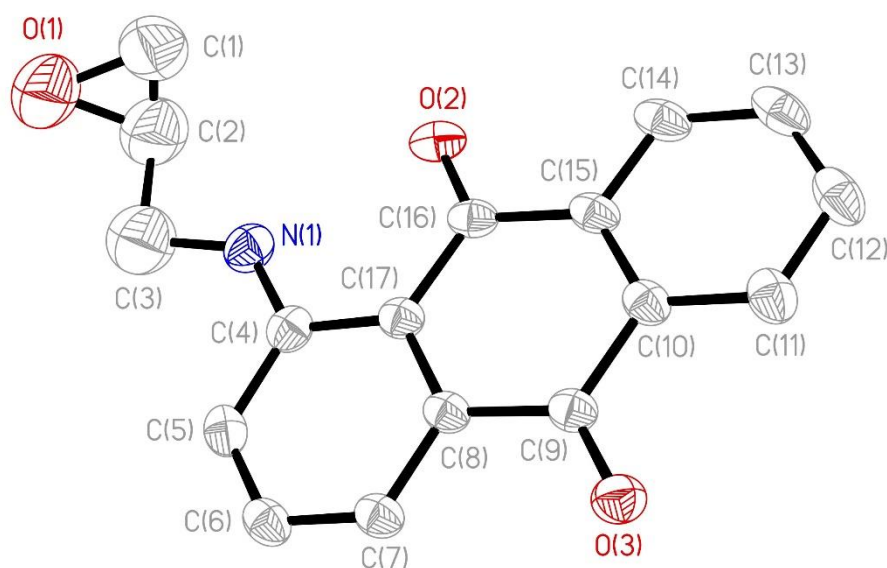


Figure 3.8: Molecular structure of 1-(propylene-oxide)aminoanthraquinone, only one orientation is shown, H atoms omitted for clarity.

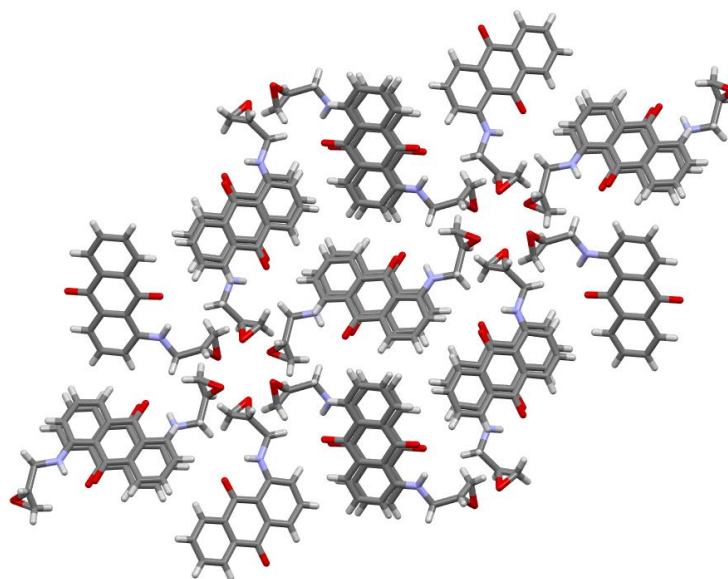


Figure 3.9: Crystal network and stacking of **58** showing the slight displacement of the anthraquinone groups between layers and the orientation of the anthraquinones such that the epoxide groups form equilateral triangles within a plane. (The apparent circular arrangement of the epoxides is from two separate layers of anthraquinones)

UV-Vis Absorption Spectroscopy

All the 4-amino substituted naphthalimides displayed a noticeable shift in their absorption spectra compared to the unsubstituted variants. The $\pi - \pi^*$ transitions typically observed in the 300 – 350 nm region were significantly weakened, with a new intramolecular charge transfer (ICT) transition beyond 400 nm. Depending upon the particular amine used, tuneability of this ICT energy can be achieved. For example, piperidine showed an absorption λ_{max} at 412 nm, whilst the less electron donating morpholine caused a blue shift to 400 nm (Appendix Figure 6.19), with the

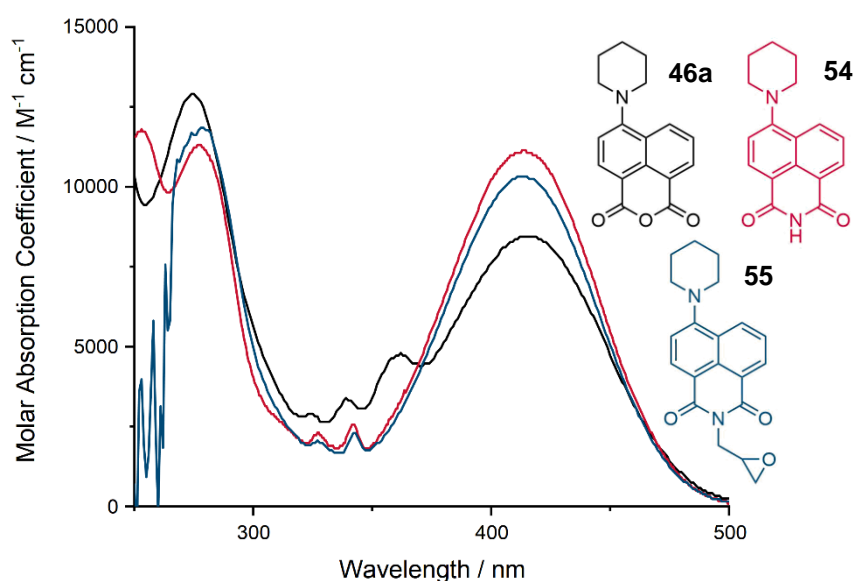


Figure 3.10: UV-Vis absorption spectra for compounds **46a**, **54**, and **55**, as chloroform solutions.

Chapter 3. Luminophore Design, Synthesis, and Characterisation

same trend observed in the $\pi - \pi^*$ transitions ca. 260 nm. Although the R group appended to the imide does not influence the energy of the ICT transition, formation of the imide did cause a noticeable increase in the intensity of the transition (Figure 3.10, Table 3.1). Presumably this was caused by the increased resonance upon forming the imide.⁴⁰ TD-DFT data supported this with an increased oscillator strength of the ICT transition for the naphthalimide, and clearly showing the shift in electron density from the nitrogen of the piperidine onto the π^* system of the naphthalimide (Figure 3.13). However, computational data failed to predict the transitions in the 320 to 370 nm regions for both compounds and underestimated the energy of the ICT transition. Whilst two small peaks of similar intensity were found in the TD-DFT calculations, they were located at a higher energy and obscured by the strong $\pi - \pi^*$ transition (Figure 3.11), and only slight changes were observed with different functionals. Whilst TD-DFT significantly overpredicted the intensity of the ϵ value with respect to experimental data for all samples, it did, however, exhibit good agreement with the trend in the intensity of the ICT and $\pi - \pi^*$ transition observed for each of the sample's experimental measurements.

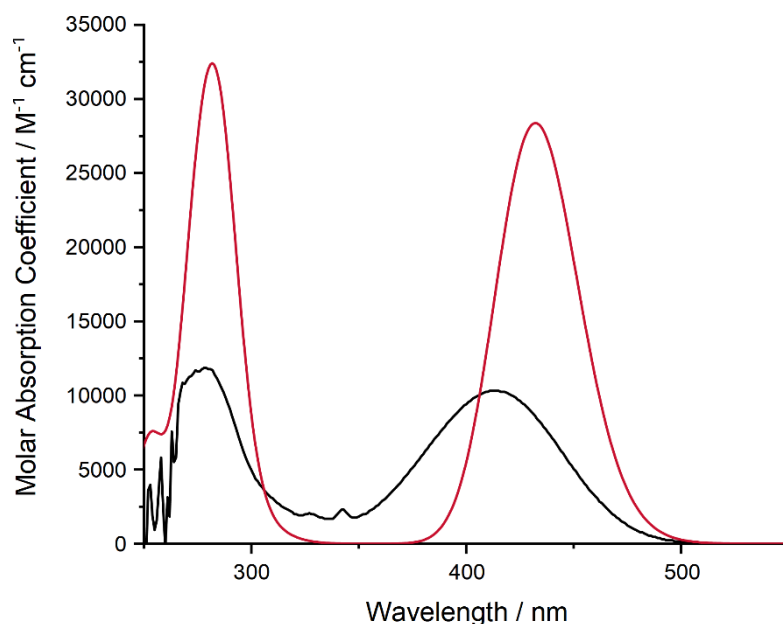


Figure 3.11: Experimental (black line) and simulated (red line, predicted ϵ) UV-Vis spectra of **55** in chloroform using TD-DFT with the B3LYP functional and cc-PVDZ basis set

Table 3.1: Absorbance wavelengths (λ) and molar absorptivity (ϵ) for 1,8-naphthalimides showing the influence of 4-position and imide substitution

Compound	λ_{abs} (nm)	ϵ ($\text{M}^{-1}\text{cm}^{-1}$)
46a	415	8439
	360	4799
	339	3392
	325	2895

Chapter 3. Luminophore Design, Synthesis, and Characterisation

	275	12907
54	413	11148
	342	2560
	327	2312
	278	11313
55	413	10321
	342	2294
	327	2064
	278	11850

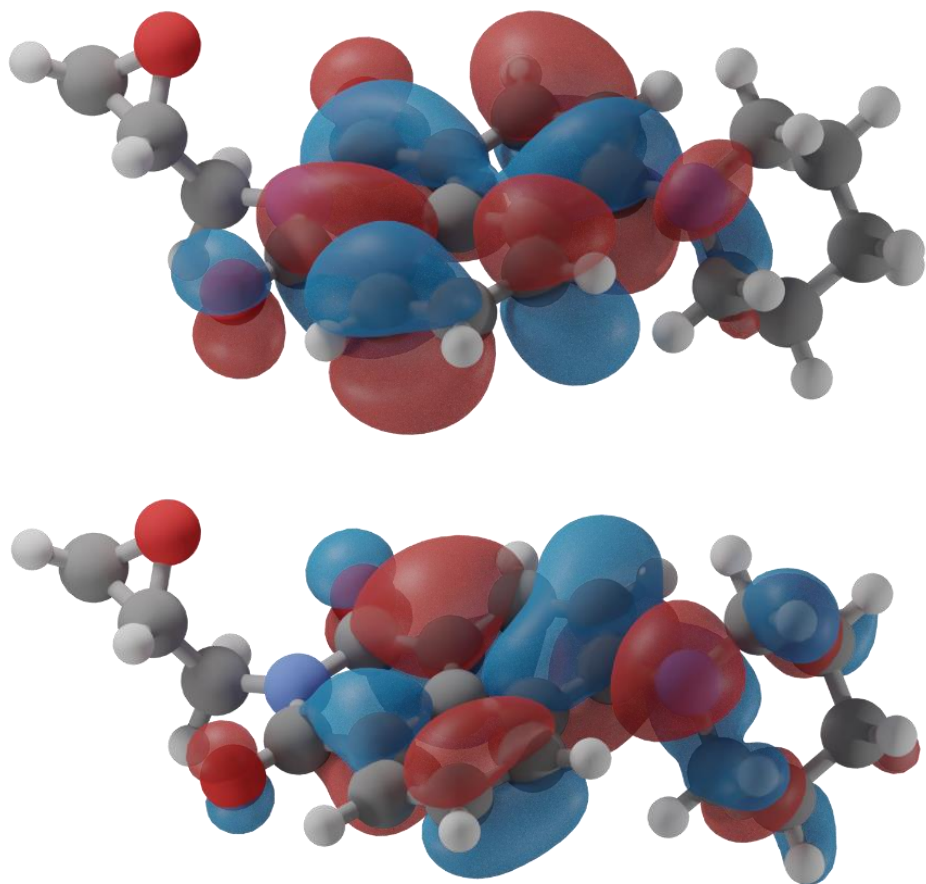


Figure 3.13: Calculated HOMO (bottom) and LUMO (top) and geometries of **55** using the B3LYP functional and cc-PVDZ basis set.

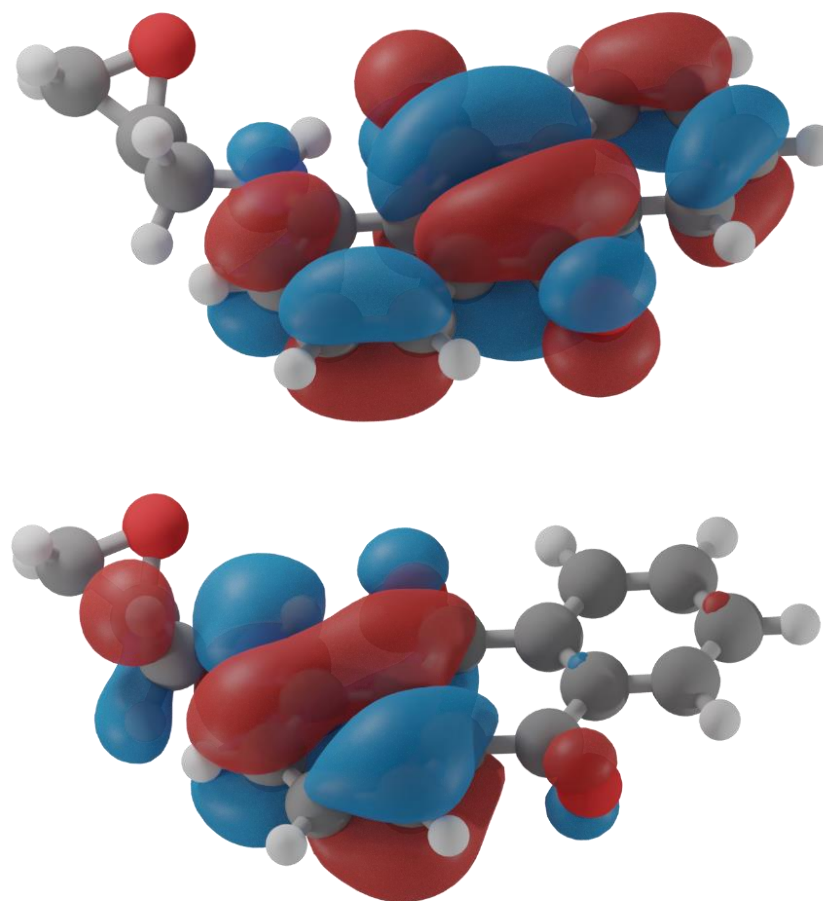


Figure 3.12: Calculated HOMO (bottom) and LUMO (top) and geometries of **58** using the B3LYP functional and cc-PVDZ basis set.

Chapter 3. Luminophore Design, Synthesis, and Characterisation

Similarly, the 1-aminoanthraquinone derived compounds, **57**, and **58**, exhibited a strong ICT transition at 496 nm with $\pi - \pi^*$ transitions below 350 nm (Figure 3.14). Agreement between the calculated transitions and experimental was good with the ICT transition being predicted exactly, and the $\pi - \pi^*$ transitions being within ~ 5 nm of experimental positions (Figure 3.15, appendix Figure 6.22). The calculated ϵ value demonstrated reasonable agreement with the experimental molar absorption coefficient, although the peak at 314 nm was particularly poor for both **57** (Appendix Figure 6.22), and **58** (Figure 3.14). The lack of a difference between these two samples' absorption spectra was not surprising as the R group attached to the amine is not conjugated to the rest of the molecule so any influence from the chlorohydrin and epoxide would be minimal upon the ICT and aromatic $\pi - \pi^*$ transitions (Figure 3.12).

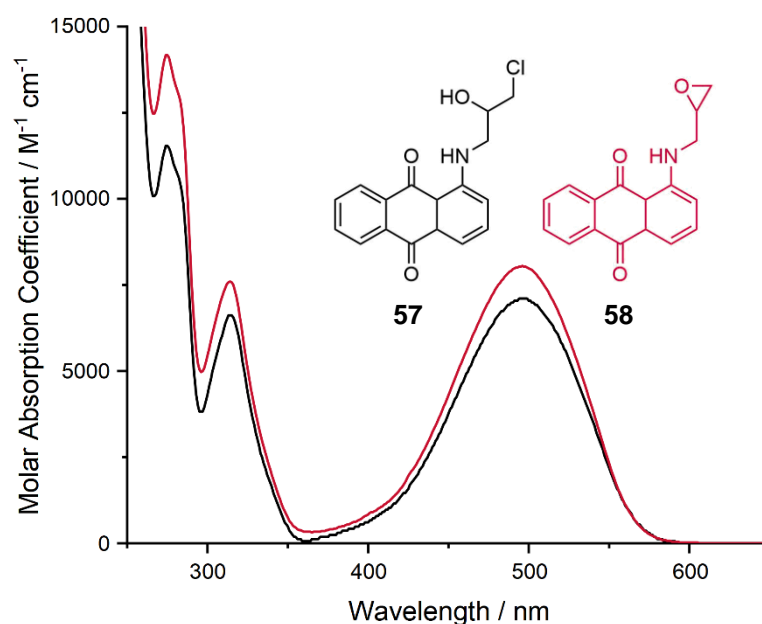


Figure 3.14: UV-Vis absorption spectra of compounds **58**, and **59**, as chloroform solutions.

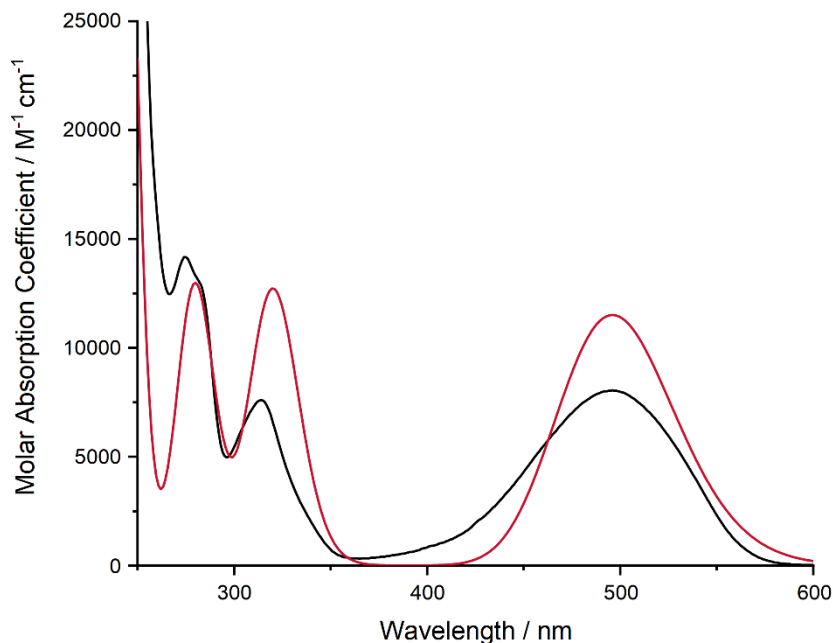


Figure 3.15: Experimental (black line) and simulated UV-Vis spectra (red line, predicted ϵ) of **58** in chloroform performed with TD-DFT using the B3LYP functional and cc-PVDZ basis set.

3.3.2 Luminescence Spectroscopy

All the naphthalimides were highly luminescent species which can be easily observed by the naked eye under 356 nm excitation of the chloroform solutions. Exciting the compounds at their lowest energy transitions results in broad featureless emissions with λ_{em} values of 480, 511, and 586 nm (Figure 3.16). As expected from the UV-Vis absorption spectra, the emission of the naphthalimide can be tuned with replacement of the piperidine group for morpholine causing a blue shift to 500 nm. This is believed to be caused by the increased electron donating ability of the morpholinyl group. The excitation profiles show no deviations from the absorption spectra and all compounds display a large Stokes shift, supporting the ICT assignment of compounds **55**, and **58**. Lifetime measurements (Table 3.2) of the naphthalimide species show only slight alteration as the alkyl group attached the imide changes, with the short lifetime confirming relaxation from a singlet excited state, agreeing with previous examples from the literature.^{16,21} The determined quantum yield values are also similar to those reported within the literature for comparable compounds, with the anthraquinone compounds showing a minor decrease after ring closing of **57** to give the epoxide, **58**.

Chapter 3. Luminophore Design, Synthesis, and Characterisation

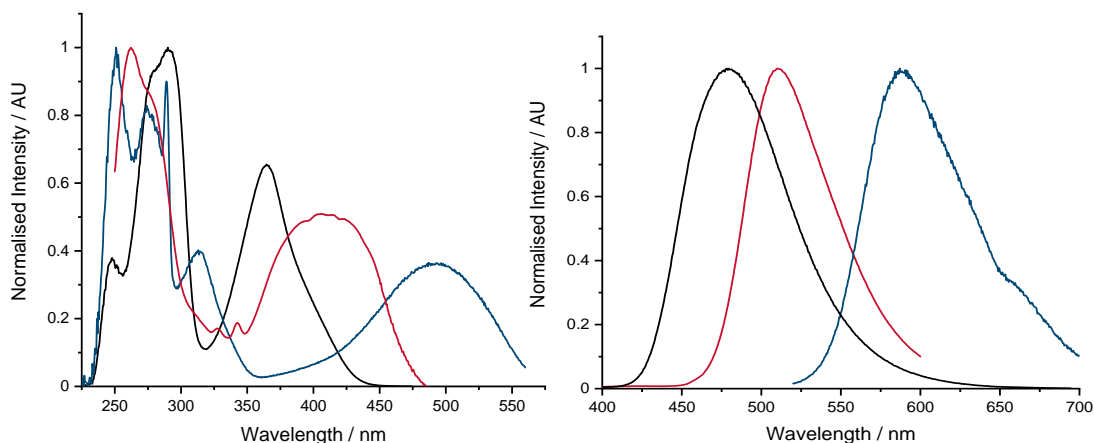


Figure 3.16: Excitation and emission spectra for compounds **47** (black line), **55** (red line), and **59** (blue line) as chloroform solutions

Table 3.2: Fluorescence properties of synthesised luminophores suitable for polymer incorporation as chloroform solutions

Compound	λ_{em} / nm	τ / ns	Φ
50a	511	8.63	-
50b	502	8.05	-
54	511	9.00	-
55	510	8.54	45.0%
58	588	<1 ns	4.5%
59	588	<1 ns	4.3%

3.4 Conclusion

A set of green, and yellow/orange emitting luminophores were synthesised using readily available reagents and common techniques. Both anthraquinone and 4-amino substituted naphthalimide materials display a strong ICT transition generating a large Stokes shift of ca. 3100, and 5100 cm^{-1} into the yellow (582 nm) and green (520 nm) regions respectively. During the preparation of luminophores for inclusion into polymers two routes were explored. Incorporation of an amine, allowing for post-polymerisation modification through an $\text{S}_{\text{N}}2$ reaction, or via the incorporation of an epoxide, enabling in-situ doping. Synthesis of an epoxide terminated naphthalimide through oxidation of an alkene presented some unusual reactivity, with the 4-amino substituted samples showing either low reactivity or no reactivity despite, in some cases, their 4-chloro precursor readily undergoing complete conversion even in mild conditions. Finally, investigations to prepare compounds with thiol containing naphthalimides appeared, in our studies, to rapidly undergo

Chapter 3. Luminophore Design, Synthesis, and Characterisation

oxidation to the disulfide form, implying limited future applications in this field of interest.

3.5 Experimental and methods

All reactions were performed using standard techniques. Reagents were of commercial grade and were used without further purification. ^1H , and ^{13}C NMR spectra were recorded on a Bruker Fourier300 (300/75 MHz), Bruker AVANCE HD III equipped with a BFFO SmartProbe™ (400/101 MHz) or Bruker AVANCE III HD with BBO Prodigy CryoProbe (500/125 MHz) was used. The obtained chemical shifts δ are reported in ppm and are referenced to the residual solvent signal. Spin–spin coupling constants J are given in Hz. UV-Visible spectroscopy was performed in aerated chloroform solutions using a Shimadzu UV-1800 spectrophotometer. IR spectra were recorded on an ATR equipped Shimadzu IRAffinity-1 spectrophotometer. Photophysical data was obtained on a JobinYvon-Horiba Fluorolog spectrometer fitted with a JY TBX picosecond photodetection module as CHCl_3 solutions. Emission spectra were uncorrected and excitation spectra were instrument corrected. The pulsed source was a Nano-LED configured with for a 295 nm output at 1 MHz. Luminescence lifetimes were obtained using the JobinYvon-Horiba FluoroHub single photon counting module fitting the lifetime data using DAS6 deconvolution software. Quantum yield measurements were obtained on aerated solutions using $[\text{Ru}(\text{bipy})_3](\text{PF}_6)_2$ in aerated MeCN ($\phi = 0.016$) or quinine sulfate in aerated 0.05 M H_2SO_4 as standards ($\phi = 0.60$)

3.5.1 X-Ray Diffraction Data Collection and Refinement

Single-crystal X-ray diffraction data ($\text{Mo-K}\alpha$) were collected on a Rigaku Saturn 724+ CCD diffractometer at low temperature, by the EPSRC National Crystallographic Service⁴¹. Crystal structures were solved by Dr. Benjamin Ward using direct methods with absorption corrections being applied as part of the data reduction scaling procedure. After refinement of the heavy atoms, difference Fourier maps revealed the maxima of residual electron density close to the positions expected for the hydrogen atoms; they were introduced as fixed contributors in the structure factor calculations and treated with a riding model, with isotropic atomic displacement parameters but not refined. Full least-square refinement was carried out on F^2 . A final difference Fourier map revealed no significant maxima or minima of residual electron density. The scattering factor coefficients and the anomalous dispersion coefficients were taken from standard sources. Crystal structures were

Chapter 3. Luminophore Design, Synthesis, and Characterisation

solved using SHELXT and refined using SHELXL-2013 via the Olex2 program^{42–44} with the epoxides refined over two sites.

3.5.2 DFT Studies

DFT calculation were carried out using the Gaussian 09 package⁴⁵. Geometry optimisations were performed using the B3LYP functional^{46,47} and cc-PVDZ double ζ basis set.⁴⁸ Time-dependant DFT (TD-DFT) calculation, employed the same function and basis set, calculating the first 20 excited states. Solvent was modelled using the polarisable continuum model,⁴⁹ with the molecular cavity defined by a united atom model that incorporated the hydrogen into the parent heavy atom and included in both geometry optimisations and TD-DFT calculations.

3.5.3 Synthetic Procedures

4-Chloro-N-(ethyl-2-thiol)-1,8-naphthalimide (43a): 4-chloro-1,8-naphthalic anhydride (1.00 g, 4.30 mmol) was added to ethanol (30 mL) along with 2-aminoethanethiol (364.8 mg, 4.73 mmol) and heated at reflux overnight. After allowing the reaction to cool, the yellow precipitate was collected on a glass sinter and washed with ice cold ethanol and dried to afford the thiol and disulfide in a 68:32 ratio as a light-yellow powder (1.05 g, 84%). ¹H NMR (500 MHz, CDCl₃) δ 8.68 (2 H, d, $J = 7.3$ Hz), 8.65 – 8.59 (3 H, m, mix of thiol and disulfide), 8.52 (2 H, d, $J = 7.9$ Hz, CH), 8.48 (1 H, d, $J = 7.9$ Hz, CH, disulfide), 7.90 – 7.80 (6 H, m, CH, mix of thiol and disulfide), 4.58 – 4.53 (2 H, m, CH₂, disulfide), 4.40 – 4.34 (4 H, m, CH₂), 3.16 – 3.10 (2 H, m, CH₂, disulfide), 2.89 (4 H, dd, $J = 15.4, 8.3$ Hz, CH₂ disulfide), 1.52 (1 H, t, $J = 8.7$ Hz, SH). ¹³C{¹H} NMR (126 MHz, CDCl₃) δ 163.84, 163.80 (disulfide), 163.58, 163.55 (disulfide), 139.50, 139.37 (disulfide), 132.40, 132.32 (disulfide), 131.51, 131.43 (disulfide), 131.06, 130.94 (disulfide), 129.55, 129.31, 128.06, 128.02 (disulfide), 127.60, 127.56 (disulfide), 123.10 (disulfide), 123.01, 121.60 (disulfide), 121.50, 43.10, 39.82 (disulfide), 35.80 (disulfide), 22.41. LRMS (ES+) m/z found 581.02 [M+H]⁺.

4-Morpholinyl-1,8-naphthalic anhydride (45a): Prepared following a literature procedure.⁵⁰ 4-chloro-1,8-naphthalic anhydride (2.00g, 8.60 mmol), and morpholine (1.85 mL, 21.49 mmol) were added to 2-methoxyethanol (10 ml) and heated at 120 °C for 5 hours. Upon cooling orange crystals were produced, which were collected by vacuum filtration and washed with ice cold ethanol to furnish **53a** as dark orange needles (2.01 g, 84%) ¹H (400 MHz, CDCl₃) δ 8.62 (2 H, dd, $J = 7.3, 1.2$ Hz, CH), 8.56 (2 H, d, $J = 8.1$ Hz, CH), 8.50 (2 H, dd, $J = 8.5, 1.2$ Hz, CH), 7.78 (2 H, dd, $J = 8.5, 7.3$ Hz, CH), 7.28 (3 H, d, $J = 8.1$ Hz, CH), 4.09 – 4.02 (8 H, m), 3.37 – 3.31 (8

Chapter 3. Luminophore Design, Synthesis, and Characterisation

H, m). $^{13}\text{C}\{^1\text{H}\}$ NMR (126 MHz, CDCl_3) δ 161.14, 160.44, 156.87, 134.88, 133.31, 132.25, 131.62, 126.18, 126.12, 119.51, 115.26, 112.39, 66.84, 53.31. LRMS (EI+) m/z found 283.08 $[\text{M}]^+$. IR $\nu_{\text{max}}/\text{cm}^{-1}$ (neat): 3069, 2955, 2927, 2896, 2870, 2853, 1757, 1744, 1717, 1618, 1584, 1570, 1518, 1472, 1542, 1433, 1396, 1375, 1344, 1325, 1300, 1263, 1234, 1228, 1211, 1171, 1140, 1007, 991, 964sh, 914, 880, 864, 849, 835, 785, 756, 729, 675, 665, 652, 608, 688, 573, 534, 492, 471, 455, 482, 415, 405. UV-vis. (CHCl_3) λ_{max} ($\epsilon / \text{dm}^3\text{mol}^{-1}\text{cm}^{-1}$): 400 (11027), 357 (18919), 344 (19728), 280sh (23168) nm.

4-Piperidiny-1,8-naphthalic anhydride (45b): Synthesised as **56a** using piperidine (2.12 mL, 21.49 mmol) to give dark orange needles (1.95 g, 80%). ^1H NMR (400 MHz, CDCl_3) δ 8.56 (1 H, dd, $J = 7.3, 1.2$ Hz, CH), 8.48 (1 H, dd, $J = 8.0, 4.0$ Hz, CH), 8.42 (1 H, dd, $J = 8.5, 1.2$ Hz, CH), 7.70 (1 H, dd, $J = 8.5, 7.3$ Hz, CH), 7.18 (1 H, d, $J = 8.2$ Hz, CH), 3.33 – 3.25 (4 H, m, CH_2), 1.94 – 1.86 (4 H, m, CH_2), 1.75 (2 H, m, CH_2). $^{13}\text{C}\{^1\text{H}\}$ NMR (126 MHz, CDCl_3) δ 164.32, 163.84, 158.12, 135.08, 133.39, 133.35, 132.22, 126.29, 125.86, 124.11, 116.04, 115.24, 54.65, 26.16, 24.35. LRMS (EI+) m/z found 280.10 $[\text{M}]^+$. IR $\nu_{\text{max}}/\text{cm}^{-1}$ (neat): 2932, 2853, 2808, 2471, 1759, 1719, 1616, 1580, 1570, 1518, 1464, 1437, 1396, 1375, 1341, 1321, 1304, 1277, 1236, 1217, 1203 (sh), 1174, 1155, 1136, 1111, 1080, 1047, 1007, 986, 859, 910, 858, 843, 827, 797, 773, 750, 725, 658, 642, 604, 579, 557, 529, 516, 490, 457, 420, 411. UV-vis. (CHCl_3) λ_{max} ($\epsilon / \text{dm}^3\text{mol}^{-1}\text{cm}^{-1}$): 415 (10248), 362 (5827), 339 (4119), 323 (3516), 274 (15673) nm.

N,N'-(disulphanediyl-bis(ethane-2,1-diyl))-bis-(4-piperidine-naphthalamide) (46b): **53b** (0.600 g, 2.13 mmol) and 2-aminoethanethiol (181 mg, 2.35 mmol) were added to ethanol (20 mL) and heated at reflux overnight. Cooling the reaction mixture to room temperature formed an orange precipitate that was collected on a glass sinter and washed with ice cold ethanol to give **52b** as an orange powder (0.560 mg, 77%) with a thiol:disulfide ratio of 15:85. ^1H NMR (400 MHz, CDCl_3) 8.59 – 8.53 (5 H, m), 8.51 – 8.44 (5 H, m, CH), 8.41 – 8.35 (5 H, m, CH), 7.70 – 7.62 (5 H, m, CH), 7.19 – 7.14 (5 H, m, CH), 4.60 – 4.47 (9 H, m, CH_2), 4.42 – 4.29 (2 H, m, CH_2), 3.31 – 3.17 (20 H, m, CH_2), 3.17 – 3.06 (10 H, m, CH_2), 2.93 – 2.81 (2 H, m, CH_2), 1.94 – 1.81 (20 H, m, CH_2), 1.81 – 1.67 (11 H, m, CH_2). $^{13}\text{C}\{^1\text{H}\}$ NMR (101 MHz, CDCl_3) δ 164.63, 164.11, 157.53, 132.95, 131.30, 130.85, 130.17, 126.43, 125.49, 123.16, 115.94, 114.87, 77.16, 54.68, 39.63, 35.91, 26.37, 24.50. LRMS (ES+) m/z found 679.24 $[\text{M}+\text{H}]^+$. UV-vis. (CHCl_3) λ_{max} ($\epsilon / \text{dm}^3\text{mol}^{-1}\text{cm}^{-1}$): 413 (8870), 342 (2201), 327 (2080), 279.5sh (8870), 261.5 (10631).

Chapter 3. Luminophore Design, Synthesis, and Characterisation

4-Chloro-N-allyl-1,8-naphthalimide (46a): 4-Chloro-1,8-naphthalic anhydride (2.00 g, 8.60 mmol) and allyl amine (650.0 μL , 8.69 mmol) were added to ethanol (40 mL) and heated at reflux for 16 hours, then allowed to cool to produce a white precipitate. The precipitate was collected on a glass sinter and washed with ice cold ethanol and dried to furnish the title compound as a fine off-white powder (2.10 g, 90%). ^1H NMR (400 MHz, CDCl_3) δ 8.63 (1 H, dd, $J = 7.3, 0.9$ Hz, CH), 8.55 (1 H, dd, $J = 8.5, 0.9$ Hz, CH), 8.46 (1 H, d, $J = 7.9$ Hz, CH), 7.82 (1 H, dd, $J = 8.4, 7.4$ Hz, CH), 7.78 (1 H, d, $J = 7.9$ Hz, CH), 6.04 – 5.92 (1 H, m, CH), 5.32 (1 H, dd, $J = 17.2, 1.3$ Hz, CH_2), 5.21 (1 H, dd, $J = 10.2, 1.1$ Hz, CH_2), 4.78 (2 H, d, $J = 5.8$ Hz, CH_2). $^{13}\text{C}\{^1\text{H}\}$ NMR (101 MHz, CDCl_3) δ 163.50, 163.25, 139.22, 132.20, 132.07, 131.31, 130.79, 129.39, 129.15, 127.95, 127.48, 123.06, 121.57, 117.96, 42.62. LRMS (EI+) found m/z 256.02 $[\text{M}-\text{CH}_2]^+$. UV-vis. (CHCl_3) λ_{max} ($\epsilon / \text{dm}^3\text{mol}^{-1}\text{cm}^{-1}$): 358 (15711), 343 (18782), 328 (12640, sh) nm.

4-Morpholinyl-N'-allyl-1,8-naphthalimide (46b): **46a** (1.00 g, 3.68 mmol) was added to a mixture of DMSO (10 mL) and morpholine (1.27 mL, 14.72 mmol) and heated at 120 $^\circ\text{C}$ overnight. The solution was allowed to cool, and water (30 mL) was added, resulting in an orange precipitate. This mixture was neutralised with 0.2 M HCl and then extracted with dichloromethane, washed with water, dried over MgSO_4 , and filtered. The solvent was reduced to a minimum, precipitated with ether and collected on a glass sinter to give **46b** as an orange powder (0.952 g, 81%). ^1H NMR (500 MHz, CDCl_3) δ 8.61 (1 H, dd, $J = 7.3, 1.2$ Hz, CH), 8.55 (1 H, d, $J = 8.0$ Hz, CH), 8.43 (1H, dd, $J = 8.4, 1.2$ Hz), 7.71 (1 H, dd, $J = 8.4, 7.3$ Hz), 7.24 (1 H, d, $J = 8.1$ Hz), 5.99 (1H, ddt, $J = 17.1, 10.3, 5.7$ Hz), 5.31 (1H, dq, $J = 17.1, 1.5$ Hz), 5.20 (1 H, dq, $J = 10.2, 1.3$ Hz), 4.80 (2H, dt, $J = 5.7, 1.4$ Hz), 4.02 (4H, t, $J = 4.6$ Hz), 3.27 (4H, t, $J = 4.6$ Hz). $^{13}\text{C}\{^1\text{H}\}$ NMR (126 MHz, CDCl_3) δ 164.32, 163.85, 155.87, 132.83, 132.48, 131.48, 130.32, 130.09, 126.32, 126.02, 123.40, 117.50, 117.21, 115.13, 67.12, 53.59, 42.44. LRMS (EI+) found m/z 322.13 $[\text{M}]^+$. IR $\nu_{\text{max}}/\text{cm}^{-1}$ (neat): 3003, 2984, 2951, 2849, 2756, 1688, 1651, 1612, 1587, 1574, 1512, 1468, 1447, 1452, 1408, 1395, 1379, 1356, 1347, 1333, 1319, 1296, 1262, 1244, 1234, 1221, 1209, 1179, 1169, 1150, 1115, 1078, 1038, 1020, 1001, 982, 957, 941, 914, 883, 864, 857, 847, 837, 796, 785, 760, 750, 739, 675, 657, 631, 588, 563, 503, 489, 476, 460, 519, 407. UV-vis. (CHCl_3) λ_{max} ($\epsilon / \text{dm}^3\text{mol}^{-1}\text{cm}^{-1}$): 393 (9296), 342 (3441), 326 (2294), 255 (14487) nm.

4-Piperidinyl-N'-allyl-1,8-naphthalimide (46c): Synthesised as **46b** using **46a** (1.00 g, 3.68 mmol) and piperidine (1.45 mL, 14.72 mmol) to afford **46c** as an orange powder (1.02 g, 87%). ^1H NMR (500 MHz, CDCl_3) δ 8.57 (1 H, dd, $J = 7.3,$

Chapter 3. Luminophore Design, Synthesis, and Characterisation

1.2 Hz), 8.49 (1 H, d, $J = 8.1$ Hz), 8.38 (1 H, dd, $J = 8.4, 1.2$ Hz), 7.66 (1 H, dd, $J = 8.4, 7.3$ Hz), 7.17 (1 H, d, $J = 8.1$ Hz), 5.99 (1 H, ddt, $J = 17.1, 10.2, 5.7$ Hz), 5.30 (1 H, dq, $J = 17.2, 1.5$ Hz), 5.18 (1 H, dq, $J = 10.2, 1.3$ Hz), 4.79 (2 H, dt, $J = 5.7, 1.4$ Hz), 3.27 – 3.18 (4 H, m), 1.88 (4 H, dt, $J = 11.0, 5.8$ Hz), 1.72 (2 H, dt, $J = 11.5, 5.9$ Hz). $^{13}\text{C}\{^1\text{H}\}$ NMR (126 MHz, CDCl_3) δ 164.34, 163.85, 157.41, 132.82, 132.50, 131.16, 130.73, 130.02, 126.31, 125.37, 123.05, 117.22, 115.82, 114.74, 54.55, 42.23, 26.24, 24.36. LRMS (EI+) found m/z 320.15 $[\text{M}]^+$. IR $\nu_{\text{max}}/\text{cm}^{-1}$ (neat): 3011, 2934, 2918, 2849, 2814, 2801, 1740, 1719, 1694, 1647, 1587, 1574, 1524, 1512, 1466, 1447, 1429, 1418, 1396, 1377, 1364, 1354, 1341, 1325, 1290, 1275, 1248, 1233, 1223, 1217, 1177, 1159, 1138, 1130, 1111, 1076, 1065, 1051, 1038, 1030, 1016, 991, 974, 957, 918, 881, 864, 851, 831, 781, 760, 746, 741, 685, 654, 625, 538, 513. UV-vis. (CHCl_3) λ_{max} ($\epsilon / \text{dm}^3\text{mol}^{-1}\text{cm}^{-1}$): 411.5 (10018), 342.5 (2210), 328 (1928), 279sh (9454), 260 (14015) nm.

4-Chloro-N-(3-(ethanethioate)propyl)-1,8-naphthalimide (47a): **46a** (500 mg, 1.84 mmol) was dissolved in dry and degassed THF (10 mL) along with thioacetic acid (520 μL , 7.38 mmol) and AIBN (40 mg) in a Schlenk tube and heated at 60 °C overnight. Upon cooling the crude mixture was diluted with water and extracted into DCM, washed with water, brine, dried of MgSO_4 , filtered and the solvent removed. The collected solid was then purified from hot acetone to afford the title compound as an off-white powder (450 mg, 70%). ^1H NMR (500 MHz, CDCl_3) δ 8.65 (1 H, dd, $J = 7.3, 1.1$ Hz, CH), 8.60 (1 H, dd, $J = 8.5, 1.1$ Hz, CH), 8.49 (1 H, d, $J = 7.9$ Hz, CH), 7.85 (1 H, dd, $J = 8.5, 7.3$ Hz, CH), 7.82 (1 H, d, $J = 7.9$ Hz, CH), 4.24 (2 H, dd, $J = 16.5, 9.2$ Hz, CH_2), 2.98 (2 H, t, $J = 7.2$ Hz), 2.33 (3 H, s). $^{13}\text{C}\{^1\text{H}\}$ NMR (126 MHz, CDCl_3) δ 195.75, 163.89, 163.63, 139.31, 132.26, 131.37, 130.89, 129.48, 129.24, 128.02, 127.55, 123.10, 121.60, 39.55, 30.76, 26.88. LRMS (ES+) m/z found 348.04 $[\text{M}+\text{H}]^+$. IR $\nu_{\text{max}}/\text{cm}^{-1}$ (neat): 3343, 3069, 3042, 2965, 2953, 2938, 1682, 1651, 1618, 1587, 1570, 1506, 1460, 1447, 1431, 1406, 1387, 1366, 1341, 1321, 1288, 1252, 1234, 1223, 1204, 1177, 1159, 1138, 1117, 1101, 1061, 1051, 1022, 1009, 951, 903, 883, 862, 851, 808, 797, 779, 752, 729, 679, 635, 623, 586, 571, 453, 440, 424. (CHCl_3) λ_{max} ($\epsilon / \text{dm}^3\text{mol}^{-1}\text{cm}^{-1}$): 359 (8412), 344 (9814), 329sh (6910) nm.

4-Piperidiny-N'-(3-(ethanethioate)propyl)-1,8-naphthalimide (47b): Synthesised as **47a** using **46b** (500 mg, 1.56 mmol), thioacetic acid (440 μL , 6.24 mmol), and AIBN (40 mg) to give the title compound as an orange solid (0.510 g, 82%). ^1H NMR (500 MHz, CDCl_3) δ 8.55 (1 H, dd, $J = 7.3, 1.2$ Hz, CH), 8.47 (1 H, d, $J = 8.1$ Hz, CH), 8.37 (1 H, dd, $J = 8.4, 1.2$, CH), 7.66 (1 H, dd, $J = 8.4, 7.3$, CH), 7.16 (1 H, d, $J =$

Chapter 3. Luminophore Design, Synthesis, and Characterisation

8.1 Hz, CH), 4.26 – 4.20 (2 H, m, CH₂), 3.25 – 3.19 (4 H, m, CH₂), 2.97 (2 H, t, *J* = 7.2 Hz, CH₂), 2.32 (3 H, s, CH₃), 2.05 – 1.99 (2 H, m, CH₂), 1.90 – 1.84 (4 H, m, CH₂), 1.75 – 1.68 (2 H, m, CH₂). ¹³C{¹H} NMR (126 MHz, CDCl₃) δ 194.69, 163.58, 163.07, 156.37, 131.75, 130.08, 129.68, 128.95, 125.24, 124.34, 121.97, 114.74, 113.71, 53.52, 38.06, 29.91, 29.59, 27.22, 25.83, 25.20, 23.32. HRMS (ES+) found *m/z* 397.1581 calcd. 397.1586 [C₂₂H₂₄N₂O₃S+H]⁺. IR $\nu_{\max}/\text{cm}^{-1}$ (neat): 3001, 2986, 2963, 2855, 2833, 2820, 1690, 1678, 1645, 1614, 1587, 1576, 1514, 1458, 1452, 1441, 1425, 1410, 1385, 1360, 1348, 1337, 1300, 1261, 1248, 1236, 1206, 1184, 1171, 1146, 1113, 1099, 1078, 1026, 976, 953, 924, 905, 895, 851, 841, 831, 799, 777, 758, 733, 719, 704, 683, 669, 662, 654, 631, 604, 590, 573, 540, 534, 513, 500, 488, 482, 467, 457, 444, 430. UV-vis (CHCl₃) λ_{\max} (ϵ / dm³mol⁻¹cm⁻¹): 412 (11290), 343 (2474), 327.5 (2242), 280sh (10594), 260 (15697) nm.

4-Morpholinyl-N'-((N''-BOC)2-aminoethyl)-1,8-naphthalimide (49a): **45a** (800 mg, 2.82 mmol) and N-BOC-ethylenediamine (547 mg, 3.41 mmol) were added to ethanol (25 mL) and heated at reflux for 16 hours. The reaction mixture was cooled to room temperature, and the yellow precipitate was filtered and washed with ice cold ethanol to yield **49b** as a yellow powder (1.08 g, 90%). ¹H NMR (400 MHz, CDCl₃) δ 8.59 (1 H, d, *J* = 7.3 Hz, CH), 8.53 (1 H, d, *J* = 8.0 Hz, CH), 8.41 (1 H, d, *J* = 8.4 Hz, CH), 7.73 – 7.66 (1 H, m), 7.22 (1 H, d, *J* = 8.1 Hz, CH), 4.35 (2 H, app t, *J* = 5.6 CH₂), 4.05 – 3.98 (4 H, m CH₂), 3.56 – 3.47 (2 H, m, CH₂), 3.30 – 3.23 (4 H, m, CH₂), 1.29 (9 H, s, CH₃). ¹³C{¹H} NMR (101 MHz, CDCl₃) δ 164.91, 164.44, 156.16, 155.90, 132.89, 131.52, 130.33, 130.12, 126.23, 125.97, 123.27, 117.08, 115.08, 79.18, 77.16, 67.10, 53.57, 40.02, 39.78, 28.37. LRMS (ES+) *m/z* found 326.15 [M-BOC+H]⁺, 426.20 [M+H]⁺. IR $\nu_{\max}/\text{cm}^{-1}$ (neat): 3366, 2959, 2847, 2824, 1686, 1665, 1641, 1612, 1591, 1578, 1528, 1508, 1458, 1449, 1431, 1389, 1362, 1344, 1321, 1283, 1261, 1244, 1234, 1163, 1144, 1115, 1088, 1065, 1040, 1030, 976, 905, 885, 862, 847, 781, 758, 671, 613, 417, 409. UV-vis (CHCl₃) λ_{\max} (ϵ / dm³mol⁻¹cm⁻¹): 394 (10778), 344 (27514), 337 (25812), 275 (20281) nm.

4-Piperidinyl-N'-((N''-BOC)2-aminoethyl)-1,8-naphthalimide (49b): Synthesised as **49a** using **46b** (800 mg, 2.84 mmol) and N-BOC-ethylenediamine (547 mg, 3.41 mmol) to give **46b** as a yellow powder (1.00 g, 83%). ¹H NMR (400 MHz, CDCl₃) δ 8.56 (1 H, d, *J* = 7.2 Hz, CH), 8.48 (1 H, d, *J* = 8.1 Hz, CH), 8.37 (1 H, d, *J* = 8.4 Hz, CH), 7.66 (1 H, app t, *J* = 7.8 Hz, CH), 7.16 (1 H, d, *J* = 8.1 Hz, CH), 4.34 (2 H, t, *J* = 5.5 CH₂), 3.51 (2 H, app m, CH₂), 3.28 – 3.15 (4 H, m, CH₂), 1.96 – 1.83 (4 H, m, CH₂), 1.76 – 1.68 (2 H, m, CH₂), 1.31 (9 H, s, CH₃). ¹³C{¹H} NMR (101 MHz, CDCl₃)

Chapter 3. Luminophore Design, Synthesis, and Characterisation

δ 165.09, 164.60, 157.59, 156.15, 133.04, 131.36, 130.90, 130.17, 126.34, 125.46, 123.03, 115.78, 114.82, 79.14, 77.16, 54.66, 40.14, 39.67, 28.39, 26.34, 24.47.

LRMS (ES+) m/z found 324.17 [M-BOC+H]⁺, 424.20 [M+H]⁺. IR $\nu_{\max}/\text{cm}^{-1}$ (neat): 3374, 2982, 2945, 2926, 2905, 2853, 2824, 2810, 1688, 1645, 1614, 1589, 1574, 1531, 1516, 1464, 1449, 1431, 1395, 1387, 1368, 1341, 1321, 1287, 1261, 1248, 1233, 1180, 1165, 1150, 1130, 1111, 1084, 1065, 1043, 1028, 991, 964, 945, 899, 885, 860, 847, 833, 781, 760, 635, 611, 417. UV-vis. (CHCl₃) λ_{\max} ($\epsilon / \text{dm}^3\text{mol}^{-1}\text{cm}^{-1}$): 412 (9410), 3343 (1344), 327 (1344), 261 (11610) nm.

(2-(4-Morpholinyl)-1,8-naphthalimide)-ethyl-ammonium trifluoroacetate (50a):

49a (500 mg, 1.22 mmol) is dissolved in DCM (20 mL) and TFA was added (4 mL) and left to stir. After TLC indicated the reaction was complete, the solvent was reduced, methanol (20 mL) added, and the solvent removed. The process was repeated three times to afford **50a** as a yellow powder (530 mg, *Quant*). ¹H NMR (500 MHz, DMSO-*d*₆) δ 8.52 – 8.44 (2 H, app m CH), 8.40 (1 H, d, $J = 8.1$ Hz, CH), 7.92 (3 H, Br s, NH₃⁺), 7.81 (1 H, dd, $J = 8.4, 7.3$ Hz, CH), 7.35 (1 H, d, $J = 8.2$ Hz, CH), 4.29 (2 H, t, $J = 5.9$ Hz, CH₂), 3.94 – 3.87 (4 H, m, CH₂), 3.24 – 3.18 (4 H, m, CH₂), 3.15 (2 H, Br s, CH₂). ¹³C{¹H} NMR (126 MHz, DMSO-*d*₆) $\delta = 164.18, 163.60, 158.08$ (q, $J_{CF} = 31.09$), 155.56, 132.14, 130.62, 129.33, 126.08, 125.20, 122.81, 116.05, 114.98, 66.18, 53.06, 39.52, 37.64, 37.33. LRMS (ES+) found m/z 326.15 [M+H]⁺. IR $\nu_{\max}/\text{cm}^{-1}$ (neat): 3111, 3084, 3049, 3032, 2999, 2972, 2889, 2866, 2855, 2812, 2762, 1684, 1647, 1628, 1585, 1570, 1514, 1472, 1454, 1422, 1396, 1385, 1369, 1348, 1337, 1304, 1263, 1240, 1223, 1184, 1140, 1109, 1099, 1084, 1065, 1053, 1026, 988, 966, 926, 899, 854, 833, 800, 781, 760, 748, 739, 719, 667, 656, 590, 577, 538, 519, 501, 473, 461, 438, 419, 411. UV-vis. (CHCl₃) λ_{\max} ($\epsilon / \text{dm}^3\text{mol}^{-1}\text{cm}^{-1}$): 400 (6519), 343 (2241), 327 (1426), 277 (6213), 252 (10389) nm. Emission (CHCl₃): λ_{em} (τ/ns) = 501 (8.62 ns) nm.

(2-(4-Piperidiny)-1,8-naphthalimide)-ethyl-ammonium trifluoroacetate (50b):

Synthesised as **50a** using **49b** (500 mg) to furnish **50b** as a crystalline yellow powder (530 mg, *Quant*). ¹H NMR (500 MHz, DMSO-*d*₆) 8.47 (1 H, dd, $J = 7.3, 1.1$ Hz, CH), 8.42 (1 H, dd, $J = 8.4, 1.1$ Hz, CH), 8.38 (1 H, d, $J = 8.1$ Hz, CH), 7.88 (3H, Br s, NH₃⁺) 7.81 (1 H, dd, $J = 8.4, 7.3$ Hz, CH), 7.32 (1 H, d, $J = 8.2$ Hz, CH), 4.29 (2 H, t, $J = 5.9$, CH₂), 3.23 – 3.17 (4 H, m, CH₂), 3.14 (2 H, Br s, CH₂), 1.88 – 1.75 (4 H, m, CH₂), 1.73 – 1.60 (2 H, m, CH₂). ¹³C{¹H} NMR (126 MHz, DMSO-*d*₆) δ 164.25, 163.64, 158.09 (d, $J_{CF} = 30.96$), 156.86, 132.25, 130.70, 130.57, 129.42, 125.82, 125.39, 122.76, 115.20, 114.86, 53.99, 39.52, 37.69, 37.30, 25.69, 23.84. LRMS (ES+) m/z found 323.16 [M+H]⁺. IR $\nu_{\max}/\text{cm}^{-1}$ (neat): 3113, 3061, 2980, 2967, 2943,

Chapter 3. Luminophore Design, Synthesis, and Characterisation

2930, 2914, 2859, 2818, 2803, 1682, 1651, 1634, 1614, 1593, 1574, 1568, 1514, 1504, 1462, 1454, 1443, 1423, 1396, 1385, 1377, 1346, 1242, 1204, 1184, 1153, 1132, 1113, 1096, 1076, 1063, 1040, 988, 966, 910, 897, 868, 856, 837, 800, 783, 760, 746, 739, 718, 660, 592, 519, 500, 474, 461, 434, 419, 405. UV-vis. (CHCl₃) λ_{\max} (ϵ / dm³mol⁻¹cm⁻¹): 416.5 (8138), 343.5 (1743), 329.5 (1743), 283.5sh (7440) 262 (10463) nm. Emission (CHCl₃): λ_{em} (τ /ns) = 510 (8.05 ns) nm.

Attempted synthesis of 4-chloro-(N-propylene-oxide)-1,8-naphthalimide (51a): **46a** (300 mg, 1.10 mmol) was dissolved in DCM (20 mL) along with mCPBA (372 mg, 1.66 mmol) and allowed to react for 16 hours. After which, the mixture was washed with water, brine, dried over MgSO₄, filtered and the solvent removed *in vacuo* to afford an off-white powder (220 mg).

Attempted synthesis of 4-morpholinyl-(N'-propylene-oxide)-1,8-naphthalimide (51b): Prepared as **51a** using **46b** (352 mg, 1.10 mmol), to furnish an orange powder (250 mg, 79%)

Attempted synthesis of 4-piperidiny-(N'-propylene-oxide)-1,8-naphthalimide (51c): Prepared as **51a** using **46c** (355 mg, 1.10 mmol), to furnish an orange powder (270 mg, 85%)

4-Chloro-N-(ethyl-2-hydroxy-3-bromo)-1,8-naphthalimide (52a): **46a** (400 mg, 1.47 mmol) was dissolved in a mixture of THF (15 mL) and water (5 mL). N-bromosuccinimide (314 mg, 1.77 mmol) was added in portions over a period of 30 minutes, and the reaction left to stir overnight. The solvent was then reduced by half and the slurry filtered, washed with water and dried to offer **52a** as an off-white solid (503 mg, 93%). ¹H NMR (500 MHz, CDCl₃) δ 8.60 (1 H, dd, J = 7.3, 1.1 Hz, CH), 8.56 (1 H, dd, J = 8.5, 1.1 Hz, CH), 8.44 (1 H, d, J = 7.9 Hz, CH), 7.80 (1 H, dd, J = 8.5, 7.3 Hz, CH), 7.77 (1 H, d, J = 7.9 Hz, CH), 4.46 (1 H, dd, J = 13.8, 8.3 Hz, CH₂), 4.31 (1 H, dd, J = 13.7, 3.7 Hz, CH₂), 4.22 – 4.14 (1 H, m, CH), 3.57 (1 H, dd, J = 10.6, 4.5 Hz, CH₂), 3.52 (1 H, dd, J = 10.6, 5.0 Hz, CH₂). ¹³C{¹H} NMR (126 MHz, CDCl₃) δ 164.65, 164.39, 139.68, 132.53, 131.63, 131.18, 129.37, 129.14, 127.98, 127.53, 122.63, 121.11, 69.63, 44.77, 37.29. HRMS (AP+) m/z found 367.9679, calcd. 367.9684 C₁₅H₁₁BrClNO₃. IR ν_{\max} /cm⁻¹ (neat): 3455, 3383, 3310, 3102, 3069, 2961, 1695, 1651, 1614, 1587, 1574, 1508, 1464, 1441, 1422, 1398, 1373, 1348, 1337, 1308, 1234, 1204, 1180, 1155, 1125, 1107, 1084, 1047, 1020, 1009, 932, 903, 849, 777, 750, 733, 665, 652, 567, 519, 440, 420. UV-vis. (CHCl₃) λ_{\max} (ϵ / dm³mol⁻¹cm⁻¹): 360.5 (11749), 344.5 (13938), 330sh (9697), 283 (2419) nm. Emission (CHCl₃): λ_{em} (τ /ns) = 377, 394, 417 nm.

Chapter 3. Luminophore Design, Synthesis, and Characterisation

Attempted synthesis of 4-morpholinyl-N'-(ethyl-2-hydroxy-3-bromo)-1,8-naphthalimide (52b): Synthesised as **52a** using **46b** but extracted into DCM, washed with water, dried over MgSO₄ and filtered to give an orange powder.

Attempted synthesis of 4-piperidinyln-N'-(ethyl-2-hydroxy-3-bromo)-1,8-naphthalimide (52c): Synthesised as **52b** using **46c** to give an orange powder.

4-Piperidinyln-1,8-naphthalimide (54): **45a** (2.00 g, 7.11 mmol), and ammonia solution (5 mL, 90.42 mmol, 35%) were added to ethanol (50 mL) and heated at reflux overnight. Additional ammonia solution (5 mL, 90.42 mmol, 35%) was added and the reaction left for a further six hours. The mixture was then cooled to precipitate an orange powder that was collected on a sinter and washed with ice cold ethanol to afford **54** as a dull orange powder (1.75 g, 88%). ¹H NMR (500 MHz, CDCl₃) δ 8.49 (1 H, dd, *J* = 7.2, 1.2 Hz), 8.42 (1 H, d, *J* = 8.1 Hz), 8.37 (1 H, dd, *J* = 8.4, 1.2 Hz), 7.63 (1 H, dd, *J* = 8.4, 7.25 Hz, CH), 7.13 (1 H, d, *J* = 8.1 Hz, CH), 3.22 – 3.15 (4 H, app t, *J* = 5.2 Hz, CH₂), 1.87 – 1.79 (4 H, q, *J* = 5.3 Hz, CH₂), 1.72 – 1.62 (2 H, m, CH₂). ¹³C{¹H} NMR (126 MHz, CDCl₃) δ 164.45, 163.90, 157.96, 132.64, 131.50, 131.48, 131.06, 126.84, 125.50, 123.15, 115.82, 114.88, 54.75, 26.32, 24.45. LRMS (EI+) *m/z* found 280.10 [M+H]⁺. IR ν_{max}/cm⁻¹ (neat): 3154, 3109, 3036, 3024, 2978, 2934, 2920, 2837, 2814, 1697, 1663, 1609, 1578, 1566, 1560, 1514, 1460, 1443, 1375, 1366, 1356, 1333, 1315, 1275, 1236, 1207, 1192, 1175, 1155, 1134, 1119, 1103, 1076, 1051, 1026, 991, 974, 959, 935, 910, 881, 858, 847, 827, 795, 779, 752, 725, 694, 660, 642, 606, 581, 500, 455, 420, 411. UV-vis. (CHCl₃) λ_{max} (ε / dm³mol⁻¹cm⁻¹): 413 (11148), 341.5 (2559), 327.5 (2312), 276.5 (11313), 253 (11809) nm.

4-Piperidinyln-(N'-propylene-oxide)-1,8-naphthalimide (55): **54** (1.00 g, 3.57 mmol) and potassium carbonate (0.493 g, 3.57 mmol) were added to epichlorohydrin (20 mL) and heated at reflux for five hours. After which, the reaction was allowed to cool, filtered, washed with DCM, and the solvent removed. The resulting orange powder was recrystallised from ethanol to give **55** as orange needles (0.960 g, 80%). ¹H NMR (500 MHz, CDCl₃) δ 8.59 (1 H, dd, *J* = 7.3, 1.2 Hz, CH), 8.51 (1 H, d, *J* = 8.1 Hz, CH), 8.40 (1 H, dd, *J* = 8.4, 1.2 Hz, CH), 7.68 (1 H, dd, *J* = 8.4, 7.3 Hz, CH), 7.18 (1 H, d, *J* = 8.1 Hz, CH), 4.52 (1 H, dd, *J* = 13.5, 4.9 Hz, CH), 4.26 (1 H, dd, *J* = 13.5, 5.4 Hz, CH), 3.39 – 3.31 (1 H, m), 3.29 – 3.20 (4 H, m, CH₂), 2.82 – 2.77 (2 H, m, CH₂), 1.93 – 1.84 (4 H, m, CH₂), 1.78 – 1.69 (2 H, m, CH₂). ¹³C{¹H} NMR (126 MHz, CDCl₃) δ 164.82, 164.27, 157.73, 133.15, 131.47, 131.07, 130.24, 126.45, 125.53, 123.00, 115.69, 114.90, 77.16, 54.70, 49.56, 46.77,

Chapter 3. Luminophore Design, Synthesis, and Characterisation

41.74, 26.37, 24.49. HRMS (ESI+) m/z found 337.1551, calcd. 337.1552
 $C_{20}H_{21}N_2O_3$. IR ν_{max}/cm^{-1} (neat): 3422, 3271, 3065, 1667, 1620, 1587, 1560, 1501, 1458, 1424, 1416, 1387, 1313, 1302, 1267, 1236, 1201, 1171, 1159, 1130, 1072, 1058, 999, 987, 908, 891, 858, 804, 777, 735, 704, 675, 644, 609, 588, 546, 494, 474, 465, 419. UV-Vis ($CHCl_3$) λ_{max} ($\epsilon / dm^3 mol^{-1} cm^{-1}$): 413 (10321), 314 (2293), 283sh (2064), 275 (11850) nm. Emission ($CHCl_3$): λ_{em} (τ/ns) = 590 (<1 ns) nm.

Attempted synthesis of 1-(propylene-oxide)aminoanthraquinone (58):

Synthesised as **55** using 1-aminoanthraquinone (797 mg, 3.57 mmol), to afford a purple solid.

1-((3-chloro-2-hydroxypropyl)amino)anthraquinone (57): Prepared following a literature procedure.³⁹ 1-Aminoanthraquinone (2.00 g, 8.96 mmol) was added to epichlorohydrin (14.05 mL, 179.19 mmol) and acetic acid (2.05 mL, 35.84 mmol) and allowed to react at 80 °C for 25 hours. After which the mixture was allowed to cool to room temperature forming a dark purple precipitate that was collected on a glass sinter and washed with ice cold IPA and dried to afford the title compound as fluffy burgundy crystals (2.24 g, 79%). 1H NMR (500 MHz, $CDCl_3$) δ 9.95 (1 H, s, NH), 8.28 (1H, d, $J = 7.26$ Hz, CH), 8.24 (1 H, d, $J = 7.58$, CH), 7.77 (1H, td, $J = 7.44$, 1.10 Hz, CH), 7.72 (1 H, td, $J = 7.45$, 1.03, CH), 7.64 (1 H, d, $J = 7.27$ Hz, CH), 7.57 (1 H, t, $J = 7.95$, CH), 7.13 (1 H, d, $J = 8.52$ Hz, CH), 4.22 (1 H, app sxt, CH), 3.77 (1 H, dd, $J = 11.31$, 4.62, CH_2), 3.72 (1 H, dd, $J = 11.31$, 5.96, CH_2), 3.62 (1 H, app dt, $J = 13.46$, 5.45 Hz, CH_2), 3.53 (1H, app dt, $J = 13.46$, 5.96 Hz, CH_2), 2.67 (1 H, d, $J = 5.2$ Hz, OH). $^{13}C\{^1H\}$ NMR (126 MHz, $CDCl_3$) δ 185.53, 183.31, 151.68, 135.64, 134.96, 134.90, 134.20, 133.32, 133.11, 126.94, 126.93, 117.88, 116.47, 113.76, 70.11, 47.63, 45.93. HRMS (ESI+) m/z found 316.0736, calcd. 316.0740 $C_{17}H_{14}ClNO_3$. IR ν_{max}/cm^{-1} (neat): 3422, 3389, 3368, 3339, 3271, 3098, 3082, 2913, 2866, 1667, 1620, 1587, 1560, 1501, 1458, 1441, 1423, 1406, 1373, 1319, 1302, 1267, 1236, 1202, 1171, 1159, 1130, 1096, 1072, 1059, 999, 988, 858, 827, 804, 735, 704, 675, 662, 644, 627, 610, 588, 546, 474, 465, 419. UV-Vis ($CHCl_3$) λ_{max} ($\epsilon / dm^3 mol^{-1} cm^{-1}$): 497 (7104), 314 (6619), 283sh (10310), 275 (11537) nm. Emission ($CHCl_3$): λ_{em} (τ/ns) = 590 (<1 ns) nm.

1-(propylene-oxide)aminoanthraquinone (58): 1-((3-chloro-2-hydroxypropyl)amino)anthraquinone (1.25 g, 3.96 mmol) was dissolved in dioxane (13 mL) along with powdered potassium hydroxide (0.777 g, 13.86 mmol) and stirred at room temperature for 2 hours. After which the mixture was extracted with DCM, washed with water, brine, dried over magnesium sulfate, filtered and the

Chapter 3. Luminophore Design, Synthesis, and Characterisation

solvent removed in *vacuo* to afford **58** as a bright red solid (0.925 g, 84 %). ¹H NMR (500 MHz, CDCl₃) δ 9.87 (1 H, s, NH), 8.29 (1 H, ddd, *J* = 7.75, 1.41, 0.52, CH), 8.25 (1 H, ddd, *J* = 7.58, 1.47, 0.52, CH), 7.77 (1 H, td, *J* = 7.33, 1.43 Hz, CH), 7.72 (1H, td, *J* = 7.43, 1.43 Hz, 1H), 7.65 (1 H, dd, *J* = 7.37, 1.15 Hz, CH), 7.58 (1 H, *J* = 8.55, 7.38, CH), 7.17 (1 H, dd, *J* = 8.56, 1.13 Hz, CH), 3.75 (1H, app dt, *J* = 15.87, 3.99 Hz, CH₂) 3.54 (1H, app dt, *J* = 14.62, 4.54 Hz, CH₂) 3.28 (1 H, dddd, *J* = 4.76, 3.93, 3.42, 2.66 Hz, CH), 2.88 (1H, dd, *J* = 4.76, 3.98 Hz, CH₂), 2.75 (1 H, dd, *J* = 4.79, 2.64 Hz, CH₂). ¹³C{¹H} NMR (126 MHz, CDCl₃) δ 185.48, 183.87, 151.85, 135.57, 135.01, 134.83, 134.17, 133.28, 133.15, 126.95, 126.92, 118.16, 116.47, 113.65, 50.92, 45.30, 44.27. HRMS (ESI+) *m/z* found 280.0963, calcd. 280.0974 C₁₇H₁₄NO₃. IR *v*_{max}/cm⁻¹ (neat):3260, 3210, 3103, 3080, 3071, 3063, 3051, 3032, 3011, 2997, 1661, 1628, 1593, 1570, 1560, 1541, 1508, 1456, 1404, 1368, 1302, 1269, 1231, 1202, 1175, 1157, 1142, 1072, 1047, 997, 955, 914, 893, 876, 856, 849, 829, 806, 787, 764, 735, 708, 662, 615, 588, 581, 548, 515, 482, 473, 463, 447, 440, 419, 411. UV-Vis (CHCl₃) λ_{max} (ε / dm³mol⁻¹cm⁻¹): 497 (8029), 315 (7586), 284sh (12684), 274 (14170) nm. Emission (CHCl₃): λ_{em} (τ/ns) = 588 (<1 ns) nm.

3.6 References

- 1 M. Gilbert, in *Brydson's Plastics Materials (Eighth Edition)*, ed. M. Gilbert, Butterworth-Heinemann, 2017, pp. 1–18.
- 2 S. Al-Malaika, F. Axtell, R. Rothon and M. Gilbert, in *Brydson's Plastics Materials (Eighth Edition)*, ed. M. Gilbert, Butterworth-Heinemann, 2017, pp. 127–168.
- 3 T. J. Suhrhoff and B. M. Scholz-Böttcher, *Mar Polly Bull*, 2016, **102**, 84–94.
- 4 I. Grabchev, X. Qian, Y. Xiao and R. Zhang, *New J. Chem.*, 2002, **26**, 920–925.
- 5 A. Merrington, in *Applied Plastics Engineering Handbook*, ed. M. Kutz, William Andrew Publishing, Oxford, 2011, pp. 177–192.
- 6 N. Malik, P. Kumar, S. Shrivastava and S. B. Ghosh, *Int J Plast Technol*, 2017, **21**, 1–24.
- 7 D. Paszun and T. Szychaj, *Ind. Eng. Chem. Res.*, 1997, **36**, 1373–1383.
- 8 N. Yi, T. T. D. Chen, J. Unruangsri, Y. Zhu and C. K. Williams, *Chem Sci*, 2019, **10**, 9974–9980.
- 9 J. G. Smith, *Synthesis*, 1984, **1984**, 629–656.
- 10 H. Q. Pham and M. J. Marks, in *Ullmann's Encyclopedia of Industrial Chemistry*, American Cancer Society, 2005.
- 11 S. Huijser, E. HosseiniNejad, R. Sablong, C. de Jong, C. E. Koning and R. Duchateau, *Macromolecules*, 2011, **44**, 1132–1139.
- 12 G. Faraca and T. Astrup, *Waste Manage*, 2019, **95**, 388–398.
- 13 A. Turner, *Environment International*, 2018, **117**, 308–318.
- 14 Y. K. Lee, K. R. Murphy and J. Hur, *Environ. Sci. Technol.*, 2020, **54**, 11905–11914.
- 15 C. E. Hoyle and C. N. Bowman, *Angw Chem Int Edit*, 2010, **49**, 1540–1573.
- 16 O. V. Prezhdo, B. V. Uspenskii, V. V. Prezhdo, W. Boszczyk and V. B. Distanov, *Dyes Pigments*, 2007, **72**, 42–46.

Chapter 3. Luminophore Design, Synthesis, and Characterisation

- 17 L. Biczók, P. Valat and V. Wintgens, *Phys. Chem. Chem. Phys.*, 1999, **1**, 4759–4766.
- 18 N. Meher and P. K. Iyer, *Nanoscale*, 2019, **11**, 13233–13242.
- 19 I. Grabchev, C. Petkov and V. Bojinov, *Macromol Mater Eng*, 2002, **287**, 904–908.
- 20 E. E. Langdon-Jones, D. Lloyd, A. J. Hayes, S. D. Wainwright, H. J. Mottram, S. J. Coles, P. N. Horton and S. J. A. Pope, *Inorg. Chem.*, 2015, **54**, 6606–6615.
- 21 L. M. Groves, C. F. Williams, A. J. Hayes, B. D. Ward, M. D. Isaacs, N. O. Symonds, D. Lloyd, P. N. Horton, S. J. Coles and S. J. A. Pope, *Dalton Trans.*, 2019, **48**, 1599–1612.
- 22 S. Jena, P. Dhanalakshmi, G. Bano and P. Thilagar, *J. Phys. Chem. B*, 2020, **124**, 5393–5406.
- 23 M. Shahid, J. Wertz, I. Degano, M. Aceto, M. I. Khan and A. Quye, *Anal. Chim. Acta.*, 2019, **1083**, 58–87.
- 24 P. Dahiya, M. Kumbhakar, T. Mukherjee and H. Pal, *J. Mol. Strut.*, 2006, **798**, 40–48.
- 25 P. Dahiya, M. Kumbhakar, D. K. Maity, T. Mukherjee, A. B. R. Tripathi, N. Chattopadhyay and H. Pal, *J. Photoch. Photobio. A*, 2006, **181**, 338–347.
- 26 P. Dahiya, D. K. Maity, S. K. Nayak, T. Mukherjee and H. Pal, *J. Photoch. Photobio. A*, 2007, **186**, 218–228.
- 27 N. S. Allen and J. F. Mckellar, *J. Photochem.*, 1977, **7**, 107–111.
- 28 T. Wang, H. Sun, T. Lu, K. C. Weerasinghe, D. Liu, W. Hu, X. Zhou, L. Wang, W. Li and L. Liu, *J. Mol. Strut.*, 2016, **1116**, 256–263.
- 29 H. Inoue, M. Hida, N. Nakashima and K. Yoshihara, *J. Phys. Chem.*, 1982, **86**, 3184–3188.
- 30 C. L. Fleming, T. D. Nalder, E. H. Doeven, C. J. Barrow, F. M. Pfeffer and T. D. Ashton, *Dyes Pigments*, 2016, **126**, 118–120.
- 31 G. Si, L. Zhang, B. Han, Z. Duan, B. Li, J. Dong, X. Li and B. Liu, *Polym. Chem.*, 2015, **6**, 6372–6377.
- 32 V. Darcos, S. Antoniacomi, C. Paniagua and J. Coudane, *Polym. Chem.*, 2012, **3**, 362–368.
- 33 B. Tonpheng, J. Yu and O. Andersson, *Phys. Chem. Chem. Phys.*, 2011, **13**, 15047–15054.
- 34 Z. Ates, P. D. Thornton and A. Heise, *Polymer Chemistry*, 2011, **2**, 309–312.
- 35 R. Iida, H. Kawamura, K. Niikura, T. Kimura, S. Sekiguchi, Y. Joti, Y. Bessho, H. Mitomo, Y. Nishino and K. Ijiro, *Langmuir*, 2015, **31**, 4054–4062.
- 36 N. J. Rogers, S. Claire, R. M. Harris, S. Farabi, G. Zikeli, I. B. Styles, N. J. Hodges and Z. Pikramenou, *Chem. Commun.*, 2013, **50**, 617–619.
- 37 R. Hartung, G. Golz, S. Schlaf, G. Silvennoinen, K. Polborn, P. Mayer and H. R. Pfaendler, *Synthesis*, 2009, **2009**, 495–501.
- 38 P. Chi, C. Xie and J. Lin, *Chin. J. Org. Chem*, 2013, **33**, 640–642.
- 39 V. Getautis, M. Dashkyavichene, I. Paulauskaite and A. Stanisauskaite, *Chem Heterocycl Compd*, 2005, **41**, 426–436.
- 40 C. M. Lee and W. D. Kumler, *J. Org. Chem.*, 1962, **27**, 2055–2059.
- 41 S. J. Coles and P. A. Gale, *Chem. Sci.*, 2012, **3**, 683–689.
- 42 G. M. Sheldrick, *Acta Cryst A*, 2008, **64**, 112–122.
- 43 G. M. Sheldrick, *Acta Cryst A*, 2015, **71**, 3–8.
- 44 O. V. Dolomanov, L. J. Bourhis, R. J. Gildea, J. A. K. Howard and H. Puschmann, *Journal of Applied Crystallography*, 2009, **42**, 339–341.
- 45 M. J. Frisch, G. W. Trucks, J. R. Cheeseman, G. Scalmani, M. Caricato, H. P. Hratchian, X. Li, V. Barone, J. Bloino, G. Zheng, T. Vreven, J. A. Montgomery, G. A. Petersson, G. E. Scuseria, H. B. Schlegel, H. Nakatsuji, A. F. Izmaylov, R. L. Martin, J. L. Sonnenberg, J. E. Peralta, J. J. Heyd, E. Brothers, F. Ogliaro, M. Bearpark, M. A. Robb, B. Mennucci, K. N. Kudin, V. N. Staroverov,

Chapter 3. Luminophore Design, Synthesis, and Characterisation

- R. Kobayashi, J. Normand, A. Rendell, R. Gomperts, V. G. Zakrzewski, M. Hada, M. Ehara, K. Toyota, R. Fukuda, J. Hasegawa, M. Ishida, T. Nakajima, Y. Honda, O. Kitao and H. Nakai, *Gaussian 09*, .
- 46 A. D. Becke, *J. Chem. Phys.*, 1993, **98**, 5648–5652.
- 47 C. Lee, W. Yang and R. G. Parr, *Phys. Rev. B*, 1988, **37**, 785–789.
- 48 T. H. Dunning, *J. Chem. Phys.*, 1989, **90**, 1007–1023.
- 49 J. Tomasi, B. Mennucci and R. Cammi, *Chem Rev*, 2005, **105**, 2999–3093.
- 50 H. Dai, Y. Yan, Y. Guo, L. Fan, Z. Che and H. Xu, *Chemistry – A European Journal*, 2012, **18**, 11188–11191.

4 Design, Synthesis, and Characterisation of Luminophore Functionalised Doped- Ring Opening Co-Polymerisation Polymers

Chapter 4. Design, Synthesis, and Characterisation of Luminophore Functionalised Doped-Ring Opening Co-Polymerisation Polymers

4.1 Aims

This chapter aims to demonstrate the synthesis, processability, application and degradation of functionalised ROCOP polymers prepared through a novel doped ring-opening co-polymerisation method. ROCOP provides a powerful approach for the synthesis of well-defined polyesters, with a range of properties afforded by the large inventory of commercially available epoxides and cyclic anhydrides.

Surprisingly, however, no work exists on the use of novel monomers to directly incorporate dye or luminophores into the backbone of a polymer. This chapter aims to change that by utilising the epoxide containing combined luminophore/chromophores synthesised in an earlier chapter. Additionally, these polymers will be synthesised at a scale that has not been demonstrated in the literature before, when employing ROCOP catalysis.

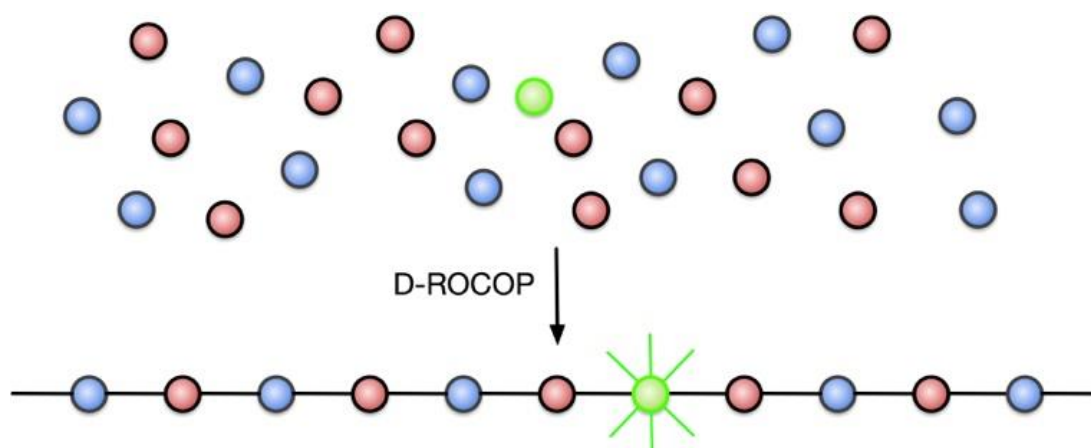


Figure 4.1: Doped ring-opening co-polymerisation (D-ROCOP).

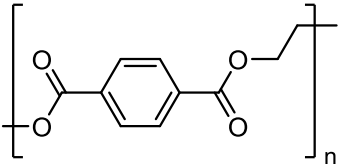
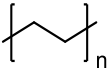
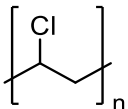
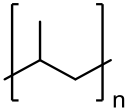
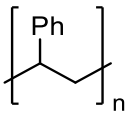
Chapter 4. Design, Synthesis, and Characterisation of Luminophore Functionalised Doped-Ring Opening Co-Polymerisation Polymers

4.2 Introduction

4.2.1 Current Plastics

Plastics, defined as synthetic polymers with an additive, e.g. plasticisers, dyes, and flame retardants, are perhaps the most commonly encountered man-made material: in the UK around five million tonnes of plastic are used every single year.¹ Such findings are unsurprising with plastics being used in all manners, such as packaging² – which accounted for two millions tonnes of plastic in the UK³ – electronic devices,⁴ clothing, and automotive industries.⁵ The majority of these plastics are one of six shown in Table 4.1, and are all synthesised from non-renewable sources.

Table 4.1: Structure and use cases of commonly encountered plastics.

Polymer	Structure	Uses
Poly(ethylene terephthalate) (PET)		Drinks bottles, medicine bottles, food grade pots, tubs, and trays
High density poly(ethylene) (HDPE)		Soap/detergent, and bleach bottles, black bags, milk bottles
Low density poly(ethylene) (LDPE)		Clingfilm, sandwich bags, plastic shopping bags
Polyvinyl chloride (PVC)		Plumbing pipes, cables, and some fencing
Poly(propylene) (PP)		Reusable food containers, bottle caps, labels
Poly(styrene) (PS)		Plastic utensils, packing material (peanuts, Styrofoam)

With almost 360 million tonnes of new plastic being produced every year,⁶ recycling of these materials has become an important avenue of research. However, since only 46% of plastic packaging is recovered or recycled in the UK,³ development of improved recycling methods, or bio renewable/biodegradable plastics is crucial.

Chapter 4. Design, Synthesis, and Characterisation of Luminophore Functionalised Doped-Ring Opening Co-Polymerisation Polymers

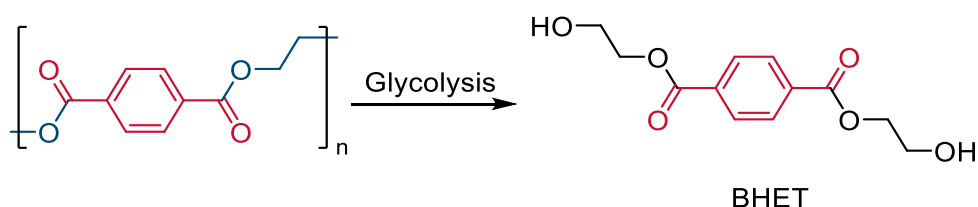
Recycling can be broken down into four areas: Primary, secondary, tertiary, and quaternary. Of these, primary and secondary are mechanical processes that seek to reuse the polymer as-is, without additional chemical processes. Tertiary is chemical degradation back to monomers, or monomer precursors, and quaternary, the least desirable, involves incineration of the material to recover energy.⁷

Poly(ethylene), and the structurally similar, poly(propylene) are among the most difficult waste plastics to recycle, due to the chemically inert nature of the carbon-carbon bonds that make up the backbone. Work by Emri studied the effect of repeated melt extrusion cycles on the properties of LDPE to simulate repeated recycling. Over the course of 100 cycles the melt flow index (MFI) decreased dramatically from 2.25 g/10 min for virgin polymer to 0.02 g/10 min creating an almost unworkable material, even after 10 cycles the MFI had dropped to around 0.6 g/10 min. A similar result was observed for the number-average molecular weight, M_n , decreasing from ~32,000 to ~21,000, to 13,000 after 0, 10 and 100 cycles respectively.⁸ These results indicate that a mixture of chain scission and crosslinking occur during the mechanical recycling process, greatly altering the properties and making the recycled material less desirable, after even a limited number of cycles. Similar degradation of physical properties were observed for HDPE,⁹ and are even more pronounced for PP due to oxidation of the tertiary carbon.¹⁰⁻¹² Whilst some of these issues can be remedied by the addition of stabilisers, and additives such as trimethylolpropanetriacrylate (TMPTA),¹³ the effect of these compounds over repeated recycling cycles is not fully understood.¹⁴ Since these plastics have a rather short mechanical recycling lifetime, they rapidly progress to the tertiary and quaternary recycling procedures.

Expectedly, the inert backbone of the plastics renders pyrolysis the only effective means of depolymerisation. Both thermal and catalytic routes have been employed, such as heating PP and HDPE at 300 or 350 °C to yield an oil comprised of various hydrocarbons in the C_6 to C_{16} range,¹⁵ which has been claimed could be used a crude oil and further separated and used as blend with fuel,¹⁶ or used as a feedstock for the creation of new plastics.¹⁷ Catalytic approaches, using zeolites, have proven adept for dealing with mixed waste streams^{18,19} reducing burden on pre-processing checks. Poly(propylene) has been successfully converted back into the propylene monomer in up to 73% yield by Grossmann and co-workers²⁰ using a plasma reactor, however, the cost involved with this method make it a less than ideal approach.

Chapter 4. Design, Synthesis, and Characterisation of Luminophore Functionalised Doped-Ring Opening Co-Polymerisation Polymers

Poly(ethylene terephthalate), similarly, experiences issues with primary and secondary recycling, as demonstrated by Rodríguez²¹. After just five extrusion cycles, both M_n and M_w had decreased to less than a third of the virgin polymer, along with reductions in the tensile and impact parameters suggesting significant decomposition of the polymer. Such issues significantly limit the number of times PET can be recycled before chemical depolymerisation must be employed. Fortunately, the ester functional groups provide an easy target for depolymerisation methods. A range of degradation routes have been examined, such as hydrolysis under acidic or basic conditions, as well as glycolysis. Acidic hydrolysis can be conducted with a range of concentrated acids, such as sulfuric,²² and nitric acid,²³ and is typically very fast, producing terephthalic acid within five minutes.²⁴ However, separation of the monomers requires various steps of raising and lowering the pH to precipitate the diacid, and organic extraction to obtain ethylene glycol. Whilst effective, the volume of acid and solvents needed are significant drawbacks. Base hydrolysis can be performed at much lower concentrations than acid hydrolysis – hydroxide concentrations between 4 and 20 wt% have been demonstrated – although reactions times are significantly longer (3 – 5 hours).²⁵ However, the terephthalic acid salt produced, will still need to be converted back to the diacid before it can be used as a feedstock. Glycolysis of PET (Scheme 4.1), has proven to be an effective method of chemical degradation, producing Bis(2-hydroxyethyl) terephthalate (BHET) as the major product, which can then be used in the formation of new PET. Although PET is not readily soluble in glycols, Zhang's group demonstrated DMSO with a zinc acetate catalyst was able to produce 83% BHET within a minute at 165 °C.²⁶ Ionic liquids have also attracted interest as catalyst for this transformation due to their high recyclability, and affording complete conversion of PET and a similar BHET yield to the zinc acetate catalysts, but at a reduced loading.²⁷



Scheme 4.1: Glycolysis of poly(ethylene terephthalate).

Chapter 4. Design, Synthesis, and Characterisation of Luminophore Functionalised Doped-Ring Opening Co-Polymerisation Polymers

4.2.2 Tuning Polymer Properties

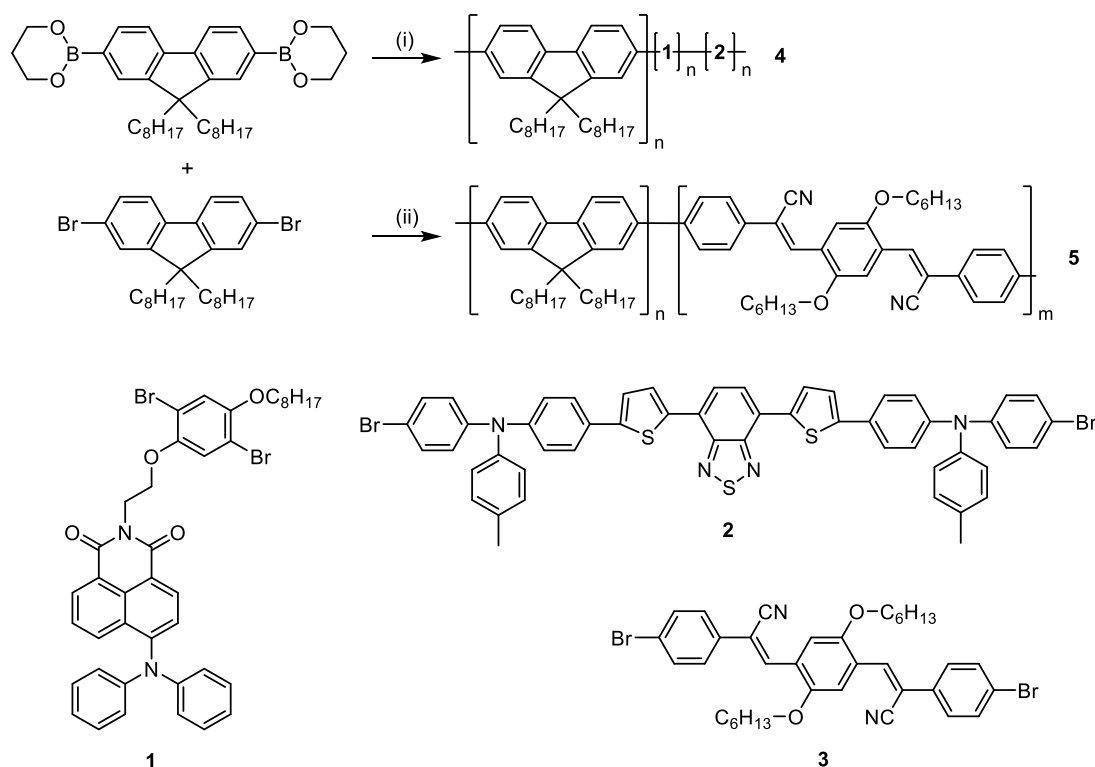
Polymers rarely possess all the required properties for a particular application, and additives are invariably added to enhance, or confer these desired properties; additives typically include flame retardants, plasticizers, or dyes.²⁸⁻³⁰ Whilst blending of these additives typically hinders reprocessing, dyes have a greater impact in plastic recyclability, as the additive is often impossible to fully remove, contaminating the newly formed plastic. Or in the case of black coloured plastics, that account for 50% of all automotive and electronic plastic waste,³¹ they are undetectable by the automated system, further increasing plastic waste.³² Since coloured plastics comprise up to 90% of hard plastics in recycling centres,³¹ this presents a significant hurdle for continued recycling of these materials. Ng's group showed mixing of ABS plastic with coloured masterbatches can significantly increase both the elongation and stress at break, compared to the unmixed plastic.³³ In the case of PET, addition of the dye has been reported to decrease the viscosity, and increase the amount of carboxylic end groups and diethylene glycol units.²⁸ Expectedly, as these additives are not bound to the polymer, leaching of additives into the environment is a serious concern. Scholz-Böttcher and co-workers examined the impact of salt water and UV radiation on the leaching of additives from poly(ethylene), poly(styrene), poly(ethylene terephthalate), and poly(vinylchloride). In all cases, leaching was observed. Of particular interest, is the significant increase in release of additives observed for printed poly(ethylene) compared to non-printed samples, and was found to be the largest source of additives in all the tested plastics.³⁴ Similar results were observed by Hur for PVC, and PS when exposed to artificial freshwater.³⁵ These results underpin the importance of the development of polymers with either covalently bound additives, or polymers that can be easily synthesised from a range of monomers to generate the desired properties without the addition of additives.

4.2.3 Luminescent Polymers

Work on luminescent polymers, within the literature, can be split into three areas: mixing the luminophore with a pre-synthesised polymer, creation of a novel polymer that either contains a luminophore, or becomes the luminophore due to polymerisation, and lastly post-polymerisation modification of a polymer to incorporate the luminophore. Since leaching of non-covalent bound additives is an issue, this area of the literature will not be discussed and will instead focus on the covalently bound luminophore/polymer systems.

Chapter 4. Design, Synthesis, and Characterisation of Luminophore Functionalised Doped-Ring Opening Co-Polymerisation Polymers

Initial work regarding luminescent polymers revolved around the poly(fluorene) system, with the addition of dopants affording tunability to the emission properties. Wang's group showed the poly(fluorene) and Suzuki reaction framework could be exploited to introduce two dopants, **1**, and **2**, to synthesise the first reported case of a single polymer with blue, green, and red emission (**4**, Scheme 4.2).³⁶ Emission from all three states was observed simultaneously, with charge transfer from the poly(fluorene) backbone onto the dopants. Promisingly, they note no energy transfer from the green luminophore (**1**) to the red luminophore (**2**) due to the large distance between the dopants, and the low chance of spatial association due to the low doping concentrations. Chen and co-workers, similarly, demonstrated the versatility of this approach by introducing the green luminophore, **3**, displaying efficient energy transfer from the poly(fluorene) backbone. However, polymers produced through this route typically show a broad poly-dispersity greater than 1.9 and contain no easily cleaved bonds making them ill-suited to the design of future plastics.

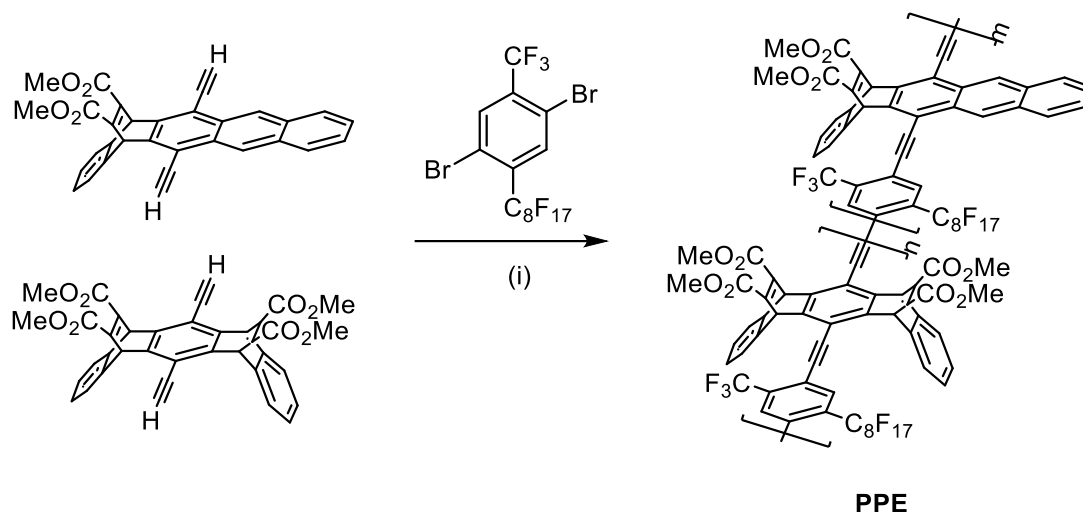


Scheme 4.2: Example synthesis of poly(fluorenes) doped with luminophores/chromophores; (i) Pd(PPh₃)₄, K₂CO₃, **1**, **2**, toluene;³⁶ (ii) Pd(PPh₃)₄, K₂CO₃, **3**, toluene.³⁷

Swager's group prepared a poly(*p*-phenylene ethynylene) (**PPE**) co-polymer (Scheme 4.3), which they claim does not suffer from blue to green emission shift as the poly(fluorene) polymers do. A THF solution of the polymer shows a strong blue emission at 437 nm, after excitation at 375 nm. Interestingly, exposure to water

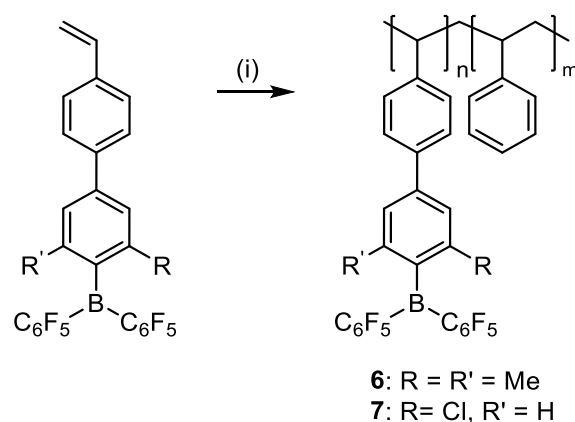
Chapter 4. Design, Synthesis, and Characterisation of Luminophore Functionalised Doped-Ring Opening Co-Polymerisation Polymers

causes aggregation of the particles and a shift in emission to 512 nm. They note, however, that this colour change was not reversible after addition of the green fluorescent polymer to THF.



Scheme 4.3: Synthesis of the **PPE** co-polymer. (i) Pd(PPh₃)₄, CuI, toluene, ⁱPr₂NH.

Whilst the previous examples showed strong luminescent properties, they used novel polymers with limited broader applications. Jäkle demonstrated the combined fluorescence and catalytic activities of triarylborane/styrene polymers, Scheme 4.4. The emission of the polymer was found to be tuneable, with an emission of 490 nm for polymer **7**, and a green emission at 543 nm for polymer **6**, which also showed a longer fluorescent lifetime and a higher quantum yield. Taking advantage of the tethered Lewis acidic borane, hydrosilylation reactions were conducted. With a catalyst loading of 0.05 mol%, both polymers proved to be effective catalysts with polymer **7** showing complete conversion of all substrates.

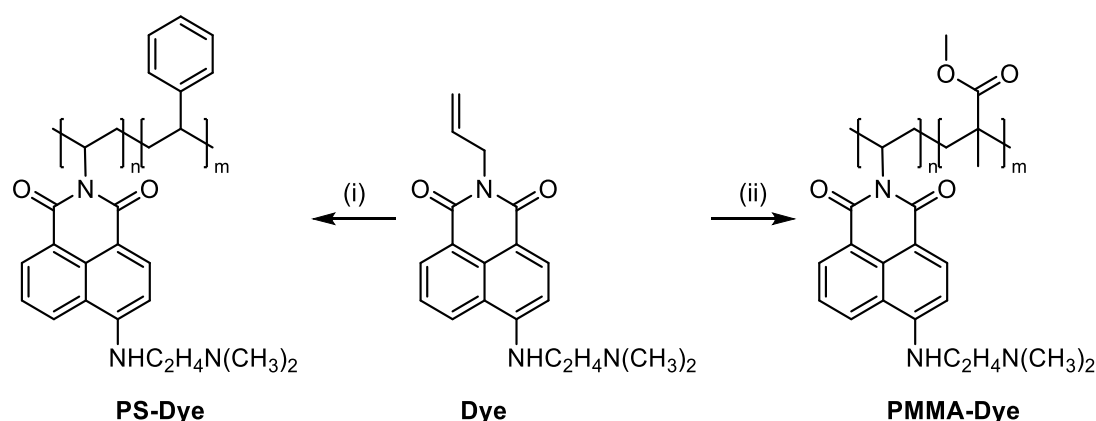


Scheme 4.4: Synthesis of triarylborane containing polymers; (i) Styrene, AIBN, anisole.³⁸

Grabchev and co-workers, used a similar approach to introduce a dopant level amount (1 wt%) of a naphthalimide dye (**Dye**) into poly(styrene) (**PS-Dye**) and

Chapter 4. Design, Synthesis, and Characterisation of Luminophore Functionalised Doped-Ring Opening Co-Polymerisation Polymers

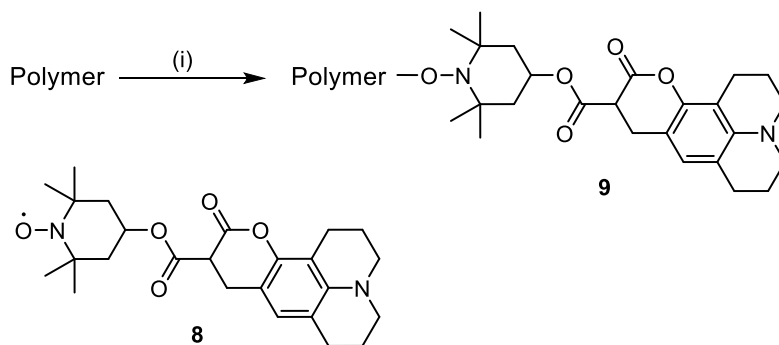
poly(methyl methacrylate) (**PMMA-Dye**) for photoinduced electron transfer (PET).³⁹ Expectedly, the prepared polymers exhibited the yellow/green colouration from the dye. However, both polymers showed an increase in the energy of emission transitions ($\lambda_{em} = 485$ nm), and absorption ($\lambda_{abs} =$ **PS-Dye**: 385 nm, **PMMA-Dye**: 396 nm), compared to the monomer ($\lambda_{abs} = 429$ nm, $\lambda_{em} = 502$ nm). Introduction of the coordinating diamine group in the 4-position of the naphthalimide presents an interesting application of doped polymers as sensors, taking advantage of the unique properties of both the dopant, and the polymer.



Scheme 4.5: Synthesis of co-polymers using a naphthalimide dye. (i) Styrene, DBP, N₂; (ii) methyl methacrylate, DBP, N₂³⁹

Recent work by Ito, displayed a post-polymerisation modification approach using mechanoradical coupling of a luminophore to the chemically inert plastics PS, PE, as well as poly(methyl methacrylate), poly(phenylene sulfide), and poly(sulfone) (Scheme 4.6).⁴⁰ Taking advantage of the tendency for the polymers to form radicals under mechanical stress through polymer cleavage, they were able to couple the fluorescent molecule, **8**, through the nitroxide radical generating a tagged polymer, **9**. Trapping of this radical restored the luminescent property of the coumarin moiety, which also functioned as an indicator that the reaction had occurred. Whilst this route provides a quick and effective means to introducing a covalently bound luminophore to a range of plastics, the emission was not consistent across the five different polymers. Although PE, PS, and PMMA displayed a blue emission with λ_{max} values of 456, 478, and 480 nm respectively, PPS and PSF resulted in yellow tinged emission with λ_{max} values of 498 and 517 nm respectively. The red shift in emission is claimed to be caused by aggregation of the coumarin groups. Additionally, the method of incorporation, chain scission, caused a significant reduction in the molecular weight (M_n) – in the best-case scenario a drop from 204 to 38.3 kg/mol was observed – with a similar increase of the dispersity by ca. 50%.

Chapter 4. Design, Synthesis, and Characterisation of Luminophore Functionalised Doped-Ring Opening Co-Polymerisation Polymers



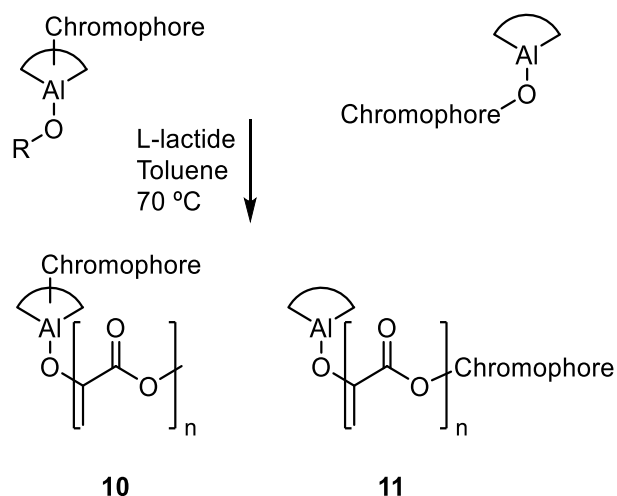
Scheme 4.6: Synthesis of fluorescent polymers via mechanoradical coupling; (i) **1**, 30 Hz milling for 30 mins.⁴⁰

4.2.4 Sustainable Polymers

Poly(lactide) (PLA) is one example of a new class of polymers, which are both biodegradable and bio-derived from renewable sources.^{41–43} As with the earlier bulk polymers, PLA is not coloured and requires modification to achieve the range of colours expected from plastics. Typically, dyeing of PLA occurs after the polymer has been processed through knitting and weaving into fibres. The first step of the process involves cleaning of the fibres with a detergent and sodium carbonate at 60 °C to remove hydrophobic additives from the initial processing. The dyeing process is then carried out using disperse dyes at around 130 °C,⁴⁴ then exposed to reducing conditions to remove excess dye and ensure a colour fast product. All of these steps produce waste, diminishing the green credentials of PLA. Work by McGowan⁴⁵ studied the incorporation of a dye into the polymerisation procedure either bound to the catalyst (**10**) or used as an initiator (**11**, Scheme 4.7). Using a range of initiators, they were able to synthesise a set of yellow, red, and purple PLA based polymers with a melting point range similar to commercial, undyed PLA. Combining both the yellow and purple polymers in a melt-spinning process, McGowan was able to achieve a strongly coloured black fibre that is of particular interest due to the difficulties in achieving black dyed PLA. Pleasingly, they note no loss of colour or staining when testing the colourfastness of the fibres. Comparison of the DyeCat and commercial fibres using optical microscopy, show the dye to be evenly dispersed throughout the entire width of the strand with the DyeCat procedure, whilst the commercial disperse dyeing technique showed poor colouration. This deep colouration is all the more impressive when the amount of dye required is taken into consideration. The DyeCat procedure utilises only 0.5-0.7 wt% dye by mass, compared to the commercial method requiring between 2 and 10 wt%. However, whilst this demonstrates the effectiveness of PLA as a textile, the

Chapter 4. Design, Synthesis, and Characterisation of Luminophore Functionalised Doped-Ring Opening Co-Polymerisation Polymers

fixed glass transition temperature of 55 °C,⁴⁶ and lack of tuneability in mechanical properties, limits the applications.

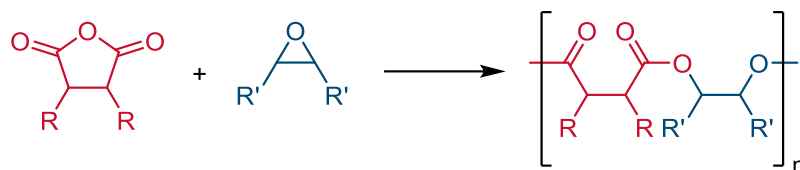


Scheme 4.7: Example approaches of chromophore introduction via the DyeCat process: chromophore attached to the ligand, or as the ligand (**10**) and as an initiator (**11**).

4.2.5 Ring Opening Co-Polymerisation (ROCOP)

The bulk properties of any given polymer are dependent upon its chemical identity, be that the identity of the monomer, molecular weight, dispersity, or the existence of side chains or functional groups. Any desired modification of these bulk properties will require a subsequent change in the monomer(s) used. Since there is a larger library of epoxides and anhydrides which are used in combination with each other, than lactones, a substantial matrix of molecular identities, and thus properties, should be achievable using these two classes of monomer. In this work the co-polymerisation of epoxides and anhydrides is explored (Scheme 4.8). These monomers are of particular importance due to the range of commercially available substrates, and the ease of synthesising new substrates – epoxides are well known to be synthesised under a range of conditions. To be considered as a plastic replacement, the synthesised polymers need to have well controlled and defined properties. A predictable, and reproducible dispersity and molecular weight is one such measure. Therefore, a significant amount of work within the literature of ROCOP polymers is focused on the development of catalysts and characterisation of the synthesised polymers' molecular weight and dispersity.

Chapter 4. Design, Synthesis, and Characterisation of Luminophore Functionalised Doped-Ring Opening Co-Polymerisation Polymers



Scheme 4.8: Generalised Ring Opening Co-Polymerisation (ROCOP) of a cyclic anhydride and epoxide to form a polyester.

Porphyrin based catalysts were among the first reported to achieve an alternating polymer microstructure and high molecular weights, through the use of ancillary ligands to help control the polymerisation reaction. Work by Inoue in 1985⁴⁷ showed complexes **11**, and **12** (Figure 4.2) with a quaternary ammonium or phosphonium catalyst was capable of achieving a highly alternating structure of phthalic anhydride and propylene oxide with high molecular weights that are comparable to the theoretical molecular weight, and a narrow dispersity (\bar{D}) around 1.1, at room temperature.

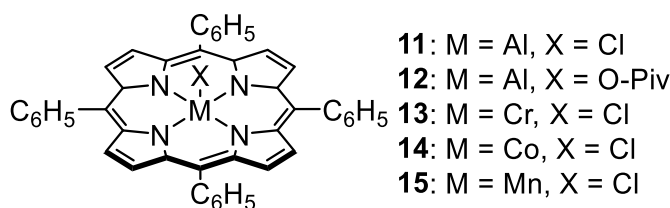


Figure 4.2: Porphyrin catalysts for the co-polymerisation of epoxides and anhydrides.

More recently, Duchateau and co-workers investigated the chromium complex, **13**, with a set of five anhydrides (succinic anhydride, cyclopropane-1,2-dicarboxylic anhydride, cyclopentane-1,2-dicarboxylic acid anhydride, and phthalic anhydride) with cyclohexene oxide at 100 °C.⁴⁸ In the absence of a cocatalyst the co-polymerisation of succinic anhydride and cyclohexene oxide was observed to be poor, with the majority of the polymer being poly(cyclohexene oxide), with only 14% ester bond formation in bulk epoxide and 0% in toluene. Addition of 4-dimethylaminopyridine (DMAP) as a cocatalyst, however, increased the ester selectivity to 100% and increased the solution conversion of epoxide to 81%, compared to less than 10% without DMAP. Similarly promising results were seen for the other anhydrides, showing perfectly alternating co-polymers, and complete conversion of the epoxide within 140 and 300 minutes for bulk and solution reactions, respectively. Although, the molecular weights for all but phthalic anhydride were significantly lower than the theoretical values, and dispersity was found to be moderate ($1.2 < \bar{D} < 1.6$). The discrepancy in experimental molecular weight was claimed to be caused by cyclisation or chain transfer reactions with

Chapter 4. Design, Synthesis, and Characterisation of Luminophore Functionalised Doped-Ring Opening Co-Polymerisation Polymers

water. Using styrene oxide and phthalic anhydride as an exemplar they also compared three different metals (**13**, **14**, and **15**) for co-polymerisation. The chromium complex proved to be the most active catalyst converting 100% of the epoxide, followed by cobalt, and manganese, with the specific ordering dependant on whether the reaction was conducted in bulk epoxide, or toluene.⁴⁹

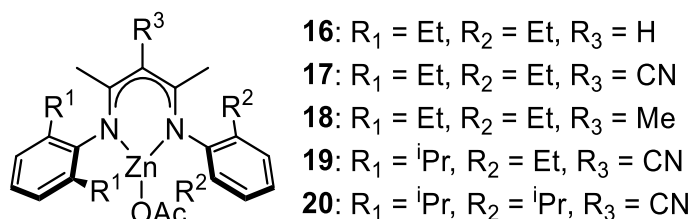


Figure 4.3: Structure of β -diimine zinc catalysts.

β -diimine zinc complexes, prepared by Coates, have shown to be highly active catalysts whilst co-polymerising of a range of epoxides and anhydrides.⁵⁰ Initial screening of diglycolic anhydride and cyclohexene oxide showed complexes **16**, and **18**, that do not contain the electron withdrawing nitrile group, decomposed rapidly upon addition of the anhydride even at 25 °C. Steric bulk was similarly shown to have a profound effect on the conversion of the monomers. Whilst both **17**, and **20** showed catalytic activity, conversion was, at best, only 33% for **20**, with both complexes showing low molecular weights. Complex **19** with a steric bulk between **17**, and **20**, proved to be the most effective with a conversion of 79%. With the initial success, a substrate scope was conducted with a set of epoxides (cyclohexene, vinylcyclohexene, limonene, propylene, cis-butene, and iso-butylene oxides) using diglycolic anhydride and limited testing with succinic and maleic anhydrides. All epoxides with diglycolic anhydride were shown to form co-polymers, with limonene oxide requiring slightly higher temperatures. The successful co-polymerisation of maleic anhydride with limonene oxide was surprising to the authors, as they noted earlier difficulties using maleic anhydride. Molecular weights were high, ranging from 10,000 up to 55,000 g/mol, with dispersity ranging from 1.1 to 1.5. However, this same catalyst struggled with the co-polymerisation of maleic anhydride and propylene oxide, with only 5% conversion and 14% selectivity.⁵¹

Salicylaldehyde and amine condensation complexes (Figure 4.4) are comparatively recent contenders in ROCOP catalysis. One of the first reported applications being by Duchateau in 2011,⁴⁸ using the salophen complex, **21**, for the co-polymerisation of CHO with SA, CPrA, CPA, and PA with a DMAP co-catalyst. As with complex **13**, the use of a co-catalyst is essential to obtain a high ester selectivity, and in the case

Chapter 4. Design, Synthesis, and Characterisation of Luminophore Functionalised Doped-Ring Opening Co-Polymerisation Polymers

of SA, any conversion when not used with an excess of epoxide. The salophen catalyst was observed to be a slower catalyst than **13**, although selectivity was similar for all but CPrA. Promisingly, molecular weights, while slightly lower than **12**, exhibited the same dispersity. Expanding upon this, Duchateau examined the influence of the metal centre upon the co-polymerisation of styrene oxide (SO) and phthalic anhydride.⁴⁹ Expectedly, the chromium complex performed well, producing good molecular weight polymers with a narrow distribution, and 100% CHO conversion. Aluminium (**22**, Figure 4.4), manganese (**23**), and cobalt (**25**) complexes, however, were not as effective, with aluminium proving the second best (60% CHO conversion), followed by cobalt (59%) and manganese (39%). Coates further explored complexes **21**, **22**, and **24** for the co-polymerisation of propylene oxide (PO), and a racemic mix of tricyclic anhydride, with a PPNCI cocatalyst.⁵² **21**, once again, proved to be the fastest catalyst, and cobalt the slowest. However, whilst the aluminium catalyst was not the fastest, it was able to maintain a reasonably low dispersity ($\mathcal{D} < 1.3$) and a very high $> 90\%$ opening of the *cis* anhydride at full conversion, unlike the chromium catalyst that experienced a drop to 52% *cis* at full conversion of the anhydride. This promising result, extended to at least 800 equivalents of anhydride and demonstrated the potential of aluminium salophen catalysts.

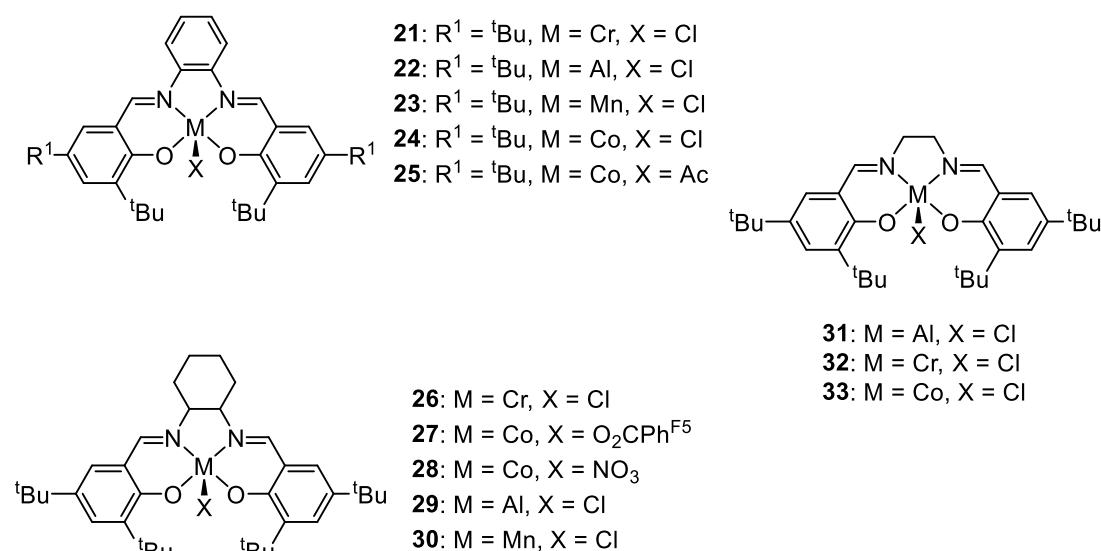


Figure 4.4: Examples of salicylaldehyde/amine based catalysts used for the co-polymerisation of epoxides and anhydrides.

Catalysts with saturated backbones have also been extensively explored in the literature. Coates and colleagues, using the cyclohexane diamine derived complexes **26**, and **27**, demonstrated the highly active nature of the chromium complexes. Cobalt complexes, once again, proved ineffective for polymerisation of

Chapter 4. Design, Synthesis, and Characterisation of Luminophore Functionalised Doped-Ring Opening Co-Polymerisation Polymers

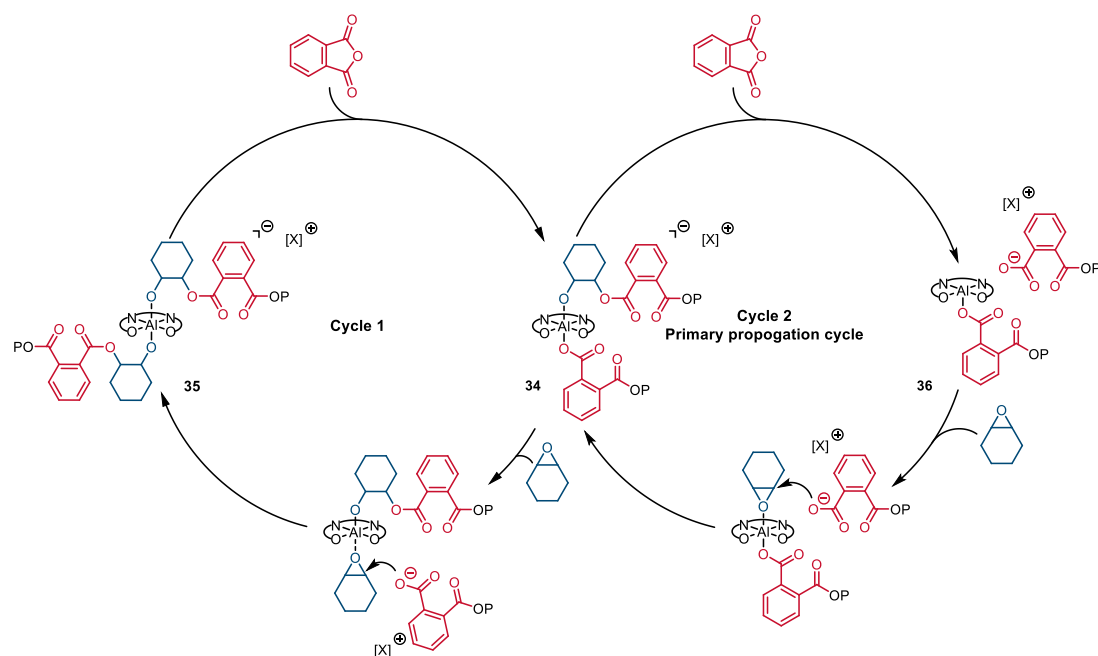
propylene oxide and maleic anhydride. The scope of monomers was expanded to include epichlorohydrin (ECH), allyl glycidyl ether, as well as glycidyl ethers and perfluorinated species. As before, the chromium complexes displayed high conversion, ester selectivity, and molecular weights, with reasonable dispersity ($1.1 < \mathcal{D} < 1.7$).⁵¹ Complexes **26**, **29**, and **30**, have also been trialled for the co-polymerisation for a set of epoxides and anhydrides. Camphoric anhydride and propylene oxide at 30 °C with PPNCI, follows the same trend as before, i.e. chromium > aluminium > manganese. Interestingly, swapping the epoxide for cyclohexene oxide, increasing the temperature to 70 °C and adding two equivalents of PPNCI showed aluminium as the best performing catalyst with a high molecular weight and low dispersity ($\mathcal{D} < 1.3$). Polymerisation with limonene oxide was also achievable.⁵³

Lastly, ethylene diamine derived ligands, known as salen ligands, have also been examined in the co-polymerisation of cyclohexene oxide with a range of anhydrides, and a DMAP cocatalyst. Regarding the aluminium catalyst (**31**), the degree of CHO conversion relied heavily upon the anhydride used, with PA showing complete conversion, and high molecular weights but a broad dispersity ($\mathcal{D} = 2.3$). SA, and CPrA, however, both showed low conversion, and low molecular weights. Chromium (**32**) and cobalt (**33**) complexes, both showed similar results to aluminium with high conversion, molecular weights, but low dispersity ($1.2 < \mathcal{D} < 1.3$) for phthalic anhydride. SA and CPrA, however, whilst displaying high conversion and low dispersity, show very low molecular weights as observed with the aluminium complex.⁵⁴

The mechanistic pathway for the co-polymerisation of cyclic anhydrides and epoxides is still not fully understood. However, recent work by the Coates and Tolman groups have examined potential pathways through a combined computational and experimental study.⁵⁵ Earlier work demonstrated that the polymerisation initiation is consistent with the ring opening of two coordinated epoxides by chloride anions.⁵⁶ After formation of this initial aluminium bis-alkoxide species, analogous to complex **35** (Scheme 4.9), reaction with an anhydride to form complex **34** is the reasonable step towards the formation of AB type polymers. This central complex can now either react with an epoxide (cycle 1) or an anhydride (cycle 2). They found the reaction rate of complex **34** with anhydrides was 50 times faster than with the epoxide, suggesting cycle 2 is the main source of polymer growth, with cycle 1 becoming the major path when conversion of anhydride nears

Chapter 4. Design, Synthesis, and Characterisation of Luminophore Functionalised Doped-Ring Opening Co-Polymerisation Polymers

100%. Thus, the rate determining step is the ring opening of the epoxide by an anhydride. As the reactivity of the initiator, epoxide, and anhydride all play a role in the formation of the polymer, alterations to these reactants could be expected to change the propagation process. For example, an epoxide far more reactive than the butylene oxide exemplar used by Coates and Tolman may be expected to either, favour cycle 1 which they claim is more likely to promote side reactions, or primarily form a poly(ether) species. Similarly, a less reactive, or unreactive anhydride will favour cycle 1, or not even allow for propagation of polymerisation. In the case of DMAP, the ring opening of the epoxide would occur through the amine of the pyridine group generating a zwitterionic polymer species taking place of the PPN cation. However, the monomers, and co-catalyst used in this work are not expected to differ significantly from the reported scheme.



Scheme 4.9: Proposed catalytic cycle for phthalic anhydride and cyclohexene oxide co-polymerisation with a PPNCI co-catalyst. Adapted from Coates and Tolman.⁵⁵

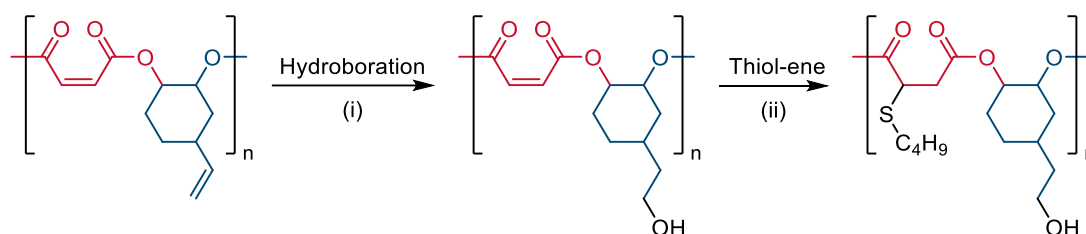
The ROCOP process of forming poly(esters) revolves around the sequential addition of monomers onto an active site in a chain growth polymerisation. Poly(ethylene terephthalate), however, is prepared through a poly-condensation reaction in a step growth process and requires the continual removal of by-products to prevent hydrolysis of the polymer chains. The reactivity of multiple growing chains with each other, and surrounding monomers, results in a high dispersity, with PET having values reported between 1.6 and 2.4.⁵⁷ Polymers produced through ROCOP typically exhibit a dispersity around 1.2, allowing far greater control over the properties of the polymer. Additionally, the lower reaction temperatures and the lack

Chapter 4. Design, Synthesis, and Characterisation of Luminophore Functionalised Doped-Ring Opening Co-Polymerisation Polymers

of continuous distillation make this new class of polymer an attractive prospect for the future of plastics.

4.2.5.1 Post-Polymerisation Modification

Post-polymerisation modification is a common technique used to impart additional properties to a ROCOP polymer, outside of those offered by the constituent monomers. Hydroboration⁵⁸, and thiol-ene click chemistry^{59–61} (Scheme 4.10) have both been used to modify the properties of the polymer.⁶² Briefly, by introducing a tolerated functional group, such as an alkene, further reactivity can be exploited to install groups that are not tolerated during polymerisation, such as alcohols or carboxylic acid groups.^{63,64} These groups can then alter physical properties, such as the glass transition temperature, or tune the solubility of the polymer.



Scheme 4.10: Hydroboration and thiol-ene coupling of ROCOP polymers.⁶⁴

4.2.5.2 Degradation of Polyesters

Although little work exists on degradation of polymers produced via the ROCOP process, a plethora of work exists on the degradation of polyesters through both chemical, and enzymatic^{65,66} means. The Williams group examined the degradation of a combined poly(lactide) cyclohexene oxide and phthalide co-polymer ($M_n \sim 100$ kg/mol) using acid catalysed, and enzymatic hydrolysis. Acidic hydrolysis using *p*-toluenesulfonic acid in toluene at 60 °C showed a reasonable rate of degradation: 60% mass loss after only four hours, and after 70 hours they report only oligomers remain ($M_n < 10$ kg/mol, $\bar{D} > 1.6$). However, after this point the reaction rate dramatically slows down, after 500 hours oligomers remain, albeit smaller than before (M_n 3.6 kg, $\bar{D} > 2.16$). In separate tests, it was observed the ROCOP co-polymer showed a degradation rate roughly half of the poly(lactide), which they attributed to the more rigid ester linkage. They also postulate the reduction in rate may be linked to a reduction of the water concentration as hydrolysis proceeds, as well as decreased solubility in toluene as hydrophilic groups make up a greater proportion of the substrate. Interestingly, even though more polar solvents like THF, acetone, and methanol, were tested, the degradation rates were all far slower than with toluene. Exposing the polymer to simulated biological conditions – phosphate

Chapter 4. Design, Synthesis, and Characterisation of Luminophore Functionalised Doped-Ring Opening Co-Polymerisation Polymers

buffered saline solution, at 37 °C, with a lipase enzyme – displayed minor degradation, with only a 58% decrease in molar mass after 4 months.

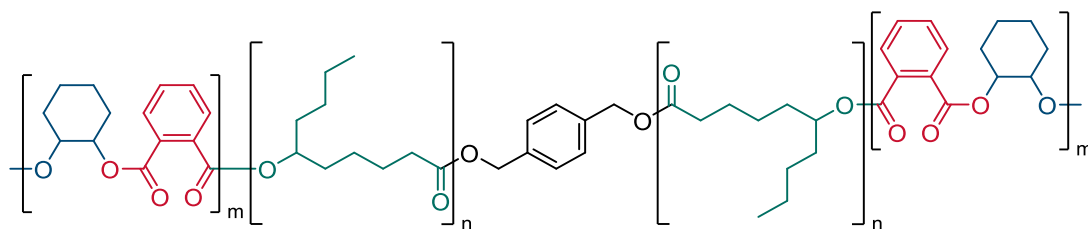
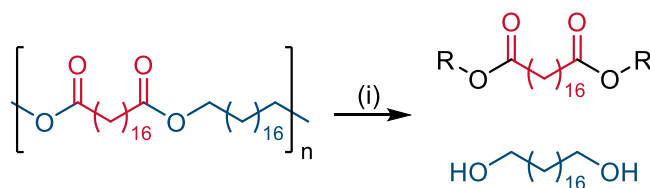


Figure 4.5: Structure of the polymer degraded by the Williams group.⁶⁷

Häußler recently demonstrated a methanolysis approach to the degradation of bio-renewable polyesters with poly(ethylene) like qualities (Scheme 4.11). Exposing the polymer to methanol at 150 °C for 12 hours showed complete conversion of the polymer into the parent diol and ester. Although, the reaction temperatures were well in excess of the boiling point for methanol, this shows a promising approach towards the closed loop recycling of polyesters.

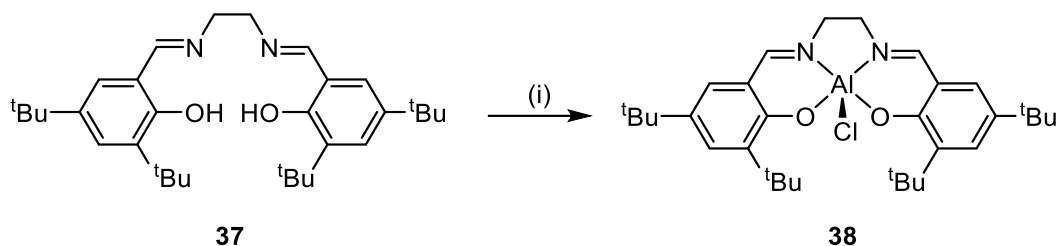


Scheme 4.11: Degradation of a polyester via methanolysis; (i) MeOH, 150 °C, 12 h.⁶⁸

Chapter 4. Design, Synthesis, and Characterisation of Luminophore Functionalised Doped-Ring Opening Co-Polymerisation Polymers

4.3 Results and Discussion

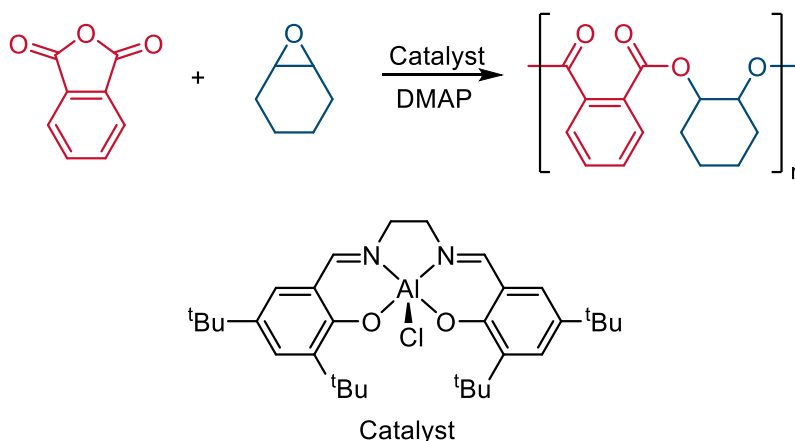
4.3.1 Catalyst Synthesis



Scheme 4.12: Synthesis of aluminium(3,5-ditertbutyl)chloride. (i) Diethylaluminium chloride, toluene.

Synthesis of the luminescent aluminium complex (**38**, Scheme 4.12)⁶⁹ was carried out using the Salen pro-ligand, **37**, and diethylaluminium chloride. Due to the pyrophoric nature of the aluminium starting material, the reaction was carried out using standard Schlenk techniques under an argon atmosphere. Stirring for an hour produced a slurry of the desired luminophore in high yields, which was easily purified by repeated washing with hexane and removal of the solvent. Production of the complex was observed through ¹H NMR analysis, showing loss of the hydroxyl proton environment at 13.63 ppm, and shifts in the phenyl and imide protons from 7.06 and 7.35 to 7.00 and 7.5 ppm, and 8.39 to 8.3 ppm respectively. As the catalyst is also a strongly luminescent material, it provided an efficient method of synthesising a luminescent polymer.

4.3.2 Polymer Synthesis



Scheme 4.13: General route for the synthesis of ROCOP polymers.

ROCOP polymers were easily synthesised in a one pot reaction using the [Al(^tBu-Salen)Cl] pre-catalyst, and a DMAP co-catalyst, along with phthalic anhydride and cyclohexene oxide monomers (Scheme 4.13). These two monomers were chosen

Chapter 4. Design, Synthesis, and Characterisation of Luminophore Functionalised Doped-Ring Opening Co-Polymerisation Polymers

as they polymerise easily under the conditions used in this work, producing polymers with a low dispersity (\mathcal{D}) and high molecular weight. Production of the polymer was monitored using ^1H NMR spectroscopy; the resonances attributed to the anhydride group shift from around 8 ppm in the monomer, to around 7.65 ppm in the polymer. Integration of these two regions was used to determine the reaction conversion. The degree to which the microstructure of the polymer is alternating was also determined using ^1H NMR spectroscopy. The sequential addition of alternating epoxides and anhydrides gives rise to ester groups between the monomers, whereas the homopolymerisation of epoxide (undesired side reaction) gives rise to ether linkages. Therefore, comparison of the ester and ether regions located around 5.0 and 3.5 ppm, respectively (Figure 4.6), affords a measure of the selectivity of the polymerisation. Since incorporation of the dopant relies upon competing with the more abundant cyclohexene oxide monomer, the reactions were carried out in toluene rather than neat epoxide. Additionally, the low concentration of luminophore used in the large scale reactions requires the polymerisation reach completion, determined as being greater than 95% conversion of anhydride, to ensure incorporation of the dopant. GPC provides a measure of both the molecular weight of the polymer and the range of molecular weights (\mathcal{D}) and can be used to determine if the dopant causes an adverse effect upon the polymerisation process. Which will be observed in either the molecular weight or dispersity substantially affected by the dopant.

Chapter 4. Design, Synthesis, and Characterisation of Luminophore Functionalised Doped-Ring Opening Co-Polymerisation Polymers

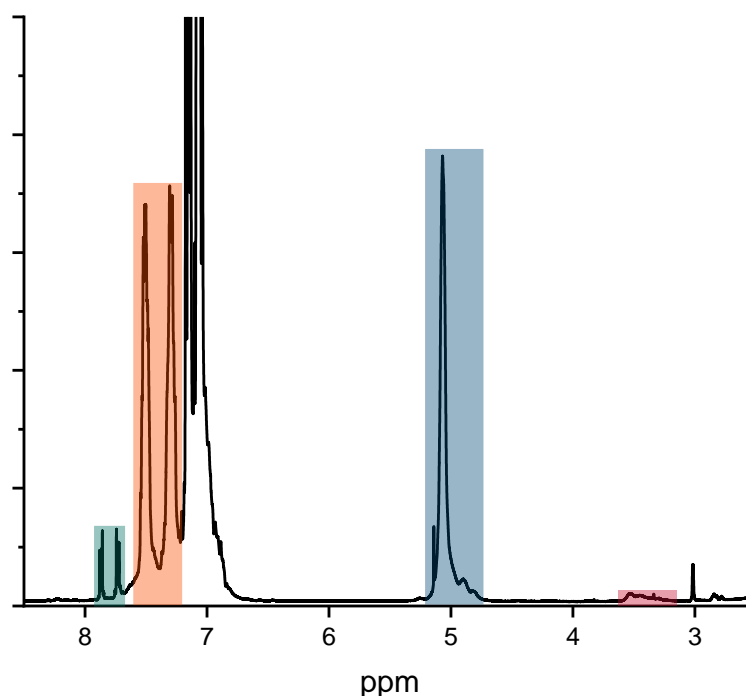


Figure 4.6: Example ^1H NMR spectra of a polymerisation reaction mixture with highlighted regions showing the conversion of monomer (green region) to polymer (orange region) and the selectivity of the ester formation (blue region) vs ether formation (red region)

4.3.2.1 Small Scale Synthesis and Characterisation

Small scale polymer syntheses were conducted in 7 mL screw cap vials at 80 °C using a multi-well hotplate, and the reactions allowed to proceed for 16 hours before precipitation of the polymer using methanol, followed by washing and drying.

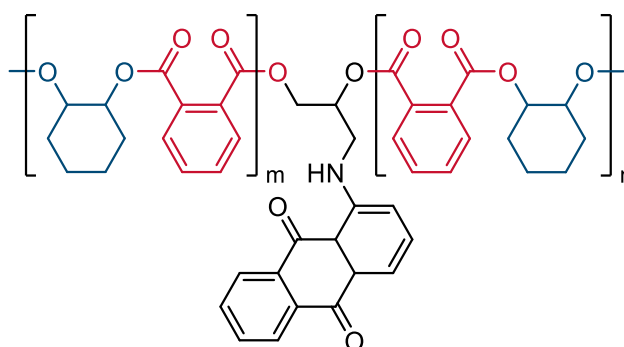


Figure 4.7: Structure of the AAQ doped PhA-CHO co-polymer.

Initial doping of polymers utilised an epoxide substituted 1-aminoanthraquinone based luminophore to form polymers with 0.05 (**AAQ3-PhA-CHO1**) and 0.10 (**AAQ-PHA-CHO2**) equivalents of dopant, substituting some of the cyclohexene oxide. NMR analysis showed ~ 60% conversion of the anhydride monomer after 16 hours, which is the expected result for the catalyst and monomers used. Selectivity of the polymers is difficult to determine with confidence due to potential overlap of the alkyl region of the dopant, and the ether region of the polymer. If no overlap is assumed,

Chapter 4. Design, Synthesis, and Characterisation of Luminophore Functionalised Doped-Ring Opening Co-Polymerisation Polymers

selectivity is determined to be at least 88% and 67% for **AAQ-PhA-CHO1** and **AAQ-PhA-CHO2**, respectively. Regarding dopant incorporation, the theoretical upper limit is predicted to be, based upon full incorporation of the dopant at the expense of cyclohexene oxide and accounting for conversion of the anhydride, 0.08, and 0.16 equivalents for **AAQ-PhA-CHO1** and **AAQ-PhA-CHO2**, respectively. Comparison of the dopant's ring opened epoxide environments with the cyclohexene oxides equivalent protons should provide an estimate of the dopant concentration (Figure 6.29, Appendix). The two dopant regions show the expected 1:2 ratio for both compounds, further supporting the assignment. A ratio of 1:10 of dopant and epoxide is observed for **AAQ-PhA-CHO1**, and 1:4 for **AAQ-PhA-CHO2** which equate to 0.09 and 0.2 equivalents, respectively. Both values are above the predicted maximum, and likely point to issues with measuring out the amount of cyclohexene oxide. However, these results do show that even at relatively low equivalents, the less hindered dopant epoxide is incorporated at a much faster rate than the cyclohexene oxide: as after only 60% conversion all of the dopant has been incorporated into the polymer.

Further analysis by gel permeation chromatography (GPC), a type of size exclusion chromatography, is essential to obtain an understanding of the polymer properties as it provides a measure of both the molecular weight and the distribution of molecular weight across a sample (For a given polymer, the brittleness, hardness, melting point, etc. are influenced by the molecular weight and dispersity). Initial analysis of the GPC trace (black line, Figure 4.8) reported a molecular weight (Mw)

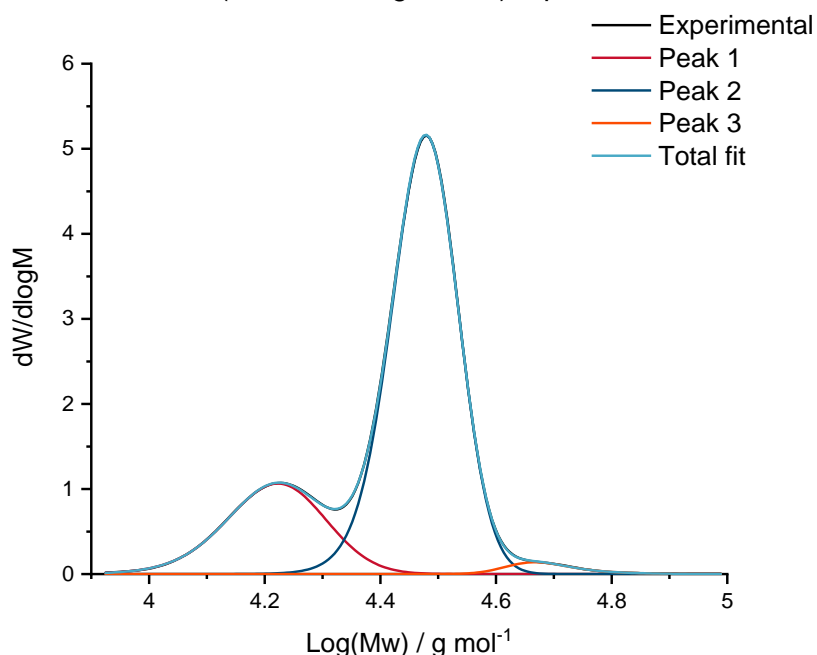


Figure 4.8: Experimental and fitted GPC data for **AAQ-PhA-CHO1**.

Chapter 4. Design, Synthesis, and Characterisation of Luminophore Functionalised Doped-Ring Opening Co-Polymerisation Polymers

and dispersity (\mathcal{D}) of 27,400 g/mol⁻¹ and 1.1, respectively. However, this is a composite value of the three peaks, and does not give a true representation of the polymer(s), which, based upon the GPC trace showed three distinct sets of polymer chains, one of which was a minor high molecular weight component. Deconvolution of this single trace into its individual components can be accomplished by fitting exponentially modified gaussian (EMG) curves⁷⁰ (Equation 4.1) to the data (red, dark blue, and orange lines, Figure 4.8). In traces such as Figure 4.8, three EMG curves are placed with their centre peak approximately lined up with the centre of each expected constituent component and the parameters (a , b , c , and d) optimised through the Levenberg-Marquardt algorithm.^{71,72} In cases where multiple overlapping peaks are involved (see Figure 4.21) the same procedure of placing peaks was followed. However, after the initial optimisation of parameters, additional EMG curves were added where the fit of the peaks was poor compared to the data and the optimisation repeated until a suitable fit was achieved, determined when the weighted sum of squared residuals was ≤ 0.003 .

This higher level of analysis can provide insight into both the polymerisation and degradation of the material by demonstrating whether the trace is comprised of a single broad peak, or multiple peaks with a well-defined dispersity. For example, regarding polymerisation, standard analysis via GPC will provide an overall measure of dispersity which will be dependent on how similar the molecular weight is for each series. If there is little difference, the dispersity will be low, however, if there is a large difference, as is the case for the polymers produced in this work, the dispersity will be higher. Deconvolution of these peaks provide information on how controlled the polymerisation is for each series.

$$y = \frac{ac\sqrt{2\pi}}{2d} \exp\left(\frac{c^2}{2d^2} - \frac{x-b}{d}\right) \left[\frac{d}{|d|} + \operatorname{erf}\left(\frac{x-b}{\sqrt{2c}} - \frac{c}{\sqrt{2d}}\right)\right]$$

Equation 4.1: Exponentially modified gaussian (EMG) used for fitting GPC data as defined in the Fityk program⁷³. Where a = Gaussian height, b = Gaussian centre, c = gaussian width, d = distortion parameter.

GPC traces for both polymers showed two major peaks, and a single minor peak (Figure 4.8, Appendix Figure 6.28). The dispersity of all the peaks was found to vary between 1.01 and 1.04 (Table 4.2) with an overall dispersity of 1.1 for **AAQ-PhA-CHO1** and 1.08 for **AAQ-PhA-CHO2**. Low dispersity values suggested a well-controlled polymerisation, with relatively minor chain transfer events during the polymerisation.

Chapter 4. Design, Synthesis, and Characterisation of Luminophore Functionalised Doped-Ring Opening Co-Polymerisation Polymers

$$M_{w_p} = \frac{(\text{Anhydride Equivalents} \times M) + (\text{Epoxide Equivalents} \times M)}{\text{Number of Growing Chains}} \times \text{Conversion}$$

Equation 4.2: Equation used to determine the predicted molecular weight for the polymers. Where M_{w_p} = predicted molecular weight, and M = molecular weight of the monomer

Following Equation 4.2, the predicted molecular weight was determined as follows, using **AAQ-PHA-CHO1** as an example accounting for the amount of dopant added (5 equivalents):

$$\frac{(400 \times 148) + (395 \times 98) + (5 \times 279)}{3} \times 0.6 \approx 20,000 \text{ g/mol}$$

The predicted molecular weight for **AAQ-PHA-CHO1**, and **AAQ-PHA-CHO2** accounting for conversion is 19,861, and 20,042 g/mol, respectively, or approximately 20,000 g/mol. **AAQ-PHA-CHO1** contained three peaks, of which, only the lowest displayed a molecular weight close to the predicted weight (Table 4.2), with the most prominent peak being 150% of this predicted value. Similarly, **AAQ-PHA-CHO2**, exhibited a molecular weights significantly higher than the predicted value. This suggested that in both cases a proportion of the catalyst had become deactivated and did not participate in the reaction leading to fewer growing chains, and thus higher molecular weights.

Table 4.2: Fitted GPC data for AAQ doped PhA-CHO co-polymers.

Sample	Peak	Mw	Mn	Đ
AAQ-PhA-CHO1	Peak 1	16705	16012	1.04
	Peak 2	30030	29466	1.01
	Peak 3	49456	48208	1.03
AAQ-PhA-CHO2	Peak 1	30808	29729	1.03
	Peak 2	51786	51084	1.01
	Peak 3	77082	76180	1.01

Using the epoxide-functionalised naphthalimide from Chapter 3, **PhA-Nap** (Figure 4.9) was synthesised, entirely replacing the cyclohexene oxide with the novel naphthalimide epoxide. This reaction was essential to confirm the novel epoxides form alternating co-polymers with the anhydride under the polymerisation conditions that will be used in the large-scale reactor synthesis. Unlike the anthraquinone-doped polymers, the reaction with the naphthalimide was observed to form a precipitate, creating a paste at the bottom of the vial after only six hours. Because of this, the reaction was terminated with the addition of methanol and the polymer worked up as described earlier. The poor solubility of the polymer in toluene did not extend to

Chapter 4. Design, Synthesis, and Characterisation of Luminophore Functionalised Doped-Ring Opening Co-Polymerisation Polymers

either of the other solvents (chloroform, and THF) used in the analysis of the polymers. ^1H NMR analysis showed that the naphthalimide had reacted, displaying the broad peaks expected of polymers as well as a slight shift from the parent monomer signals. Unlike cyclohexene oxide, the ether peaks are not easily distinguishable from the alkyl chain of the naphthalimide.

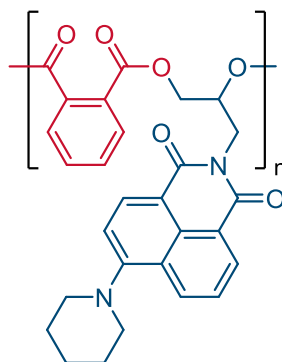


Figure 4.9: repeat unit of PhA-Nap co-polymer, **PhA-Nap**.

However, comparison of the aromatic regions for the phthalic anhydride and the naphthalimide should provide similar information about the alternating nature of the polymer – an equal ratio would imply polyester, while an excess of the naphthalimide would imply polyether. A 1:1 ratio is inferred from the integrations and suggests the synthesised polymer has the desired alternating microstructure. Since the epoxide is less hindered than cyclohexene oxide, the reaction rate is expected to be faster, and is likely an explanation for why precipitation happened so rapidly. However, precipitation from the hot toluene solution was unexpected, as the epoxide monomer is readily soluble in toluene. GPC analysis (Appendix Figure 6.30) showed a very broad trace with a molecular weight, and dispersity of 11200 g/mol, and 3.27 respectively. As before, the trace was deconvoluted into five peaks (Table 4.3). The first peak with a Mw of 337 g/mol is in close agreement with the epoxide starting material and is assigned as such. It should be noted, however, that at these low values, molecular weight data are not reliable, and only indicates the presence of low molecular weight species. Peaks 2 and 3 were similarly assigned to short chain length oligomers between two and five repeat units long. The last two peaks, which comprised the bulk of the polymer, displayed molecular weights within the same region as seen for other epoxides. However, the large dispersity was unusual for aluminium salen complexes, and points towards an uncontrolled polymerisation. It is unknown whether the material that precipitated out of solution remained bound to a catalyst, but if this were the case, the polymerisation would shift from a homogenous phase reaction to heterogenous phase, altering the

Chapter 4. Design, Synthesis, and Characterisation of Luminophore Functionalised Doped-Ring Opening Co-Polymerisation Polymers

reaction kinetics. The high degree of variability suggests either the precipitation of the higher molecular weight polymers may also be tangled with the shorter chains and some of the parent epoxide monomer. Or the presence of a high number of chain transfer reagents, the most likely of which being naphthalic acid.

Table 4.3: Fitted GPC data for **PhA-CHO**.

Peak	Mw	Mn	Đ
Peak 1	337	284	1.18
Peak 2	1273	1109	1.14
Peak 3	2892	2830	1.02
Peak 4	9261	5383	1.72
Peak 5	14336	11217	1.28

4.3.2.2 Large Scale (300 g) Synthesis and Characterisation

To prove viability for materials chemistry, for future applications, the synthesis of polymers on scales, significantly greater than the typical lab reaction of 0.5 g is required. Therefore, we used a reactor with a 2 L reaction vessel (Figure 4.10) to prepare polymers on a 300 g scale with and without dopants as a proof-of-concept method.



Figure 4.10: 2 litre reaction vessel used for large scale polymerisation reactions (**AAQ-PHA-CHO3**).

The typical small scale preparation utilises dried and distilled epoxide, sublimed anhydride, and toluene stored over a potassium mirror, all handled within a

Chapter 4. Design, Synthesis, and Characterisation of Luminophore Functionalised Doped-Ring Opening Co-Polymerisation Polymers

glovebox. Since the reactor vessel cannot be used within a glovebox, and the scale of the reactions means the same purification of the monomers is unfeasible, a modified procedure was developed. Specifically, the epoxide was dried over vacuum oven dried molecular sieves, toluene was dried using a solvent purification system and stored over vacuum oven dried molecular sieves, the anhydride was used new – to limit the amount of diacid formed due to contact with moisture – and the reactor vessel was purged with argon for 15 minutes with circulation (to create a dynamic atmosphere within the vessel). As mentioned earlier, the low concentration of dopant, coupled with the reaction using toluene as a solvent, necessitated the use of long reaction times of around 3 days to ensure a high conversion, and incorporation of the dopant. After confirming incorporation with the small scale trial reactions, three polymers were synthesised (Figure 4.11): undoped (using the catalyst as a luminophore, **PhA-CHO**), 1-aminoanthraquinone doped (**AAQ-PhA-CHO3**), and 4-piperidinyl-1,8-naphthalimide doped (**Nap-PhA-CHO**). By performing these reactions on such a large scale, smaller dopant concentrations could be more easily handled; in these examples 0.2 mol% dopant epoxide, with respect to total epoxide concentration, was chosen.

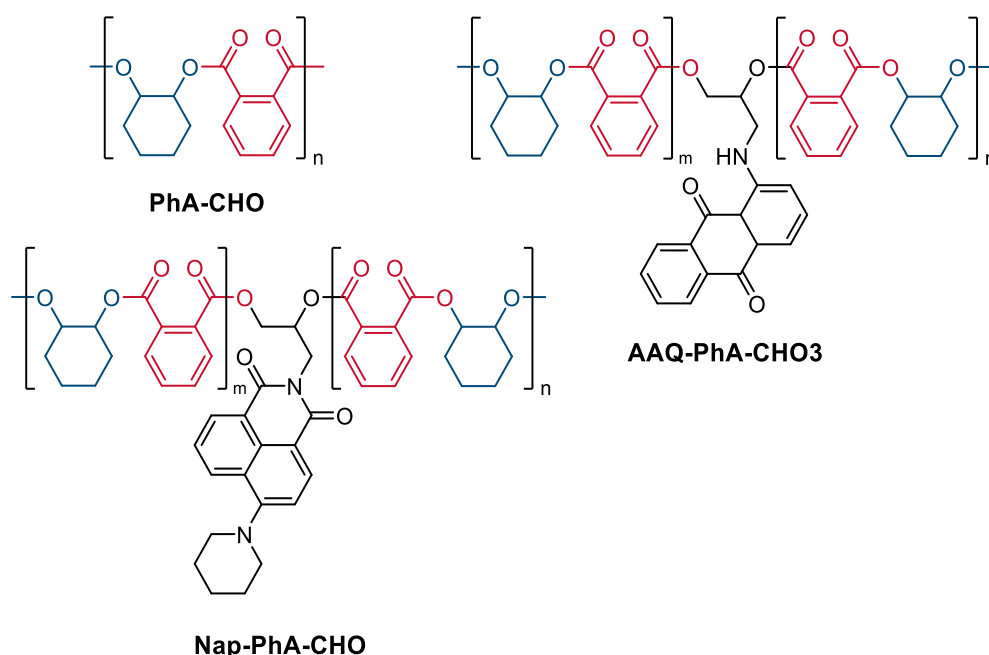


Figure 4.11: Structure of the polymer repeat unit and the luminophore dopants.

Purification of these large scale reactions also required a modification of the standard procedure. Draining of the reaction vessel into methanol did not cause precipitation of the polymer, as it did with small scale samples, instead producing a thick viscous layer that settled on the bottom of the flask. Further agitation of this

Chapter 4. Design, Synthesis, and Characterisation of Luminophore Functionalised Doped-Ring Opening Co-Polymerisation Polymers

mixture also did not induce precipitation of the polymer. After a series of tests, it was discovered decanting the methanol solution, followed by addition of IPA with rigorous mechanical stirring, and repeating several times caused precipitation of the polymer which can then be collected on a glass sinter. NMR analysis shows high selectivity, with ester compositions of 95%, 94%, and 93% for **PhA-CHO**, **AAQ-PhA-CHO3**, and **Nap-PhA-CHO** respectively. Such high selectivity was promising, as it demonstrated the alternating polymerisation remained a controlled process even at large scales, with less rigorous purification techniques. NMR spectra also showed the presence of trace amounts of isopropanol; whilst this did not influence the appearance of the polymers, it was found to cause a problem with the extrusion of these materials, and thus further drying was required. The first method attempted, was dissolving the polymer in a minimal amount of DCM followed by slow, drop wise addition to hexanes, and then drying under reduced pressure. Unfortunately, a high concentration of hexanes was present – approximately 0.97 hexanes per repeat unit, determined through comparison of ^1H NMR integrations. Further drying under reduced pressure at 80 °C for 16 hours, caused a moderate reduction in the hexanes concentration to 0.75 per repeat unit. The minor decrease in the hexanes concentration suggested either the boiling point of hexane was too high to be effectively removed under the conditions used, or the polymer was trapping the solvent preventing evaporation. Therefore, it was believed pentane, with a lower boiling point, would not have this issue. Gratifyingly, an improvement was observed, with the concentration of pentane depending on the method of drying used. Rotary evaporation performed the worst of the three methods, resulting in 0.56 pentane molecules per repeat unit (as determined by ^1H NMR) after 16 hours in a 60 °C water bath. Treatment overnight in a vacuum oven at 100 °C afforded only a minor reduction in the pentane concentration to 0.53 molecules per repeat unit. Blowing compressed air across the sample overnight resulted in the lowest pentane concentration of all the attempted methods, with 0.47 pentane molecules per repeat unit. Surprisingly, even though all these samples contained a reasonably high weighting of solvent molecules, the polymer appeared dry, with the vacuum oven pentane sample appearing as a fine powder with no obvious clumping. This suggests a significant van der Waals interaction between the non-polar solvent molecules, as well as mechanical trapping, preventing evaporation of the solvent even under forcing conditions. However, while this route removed the last traces of IPA from the polymers, it presented the issue of removing a second solvent, which so far, had proved to be even more difficult to remove. Therefore, an attempt was

Chapter 4. Design, Synthesis, and Characterisation of Luminophore Functionalised Doped-Ring Opening Co-Polymerisation Polymers

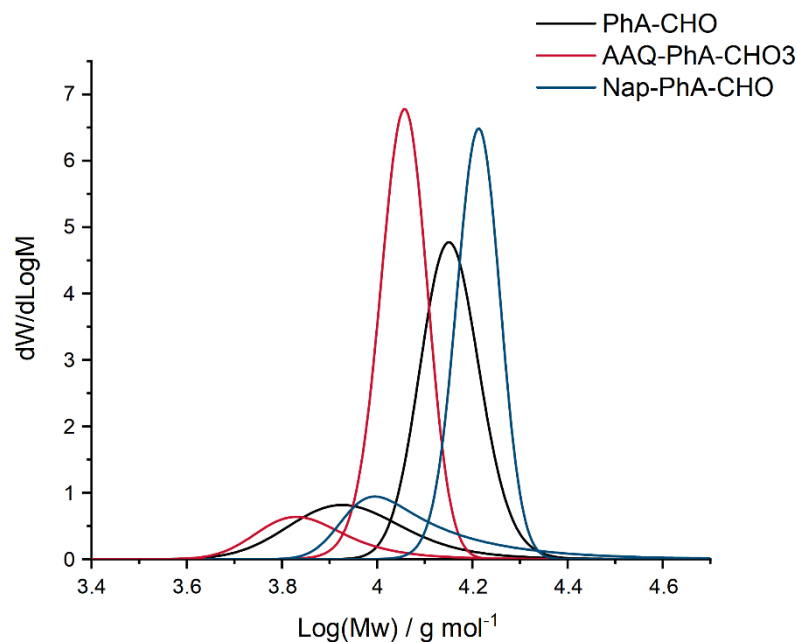


Figure 4.12: Deconvoluted GPC traces of vacuum oven dried large scale polymers.

made to dry the polymer and remove the IPA without further precipitation.

Pleasingly, treatment of the polymer samples in a vacuum oven at 120 °C for 24 hours, reduced the IPA concentration to below the detection limits of the NMR experiment.

Analysis of the polymers via GPC displayed three different molecular weights for the three polymers (Figure 4.12). As expected from ring opening co-polymerisation of anhydrides and epoxides, the traces are bimodal due to the presence of diacids and water acting as chain transfer agents.⁴⁹ Interestingly, the intensity ratio of these two peaks was lowest for the sample without a dopant, **PhA-CHO**. However, as this was the first batch prepared using the reactor it is likely this was an issue associated with varying amounts of water between each batch of reactant. The predicted molecular weight for these polymers, not accounting for the dopant, as it is sub-stoichiometric, is 32,800 g/mol.

As shown in Table 4.4 all three polymers displayed molecular weights significantly below the predicted value. **AAQ-PhA-CHO₃** exhibited the lowest molecular weight for both peaks, but also the narrowest dispersity of all the samples. The reduction in molecular weight is likely caused by varying amounts of amounts of water, since the reactants were not dried in an analogous fashion to the small scale reactions, and inaccuracies in measuring the amount of anhydride and epoxide. Similar reasons are expected to explain the difference in molecular weights between each sample, too.

Chapter 4. Design, Synthesis, and Characterisation of Luminophore Functionalised Doped-Ring Opening Co-Polymerisation Polymers

As alluded to earlier, there is the potential for strong solvent-polymer interactions allowing these two components to remain associated, even in conditions that would otherwise be expected to cause separation of them. The undried polymers, containing toluene and IPA, all show significantly higher molecular weights than their dried counterparts. The difference between the two GPC measurements suggested a significant portion of solvent was trapped within the polymers, and that adsorption of THF into the polymer pores is a rather slow process that is not observed on the GPC time frame. In the case of **AAQ-PhA-CHO3**, the molecular weight is more than double the dried sample. NMR would not suggest the presence of enough solvent to double the molecular weight based on mass alone. This suggests that the difference is caused by subtleties in how the polymer folds in solvent based upon the presence of H-bonding and van der Waals interactions.

Table 4.4: Fitted GPC data for large scale polymers.

Polymer	Peak	Mw	Mn	Đ
PhA-CHO	1		13293	1.02
	2		19478	1.01
PhA-CHO^a	1	9286	8508	1.09
	2	14448	14143	1.02
AAQ-PhA-CHO3	1		17513	1.04
	2		23107	1.01
AAQ-PhA-CHO3^a	1	6745	6510	1.04
	2	11347	11181	1.01
Nap-PhA-CHO	1		11352	1.08
	2		18137	1.01
Nap-PhA-CHO^a	1	12010	11141	1.08
	2	16347	16160	1.01

^aPolymer was dried in a vacuum oven overnight at 120 °C.

Whilst the polymers were coloured by the addition of the chromophore (Figure 4.13, Top), the doping procedure utilised in this approach aimed to incorporate the chromophore directly into the polymer chain, rather than as a mixed in additive. Using **Nap-PhA-CHO** as an exemplar, a sample was dissolved in chloroform, and added drop wise to a rapidly stirring flask of ethanol at 70 °C – chosen because the naphthalimide monomer is readily soluble in hot ethanol but the polymer is not. After being allowed to stir for 15 minutes, the polymer was allowed to settle, with no coloration of the solvent mixture observed. Furthermore, the eluted solvent from a GPC run was collected in vials and exposed to UV light. If the epoxide was not

Chapter 4. Design, Synthesis, and Characterisation of Luminophore Functionalised Doped-Ring Opening Co-Polymerisation Polymers

covalently bound, then it would be expected to see a strong green luminescence in the low molecular weight fractions, and potentially due to trapping, also in the polymer fractions. However, emission was only observed within the polymer fractions (Figure 4.13, Bottom), further supporting the claim of the dopant monomer being directly incorporated into the polymer backbone.

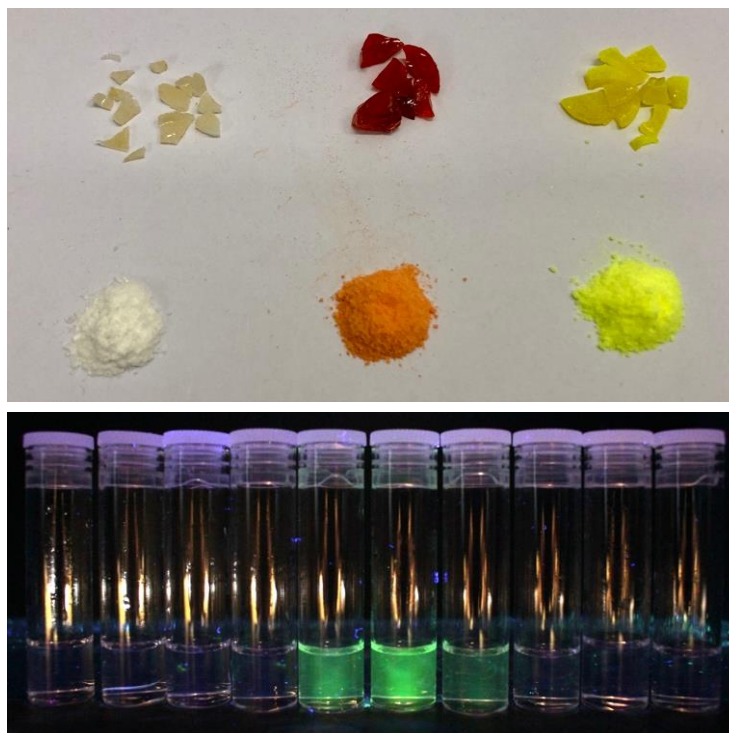


Figure 4.13: Solid polymer samples (L to R) **PhA-CHO**, **AAQ-PhA-CHO₃**, **Nap-PhA-CHO** under ambient light (Top). Eluted GPC solvent showing the emissive polymer (**Nap-PhA-CHO**) fractions (Bottom)

Chapter 4. Design, Synthesis, and Characterisation of Luminophore Functionalised Doped-Ring Opening Co-Polymerisation Polymers

4.3.3 UV-Vis Absorption Spectroscopy

4.3.3.1 [Al(^tBu-salen)Cl]

The ^tBu-Salen ligand (**36**) exhibits two peaks at 332 and 265 nm corresponding to $\pi - \pi^*$ transitions (Figure 4.14). Upon complexation with aluminium (**37**), both these transitions experienced a shift to lower energies (364, and 291 nm respectively). The appearance of additional peaks was also observed around 280 and 400 nm. Presumably, the shift in absorption was caused forcing of a more strained conformer and the bridging aluminium creating an extended molecular orbital, stabilising the HOMO and LUMO across the entire complex. Similarly, the additional peaks are believed to be caused by differences in the stabilisation of these molecular orbitals.

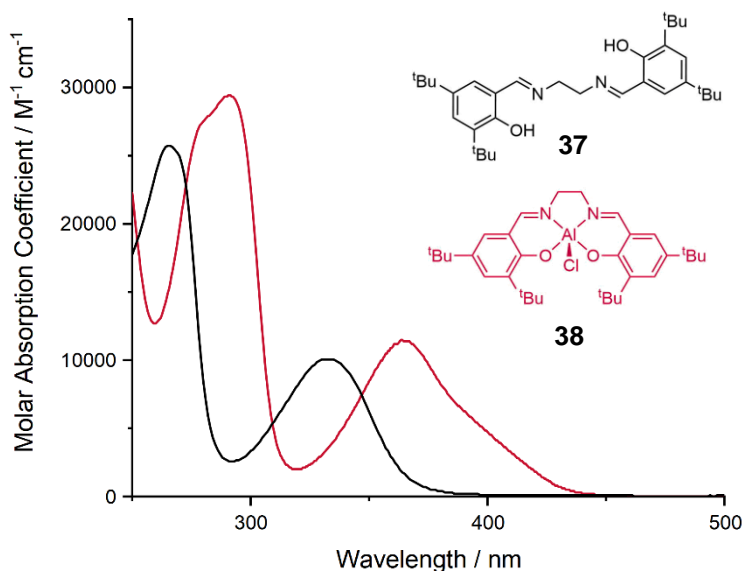


Figure 4.14: UV-Vis absorption spectra for compounds **37**, and **38** as chloroform solutions.

Computational analysis carried out using the B3LYP functional and cc-PVDZ basis set, suggests this to be the case, with TD-DFT data showing good agreement with peak positions of the experimental data for both the aluminium complex and the ligand (Figure 4.16, Appendix Figure 6.34). Additionally, the calculated ϵ value of the transitions show good agreement with the experimental molar absorption coefficient, with only the highest energy peak showing a poor prediction for **38**.

Chapter 4. Design, Synthesis, and Characterisation of Luminophore Functionalised Doped-Ring Opening Co-Polymerisation Polymers

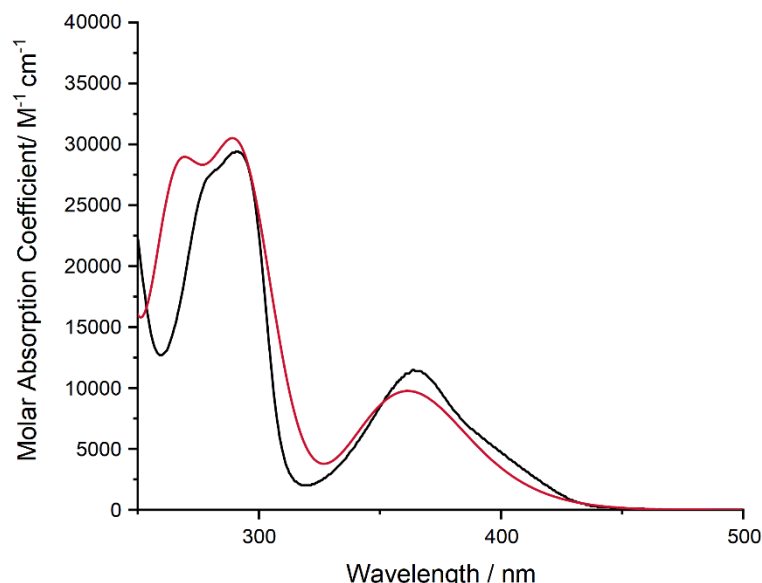


Figure 4.16: Experimental (black line) and simulated (red line, predicted ϵ) UV-Vis spectra of **38** in chloroform using TD-DFT with the B3LYP functional and cc-PVDZ basis set.

The HOMO showed little difference after complexation, with only some additional density from the chloride being obvious. The LUMO, however, displayed a shift in electron density from the ethyl bridge onto the imine portion of the backbone creating a larger in-phase contribution between the two nitrogen atoms, and therefore, across the aromatic systems (Figure 4.15).

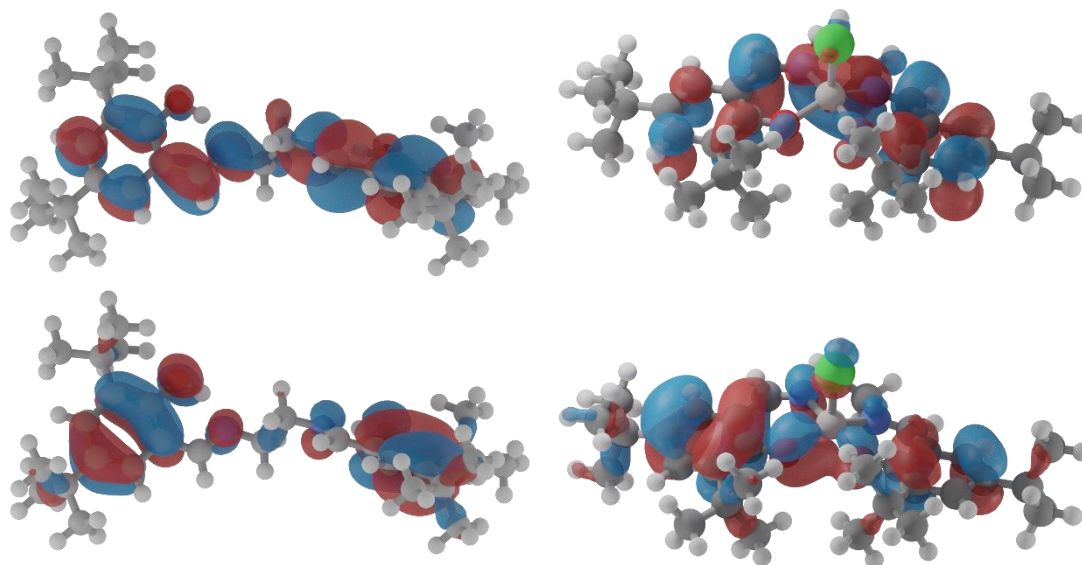


Figure 4.15: Calculated HOMO (bottom) and LUMO (top) and geometries of the ^tBu-Salen ligand (L) (**37**) and [Al(^tBu-Salen)Cl] (R) (**38**) using the B3LYP functional and cc-PVDZ basis set.

4.3.3.2 Functionalised Polymers

Expectedly, the absorption spectra of the polymers are dominated by the $\pi - \pi^*$ transitions of the polymer backbone, requiring high concentration solutions to observe the dopant absorption (Figure 4.17). No polymer absorbance is observed

Chapter 4. Design, Synthesis, and Characterisation of Luminophore Functionalised Doped-Ring Opening Co-Polymerisation Polymers

above 315 nm, allowing a wide range of dopants to be used without the polymer absorbance competing with the dopant. Upon incorporation of a dopant, the absorption of the material alters to feature an absorption in the visible region, giving rise to the colour of the doped polymer. For example, introduction of the naphthalimide shows an absorbance at 410 nm corresponding to an intramolecular charge transfer (ICT) and weak $\pi - \pi^*$ transitions around 340 and 320 nm. Using 1-aminoanthraquinone as the dopant, similarly, generates a broad absorption at 490 nm, and is assigned to the ICT transition of the amine and quinone. Additionally, the consistency in the peak position before and after incorporation suggests, at least in while in solution, the local environment of the luminophore is the same as the monomer.

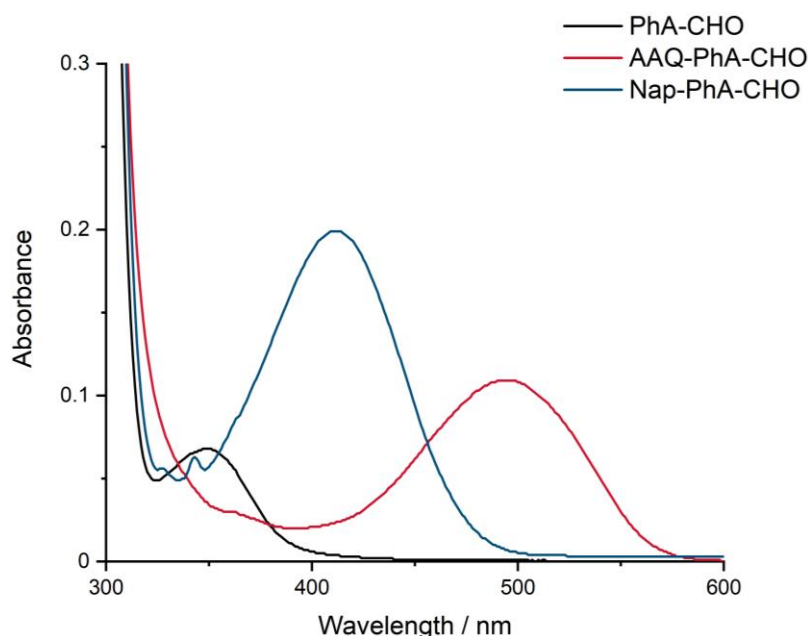


Figure 4.17: UV-Vis absorption spectra for the three large scale doped polymers.

Whilst it was not possible to determine the degree of dopant incorporation through ^1H NMR analysis due to the low concentration of the dopant, examination of the absorbance of the dopant associated peaks, assuming no significant deviation from the molar absorption coefficient due to polymerisation, and estimation of the dopant concentration can be achieved (Equation 4.3).

$$\text{Dopant Incorporation \%} = \frac{\left(\frac{A_{\text{Polymer}}}{\epsilon_{\text{Monomer}}}\right)}{C_{\text{Theoretical}}} \times 100$$

Equation 4.3: Determination of dopant concentration relative to theoretical via UV-Vis spectroscopy. Where, C = concentration, A = absorbance, and ϵ = molar absorptivity. As the path length was 1 cm it has been omitted from the equation.

Chapter 4. Design, Synthesis, and Characterisation of Luminophore Functionalised Doped-Ring Opening Co-Polymerisation Polymers

Following the above equation, the concentration of the anthraquinone dopant (**AAQ-PhA-CHO3**) and naphthalimide dopant (**Nap-PhA-CHO**) was determined to be 0.17 and 0.24 mol%, respectively. The larger than expected concentration of the naphthalimide may be explained by a combination of loss of reagents during transfer to the reactor and the removal of low molecular weight polymers during the purification steps that did not contain a naphthalimide unit. However, these values are not too dissimilar from the idealised doping concentration, in which all the dopant has been incorporated into polymer chains.

4.3.4 Luminescence Spectroscopy

As with their monomer counterparts, **PhA-CHO**, and **Nap-PhA-CHO** displayed a strong luminescence that was visible to the naked eye at 356 nm excitation, as both solids and chloroform solutions. The excitation spectra (Figure 4.18) of **PhA-CHO**, and **Nap-PhA-CHO** aligned closely with the absorption spectra of the parent monomers, with the major difference occurring below 300 nm where the absorbance of the polymer dominates. **AAQ-PhA-CHO3**, however, exhibited a significant deviation from the absorbance of both the polymer and the monomer, with the strong peaks from the aluminium complex present in the excitation spectrum (Figure 4.19).

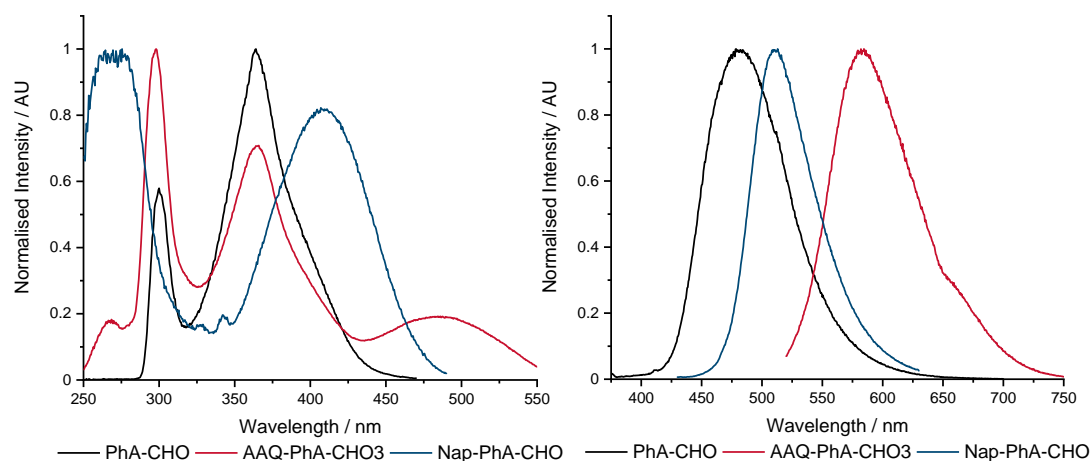


Figure 4.18: Excitation (L) ($\lambda_{em} = 480$ nm (**PhA-CHO**), 583 nm (**AAQ-PhA-CHO3**), and 510 nm (**Nap-PhA-CHO**)) and emission (R) ($\lambda_{ex} = 370$ nm (**PhA-CHO**), 490 nm (**AAQ-PhA-CHO3**), and 410 nm (**Nap-PhA-CHO**)) spectra of the large scale polymers.

Whilst a peak relating to the catalyst was observed in the absorbance spectra, it was weaker than the ICT transition. Given the overlap of the complex and the anthraquinone's emission, it was assumed this was not related to energy transfer due to the large distance between the catalyst and dopant. The emission spectra, similarly, showed no shift in the λ_{max} values of the emission and retained the broad

Chapter 4. Design, Synthesis, and Characterisation of Luminophore Functionalised Doped-Ring Opening Co-Polymerisation Polymers

featureless nature expected of the ICT transitions in **AAQ-PhA-CHO3**, and **Nap-PhA-CHO**.

Lifetime measurements (τ , Table 4.5) of the polymers showed no significant deviation from measurements of the monomers. Quantum yield measurements (Φ), likewise, displayed little difference for the chromophoric dopants. The aluminium complex, however, exhibited a decrease in the quantum yield of just over 50% compared to the pre-catalyst. The significant drop may be explained by two factors: the poor absorption signal measured for the polymer bound complex for the quantum yield measurements, and the alteration of the pre-catalyst containing a chloride, and the polymer bound species with an alkoxide (Figure 4.19).

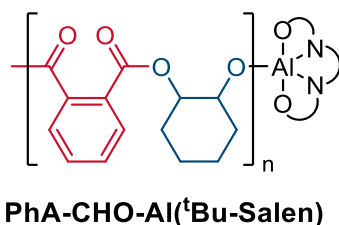


Figure 4.19: Structure of the PhA-CHO catalyst with the alkoxide aluminium species bound.

Table 4.5: Fluorescence properties of the large scale polymers as chloroform solutions.

Polymer	λ_{em} / nm	τ / ns	Φ
PhA-CHO	481	10.73	16.2%
Nap-PhA-CHO	512	8.88	45.0%
AAQ-PhA-CHO3	583	< 1	4.3%

Overall, this has demonstrated the incorporation of dopant level amounts of a luminophore/chromophore using a ROCOP approach with no alteration of the conditions. Since this method required no change to the polymerisation conditions, beyond the addition of a dopant, this method is therefore termed doped ROCOP (D-ROCOP).

4.3.5 Post-Polymerisation Modification of Polymers

In collaboration with an MChem project student (Alysia Draper), the second pathway for the preparation of functionalised polymers, post-polymerisation modification, was also explored using an amine-terminated naphthalimide in an S_N2 reaction (Scheme 4.14). The modification was performed using a chloride-functionalised polymer, **ECH-PhA** (Scheme 4.14), with the aim of promoting a substitution of the chloride by

Chapter 4. Design, Synthesis, and Characterisation of Luminophore Functionalised Doped-Ring Opening Co-Polymerisation Polymers

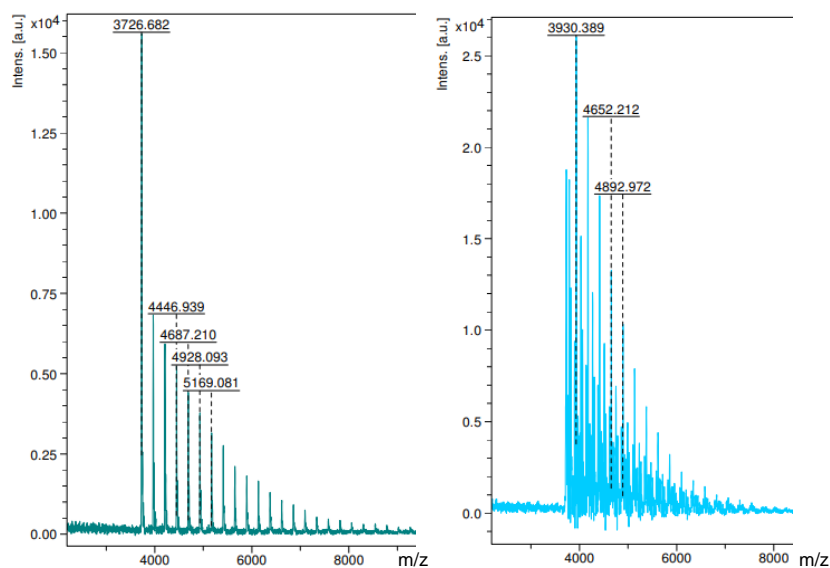
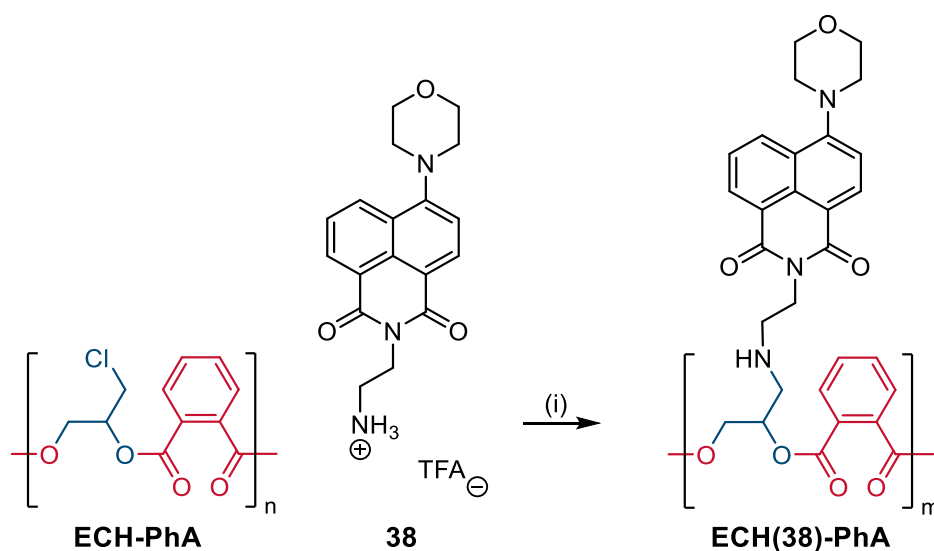


Figure 4.20: MALDI spectrum for un-functionalised (L) and functionalised (R) co-polymers.

the naphthalimide's amine, thereby affording **ECH(38)-PhA**, that contains a tethered luminophore/chromophore.



Scheme 4.14: Post-polymerisation modification of ECH-PhA using an amine-terminated naphthalimide showing the luminophore component. (i) MeCN, K_2CO_3 .

1H NMR analysis shows the presence of the naphthalimide after aqueous work-up, however this does not show the naphthalimide is bound to the polymer, nor prove the polymer itself has not been degraded during the reaction. MALDI data (Figure 4.20) demonstrates the functionalised polymer is no longer well-defined with a repeat unit of 240.9 g/mol and is likely comprised of a number of partially degraded chains and naphthalimide bound polymer. GPC data similarly suggests a degraded polymer with a single broad unsymmetrical peak accounting for the majority of the spectrum, and deconvolution showing at least seven different peaks (Figure 4.21).

Chapter 4. Design, Synthesis, and Characterisation of Luminophore Functionalised Doped-Ring Opening Co-Polymerisation Polymers

The range of molecular weights obtained, and their significantly higher dispersity compared to the D-ROCOP method, demonstrate this method of functionalisation is an undesirable route towards incorporating the desired properties. Whilst other routes of modification exist, such as thiol-ene click reactions, methods demand additional functionality be present within the monomers. Which, if not present will require the addition of a monomer that does contain the desired functional group. Secondly, post-polymerisation reactions, as the name implies, increases the amount of processing of the produced polymer. The D-ROCOP approach described above does not require any additional processing of the synthesised polymer, nor is it expected to adversely affect the molecular weight or the dispersity of the material. However, expectedly, this method cannot overcome the functional group limitations of the catalytic process.

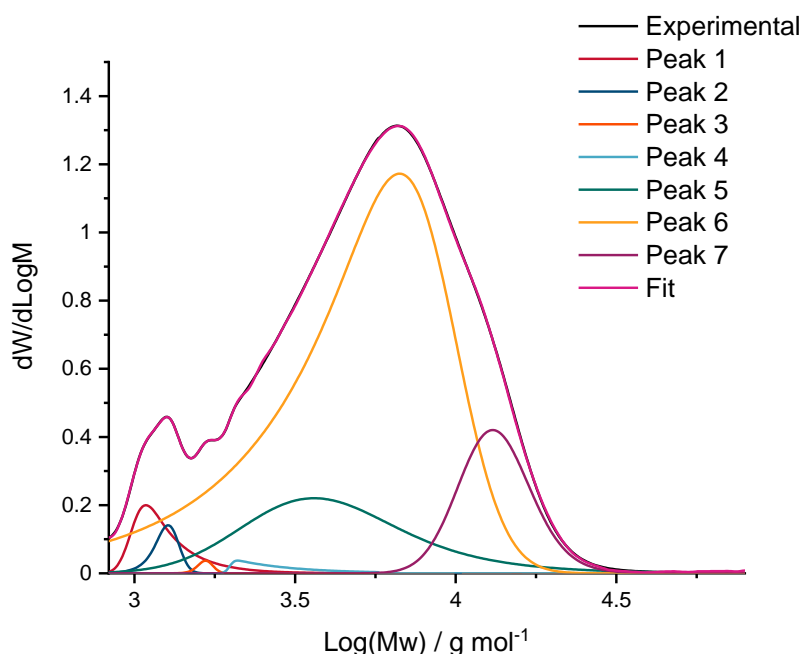
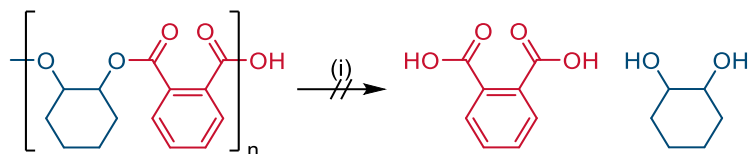


Figure 4.21: Experimental and fitted GPC data for **ECH(38)-PhA**

4.3.6 Polymer degradation

One of the key advantages of polymers produced through the co-polymerisation of epoxides and anhydrides is the formation of the ester functional group. This ester group provides a target for depolymerisation reactions, which are not offered in most polymers used within everyday life. As with non-polymeric esters, two chemical routes are possible for cleaving the bond: acid catalysed (Scheme 4.15), and base hydrolysis to form the diol and diacid salt. Following the work of the Williams group,⁶⁷ a polymer was dissolved in toluene along with para-toluene sulfonic acid and then analysed after 16 hours of reaction time.

Chapter 4. Design, Synthesis, and Characterisation of Luminophore Functionalised Doped-Ring Opening Co-Polymerisation Polymers



Scheme 4.15: Degradation of doped polyesters under acidic conditions. (i) Toluene, pTSA•H₂O, 60 °C.

¹H NMR analysis indicated degradation had occurred, through the appearance of new signals located between 8.1 and 7.9 ppm corresponding to phthalic acid and/or oligomers. Further analysis, using mass spectrometry agrees with this assessment and shows a range of oligomers (Appendix Figure 6.35) separated by the repeat unit, with an example oligomer shown in Figure 4.22. Whilst this route is promising in that it provides a comparatively green route for the degradation of polyesters, compared to the method of recycling for PET (temperatures above 200 °C), it was not optimal for these polymers. The reaction rate rapidly slows down as more of the polymer is consumed⁶⁶, with the rate plateauing, showing only minor conversion to shorter chain oligomers. The Williams group also do not report any conversion to the diol or diacid, which was one of the targets of this. Further work investigating the base hydrolysis route was postulated to afford a more effective and time efficient route for the formation of monomer precursors, and even allow for separation of the dopant and the major diol product. After finishing my time in the lab, the project was continued by Taylor Young who used sodium hydroxide in a water/THF mix to fully degrade the polymer to potassium phthalate, cyclohexene diol, as well as the diol of the dopant, once again showing the material had polymerised. In addition separation of all three components was achieved, demonstrating the circular economy of D-ROCOP polymers.⁷⁴

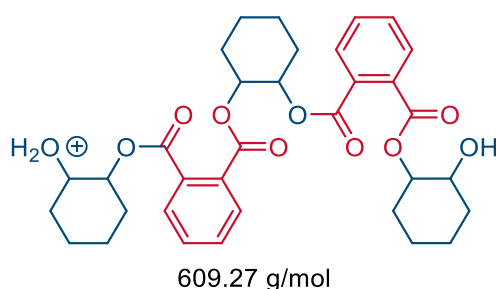


Figure 4.22: Example structure from acidic hydrolysis of a polyester.

Chapter 4. Design, Synthesis, and Characterisation of Luminophore Functionalised Doped-Ring Opening Co-Polymerisation Polymers

4.3.7 Doped Polymers as Functionalised Materials

Taking advantage of the successful scale up reaction, the processability of the of the phthalic anhydride and cyclohexene oxide co-polymer was examined with the aim of testing the processability of these materials and to determine their viability in real world applications. Initial testing indicated the polymer was processable from a powder into an extruded material, producing a relatively clear polymer strand with only minor discolouration, presumably due to decomposition of the catalyst. However, the material was also very brittle and unable to be pelletized for further processing. Following this, direct injection moulding was trailed (Figure 4.23, for method see Section 4.5). Whilst moulding of the polymer was successful in forming the dog bone shape, the material adhered to the mould requiring mechanical force to separate the polymer from the mould. Unfortunately, due to the brittleness, the polymer snapped easily, and proved this polymer was not suitable for processing. The brittle nature of the material is believed to be caused by the highly crystalline nature of phthalic anhydride, and cyclohexene oxide not affording a great deal of flexibility in the backbone of the material and favouring stacking due to π interactions.

4.4 Conclusion

In conclusion, this chapter has shown the scale up of the ROCOP polymerisation is easily achievable using an aluminium salen catalyst and does not require extensive purification of the epoxide nor anhydride to produce well controlled selective polymerisation, with molecular weights and dispersities comparable to those of small scale reactions that are typically conducted with rigorous air exclusion



Figure 4.23: Images of extruded polymer showing the high crystallinity and brittleness of the extruded material.

Chapter 4. Design, Synthesis, and Characterisation of Luminophore Functionalised Doped-Ring Opening Co-Polymerisation Polymers

techniques. A doped ROCOP approach has also been demonstrated, using epoxide functionalised chromophores/luminophores through an in-situ, sub-stoichiometric approach. Similarly, dispersity was observed to show no significant alterations from small scale reactions, and similar molecular weights for **PhA-CHO**, and **Nap-PhA-CHO** were obtained. Although the molecular weight for one sample, **AAQ-PhA-CHO3** was observed to be lower, it is not believed to be related to the dopant and caused by a lack of stirring during the polymerisation. Photophysical characteristics of the doped polymers have also been explored, showing no changes in the absorption or emission wavelengths, nor in the measured lifetimes or quantum yields of the samples, upon polymer incorporation. The advantage of the D-ROCO approach lies in the one pot nature of the reaction, not requiring additional functional groups, and allowing a variable number of dopants to be incorporated into the polymer chain, unlike other methods reported within the literature. The potential for recycling of the polyester has also been demonstrated through acid catalysed hydrolysis using *p*-toluenesulfonic acid. Processability of the polymer was also examined, however, the material proved too brittle, and whilst moulding of the material was possible, the mechanical properties of the material could not be further explored.

These early results provide a vital starting point for further development of these materials. The vast library of epoxides and anhydrides allows for further exploration into how these different monomers will influence the mechanical properties.

Allowing creation of a malleable polymer with industrially relevant properties, that can undergo both traditional moulding, and 3D printing. An example of this can be seen in the properties of poly(ethylene) and poly(hex-1-ene). The non-branched poly(ethylene) is a hard solid material, while the highly branched poly(hex-1-ene) is a rubbery solid due to the long chains disrupting the stacking of the polymer chains. Such a feature may be taken advantage of with long chain epoxides such as epoxy-dodecane. Further research into the degradation of these materials within the group has shown base hydrolysis affords to monomer precursors in high yield and purity, even allowing the separation of the dopant and epoxide and thus demonstrating a circular economy of luminescent polymers.

4.5 Experimental and Methods

All reactions were performed using standard non-air exclusion techniques with the exception of the [Al(Salen)Cl] luminophore that utilised the use of vacuum line and Schlenk techniques. Reagents were of commercial grade and were used without

Chapter 4. Design, Synthesis, and Characterisation of Luminophore Functionalised Doped-Ring Opening Co-Polymerisation Polymers

further purification, except for small scale reactions which were carried out using sublimed anhydride, dried and degassed epoxide and toluene, handled in a glovebox under a nitrogen atmosphere. ^1H , and ^{13}C NMR spectra were recorded on a Bruker Fourier300 (300/75 MHz), Bruker AVANCE HD III equipped with a BFFO SmartProbe™ (400/101 MHz) or Bruker AVANCE III HD with BBO Prodigy CryoProbe (500/125 MHz) was used. The obtained chemical shifts δ are reported in ppm and are referenced to the residual solvent signal. Spin–spin coupling constants J are given in Hz. UV-Visible spectroscopy was performed in aerated chloroform solutions using a Shimadzu UV-1800 spectrophotometer. IR spectra were recorded on an ATR equipped Shimadzu IRAffinity-1 spectrophotometer. GPC data were measured on an Agilent 1260 II triple-detection GPC system. Photophysical data was obtained on a JobinYvon-Horiba Fluorolog spectrometer fitted with a JY TBX picosecond photodetection module as CHCl_3 solutions. Emission spectra were uncorrected and excitation spectra were instrument corrected. The pulsed source was a Nano-LED configured with for a 295 nm output at 1 MHz. Luminescence lifetimes were obtained using the JobinYvon-Horiba FluoroHub single photon counting module fitting the lifetime data using DAS6 deconvolution software. Quantum yield measurements were obtained on aerated solutions using $[\text{Ru}(\text{bipy})_3](\text{PF}_6)_2$ in aerated MeCN ($\phi = 0.016$) or quinine sulfate in aerated 0.05 M H_2SO_4 as standards ($\phi = 0.60$)

[Al(^tBu-Salen)Cl] (38): Synthesised according to a modified literature method.⁶⁹ ^tBu-Salen-H₂ (1.00 g, 2.03 mmol) was dissolved in toluene and diethylaluminium chloride (2.03 mL, 2.03 mmol, 1 M solution in toluene) was added dropwise, and the reaction allowed to stir at room temperature for an hour. Afterwards the solvent was removed, washed with hexane, and dried *in vacuo* to furnish the desired compound as a yellow solid (1.05 g, 93%). ^1H NMR (300 MHz, CDCl_3) δ 8.31 (2 H, s, CH), 7.49 (2 H, d, $J = 2.59$, CH), 6.98 (2 H, d, $J = 2.58$, CH) 4.17 – 3.98 (2 H, m, CH_2), 3.79 – 3.57 (2 H, m, CH_2), 1.47 (9 H, s, CH_3), 1.23 (9 H, s, CH_3). UV-Vis (CHCl_3) λ_{max} ($\epsilon / \text{dm}^3\text{mol}^{-1}\text{cm}^{-1}$): 364 (11459), 280sh (27513), 291 (29419) nm. Emission (CHCl_3): λ_{em} (τ/ns) = 480 (10.45) nm.

0.05 equivalent 1-AAQ doping (AAQ-PhA-CHO1): Phthalic anhydride (379 mg, 2.56 mmol), cyclohexene oxide (246 μL , 2.43 mmol), Al(Salen)Cl catalyst (3.56mg, 0.0064 mmol), dimethylaminopyridine (1.56 mg, 0.0128 mmol) and the 1-AAQ dopant (36 mg, 0.127 mmol) were all dissolved in toluene (1 mL). After being allowed to react for 16 hours at 80 °C the mixture was poured into methanol, the

Chapter 4. Design, Synthesis, and Characterisation of Luminophore Functionalised Doped-Ring Opening Co-Polymerisation Polymers

solvent decanted and the solid washed with IPA to afford **AAQ-PhA-CHO1** as a red solid (0.322 g). $^1\text{H NMR}$ (500 MHz, CDCl_3) δ 10.07 – 9.73 (7 H, m, NH), 8.26 – 8.07 (9 H, m, CH), 7.83 – 7.30 (226 H, m, CH), 5.59 (5 H, Br s, CH), 5.14 (90 H, Br s, CH_2), 4.65 (9 H, Br s, CH_2), 3.80 – 3.60 (9 H, m, CH_2), 2.22 (88 H, Br s, CH_2), 1.76 (88 H, Br s, CH_2), 1.51 (89 H, Br s, CH_2), 1.44 – 1.26 (92 H, m, CH_2).

0.10 equivalent 1-AAQ doping (AAQ-PhA-CHO2): Prepared following **AAQ-PhA-CHO1** but using cyclohexene oxide (233 μL , 2.3 mmol) and 1-AAQ (72 mg, 0.256 mmol) to furnish **AAQ-PhA-CHO2** as a red solid (0.341 g). $^1\text{H NMR}$ (500 MHz, CDCl_3) δ 10.06 – 9.62 (1 H, m, NH), 8.28 – 7.95 (2 H, m, CH), 7.81 – 7.31 (22 H, m, CH), 5.58 (1 H, Br s, CH), 5.14 (7 H, Br s, CH_2), 4.64 (2 H, Br s, CH_2), 3.82 – 3.52 (2 H, m, CH_2), 2.22 (7 H, Br s, CH_2), 1.75 (7 H, Br s, CH_2), 1.50 (7 H, Br s, CH_2), 1.42 – 1.26 (7 H, m, CH_2).

Phthalic Anhydride Naphthalimide Co-Polymer (Nap-PhA): Phthalic anhydride (132 mg, 0.892 mmol), Naphthalimide dopant (0.300 mg, 892 μmol) Al(Salen)Cl catalyst (1.24 mg, 0.0023 mmol), and dimethylaminopyridine (0.54 mg, 0.0045 mmol) were all dissolved in toluene (1 mL). After 6 hours an orange precipitate formed that was dissolved in DCM and precipitated into ethanol to afford **Nap-PhA** as an orange solid (0.254 mg). $^1\text{H NMR}$ (500 MHz, CDCl_3) δ 8.54 – 8.21 (3 H, m, CH), 7.79 – 7.30 (5 H, m, CH), 7.10 – 6.94 (1 H, m, CH), 6.04 – 5.49 (1 H, m, CH), 4.99 – 4.06 (4 H, m, CH_2), 3.25 – 3.08 (4 H, m, CH_2), 1.92 – 1.76 (4 H, m, CH_2), 1.69 (2 H, Br s, CH_2).

General large scale (300g) polymer synthesis: Phthalic anhydride (189.50 g, 1280 mmol), cyclohexene oxide (130 mL, 1277 mmol), toluene (500 mL), Al(Salen)Cl catalyst (1.75 g, 3.16 mmol), and dimethylaminopyridine (0.78 g, 6.38 mmol). After being allowed to react for 3 days the mixture was cooled poured into methanol and the resulting precipitate was allowed to settle and the solvent decanted. IPA was added to the precipitate and stirred before being collected on a glass sinter and dried.

Undoped Polymer (PhA-CHO): Synthesised as general procedure with no alternations to yield **PhA-CHO** as a white powder (310 g). $^1\text{H NMR}$ (500 MHz, CDCl_3) δ 7.64 – 7.53 (2 H, Br. m CH), 7.46 – 7.33 (2 H, Br. m, CH), 5.26 – 5.06 (2 H, Br. m, CH), 2.29 – 2.13 (2 H, Br. m, CH_2), 1.84 – 1.65 (2 H, Br. m, CH_2), 1.62 – 1.45 (2 H, Br. m, CH_2), 1.42 – 1.17 (2H, Br. m, CH_2). (CHCl_3) λ_{max} ($\epsilon / \text{dm}^3\text{mol}^{-1}\text{cm}^{-1}$): 283sh (67315), 277 (73741) nm. Emission (CHCl_3): λ_{em} (τ/ns) = 482 (10.73) nm.

Chapter 4. Design, Synthesis, and Characterisation of Luminophore Functionalised Doped-Ring Opening Co-Polymerisation Polymers

Aminoquinoline doped polymer (AAQ-PhA-CHO3): Synthesised as general procedure but using **AAQ** (0.706 g, 2.53 mmol) as the dopant to yield **AAQ-PhA-CHO3** as a light red solid (280 g). $^1\text{H NMR}$ (500 MHz, CDCl_3) δ 7.64 – 7.53 (2 H, Br. m, CH), 7.45 – 7.34 (2 H, Br. m, CH), 5.23 – 5.04 (2 H, Br. m, CH), 2.31 – 2.15 (2 H, Br. m, CH_2), 1.86 – 1.68 (2 H, Br. m, CH_2), 1.85 – 1.67 (2 H, Br. m, CH_2), 1.46 – 1.25 (2H, Br. m, CH_2). UV-Vis (CHCl_3) λ_{max} ($\epsilon / \text{dm}^3\text{mol}^{-1}\text{cm}^{-1}$): 493 (13262), 360 (9126) nm. Emission (CHCl_3): λ_{em} (τ/ns) = 584 (<1 ns) nm.

Naphthalimide doped polymer (Nap-PhA-CHO): Synthesised as general procedure but using **Nap** (0.850 g, 2.53 mmol) as the dopant to yield **Nap-PhA-CHO** as a bright yellow/green powder (320 g). $^1\text{H NMR}$ (500 MHz, CDCl_3) δ 7.64 – 7.53 (2 H, Br. m, CH), 7.45 – 7.34 (2 H, Br. m CH), 5.21 – 5.04 (2 H, Br. m, CH), 2.30 – 2.16 (2 H, Br. m, CH_2), 1.84 – 1.68 (2 H, Br. m, CH_2), 1.60 – 1.45 (2 H, Br. m, CH_2), 1.44 – 1.31 (2 H, Br. m, CH_2). UV-Vis (CHCl_3) λ_{max} ($\epsilon / \text{dm}^3\text{mol}^{-1}\text{cm}^{-1}$): 411 (11639), 343 (3249), 327 (2772) nm. Emission (CHCl_3): λ_{em} (τ/ns) = 510 (8.88) nm.

Polymer Degradation: Phthalic anhydride and cyclohexene oxide co-polymer (200 mg) was dissolved in toluene (10 mL) along with para-toluenesulfonic acid (1 mg) and heated at 100 °C overnight.

Polymer Extrusion: **PHA-CHO** (20 g) was fed into a Thermo Scientific Process 11 Parallel Twin-Screw Extruder with the temperature in front of the hopper set to 100 °C, and a linear temperature ramp to 140 °C in the zones in front of the die, with the die temperature set to 170 °C. The melted polymer was then passed into a Thermo Scientific HAAKE MiniJet Pro Piston Injection Molding System for forming the dogbone shaped polymer.

4.6 References

- 1 Our waste, our resources: a strategy for England, .
- 2 N. Malik, P. Kumar, S. Shrivastava and S. B. Ghosh, *Int J Plast Technol*, 2017, **21**, 1–24.
- 3 UK Statistics on Waste, .
- 4 M. Day, J. D. Cooney, C. Touchette-Barrette and S. E. Sheehan, *J Anal Appl Pyrol*, 1999, **52**, 199–224.
- 5 A. Rahimi and J. M. García, *Nat Rev Chem*, 2017, **1**, 1–11.
- 6 *Plastics Europe (2017) Plastics—The facts*. Plastic Europe., .
- 7 A. Merrington, in *Applied Plastics Engineering Handbook*, ed. M. Kutz, William Andrew Publishing, Oxford, 2011, pp. 177–192.
- 8 H. Jin, J. Gonzalez-Gutierrez, P. Oblak, B. Zupančič and I. Emri, *Polym Degrad Stabil*, 2012, **97**, 2262–2272.
- 9 P. Oblak, J. Gonzalez-Gutierrez, B. Zupančič, A. Aulova and I. Emri, *Polym Degrad Stabil*, 2015, **114**, 133–145.

Chapter 4. Design, Synthesis, and Characterisation of Luminophore Functionalised Doped-Ring Opening Co-Polymerisation Polymers

- 10 J. Aurrekoetxea, M. A. Sarrionandia, I. Urrutibeascoa and M. Ll. MasPOCH, *J Mater Sci*, 2001, **36**, 2607–2613.
- 11 H. M. da Costa, V. D. Ramos and M. C. G. Rocha, *Polym Test*, 2005, **24**, 86–93.
- 12 M. Xanthos, *Science*, 2012, **337**, 700–702.
- 13 K. J. Kim and B. K. Kim, *J Appl Polym Sci*, 1993, **48**, 981–986.
- 14 L. Maringer, M. Himmelsbach, M. Nadlinger, G. Wallner and W. Buchberger, *Polym Degrad Stabil*, 2015, **121**, 378–384.
- 15 I. Ahmad, M. I. Khan, H. Khan, M. Ishaq, R. Tariq, K. Gul and W. Ahmad, *Int J Green Energy*, 2015, **12**, 663–671.
- 16 R. Palos, A. Gutiérrez, F. J. Vela, J. A. Maña, I. Hita, A. Asueta, S. Arnaiz, J. M. Arandes and J. Bilbao, *J Anal Appl Pyrol*, 2019, **142**, 104668.
- 17 E. Bäckström, K. Odelius and M. Hakkarainen, *ACS Sustainable Chem. Eng.*, 2019, **7**, 11004–11013.
- 18 B. P. S. Santos, D. Almeida, M. de F. V. Marques and C. A. Henriques, *Fuel*, 2018, **215**, 515–521.
- 19 J. Chattopadhyay, T. S. Pathak, R. Srivastava and A. C. Singh, *Energy*, 2016, **103**, 513–521.
- 20 R. R. Guddeti, R. Knight and E. D. Grossmann, *Ind. Eng. Chem. Res.*, 2000, **39**, 1171–1176.
- 21 M. del M. C. López, A. I. Ares Pernas, M. J. Abad López, A. L. Latorre, J. M. López Vilariño and M. V. González Rodríguez, *Mater Chem Phys*, 2014, **147**, 884–894.
- 22 T. Yoshioka, T. Motoki and A. Okuwaki, *Ind. Eng. Chem. Res.*, 2001, **40**, 75–79.
- 23 T. Yoshioka, N. Okayama and A. Okuwaki, *Ind. Eng. Chem. Res.*, 1998, **37**, 336–340.
- 24 United States, US3952053A, 1976.
- 25 D. Paszun and T. Szychaj, *Ind. Eng. Chem. Res.*, 1997, **36**, 1373–1383.
- 26 B. Liu, X. Lu, Z. Ju, P. Sun, J. Xin, X. Yao, Q. Zhou and S. Zhang, *Ind. Eng. Chem. Res.*, 2018, **57**, 16239–16245.
- 27 Q. F. Yue, L. F. Xiao, M. L. Zhang and X. F. Bai, *Polymers*, 2013, **5**, 1258–1271.
- 28 C. V. Uglea, H. Ofenberg and A. Caçcaval, *Eur Polym J*, 1985, **21**, 681–683.
- 29 J. Davis, in *Plastics Additives: An A-Z reference*, ed. G. Pritchard, Springer Netherlands, Dordrecht, 1998, pp. 277–286.
- 30 J. Murphy, *Additives for Plastics Handbook*, Elsevier, 2001.
- 31 G. Faraca and T. Astrup, *Waste Manage*, 2019, **95**, 388–398.
- 32 A. Turner, *Environment International*, 2018, **117**, 308–318.
- 33 A. C.-Y. Wong, N. S. K. Ng and V. L. F. Ng, *J. Mater. Process. Tech.*, 1997, **63**, 468–471.
- 34 T. J. Suhrhoff and B. M. Scholz-Böttcher, *Mar Polym Bull*, 2016, **102**, 84–94.
- 35 Y. K. Lee, K. R. Murphy and J. Hur, *Environ. Sci. Technol.*, 2020, **54**, 11905–11914.
- 36 J. Liu, Q. G. Zhou, Y. X. Cheng, Y. H. Geng, L. X. Wang, D. G. Ma, X. B. Jing and F. S. Wang, *Adv Matter*, 2005, **17**, 2974–2978.
- 37 C.-F. Liao, B.-Y. Hsieh and Y. Chen, *J Polym Sci A1*, 2009, **47**, 149–160.
- 38 H. Lin, S. Patel and F. Jäkle, *Macromolecules*, 2020, **53**, 10601–10612.
- 39 I. Grabchev, X. Qian, Y. Xiao and R. Zhang, *New J. Chem.*, 2002, **26**, 920–925.
- 40 K. Kubota, N. Toyoshima, D. Miura, J. Jiang, S. Maeda, M. Jin and H. Ito, *Angw Chem Int Edit*, DOI:<https://doi.org/10.1002/anie.202105381>.
- 41 D. Garlotta, *J. Polym. Environ.*, 2001, **9**, 63–84.

Chapter 4. Design, Synthesis, and Characterisation of Luminophore Functionalised Doped-Ring Opening Co-Polymerisation Polymers

- 42 K. J. Jem and B. Tan, *Advanced Industrial and Engineering Polymer Research*, 2020, **3**, 60–70.
- 43 A. Z. Naser, I. Deiab and B. M. Darras, *RSC Adv.*, 2021, **11**, 17151–17196.
- 44 DyStar, *Ingeo Coloration Pack*, .
- 45 R. O. MacRae, C. M. Pask, L. K. Burdsall, R. S. Blackburn, C. M. Rayner and P. C. McGowan, *Angw. Chem. Int. Edit.*, 2011, **50**, 291–294.
- 46 A. Södergård and M. Stolt, *Prog Polym Sci*, 2002, **27**, 1123–1163.
- 47 T. Aida and S. Inoue, *J. Am. Chem. Soc.*, 1985, **107**, 1358–1364.
- 48 S. Huijser, E. HosseiniNejad, R. Sablong, C. de Jong, C. E. Koning and R. Duchateau, *Macromolecules*, 2011, **44**, 1132–1139.
- 49 E. H. Nejad, A. Paoniasari, C. E. Koning and R. Duchateau, *Polym. Chem.*, 2012, **3**, 1308–1313.
- 50 R. C. Jeske, A. M. DiCiccio and G. W. Coates, *J. Am. Chem. Soc.*, 2007, **129**, 11330–11331.
- 51 A. M. DiCiccio and G. W. Coates, *J. Am. Chem. Soc.*, 2011, **133**, 10724–10727.
- 52 N. J. Van Zee and G. W. Coates, *Angw. Chem. Int. Edit.*, 2015, **54**, 2665–2668.
- 53 C. Robert, F. de Montigny and C. M. Thomas, *Nat Commun*, 2011, **2**, 586.
- 54 E. Hosseini Nejad, C. G. W. van Melis, T. J. Vermeer, C. E. Koning and R. Duchateau, *Macromolecules*, 2012, **45**, 1770–1776.
- 55 M. E. Fieser, M. J. Sanford, L. A. Mitchell, C. R. Dunbar, M. Mandal, N. J. Van Zee, D. M. Urness, C. J. Cramer, G. W. Coates and W. B. Tolman, *J. Am. Chem. Soc.*, 2017, **139**, 15222–15231.
- 56 N. J. Van Zee, M. J. Sanford and G. W. Coates, *J. Am. Chem. Soc.*, 2016, **138**, 2755–2761.
- 57 K. Weisskopf, *J. Polym. Sci. A Polym. Chem.*, 1988, **26**, 1919–1935.
- 58 J. V. Obligacion and P. J. Chirik, *Nat Rev Chem*, 2018, **2**, 15–34.
- 59 C. E. Hoyle and C. N. Bowman, *Angw Chem Int Edit*, 2010, **49**, 1540–1573.
- 60 M. J. Kade, D. J. Burke and C. J. Hawker, *J Polym Sci A1*, 2010, **48**, 743–750.
- 61 A. B. Lowe, *Polym. Chem.*, 2014, **5**, 4820–4870.
- 62 M. J. Sanford, N. J. V. Zee and G. W. Coates, *Chem. Sci.*, 2017, **9**, 134–142.
- 63 G. Si, L. Zhang, B. Han, Z. Duan, B. Li, J. Dong, X. Li and B. Liu, *Polym. Chem.*, 2015, **6**, 6372–6377.
- 64 N. Yi, T. T. D. Chen, J. Unruangsri, Y. Zhu and C. K. Williams, *Chem Sci*, 2019, **10**, 9974–9980.
- 65 Y. Tokiwa and T. Suzuki, *Nature*, 1977, **270**, 76–78.
- 66 S. Kobayashi, H. Uyama and T. Takamoto, *Biomacromolecules*, 2000, **1**, 3–5.
- 67 G. L. Gregory, G. S. Sulley, L. P. Carrodeguas, T. T. D. Chen, A. Santmarti, N. J. Terrill, K.-Y. Lee and C. K. Williams, *Chem. Sci.*, 2020, **11**, 6567–6581.
- 68 M. Häußler, M. Eck, D. Rothauer and S. Mecking, *Nature*, 2021, **590**, 423–427.
- 69 G. M. Sammis, H. Danjo and E. N. Jacobsen, *J. Am. Chem. Soc.*, 2004, **126**, 9928–9929.
- 70 L. A. Clementi, G. R. Meira, D. Berek, L. I. Ronco and J. R. Vega, *Polymer Testing*, 2015, **43**, 58–67.
- 71 K. Levenberg, *Quart. Appl. Math.*, 1944, **2**, 164–168.
- 72 D. W. Marquardt, *Journal of the Society for Industrial and Applied Mathematics*, 1963, **11**, 431–441.
- 73 M. Wojdyr, *Journal of Applied Crystallography*, 2010, **43**, 1126–1128.
- 74 O. G. Guppy, T. B. Young, A. J. Draper, B. M. Kariuki, A. Paul, S. J. A. Pope and B. D. Ward, *Manuscript in preparation*.

5 Thesis Summary and Future Work

5.1 Summary

This thesis aimed to explore and examine two approaches to preparing luminescent materials for display technologies: inorganic particles and luminescent polymers. Whilst the color gamut of the luminescent polymers was very narrow, this work presents a viable proof of concept alternative to current polymer LEDs. The luminescent polymers were also found to function as color fast plastics which are amenable to chemical depolymerisation through ester linkages.

Chapter 1 examined two areas of zinc sulfide luminescence: the origin of the emission and the tuneability that can be achieved. Determination of the defect states caused by doping zinc sulfides was examined through a combined experimental and computational approach, showing good agreement between computationally determined results and experimentally observed values. The four defects identified in this work are interstitial zinc and sulfur, and zinc and sulfur vacancy defects, corresponding to emission values of 520, 605, 450, and 490 nm respectively. Interestingly, interstitial sulfur was the least commonly observed defect and only observed for an undoped zinc sulfide exposed to the wet impregnation method and calcium sulfide doped samples. Therefore, only blue and green emission can be reliably obtained from native defects. However, a red (620 nm) emitting material could be produced by the combination of manganese oxide and barium sulfide (10 mol%). Whilst two other group 2 metals, calcium and strontium, were combined in an analogous manner with manganese, only an emission at 580 nm was observed. It is believed the origin of the red shift is caused by the formation of Ba_2ZnS_3 , it is unknown, however, if calcium and strontium formed a similar phase. Tuneability of the individual wavelengths in doped zinc sulfides was found to be minimal, with barium and strontium doped zinc sulfides generating the same defects, and emission wavelengths, as aluminium, copper, and halogen doped samples. Whilst high concentrations of barium (8 mol%) were observed to broaden the emission there was no significant change in the peak wavelength, although similar effects were not observed for calcium or strontium doped zinc sulfides. Combination of the blue (450 nm), green (520 nm), and red (620 nm) emission using an International Commission on Illumination (CIE) 1931 color space chromaticity diagram showed the doped zinc sulfides prepared within this work are only capable of reproducing 47% of the sRGB color space, significantly below the 90%+ consumer displays are capable of reproducing. Silica coating was also examined as a method to decrease the oxidation of the zinc sulfides degrading the desired luminescent properties. Promisingly, it was observed at 800 °C under an air

atmosphere the degree of oxidation had been significantly reduced with minimal zinc oxide observed, potentially increasing their longevity. Overall, whilst the emission properties were found to be less than desirable for modern use, the materials are easy to prepare and protect from oxidation. In applications where a wide color gamut is not a requirement these materials may still find use.

Chapters 2 and 3 developed luminescent polymers as an alternative to inorganic particles with the two chapters focusing on the creation of luminescent monomers or additive, and creation of the polymers, respectively. In chapter 2, two luminescent frameworks were selected: 1,8-naphthalimides and 1-aminoanthraquinones. In this work the stepwise functionalisation of the naphthalimide was exploited to introduce a piperidine or morpholine group into the 4-position of the naphthalimide, generating an intramolecular charge transfer, producing a bright green emission, and an epoxide, amine or thiol functionality in the imide position for incorporation into the polymer. The second luminescent material, 1-aminoanthraquinone, was selected as it similarly afforded ease of functionalisation and generated a yellow emission whilst maintaining solubility in the conditions used and did not contain a metal or other functional groups that may disrupt polymerisation. The epoxidation of these two frameworks was found to be accomplished with relative ease and high yields serving as an effective proof of concept for the production of luminescent monomers for the ring opening co-polymerisation of anhydrides and epoxides to produce polyesters with a color fast additive. Thiol functionalisation was hoped to present a second method of functionalisation through post-polymerisation modification coupling of a thiol and an alkene in a thiol-ene reaction. Unfortunately, however, it was not possible to isolate a free thiol during this work for polymer modification.

Using the luminescent compounds synthesised in chapter 2 and the blue emitting aluminium salen catalyst, three luminescent polymers with a covalently bound luminophore were prepared emitting in the blue (481 nm), green (512 nm), and yellow (583 nm) regions. Pleasingly, despite the significant scale up from ca. 0.6 g to 300 g no significant degradation of the catalytic process was observed even with incorporation of the dopant, producing bimodal polymers with a well-defined dispersity of less than 1.10. Post-polymerisation was also examined using an epichlorohydrin derived polymer and a pendant amine functionalised naphthalimide. MALDI analysis showed the polymer had degraded – showing a broad range of molecular weights instead of well-defined repeat unit spacings. As such, this demonstrated that the post-polymerisation approach trialled was not as effective as the in-situ doping method. As with the inorganic particles, the color

space coverage was low, covering only 29% of the sRGB color space. However, this is not a limitation of luminescent polymers but due to the choice of luminophores creating a reduced color space. Since these polymers contain ester groups, which are a target for chemical depolymerisation, recycling of a polymer was attempted using an organic acid. Whilst the material was degraded, showing short chain oligomers, no conversion to the diol or diacid was observed. Additionally, the pure phthalic anhydride, cyclohexene oxide co-polymer was examined for use as an alternative material to the traditional plastics. While the polymer was processable from a powder through extrusion, the material thereby produced was brittle and snapped easily. Similarly, direct injection moulding of the polymer was possible, but the highly crystalline nature of the polymer caused the dog-bone shape to snap upon removal from the mould. Whilst the material properties are poor in comparison to commercially available polymers, this work shows the potential for ROCOP polymers as both polymer based OLEDs and as a potential alternative to the non-renewable and difficult to recycle plastics currently used today.

5.2 Future Work

Regarding zinc sulfide, it is believed that further work in the production of luminescent zinc sulfides for displays is limited. The broad emission generated for each defect, the narrow color gamut, and the relatively low quantum yield values reported within the literature,¹⁻³ combine to make a material with few desirable properties when compared to inorganic particles within the literature. For example, perovskites are well known for their narrow bandwidth (high color purity) and almost unity quantum yield for lead perovskites⁴⁻⁷. Recently in 2019 an indium phosphide coated with zinc selenide and zinc sulfide was reported by Samsung⁸ providing almost unity quantum yield and a narrow bandwidth. Similar results have been reported for other examples of quantum dots throughout the literature, which are able to provide a narrow emission due to the quantum confinement effect. Such materials are likely to provide the most desirable properties for display technologies.^{9,10} Indeed, Samsung are already producing TVs using quantum dots to enhance the color saturation and peak brightness of consumer displays.

In contrast, the luminescent polymers prepared in this thesis represent a proof of concept for further development towards more commercially relevant properties in both luminescence and mechanical properties. With regards to luminescence, the color space can be improved by incorporating an epoxide

functionalised deep blue emitter such as a coumarin and a red emitter with a higher quantum yield than the anthraquinone, such as an iridium complex through the incorporation of an epoxide functionalised ligand during polymerisation. One of the key advantages of a polymer over traditional OLEDs is the increased solubility that can be afforded to the luminophore through incorporation into the polymer.

Therefore, combining the desirable photophysical properties of an OLED with the solution processability of a polymer would create an attractive alternative. Literature reports have shown the potential for a synergic effect between a polymer and an additive,^{11,12} potentially leading to enhanced photophysical properties. An example in this work is seen in the bright green luminescence of the naphthalimide doped polymer in the solid state as the surrounding polymer units prevent the self-quenching of the naphthalimide. Additionally, judicious choice of the monomers may afford a device with fewer layers and a high degree of flexibility decreasing costs and increasing the applications of the device and materials.

Therefore, examination of the mechanical properties that can be obtained through substitution of monomers is believed to warrant further investigation. Introduction of more sterically demanding groups may disrupt the packing of the polymer decreasing the degree of rigid packed crystalline regions forming that limit the processability, as observed for phthalic anhydride and cyclohexene oxide copolymers. Investigation into the effect of polymer chain length on mechanical properties and examination into how, if at all, the polydispersity of the polymer chains alters as the molecular weight increases is essential for further commercial use. The search for suitable monomers is considered to be a worthwhile endeavour as the replacement of difficult to recycle plastics with ester linked polymer units could help to reduce plastic pollution, which is reported frequently within both the literature and within the consumer facing news articles. Two recent papers reported microplastics within the blood and lungs of humans,^{13,14} detailing the extent of plastic pollution in the world today. Thus, it is also crucial to develop an effective method of degradation in these polymers. While work within the Ward group has shown potassium hydroxide in THF/water can cause complete conversion into the diol and diacid monomers this is harsh process and less hazardous methods are preferable to create a less environmentally damaging method of recycling.

5.3 References

- 1 Z. Deng, L. Tong, M. Flores, S. Lin, J.-X. Cheng, H. Yan and Y. Liu, *J. Am. Chem. Soc.*, 2011, 133, 5389–5396.
- 2 R. Begum and A. Chattopadhyay, *J. Phys. Chem. Lett.*, 2014, 5, 126–130.
- 3 R. Bose, U. Thupakula, J. K. Bal and N. Pradhan, *J. Phys. Chem. C*, 2012, 116, 16680–16686.
- 4 Q. A. Akkerman, V. D’Innocenzo, S. Accornero, A. Scarpellini, A. Petrozza, M. Prato and L. Manna, *J. Am. Chem. Soc.*, 2015, 137, 10276–10281.
- 5 V. G. V. Dutt, S. Akhil and N. Mishra, *ChemNanoMat*, 2020, 6, 1730–1742.
- 6 Y. Ling, Z. Yuan, Y. Tian, X. Wang, J. C. Wang, Y. Xin, K. Hanson, B. Ma and H. Gao, *Advanced Materials*, 2016, 28, 305–311.
- 7 L. Protesescu, S. Yakunin, M. I. Bodnarchuk, F. Krieg, R. Caputo, C. H. Hendon, R. X. Yang, A. Walsh and M. V. Kovalenko, *Nano Lett.*, 2015, 15, 3692–3696.
- 8 Y.-H. Won, O. Cho, T. Kim, D.-Y. Chung, T. Kim, H. Chung, H. Jang, J. Lee, D. Kim and E. Jang, *Nature*, 2019, 575, 634–638.
- 9 J. R. Manders, L. Qian, A. Titov, J. Hyvonen, J. Tokarz-Scott, K. P. Acharya, Y. Yang, W. Cao, Y. Zheng, J. Xue and P. H. Holloway, *Journal of the Society for Information Display*, 2015, 23, 523–528.
- 10 Y. Shu, X. Lin, H. Qin, Z. Hu, Y. Jin and X. Peng, *Angewandte Chemie International Edition*, 2020, 59, 22312–22323.
- 11 M. Y. Wong, *Journal of Elec Materi*, 2017, 46, 6246–6281.
- 12 Y. Ma, Z. Zhong, F. Peng, L. Ying, J. Xiong, J. Peng and Y. Cao, *Organic Electronics*, 2019, 68, 103–107.
- 13 L. C. Jenner, J. M. Rotchell, R. T. Bennett, M. Cowen, V. Tentzeris and L. R. Sadosky, *Science of The Total Environment*, 2022, 831, 154907.
- 14 H. A. Leslie, M. J. M. van Velzen, S. H. Brandsma, A. D. Vethaak, J. J. Garcia-Vallejo and M. H. Lamoree, *Environment International*, 2022, 107199.

6 Appendix

6.1 Chapter 2 Appendix

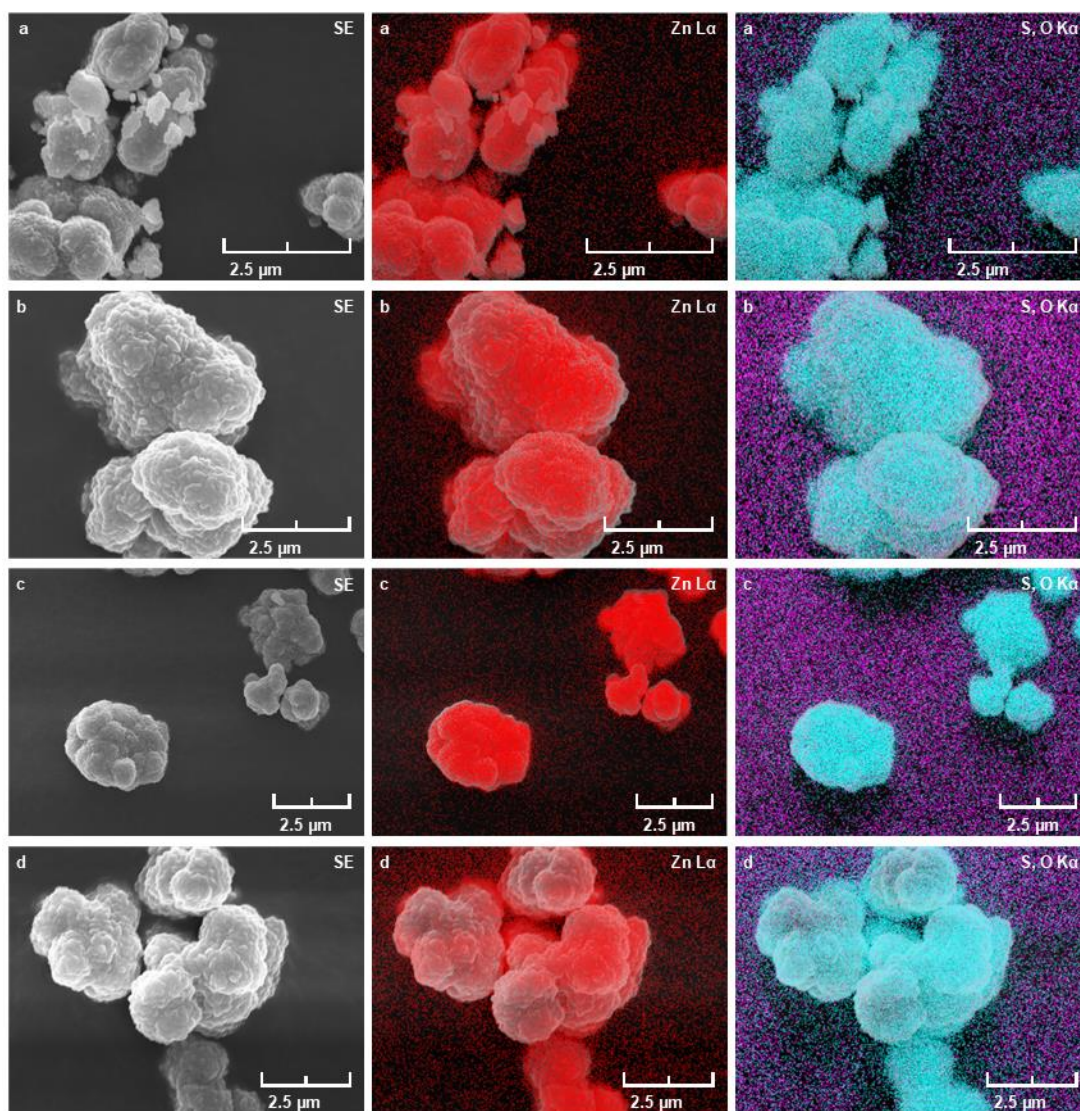


Figure 6.1: SEM and EDX images of ZnS samples a) No dopant, b) NH_4Cl , c) CuSO_4 , and d) CuSO_4 , NH_4Cl prepared by wet impregnation showing contributions from zinc, sulfur, and oxygen.

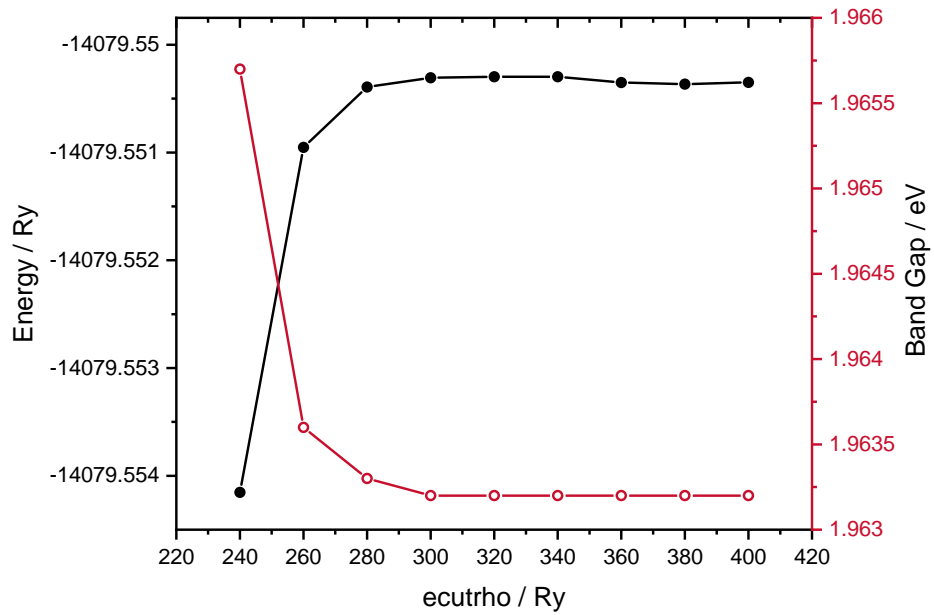


Figure 6.2: Energy (black line, ●) and band gap (red line, o) of a 64 atom zinc sulfide cell with a lattice parameter of 20.44408 Bohr (10.81854 Å) as the kinetic energy cutoff of the charge density and potential (ecutrho) is altered.

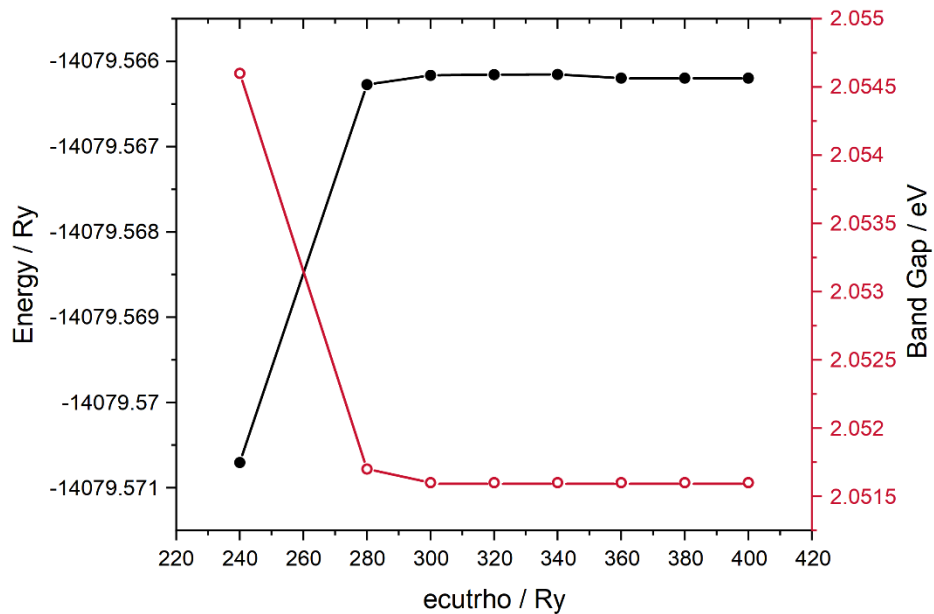


Figure 6.3: Energy (black line, ●) and band gap (red line, o) of a 64 atom zinc sulfide cell with a lattice parameter of 20.24749 Bohr (10.71451 Å) as the kinetic energy cutoff of the charge density and potential (ecutrho) is altered.

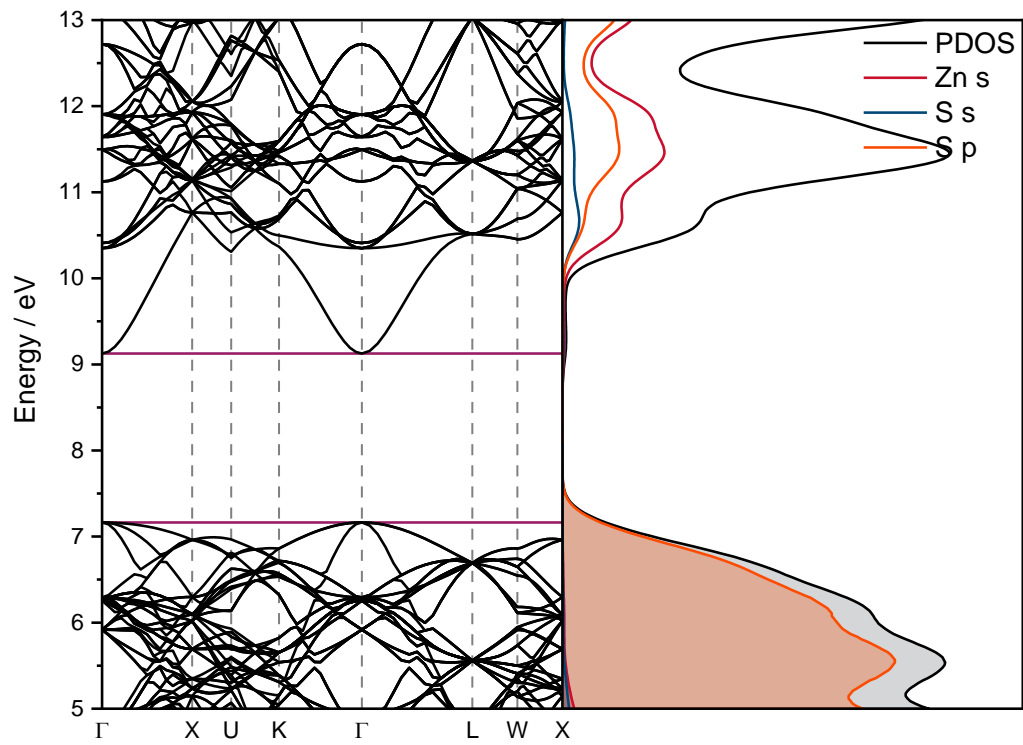


Figure 6.4: Band structure (L) where purple lines indicate the top and bottom of the valence and conduction bands respectively. PDOS (R) showing the contribution of orbitals towards the filled (shaded) and empty bands for a fixed ZnS supercell of 64 atoms with no defects.

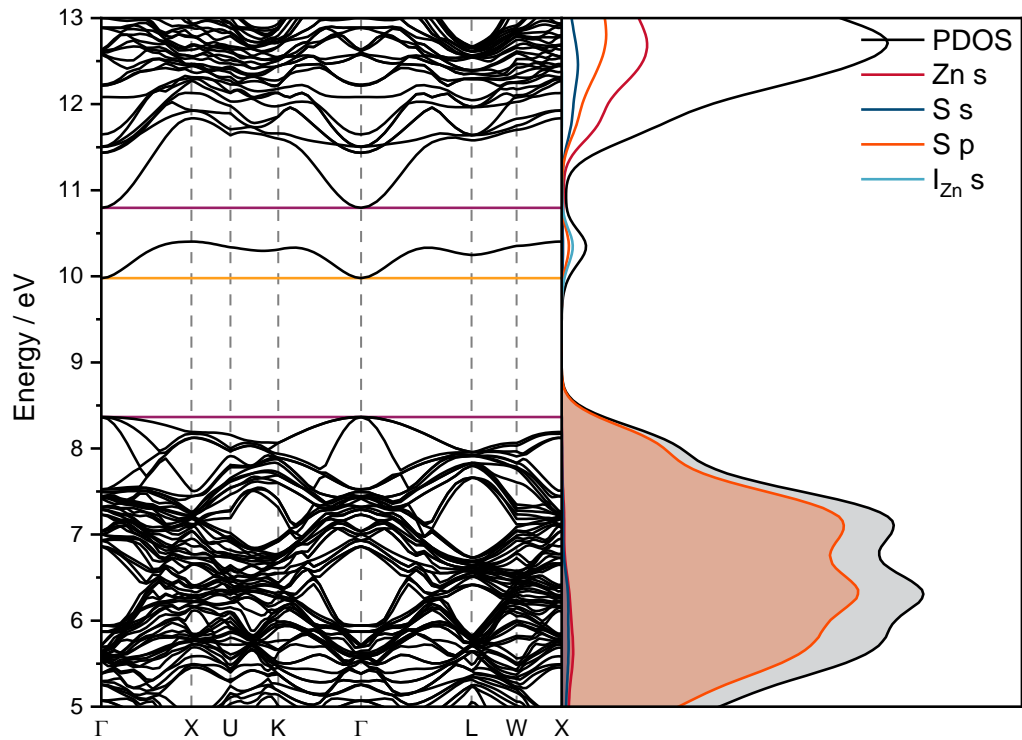


Figure 6.5: Band structure (L) where purple lines indicate the top and bottom of the valence and conduction bands of the bulk ZnS, respectively; and the yellow line indicates the bottom of the conduction band caused by the zinc defect. PDOS (R) showing the contribution of orbitals towards the filled (shaded) and empty bands for an optimised ZnS supercell of 64 atoms with an interstitial zinc.

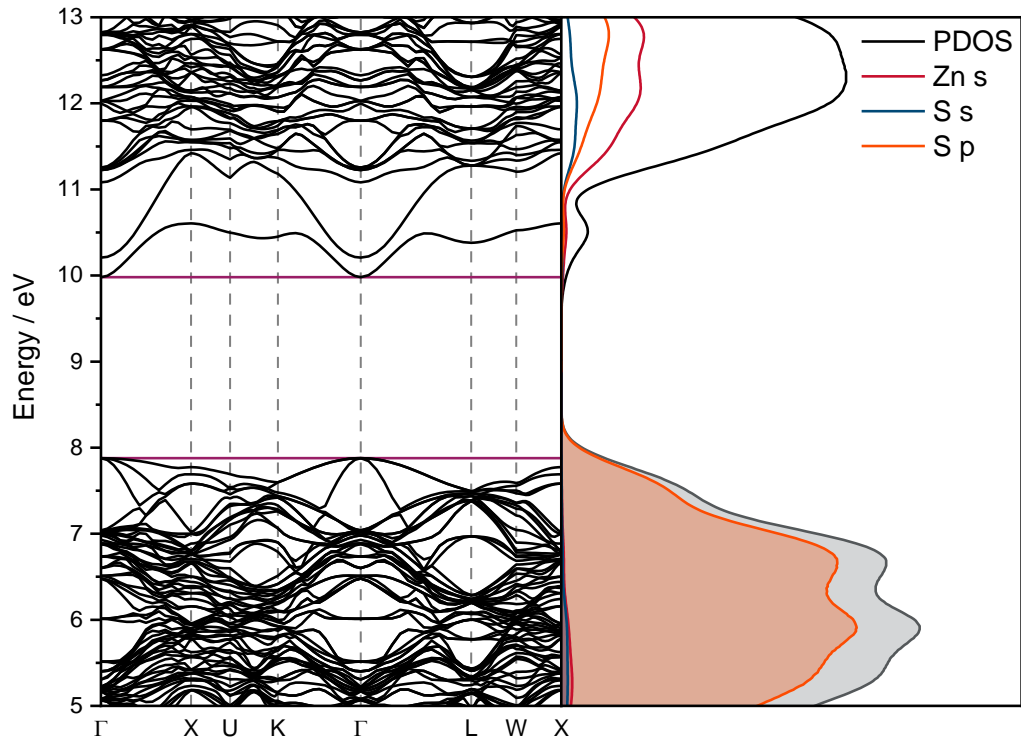


Figure 6.6: Band structure (L) where purple lines indicate the top and bottom of the valence and conduction bands respectively. PDOS (R) showing the contribution of orbitals towards the filled (shaded) and empty bands for a fixed ZnS supercell of 64 atoms with a sulfur vacancy.

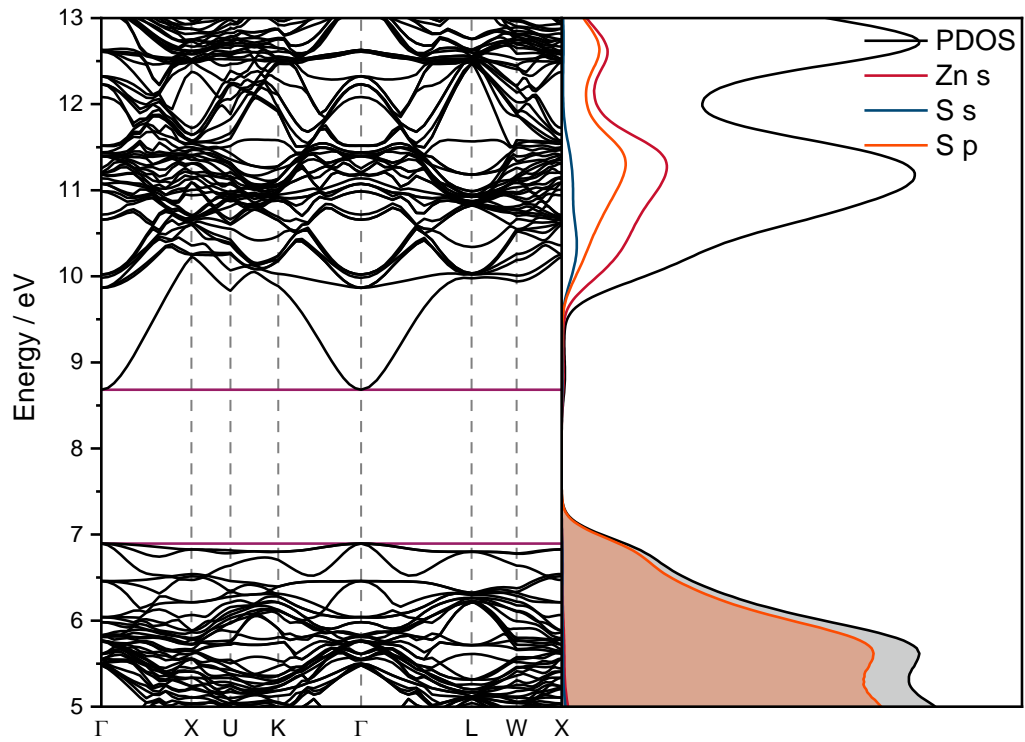


Figure 6.7: Band structure (L) where purple lines indicate the top and bottom of the valence and conduction bands respectively. PDOS (R) showing the contribution of orbitals towards the filled (shaded) and empty bands for a fixed ZnS supercell of 64 atoms with a zinc vacancy.

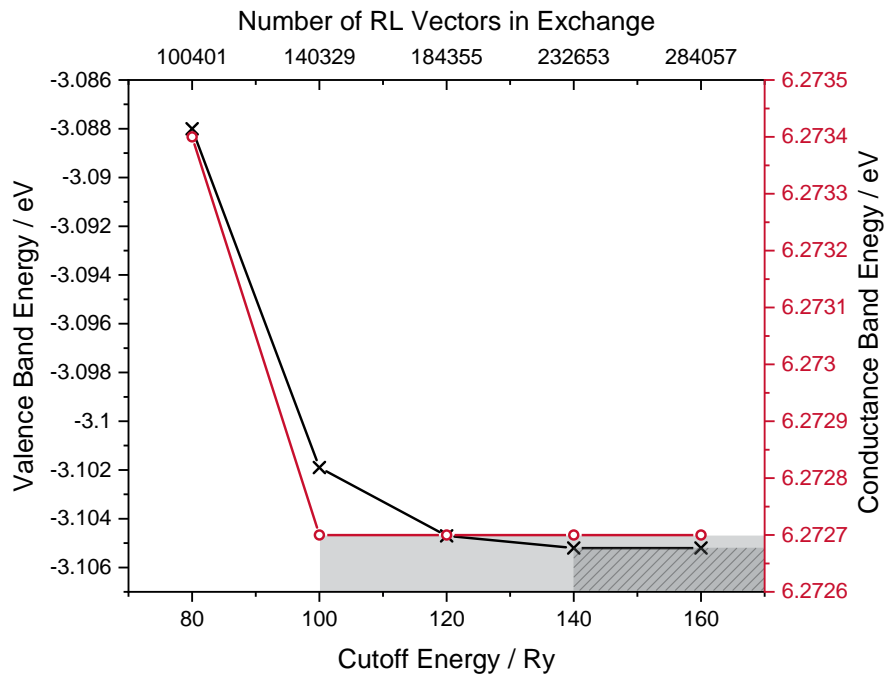


Figure 6.8: Energy of the valence and conduction bands for an optimised ZnS supercell with 64 atoms as the cutoff energy governing the number of RL vectors is changed.

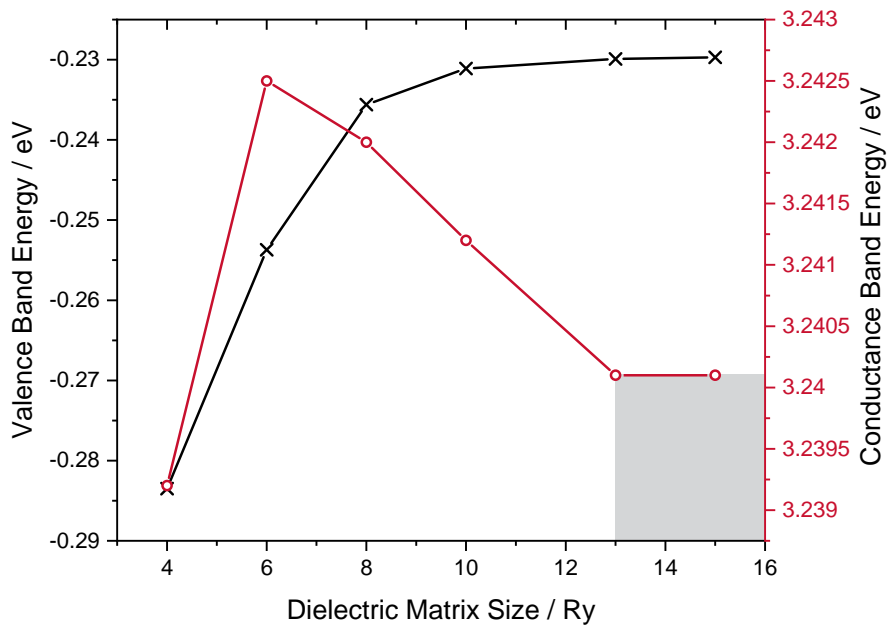


Figure 6.9: Energy of the valence and conduction bands for an optimised ZnS supercell with 64 atoms as the cutoff energy governing the size of the dielectric matrix is changed.

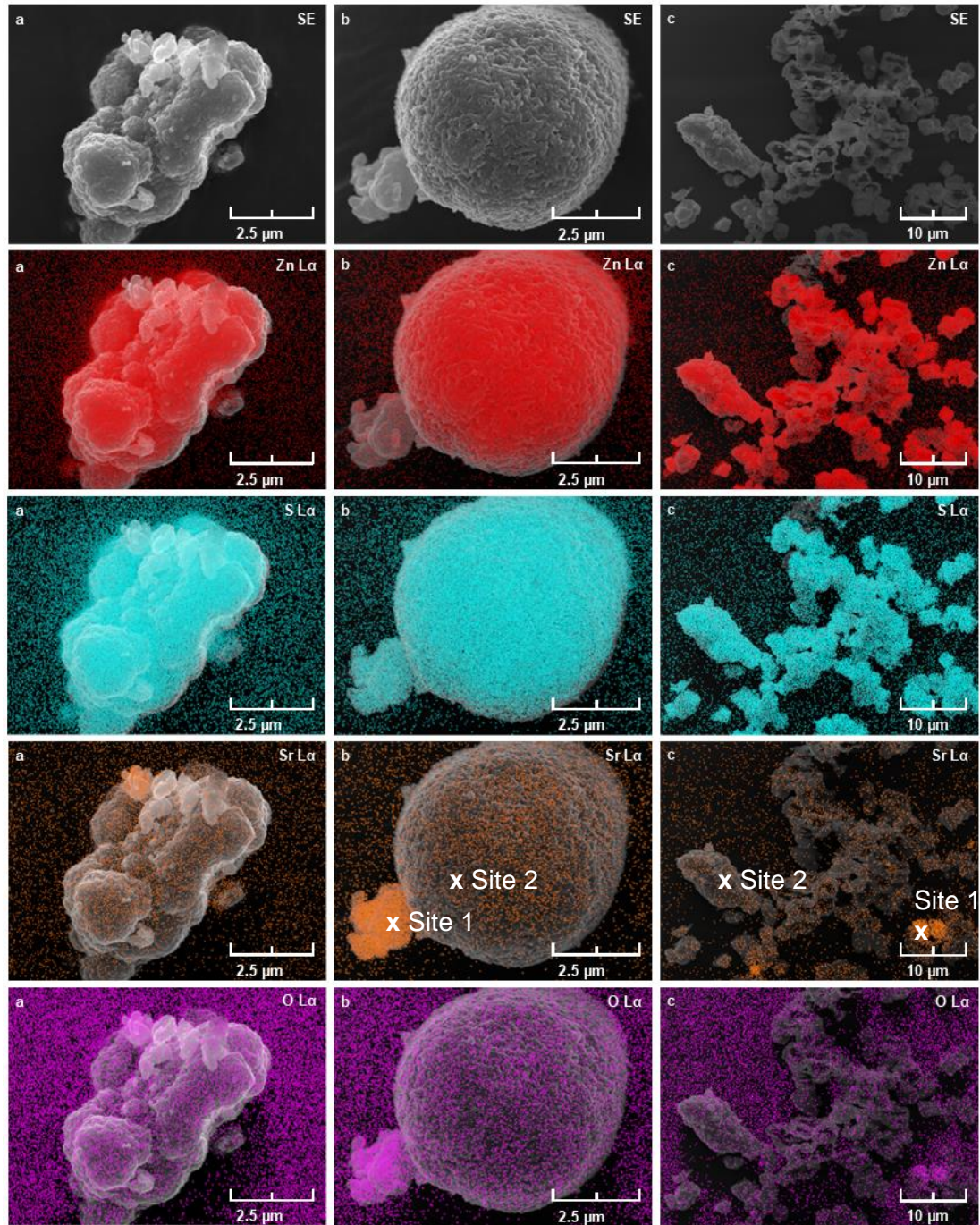


Figure 6.10: SEM and EDX data for strontium doped zinc sulfides at varying dopant levels; a) 8 mol%, b) 4 mol%, c) 2 mol% showing contributions from zinc, sulfur, strontium, and oxygen.

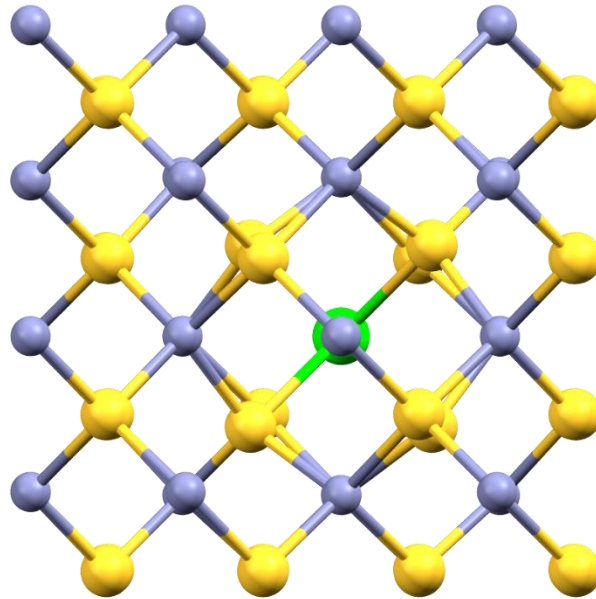


Figure 6.11: Calculated structure of a 64 atom ZnS supercell with a strontium defect (green) using the PBEsol functional.

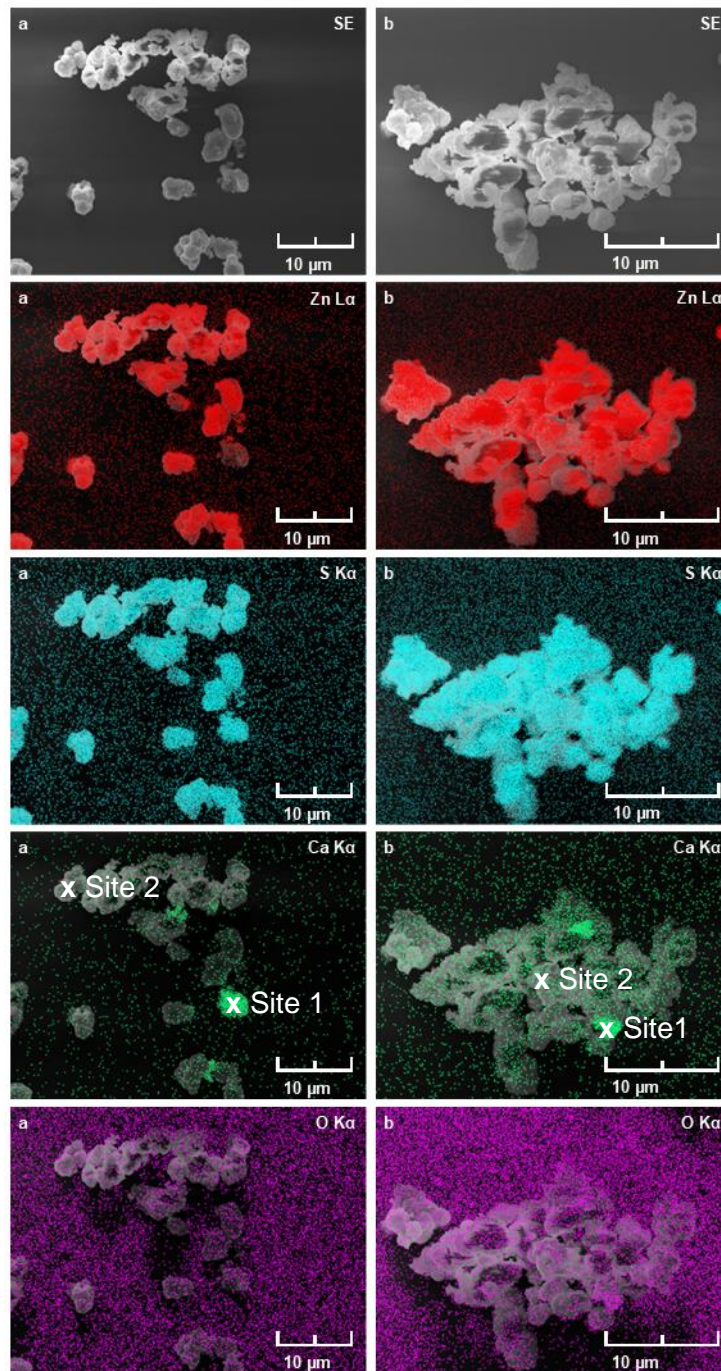


Figure 6.12: SEM and EDX data for calcium doped zinc sulfides at varying dopant levels; a) 12 mol%, b) 8 mol% showing contributions from zinc, sulfur, calcium, and oxygen.

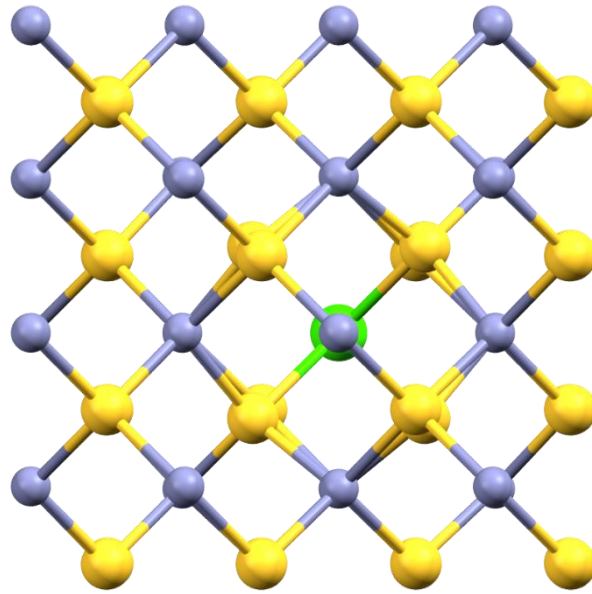


Figure 6.13: Calculated structure of a 64 atom ZnS supercell with a calcium defect (green) using the PBEsol functional.

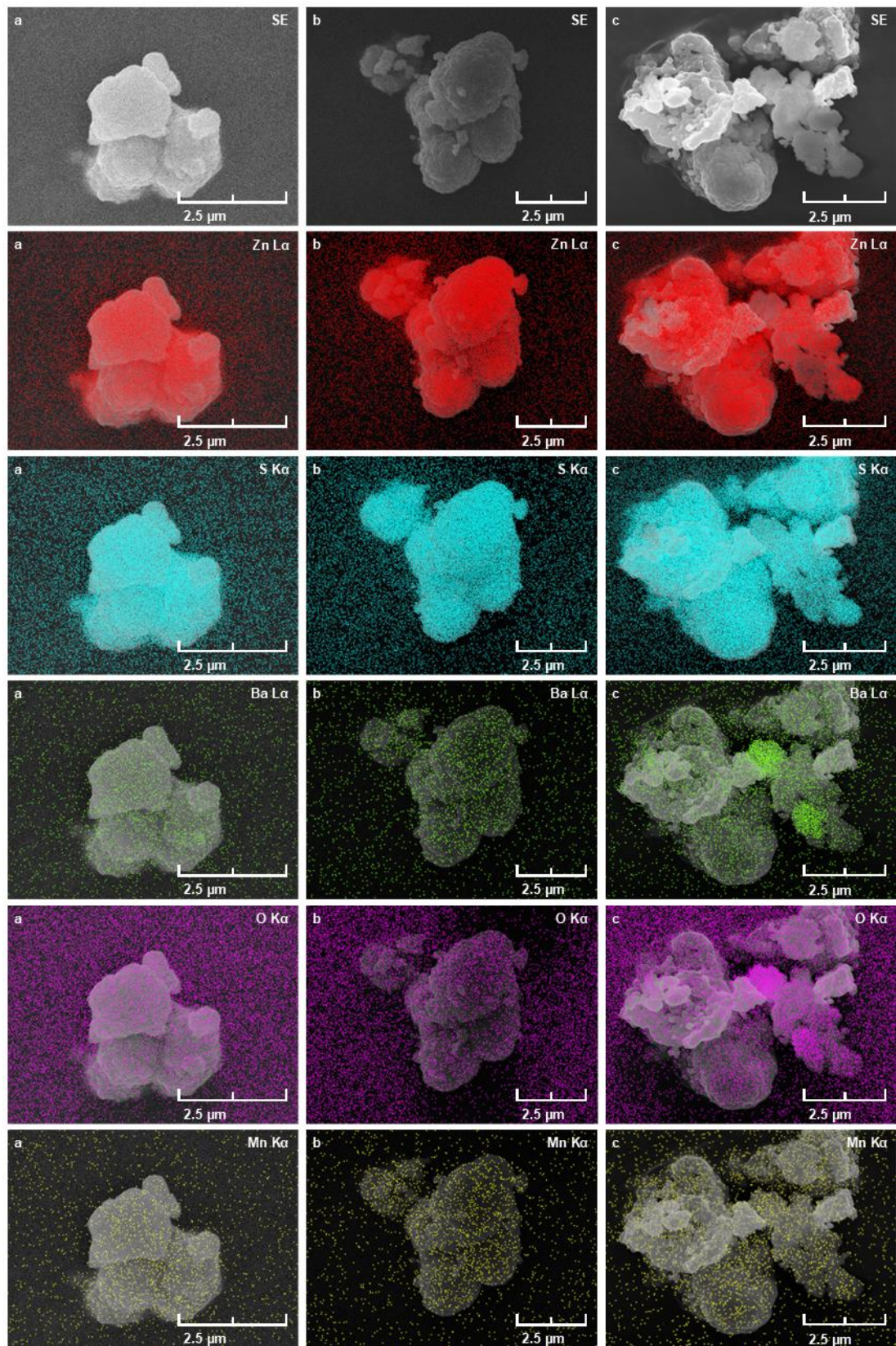


Figure 6.14: SEM and EDX images for barium sulfide and manganese nitrate doped zinc sulfides a) 8 mol% Ba, b) 4 mol% Ba, c) 2 mol% Ba showing contributions from zinc, sulfur, barium, oxygen, and manganese

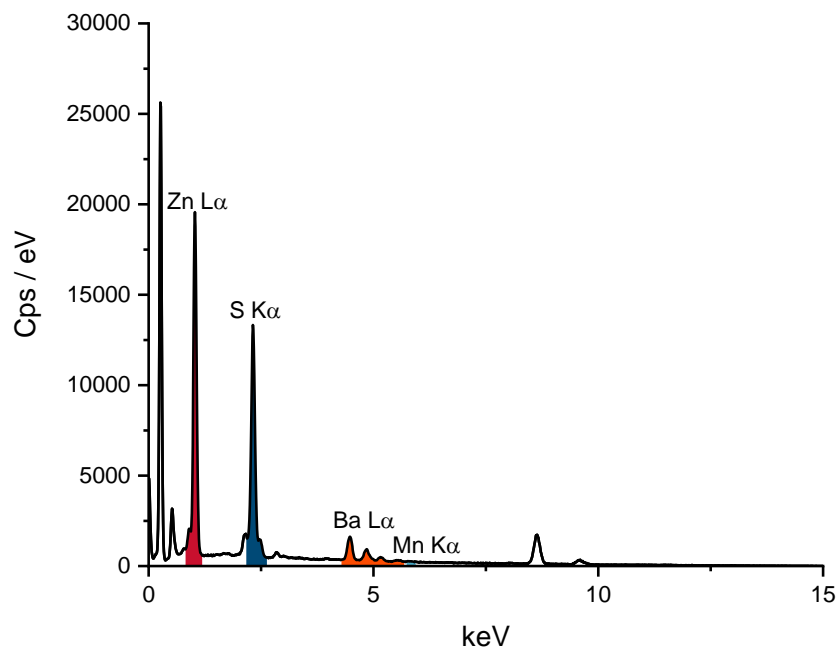


Figure 6.15: X-ray spectrum for 8 mol% barium and manganese oxide doped zinc sulfide

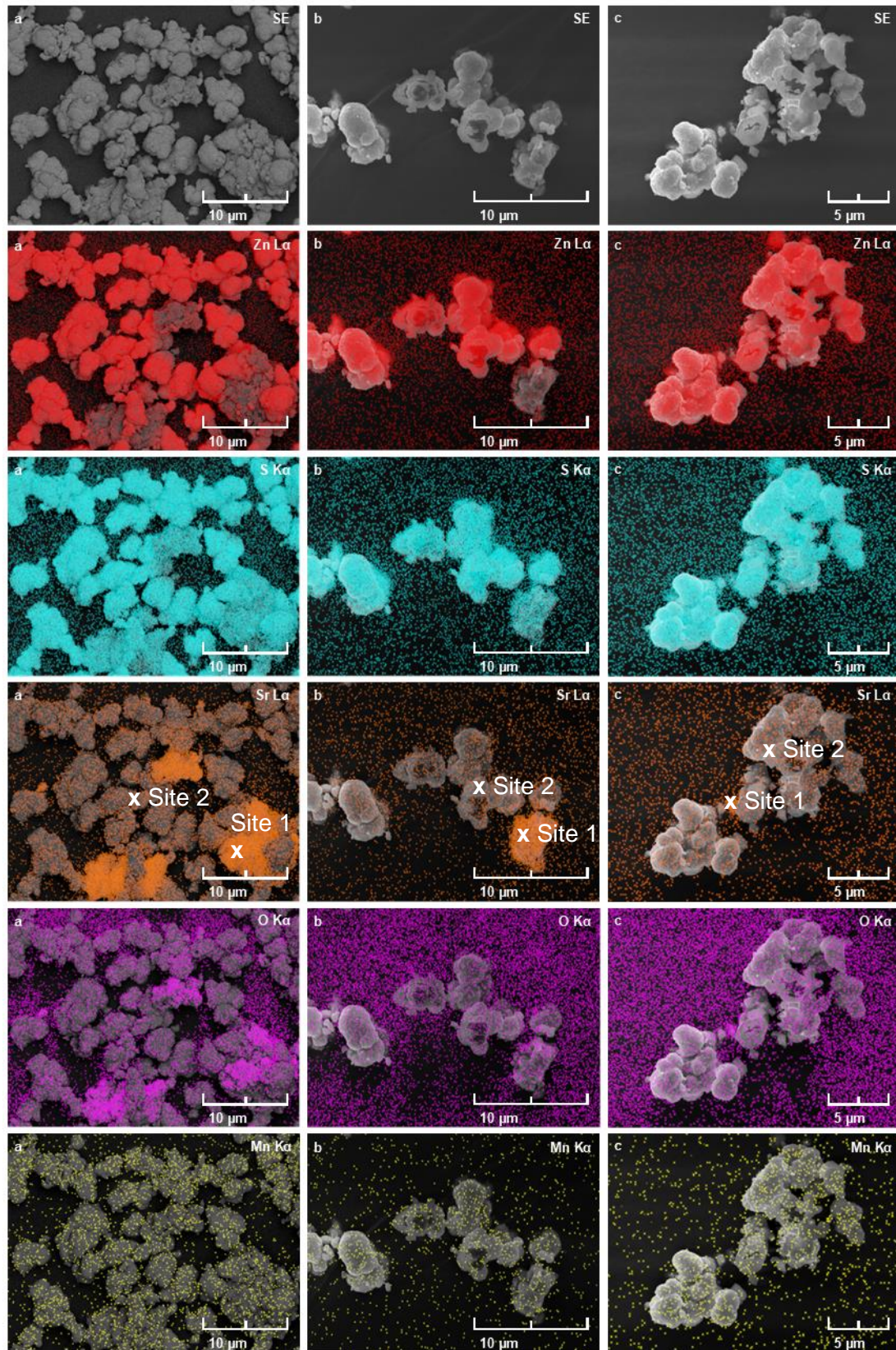


Figure 6.16: SEM and EDX images for strontium sulfide and manganese oxide doped zinc sulfides a) 8 mol% Sr, b) 4 mol% Sr, c) 2 mol% Sr showing contributions from zinc, sulfur, strontium, oxygen, and manganese

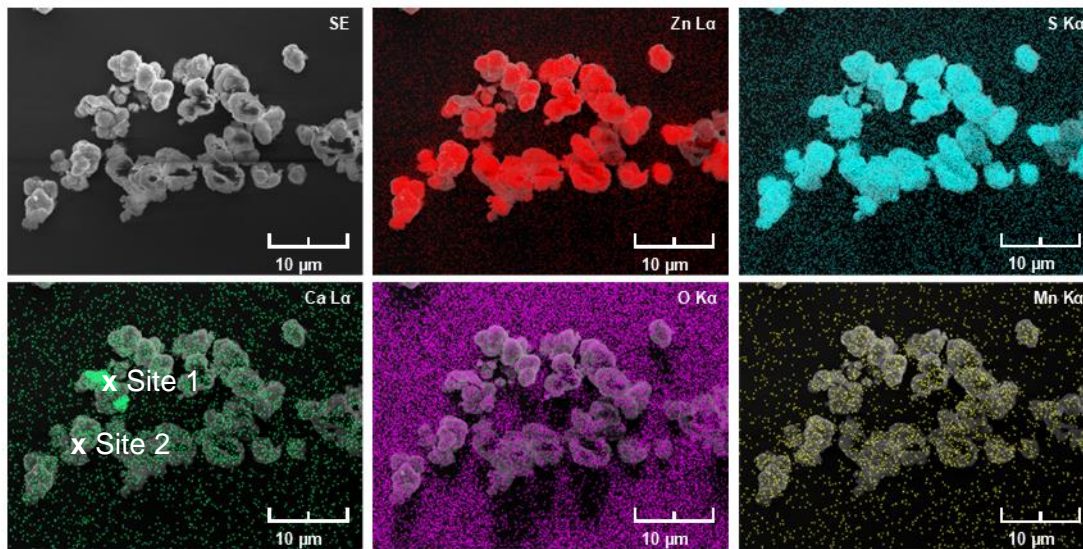


Figure 6.17: SEM and EDX images for 8 mol% calcium sulfide and manganese sulfide doped zinc sulfides showing contributions from zinc, sulfur, calcium, oxygen, and manganese

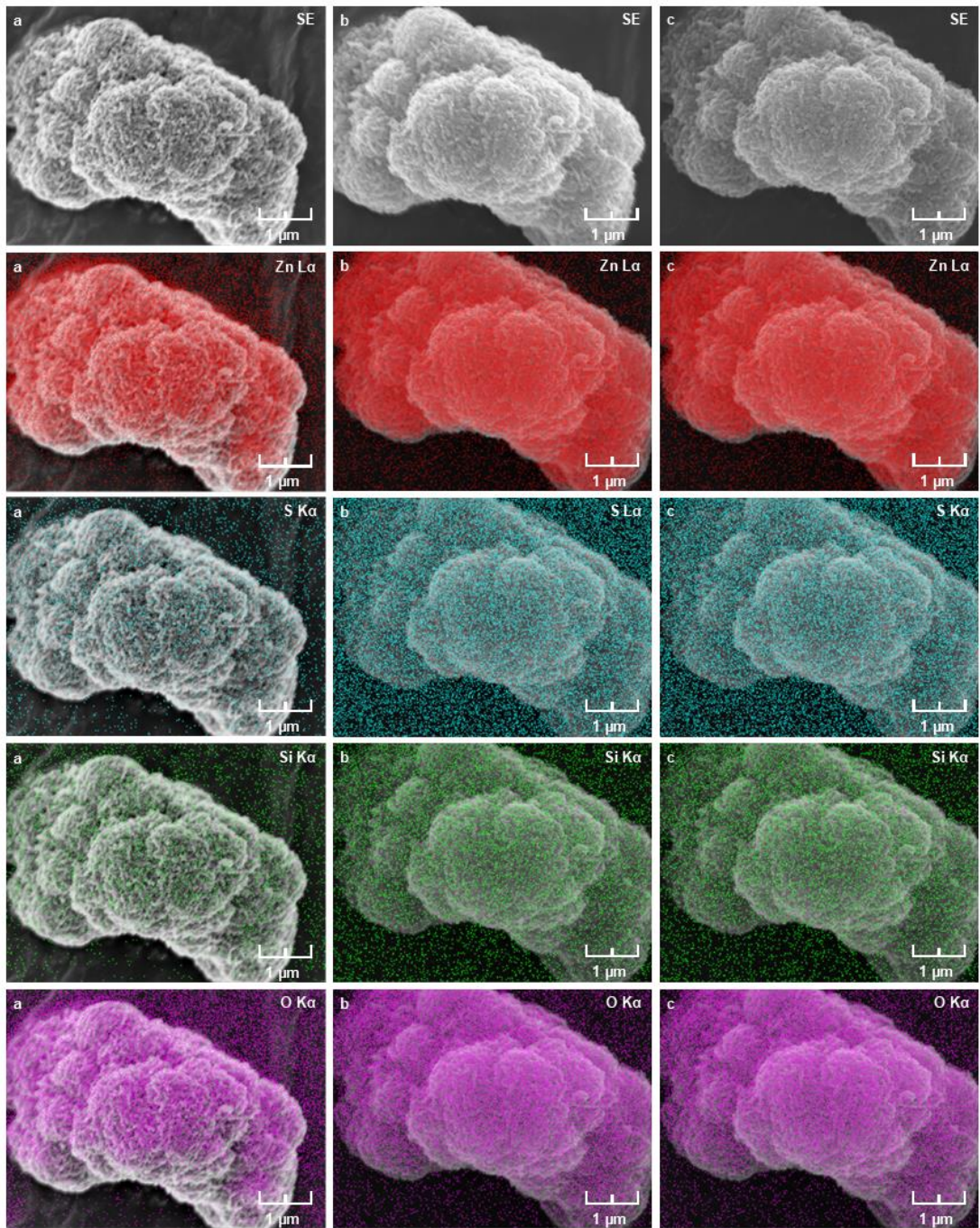


Figure 6.18: SEM and EDX images of uncoated zinc sulfides heat treated at 800 °C in air at difference accelerating voltages: a) 5kV, b) 15 kV, c) 30 kV showing contributions from zinc, sulfur, silicon, and oxygen

6.2 Chapter 3 Appendix

6.2.1 UV-Vis Absorption Graphs

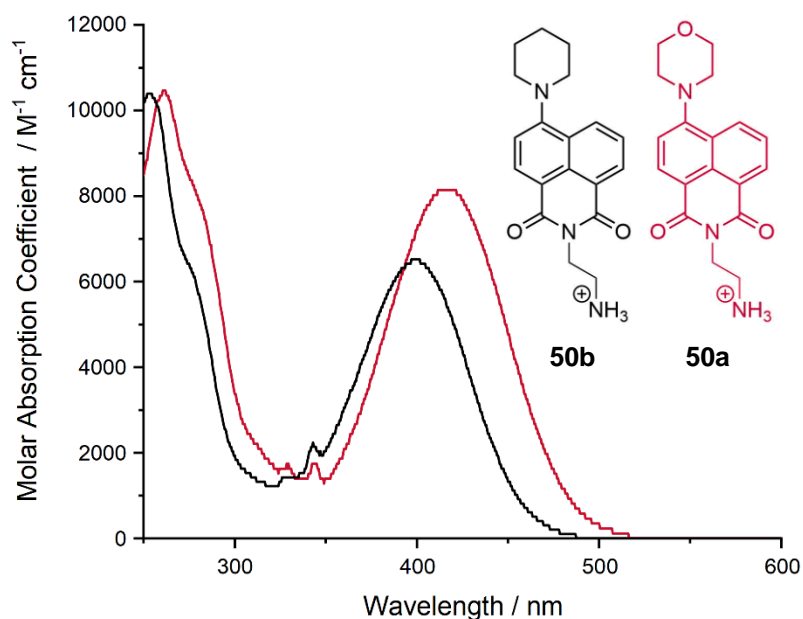


Figure 6.19: UV-Vis absorption spectra of **50a**, and **50b** as chloroform solutions, with the TFA counterion omitted for clarity.

6.2.2 TD-DFT Graphs

Compound 45b

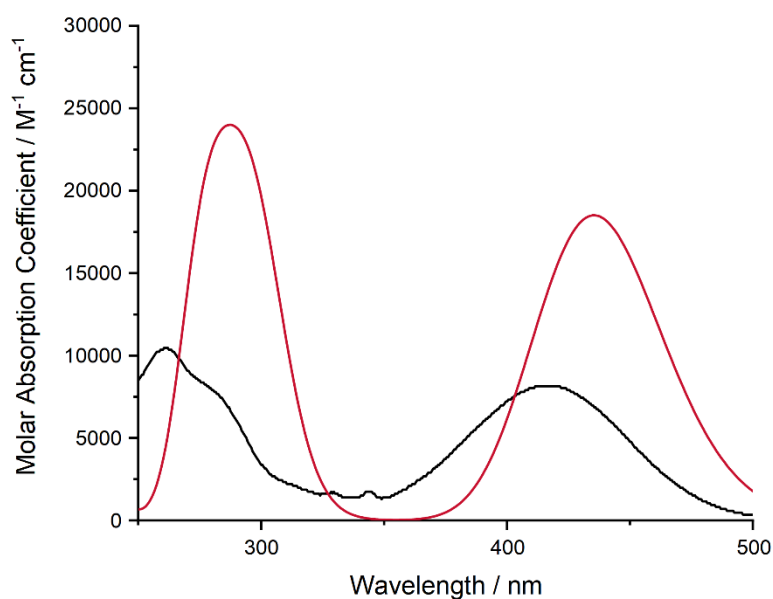


Figure 6.20: Experimental (black line) and simulated UV-Vis spectra (red line, predicted ϵ) of **45b** in chloroform performed with TD-DFT using the B3LYP functional and cc-PVDZ basis set.

Compound 54

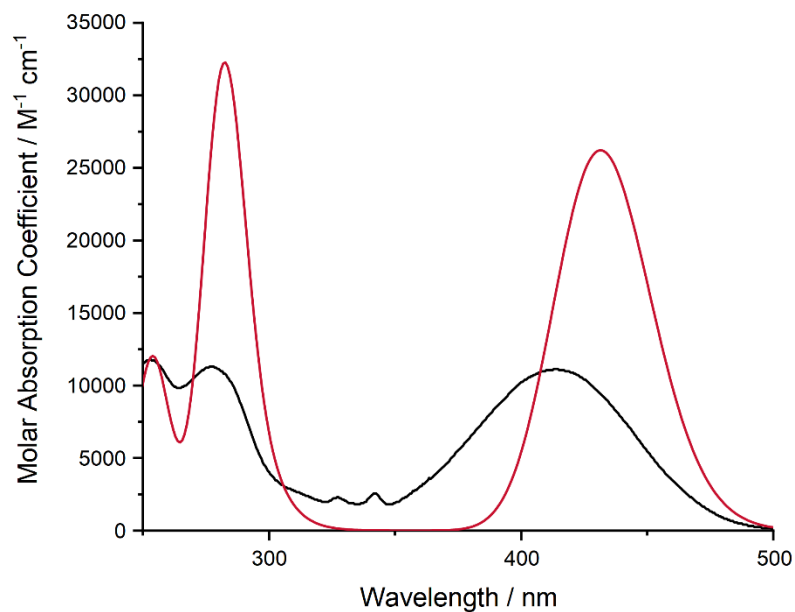


Figure 6.21: Experimental (black line) and simulated UV-Vis spectra (red line, predicted ϵ) of **54** in chloroform performed with TD-DFT using the B3LYP functional and cc-PVDZ basis set.

Compound 58

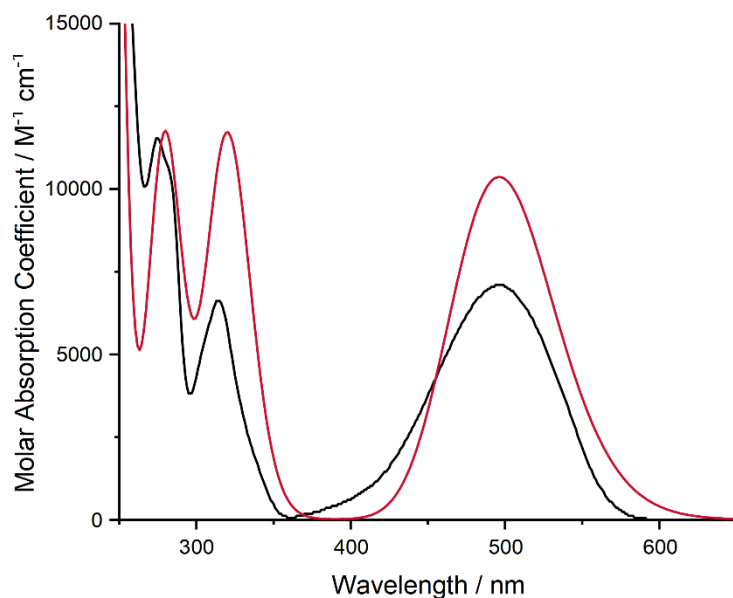


Figure 6.22: Experimental (black line) and simulated UV-Vis spectra (red line, predicted ϵ) of **58** in chloroform performed with TD-DFT using the B3LYP functional and cc-PVDZ basis set.

Table 6.1: Crystal data and structure refinement for 55.

Identification code	og5
Empirical formula	C ₂₀ H ₂₀ N ₂ O ₃
Formula weight	336.38
Temperature	100(2) K
Wavelength	0.71073 Å
Crystal system	Orthorhombic
Space group	Pbca
Unit cell dimensions	$a = 12.782(3) \text{ \AA}$, $\alpha = 90^\circ$ $b = 7.6564(15) \text{ \AA}$, $\beta = 90^\circ$ $c = 32.715(7) \text{ \AA}$, $\gamma = 90^\circ$
Volume	3201.5(11) Å ³
Z	8
Density (calculated)	1.396 Mg/m ³
Absorption coefficient	0.095 mm ⁻¹
F(000)	1424
Crystal size	0.180 × 0.080 × 0.020 mm ³
θ range for data collection	2.022 to 32.669 °
Index ranges	-14 ≤ h ≤ 19, -10 ≤ k ≤ 9, -47 ≤ l ≤ 47
Reflections collected	43523
Independent reflections	5218 [R(int) = 0.0280]
Completeness to θ = 25.242 °	100.00%
Absorption correction	Semi-empirical from equivalents
Max. and min. transmission	1.00000 and 0.82305
Refinement method	Full-matrix least-squares on F ²
Data / restraints / parameters	5218 / 138 / 263
Goodness-of-fit on F ²	1.187
Final R indices [I > 2σ(I)]	R ₁ = 0.0764, wR ₂ = 0.2052
R indices (all data)	R ₁ = 0.0870, wR ₂ = 0.2115
Extinction coefficient	n/a
Largest diff. peak and hole	0.485 and -0.423 e.Å ⁻³

Table 6.2: Atomic coordinates (× 10⁴) and equivalent isotropic displacement parameters (Å² × 10³) for 55. U(eq) is defined as one third of the trace of the orthogonalized U^{ij} tensor

	x	y	z	U(eq)
O(1)	4238(2)	7491(3)	5239(1)	50(1)
C(1)	3974(2)	7074(3)	5584(1)	34(1)
N(1)	4731(1)	6800(2)	5885(1)	31(1)
N(2)	254(1)	5298(2)	6741(1)	21(1)
O(2)	5247(1)	5907(2)	6514(1)	33(1)
C(2)	4525(1)	6186(2)	6279(1)	26(1)
C(3)	3422(1)	5900(2)	6387(1)	22(1)

C(5)	2122(1)	5022(2)	6886(1)	22(1)
C(4)	3166(1)	5251(2)	6767(1)	23(1)
C(6)	1305(1)	5445(2)	6624(1)	20(1)
C(7)	1549(1)	5994(2)	6213(1)	21(1)
C(9)	1046(2)	6752(3)	5518(1)	38(1)
C(8)	780(2)	6206(3)	5906(1)	28(1)
C(10)	2097(2)	7087(3)	5419(1)	38(1)
C(11)	2869(2)	6820(3)	5704(1)	28(1)
C(12)	2615(1)	6252(2)	6104(1)	22(1)
C(13)	-364(2)	6927(2)	6722(1)	26(1)
C(14)	-1528(2)	6504(3)	6706(1)	30(1)
C(15)	-1840(2)	5492(3)	7087(1)	29(1)
C(16)	-1145(2)	3880(3)	7132(1)	27(1)
C(17)	20(1)	4335(3)	7117(1)	25(1)
O(3)	7333(3)	5258(8)	5524(1)	44(1)
C(18)	5834(3)	7112(7)	5771(2)	40(1)
C(19)	6223(2)	5519(4)	5520(1)	35(1)
C(20)	6637(3)	4051(5)	5741(1)	48(1)
O(3A)	7441(12)	5350(30)	5623(6)	54(3)
C(18A)	5835(10)	6960(30)	5742(6)	35(3)
C(19A)	6484(8)	5304(14)	5823(3)	36(2)
C(20A)	6499(9)	4402(18)	5440(4)	47(2)

Table 6.3: Bond lengths [\AA] and angles [$^\circ$] for 55.

O(1)-C(1)	1.220(3)
C(1)-N(1)	1.396(3)
C(1)-C(11)	1.478(3)
N(1)-C(2)	1.398(3)
N(1)-C(18)	1.479(4)
N(1)-C(18A)	1.492(13)
N(2)-C(6)	1.402(2)
N(2)-C(17)	1.465(2)
N(2)-C(13)	1.477(2)
O(2)-C(2)	1.221(2)
C(2)-C(3)	1.470(2)
C(3)-C(4)	1.378(3)
C(3)-C(12)	1.411(2)
C(5)-C(6)	1.391(2)
C(5)-C(4)	1.402(2)

C(6)-C(7)	1.441(2)
C(7)-C(8)	1.416(2)
C(7)-C(12)	1.422(2)
C(9)-C(8)	1.377(3)
C(9)-C(10)	1.406(3)
C(10)-C(11)	1.372(3)
C(11)-C(12)	1.419(2)
C(13)-C(14)	1.523(3)
C(14)-C(15)	1.523(3)
C(15)-C(16)	1.528(3)
C(16)-C(17)	1.530(3)
O(3)-C(19)	1.433(5)
O(3)-C(20)	1.466(5)
C(18)-C(19)	1.552(6)
C(19)-C(20)	1.439(4)
O(3A)-C(19A)	1.388(15)
O(3A)-C(20A)	1.529(15)
C(18A)-C(19A)	1.538(16)
C(19A)-C(20A)	1.431(13)
O(1)-C(1)-N(1)	119.9(2)
O(1)-C(1)-C(11)	122.9(2)
N(1)-C(1)-C(11)	117.13(18)
C(1)-N(1)-C(2)	124.78(17)
C(1)-N(1)-C(18)	117.3(3)
C(2)-N(1)-C(18)	117.9(3)
C(1)-N(1)-C(18A)	114.9(8)
C(2)-N(1)-C(18A)	119.7(7)
C(6)-N(2)-C(17)	117.70(14)
C(6)-N(2)-C(13)	115.65(14)
C(17)-N(2)-C(13)	110.57(14)
O(2)-C(2)-N(1)	119.84(17)
O(2)-C(2)-C(3)	123.24(18)
N(1)-C(2)-C(3)	116.91(17)
C(4)-C(3)-C(12)	119.17(16)
C(4)-C(3)-C(2)	119.86(16)
C(12)-C(3)-C(2)	120.96(16)
C(6)-C(5)-C(4)	120.92(16)
C(3)-C(4)-C(5)	121.46(16)
C(5)-C(6)-N(2)	122.18(15)
C(5)-C(6)-C(7)	118.77(16)
N(2)-C(6)-C(7)	119.01(15)
C(8)-C(7)-C(12)	118.04(16)
C(8)-C(7)-C(6)	123.09(16)
C(12)-C(7)-C(6)	118.79(15)
C(8)-C(9)-C(10)	120.30(19)

C(9)-C(8)-C(7)	121.20(18)
C(11)-C(10)-C(9)	120.15(19)
C(10)-C(11)-C(12)	120.60(18)
C(10)-C(11)-C(1)	119.19(18)
C(12)-C(11)-C(1)	120.18(18)
C(3)-C(12)-C(11)	119.85(17)
C(3)-C(12)-C(7)	120.57(15)
C(11)-C(12)-C(7)	119.55(16)
N(2)-C(13)-C(14)	110.11(15)
C(15)-C(14)-C(13)	109.62(16)
C(14)-C(15)-C(16)	109.78(15)
C(15)-C(16)-C(17)	112.25(16)
N(2)-C(17)-C(16)	109.96(15)
C(19)-O(3)-C(20)	59.5(2)
N(1)-C(18)-C(19)	108.2(4)
O(3)-C(19)-C(20)	61.4(3)
O(3)-C(19)-C(18)	114.9(3)
C(20)-C(19)-C(18)	117.7(3)
C(19)-C(20)-O(3)	59.1(3)
C(19A)-O(3A)-C(20A)	58.5(7)
N(1)-C(18A)-C(19A)	112.8(12)
O(3A)-C(19A)-C(20A)	65.7(8)
O(3A)-C(19A)-C(18A)	111.7(15)
C(20A)-C(19A)-C(18A)	104.6(13)
C(19A)-C(20A)-O(3A)	55.8(7)

Table 6.4: Crystal data and structure refinement for 58.

Identification code	og4
Empirical formula	C ₁₇ H ₁₃ NO ₃
Formula weight	279.28
Temperature	100(2) K
Wavelength	0.71073 Å
Crystal system	Trigonal
Space group	$R\bar{3}$
Unit cell dimensions	$a = 29.6286(6)$ Å, $a = 90^\circ$ $b = 29.6286(6)$ Å, $b = 90^\circ$ $c = 7.6747(3)$ Å, $g = 120^\circ$
Volume	5834.6(3) Å ³
Z	18
Density (calculated)	1.431 Mg/m ³
Absorption coefficient	0.099 mm ⁻¹
F(000)	2628
Crystal size	0.300 × 0.058 × 0.020 mm ³
θ range for data collection	2.381 to 27.481 °
Index ranges	-38 ≤ h ≤ 38, -38 ≤ k ≤ 38, -9 ≤ l ≤ 9

Reflections collected	33544
Independent reflections	2976 [R(int) = 0.0710]
Completeness to $\theta = 25.242^\circ$	100.00%
Absorption correction	Gaussian
Max. and min. transmission	1.000 and 0.792
Refinement method	Full-matrix least-squares on F^2
Data / restraints / parameters	2976 / 103 / 230
Goodness-of-fit on F^2	1.063
Final R indices [$ I > 2\sigma(I)$]	$R_1 = 0.0668$, $wR_2 = 0.2022$
R indices (all data)	$R_1 = 0.0799$, $wR_2 = 0.2181$
Extinction coefficient	n/a
Largest diff. peak and hole	0.316 and -0.332 e. \AA^{-3}

Table 6.5: Atomic coordinates ($\times 10^4$) and equivalent isotropic displacement parameters ($\text{\AA}^2 \times 10^3$) for **58**. $U(\text{eq})$ is defined as one third of the trace of the orthogonalized U^{ij} tensor

	x	y	z	U(eq)
O(1)	5989(3)	3052(3)	6394(11)	157(3)
C(1)	5662(5)	2550(6)	5450(20)	131(4)
C(2)	5605(6)	2867(6)	4990(20)	141(4)
C(3)	5178(7)	3035(8)	5790(30)	137(5)
O(1A)	5542(2)	2553(3)	6532(9)	142(3)
C(1A)	5581(3)	2613(4)	4615(9)	96(2)
C(2A)	5579(2)	3000(3)	5770(9)	86(2)
C(3A)	5135(2)	3084(4)	5655(11)	66(2)
O(2)	4177(1)	1684(1)	3669(2)	58(1)
O(3)	2320(1)	1566(1)	4691(2)	55(1)
N(1)	4659(1)	2610(1)	5173(3)	62(1)
C(4)	4183(1)	2558(1)	5364(2)	49(1)
C(5)	4121(1)	2958(1)	6153(2)	51(1)
C(6)	3638(1)	2902(1)	6376(2)	50(1)
C(7)	3192(1)	2455(1)	5837(2)	46(1)
C(8)	3237(1)	2059(1)	5038(2)	41(1)
C(9)	2744(1)	1597(1)	4458(2)	44(1)
C(10)	2781(1)	1175(1)	3547(2)	46(1)
C(11)	2327(1)	739(1)	2937(3)	56(1)
C(12)	2364(1)	346(1)	2075(3)	63(1)
C(13)	2844(1)	389(1)	1814(3)	64(1)
C(14)	3293(1)	817(1)	2408(2)	56(1)
C(15)	3267(1)	1216(1)	3293(2)	46(1)
C(16)	3756(1)	1674(1)	3914(2)	46(1)
C(17)	3728(1)	2097(1)	4785(2)	43(1)

Table 6.6: Bond lengths [\AA] and angles [$^\circ$] for **58**.

O(1)-C(2)	1.458(12)
O(1)-C(1)	1.497(12)
C(1)-C(2)	1.090(19)
C(2)-C(3)	1.69(3)
C(3)-N(1)	1.496(18)
O(1A)-C(2A)	1.399(9)
O(1A)-C(1A)	1.479(9)
C(1A)-C(2A)	1.451(10)
C(2A)-C(3A)	1.459(10)
C(3A)-N(1)	1.454(7)
O(2)-C(16)	1.244(2)
O(3)-C(9)	1.225(2)
N(1)-C(4)	1.346(3)
C(4)-C(5)	1.422(3)
C(4)-C(17)	1.428(3)
C(5)-C(6)	1.367(3)
C(6)-C(7)	1.387(3)
C(7)-C(8)	1.386(2)
C(8)-C(17)	1.415(2)
C(8)-C(9)	1.485(3)
C(9)-C(10)	1.484(2)
C(10)-C(15)	1.396(3)
C(10)-C(11)	1.400(3)
C(11)-C(12)	1.388(3)
C(12)-C(13)	1.379(4)
C(13)-C(14)	1.379(3)
C(14)-C(15)	1.400(3)
C(15)-C(16)	1.484(3)
C(16)-C(17)	1.463(2)
C(2)-O(1)-C(1)	43.3(8)
C(2)-C(1)-O(1)	66.4(9)
C(1)-C(2)-O(1)	70.3(9)
C(1)-C(2)-C(3)	127(2)
O(1)-C(2)-C(3)	100.4(14)
N(1)-C(3)-C(2)	104.2(13)
C(2A)-O(1A)-C(1A)	60.5(5)
C(2A)-C(1A)-O(1A)	57.0(4)
O(1A)-C(2A)-C(1A)	62.5(5)
O(1A)-C(2A)-C(3A)	122.4(7)
C(1A)-C(2A)-C(3A)	117.3(6)
N(1)-C(3A)-C(2A)	111.9(7)
C(4)-N(1)-C(3A)	122.6(4)
C(4)-N(1)-C(3)	129.8(8)
N(1)-C(4)-C(5)	120.91(18)
N(1)-C(4)-C(17)	120.81(19)

C(5)-C(4)-C(17)	118.28(17)
C(6)-C(5)-C(4)	121.11(17)
C(5)-C(6)-C(7)	121.22(18)
C(8)-C(7)-C(6)	119.39(18)
C(7)-C(8)-C(17)	121.49(17)
C(7)-C(8)-C(9)	116.45(16)
C(17)-C(8)-C(9)	122.06(15)
O(3)-C(9)-C(10)	120.65(17)
O(3)-C(9)-C(8)	121.70(16)
C(10)-C(9)-C(8)	117.64(16)
C(15)-C(10)-C(11)	120.36(18)
C(15)-C(10)-C(9)	120.06(17)
C(11)-C(10)-C(9)	119.58(18)
C(12)-C(11)-C(10)	119.5(2)
C(13)-C(12)-C(11)	120.1(2)
C(12)-C(13)-C(14)	120.94(19)
C(13)-C(14)-C(15)	120.1(2)
C(10)-C(15)-C(14)	119.07(19)
C(10)-C(15)-C(16)	121.94(15)
C(14)-C(15)-C(16)	118.99(18)
O(2)-C(16)-C(17)	122.36(18)
O(2)-C(16)-C(15)	118.92(17)
C(17)-C(16)-C(15)	118.73(16)
C(8)-C(17)-C(4)	118.49(16)
C(8)-C(17)-C(16)	119.55(16)
C(4)-C(17)-C(16)	121.94(17)

4-Piperidiny-1,8-naphthalic anhydride (45a)

#	State	Transition energy (nm)	Participating MO	Transition character
1	Singlet	435.40 (0.2745) ^a	HOMO → LUMO (0.69690) ^b	Intramolecular charge transfer
2	Singlet	313.86 (0.0046)	HOMO-2 → LUMO (0.40489)	π → π*
	Singlet		HOMO → LUMO+2 (0.56125)	Intramolecular charge transfer
3	Singlet	297.91 (0.2042)	HOMO-1 → LUMO (-0.10971)	Intramolecular charge transfer
	Singlet		HOMO → LUMO+1 (0.67446)	Intramolecular charge transfer

Chapter 6. Appendix

4	Singlet	297.59 (0.0049)	HOMO-3 → LUMO (0.68226)	n → π*
5	Singlet	293.43 (0.0543)	HOMO-2 → LUMO (0.11392)	π → π*
	Singlet		HOMO-1 → LUMO (0.67680)	Intramolecular charge transfer
6	Singlet	277.53 (0.2526)	HOMO-2 → LUMO (0.52465)	π → π*
	Singlet		HOMO-1 → LUMO+2 (-0.19374)	Intramolecular charge transfer
	Singlet		HOMO → LUMO+2 (-0.40464)	Intramolecular charge transfer
7	Singlet	526.23 (0.0003)	HOMO-4 → LUMO (0.65267)	n → π*
	Singlet		HOMO-3 → LUMO+1 (-0.23424)	n → π*
8	Singlet	233.54 (0.0165)	HOMO-5 → LUMO (-0.11937)	π → π*
	Singlet		HOMO-2 → LUMO+1 (0.14006)	π → π*
	Singlet		HOMO-1 → LUMO+1 (-0.16651)	Intramolecular charge transfer
	Singlet		HOMO-1 → LUMO+2 (-0.16651)	Intramolecular charge transfer
	Singlet		HOMO → LUMO+3 (0.62763)	Intramolecular charge transfer
9	Singlet	232.11 (0.0414)	HOMO-5 → LUMO (0.47729)	π → π*
	Singlet		HOMO-1 → LUMO+1 (0.43908)	Intramolecular charge transfer
	Singlet		HOMO → LUMO+3 (0.222777)	Intramolecular charge transfer
10	Singlet	255.42 (0.1298)	HOMO-6 → LUMO (-0.26992)	π → π*
	Singlet		HOMO-5 → LUMO (-0.22748)	π → π*
	Singlet		HOMO-2 → LUMO+1 (-0.31757)	π → π*
	Singlet		HOMO-1 → LUMO+1 (0.10250)	Intramolecular charge transfer

	Singlet		HOMO-1 → LUMO+2 (0.73913)	Intramolecular charge transfer
	Singlet		HOMO → LUMO+3 (0.20173)	Intramolecular charge transfer
11	Singlet	224.70 (0.0005)	HOMO-4 → LUMO (0.23844)	n → π*
	Singlet		HOMO-3 → LUMO+1 (0.62073)	n → π*
	Singlet		HOMO-3 → LUMO+2 (0.13272)	n → π*
12	Singlet	220.82 (0.0347)	HOMO-6 → LUMO (-0.17547)	π → π*
	Singlet		HOMO-5 → LUMO (-0.26287)	π → π*
	Singlet		HOMO-2 → LUMO+1 (0.47844)	π → π*
	Singlet		HOMO-2 → LUMO+2 (0.14310)	π → π*
	Singlet		HOMO-1 → LUMO+1 (0.32397)	Intramolecular charge transfer
13	Singlet	218.68 (0.0234)	HOMO-6 → LUMO (0.23659)	π → π*
	Singlet		HOMO-5 → LUMO (-0.30833)	π → π*
	Singlet		HOMO-2 → LUMO (-0.10050)	π → π*
	Singlet		HOMO-2 → LUMO+1 (-0.30358)	π → π*
	Singlet		HOMO-1 → LUMO+1 (0.35955)	Intramolecular charge transfer
	Singlet		HOMO-1 → LUMO+2 (-0.29073)	Intramolecular charge transfer
14	Singlet	212.92 (0.3271)	HOMO-6 → LUMO (0.5572)	π → π*
	Singlet		HOMO-5 → LUMO (-0.13895)	π → π*
	Singlet		HOMO-2 → LUMO (0.11515)	π → π*
	Singlet		HOMO-1 → LUMO+1 (0.12886)	Intramolecular charge transfer
	Singlet		HOMO-1 → LUMO+2 (0.32000)	Intramolecular charge transfer
15	Singlet	209.70 (0.0437)	HOMO-10 → LUMO (0.14086)	σ → π*
	Singlet		HOMO-7 → LUMO (0.65974)	σ → π*

Chapter 6. Appendix

16	Singlet	209.05 (0.0013)	HOMO-3 → LUMO+1 (-0.12848)	n → π*
	Singlet		HOMO-3 → LUMO+2 (0.68444)	n → π*
17	Singlet	205.19 (0.0990)	HOMO-9 → LUMO (0.14460)	σ → π*
	Singlet		HOMO-8 → LUMO+ (0.58538)	σ → π*
	Singlet		HOMO-4 → LUMO+1 (0.17659)	n → π*
	Singlet		HOMO-2 → LUMO+2 (-0.23556)	π → π*
	Singlet		HOMO-10 → LUMO (0.10716)	σ → π*
18	Singlet	203.72 (0.2731)	HOMO-9 → LUMO (-0.15399)	σ → π*
	Singlet		HOMO-8 → LUMO (0.32415)	σ → π*
	Singlet		HOMO-4 → LUMO+1 (-0.18111)	n → π*
	Singlet		HOMO-2 → LUMO+2 (0.51016)	π → π*
	Singlet		HOMO-4 → LUMO+1 (0.57969)	n → π*
19	Singlet	203.31 (0.0827)	HOMO-4 → LUMO+2 (0.13802)	n → π*
	Singlet		HOMO-3 → LUMO+1 (0.10908)	n → π*
	Singlet		HOMO-3 → LUMO+3 (0.19080)	n → π*
	Singlet		HOMO-2 → LUMO+2 (0.21363)	π → π*
	Singlet		HOMO-13 → LUMO (-0.20825)	σ → π*
20	Singlet	199.43 (0.0006)	HOMO-12 → LUMO (0.17087)	σ → π*
	Singlet		HOMO-10 → LUMO (0.51419)	σ → π*
	Singlet		HOMO-9 → LUMO (0.32379)	σ → π*
	Singlet		HOMO-8 → LUMO (-0.11649)	σ → π*
	Singlet		HOMO-7 → LUMO (-0.16234)	σ → π*

^a Oscillator strength, ^b Orbital coefficient

4-Piperidiny1-1,8-naphthalimide (54)

#	State	Transition energy (nm)	Participating MO	Transition character
1	Singlet	431.52 (0.2916) ^a	HOMO → LUMO (0.69910) ^b	Intramolecular charge transfer

Chapter 6. Appendix

2	Singlet	323.84 (0.0003)	HOMO-3 → LUMO (-0.11297)	$\pi \rightarrow \pi^*$
	Singlet		HOMO-2 → LUMO (0.68317)	$n \rightarrow \pi^*$
3	Singlet	313.94 (0.0018)	HOMO-3 → LUMO (0.43384)	$\pi \rightarrow \pi^*$
	Singlet		HOMO → LUMO+1 (0.53933)	Intramolecular charge transfer
4	Singlet	299.23 (0.0265)	HOMO-3 → LUMO (0.13293)	$\pi \rightarrow \pi^*$
	Singlet		HOMO-1 → LUMO (0.67474)	Intramolecular charge transfer
5	Singlet	283.95 (0.1657)	HOMO-4 → LUMO (0.20243)	$n \rightarrow \pi^*$
	Singlet		HOMO-3 → LUMO (-0.22063)	$\pi \rightarrow \pi^*$
	Singlet		HOMO-1 → LUMO (0.12221)	Intramolecular charge transfer
	Singlet		HOMO → LUMO+1 (0.19590)	Intramolecular charge transfer
	Singlet		HOMO → LUMO+2 (0.57887)	Intramolecular charge transfer
6	Singlet	282.38 (0.0381)	HOMO-5 → LUMO (0.58988)	$n \rightarrow \pi^*$
	Singlet		HOMO-4 → LUMO (-0.11295)	$n \rightarrow \pi^*$
	Singlet		HOMO-3 → LUMO (0.16067)	$\pi \rightarrow \pi^*$
	Singlet		HOMO-2 → LUMO+2 (-0.14755)	$n \rightarrow \pi^*$
	Singlet		HOMO → LUMO+1 (-0.15490)	Intramolecular charge transfer
	Singlet		HOMO → LUMO+2 (0.19187)	Intramolecular charge transfer
7	Singlet	280.49 (0.1583)	HOMO-6 → LUMO (0.10419)	$\pi \rightarrow \pi^*$
	Singlet		HOMO-5 → LUMO (-0.30026)	$n \rightarrow \pi^*$
	Singlet		HOMO-3 → LUMO (0.40268)	$\pi \rightarrow \pi^*$
	Singlet		HOMO-1 → LUMO+1 (-0.13118)	Intramolecular charge transfer

Chapter 6. Appendix

	Singlet		HOMO → LUMO+1 (-0.34296)	Intramolecular charge transfer
	Singlet		HOMO → LUMO+2 (0.29091)	Intramolecular charge transfer
8	Singlet	253.86 (0.1335)	HOMO-5 → LUMO (0.11896)	n → π*
	Singlet		HOMO-4 → LUMO (0.61893)	n → π*
	Singlet		HOMO-1 → LUMO+1 (-0.22211)	Intramolecular charge transfer
	Singlet		HOMO → LUMO+1 (-0.11153)	Intramolecular charge transfer
	Singlet		HOMO → LUMO+2 (-0.13964)	Intramolecular charge transfer
9	Singlet	235.13 (0.0172)	HOMO-6 → LUMO (-0.14505)	
	Singlet		HOMO-1 → LUMO+1 (-0.10299)	Intramolecular charge transfer
	Singlet		HOMO → LUMO+3 (0.66419)	Intramolecular charge transfer
10	Singlet	231.71 (0.0025)	HOMO-6 → LUMO (0.62628)	π → π*
	Singlet		HOMO-1 → LUMO+2 (-0.24138)	Intramolecular charge transfer
	Singlet		HOMO → LUMO+3 (0.16220)	Intramolecular charge transfer
11	Singlet	226.29 (0.0001)	HOMO-5 → LUMO (0.16442)	n → π*
	Singlet		HOMO-3 → LUMO+2 (-0.10499)	π → π*
	Singlet		HOMO-2 → LUMO+1 (0.23456)	n → π*
	Singlet		HOMO-2 → LUMO+2 (0.61969)	n → π*
12	Singlet	223.37 (0.3679)	HOMO-4 → LUMO (0.18218)	n → π*
	Singlet		HOMO-3 → LUMO (0.14099)	π → π*
	Singlet		HOMO-3 → LUMO+2 (-0.20177)	π → π*
	Singlet		HOMO-1 → LUMO+ (0.53159)	Intramolecular charge transfer

	Singlet		HOMO-1 → LUMO+2 (0.25571)	Intramolecular charge transfer
	Singlet		HOMO → LUMO+3 (0.13011)	Intramolecular charge transfer
13	Singlet	221.15 (0.0006)	HOMO-3 → LUMO+1 (-0.11186)	$\pi \rightarrow \pi^*$
	Singlet		HOMO-2 → LUMO+1 (0.65430)	$n \rightarrow \pi^*$
	Singlet		HOMO-2 → LUMO+2 (-0.21812)	$n \rightarrow \pi^*$
14	Singlet	216.32 (0.0614)	HOMO-6 → LUMO (0.21422)	$\pi \rightarrow \pi^*$
	Singlet		HOMO-3 → LUMO+1 (0.17547)	$\pi \rightarrow \pi^*$
	Singlet		HOMO-3 → LUMO+2 (0.18241)	$\pi \rightarrow \pi^*$
	Singlet		HOMO-1 → LUMO+1 (-0.18022)	Intramolecular charge transfer
	Singlet		HOMO-1 → LUMO+2 (0.56062)	Intramolecular charge transfer
15	Singlet	212.70 (0.0481)	HOMO-6 → LUMO+1 (-0.17918)	$\pi \rightarrow \pi^*$
	Singlet		HOMO-3 → LUMO+2 (0.59272)	$\pi \rightarrow \pi^*$
	Singlet		HOMO-2 → LUMO+2 (0.10637)	$n \rightarrow \pi^*$
	Singlet		HOMO-1 → LUMO+1 (0.23606)	Intramolecular charge transfer
16	Singlet	209.01 (0.0232)	HOMO-11 → LUMO (0.11147)	$\sigma \rightarrow \pi^*$
	Singlet		HOMO-10 → LUMO (0.18323)	$\sigma \rightarrow \pi^*$
	Singlet		HOMO-7 → LUMO (0.64451)	$\sigma \rightarrow \pi^*$
17	Singlet	206.41 (0.0470)	HOMO-5 → LUMO+1 (0.12312)	$n \rightarrow \pi^*$
	Singlet		HOMO-5 → LUMO+2 (0.51097)	$n \rightarrow \pi^*$
	Singlet		HOMO-4 → LUMO+2 (-0.11759)	$n \rightarrow \pi^*$
	Singlet		HOMO-3 → LUMO+1 (-0.23395)	$\pi \rightarrow \pi^*$
	Singlet		HOMO-2 → LUMO (0.10399)	$n \rightarrow \pi^*$
	Singlet		HOMO-2 → LUMO+3 (0.31377)	$n \rightarrow \pi^*$
18	Singlet	205.70 (0.3926)	HOMO-9 → LUMO (0.10931)	$\sigma \rightarrow \pi^*$
	Singlet		HOMO-5 → LUMO+1 (0.11145)	$n \rightarrow \pi^*$

	Singlet		HOMO-5 → LUMO+2 (0.19158)	n → π*
	Singlet		HOMO-4 → LUMO+1 (-0.22835)	n → π*
	Singlet		HOMO-3 → LUMO+1 (0.52742)	π → π*
	Singlet		HOMO-2 → LUMO+3 (0.11055)	n → π*
	Singlet		HOMO-1 → LUMO+2 (-0.15914)	Intramolecular charge transfer
	Singlet		HOMO-1 → LUMO+3 (0.10514)	Intramolecular charge transfer
19	Singlet	203.72 (0.0074)	HOMO-10 → LUMO (0.11272)	σ → π*
	Singlet		HOMO-8 → LUMO (0.64153)	σ → π*
	Singlet		HOMO-4 → LUMO+1 (-0.16903)	n → π*
20	Singlet	201.36 (0.0195)	HOMO-5 → LUMO+1 (0.64466)	n → π*
	Singlet		HOMO-4 → LUMO+1 (-0.13797)	n → π*
	Singlet		HOMO-2 → LUMO+3 (-0.14937)	n → π*

^a Oscillator strength, ^b Orbital coefficient

4-PiperidinyI-(N-propylene-oxide)-1,8-naphthalimide (55)

#	State	Transition energy (nm)	Participating MO	Transition character
1	Singlet	432.21 (0.3156) ^a	HOMO → LUMO (0.69912) ^b	Intramolecular charge transfer
2	Singlet	319.47 (0.0003)	HOMO-3 → LUMO (0.68527)	n → π*
3	Singlet	313.13 (0.0028)	HOMO-4 → LUMO (0.32246)	π → π*
	Singlet		HOMO-2 → LUMO (-0.33684)	π → π*
	Singlet		HOMO-1 → LUMO (-0.12053)	Intramolecular charge transfer
	Singlet		HOMO → LUMO (0.50654)	Intramolecular charge transfer

Chapter 6. Appendix

4	Singlet	304.55 (0.0071)	HOMO-6 → LUMO (0.12449)	n → π*
	Singlet		HOMO-4 → LUMO (0.12673)	π → π*
	Singlet		HOMO-2 → LUMO (0.21369)	π → π*
	Singlet		HOMO-1 → LUMO (0.58162)	Intramolecular charge transfer
	Singlet		HOMO → LUMO +1 (0.20705)	Intramolecular charge transfer
	Singlet		HOMO → LUMO+2 (- 0.16230)	Intramolecular charge transfer
5	Singlet	291.59 (0.0539)	HOMO-4 → LUMO (0.20646)	π → π*
	Singlet		HOMO-2 → LUMO (0.51772)	π → π*
	Singlet		HOMO-1 → LUMO (-0.34793)	Intramolecular charge transfer
	Singlet		HOMO → LUMO+1 (0.13834)	Intramolecular charge transfer
	Singlet		HOMO → LUMO+2 (- 0.13329)	Intramolecular charge transfer
6	Singlet	286.02 (0.1422)	HOMO-6 → LUMO (0.15480)	n → π*
	Singlet		HOMO-5 → LUMO (0.38543)	n → π*
	Singlet		HOMO → LUMO+2 (0.54450)	Intramolecular charge transfer
7	Singlet	281.65 (0.1275)	HOMO-6 → LUMO (0.22614)	n → π*
	Singlet		HOMO-5 → LUMO (0.35288)	n → π*
	Singlet		HOMO-4 → LUMO (0.23856)	π → π*
	Singlet		HOMO-3 → LUMO (-0.22639)	n → π*
	Singlet		HOMO-2 → LUMO+1 (- 0.29416)	π → π*
	Singlet		HOMO → LUMO+2 (-30844)	Intramolecular charge transfer
8	Singlet	272.61 (0.1582)	HOMO-6 → LUMO (-0.27213)	n → π*
	Singlet		HOMO-5 → LUMO (-0.17013)	n → π*

	Singlet		HOMO-4 → LUMO (0.48099)	$\pi \rightarrow \pi^*$
	Singlet		HOMO-1 → LUMO+1 (- 0.15821)	Intramolecular charge transfer
	Singlet		HOMO → LUMO+1 (- 0.26347)	Intramolecular charge transfer
	Singlet		HOMO → LUMO+2 (0.18183)	Intramolecular charge transfer
9	Singlet	253.01 (0.0799)	HOMO-6 → LUMO (0.53703)	$n \rightarrow \pi^*$
	Singlet		HOMO-5 → LUMO (-0.38486)	$n \rightarrow \pi^*$
	Singlet		HOMO-1 → LUMO+1 (- 0.15474)	Intramolecular charge transfer
	Singlet		HOMO → LUMO+2 (0.10674)	Intramolecular charge transfer
10	Singlet	235.32 (0.0160)	HOMO → LUMO+3 (0.68101)	Intramolecular charge transfer
11	Singlet	230.65 (0.0051)	HOMO-7 → LUMO (0.62820)	$\pi \rightarrow \pi^*$
	Singlet		HOMO-1 → LUMO+2 (- 0.25505)	Intramolecular charge transfer
12	Singlet	226.63 (0.0018)	HOMO-8 → LUMO (0.13691)	$n \rightarrow \pi^*$
	Singlet		HOMO-6 → LUMO (0.11752)	$n \rightarrow \pi^*$
	Singlet		HOMO-5 → LUMO (0.12982)	$n \rightarrow \pi^*$
	Singlet		HOMO-3 → LUMO+2 (0.63443)	$n \rightarrow \pi^*$
13	Singlet	223.09 (0.2520)	HOMO-4 → LUMO (0.14547)	$\pi \rightarrow \pi^*$
	Singlet		HOMO-4 → LUMO+2 (- 0.15267)	$\pi \rightarrow \pi^*$
	Singlet		HOMO-2 → LUMO+2 (0.25145)	$\pi \rightarrow \pi^*$
	Singlet		HOMO-1 → LUMO+1 (0.51580)	Intramolecular charge transfer
	Singlet		HOMO-1 → LUMO+2 (- 0.22968)	Intramolecular charge transfer

Chapter 6. Appendix

14	Singlet	218.95 (0.0134)	HOMO-4 → LUMO+1 (0.10025)	$\pi \rightarrow \pi^*$	
	Singlet		HOMO-3 → LUMO+1 (0.65837)	$n \rightarrow \pi^*$	
	Singlet		HOMO-1 → LUMO+2 (0.18283)	Intramolecular charge transfer	
15	Singlet	217.70 (0.0705)	HOMO-8 → LUMO (-0.16924)	$n \rightarrow \pi^*$	
	Singlet		HOMO-7 → LUMO (19395)	$\pi \rightarrow \pi^*$	
	Singlet		HOMO-5 → LUMO+2 (0.11387)	$n \rightarrow \pi^*$	
	Singlet		HOMO-3 → LUMO+1 (- 0.17609)	$n \rightarrow \pi^*$	
	Singlet		HOMO-2 → LUMO+1 (- 0.12791)	$\pi \rightarrow \pi^*$	
	Singlet		HOMO-2 → LUMO+2 (0.22913)	$\pi \rightarrow \pi^*$	
	Singlet		HOMO → LUMO+2 (0.51502)	Intramolecular charge transfer	
	Singlet	216.02 (0.0205)	HOMO-8 → LUMO (0.62407)	$n \rightarrow \pi^*$	
	Singlet		HOMO-3 → LUMO+1 (- 0.14435)	$n \rightarrow \pi^*$	
16	Singlet		HOMO-3 → LUMO+2 (- 0.14895)	$n \rightarrow \pi^*$	
	Singlet		HOMO-2 → LUMO+1 (0.16732)	$\pi \rightarrow \pi^*$	
	Singlet		HOMO-1 → LUMO+2 (0.12898)	Intramolecular charge transfer	
	17	Singlet	215.88 (0.1109)	HOMO-8 → LUMO (-0.21120)	$n \rightarrow \pi^*$
		Singlet		HOMO-6 → LUMO+1 (0.10813)	$n \rightarrow \pi^*$
Singlet			HOMO-4 → LUMO+1 (0.18356)	$\pi \rightarrow \pi^*$	

Chapter 6. Appendix

	Singlet		HOMO-2 → LUMO+1 (0.59529)	$\pi \rightarrow \pi^*$
	Singlet		HOMO-2 → LUMO+2 (- 0.11828)	$\pi \rightarrow \pi^*$
	Singlet		HOMO-1 → LUMO+1 (0.10946)	Intramolecular charge transfer
18	Singlet	214.44 (0.0725)	HOMO-7 → LUMO (-0.12850)	$\pi \rightarrow \pi^*$
	Singlet		HOMO-5 → LUMO+2 (0.10319)	$n \rightarrow \pi^*$
	Singlet		HOMO-4 → LUMO+1 (- 0.11414)	$\pi \rightarrow \pi^*$
	Singlet		HOMO-2 → LUMO+1 (0.19519)	$\pi \rightarrow \pi^*$
	Singlet		HOMO-2 → LUMO+2 (0.53343)	$\pi \rightarrow \pi^*$
	Singlet		HOMO-1 → LUMO+1 (- 0.26311)	Intramolecular charge transfer
19	Singlet	211.47 (0.0122)	HOMO-7 → LUMO+1 (- 0.14348)	$\pi \rightarrow \pi^*$
	Singlet		HOMO-6 → LUMO+2 (0.12115)	$n \rightarrow \pi^*$
	Singlet		HOMO-5 → LUMO+2 (0.11779)	$n \rightarrow \pi^*$
	Singlet		HOMO-4 → LUMO+2 (0.60830)	$\pi \rightarrow \pi^*$
	Singlet		HOMO-3 → LUMO+2 (- 0.12052)	$n \rightarrow \pi^*$
	Singlet		HOMO-1 → LUMO+1 (0.15944)	Intramolecular charge transfer
20	Singlet	207.94 (0.0202)	HOMO-13 → LUMO (- 0.11291)	$\sigma \rightarrow \pi^*$
	Singlet		HOMO-12 → LUMO (0.23101)	$\sigma \rightarrow \pi^*$
	Singlet		HOMO-9 → LUMO (0.62460)	$\sigma \rightarrow \pi^*$

^a Oscillator strength, ^b Orbital coefficient

1-((3-chloro-2-hydroxypropyl)amino)anthraquinone (57)

#	State	Transition energy (nm)	Participating MO	Transition character
1	Singlet	496.31 (0.1537) ^a	HOMO → LUMO (0.70734) ^b	Intramolecular charge transfer
2	Singlet	411.04 (0.0002)	HOMO-4 → LUMO (-0.10300)	n → π*
	Singlet		HOMO-4 → LUMO+1 (-0.10501)	n → π*
	Singlet		HOMO-1 → LUMO (0.68730)	n → π*
3	Singlet	375.20 (0.0001)	HOMO-4 → LUMO (0.67457)	n → π*
	Singlet		HOMO-1 → LUMO (0.10604)	n → π*
	Singlet		HOMO-1 → LUMO+1 (-0.14964)	n → π*
4	Singlet	339.99 (0.0013)	HOMO-2 → LUMO (0.65545)	π → π*
	Singlet		HOMO → LUMO+1 (0.25108)	Intramolecular charge transfer
5	Singlet	323.87 (0.0213)	HOMO-3 → LUMO (0.40193)	π → π*
	Singlet		HOMO-2 → LUMO (-0.21601)	π → π*
	Singlet		HOMO → LUMO+1 (0.52495)	Intramolecular charge transfer
6	Singlet	319.69 (0.1520)	HOMO-3 → LUMO (0.55761)	π → π*
	Singlet		HOMO-2 → LUMO (0.12469)	π → π*
	Singlet		HOMO → LUMO+1 (-0.39188)	Intramolecular charge transfer
7	Singlet	279.91 (0.1676)	HOMO-5 → LUMO (0.68000)	π → π*
	Singlet		HOMO-2 → LUMO+2 (-0.10278)	π → π*
8	Singlet	276.02 (0.0060)	HOMO → LUMO+2 (0.69234)	Intramolecular charge transfer
9	Singlet	268.69 (0.0002)	HOMO-6 → LUMO (0.65054)	n → π*
	Singlet		HOMO-1 → LUMO+1 (0.24688)	n → π*

Chapter 6. Appendix

10	Singlet	266.49 (0.0001)	HOMO-6 → LUMO (-0.26064)	n → π*
	Singlet		HOMO-4 → LUMO (0.13254)	n → π*
	Singlet		HOMO-1 → LUMO+1 (0.63941)	n → π*
11	Singlet	251.01 (0.0000)	HOMO-4 → LUMO+1 (0.68655)	n → π*
	Singlet		HOMO-1 → LUMO (0.11369)	n → π*
12	Singlet	250.21 (0.0164)	HOMO-9 → LUMO (-0.12892)	σ → π*
	Singlet		HOMO-8 → LUMO (0.53995)	π → π*
	Singlet		HOMO-7 → LUMO (-0.28985)	n → π*
	Singlet		HOMO-2 → LUMO+1 (0.20592)	π → π*
	Singlet		HOMO → LUMO+3 (0.18264)	Intramolecular charge transfer
13	Singlet	243.30 (0.0082)	HOMO-8 → LUMO (0.25942)	π → π*
	Singlet		HOMO-7 → LUMO (0.64224)	n → π*
	Singlet		HOMO-2 → LUMO+1 (0.10058)	π → π*
14	Singlet	241.31 (0.5601)	HOMO-8 → LUMO (-0.10404)	π → π*
	Singlet		HOMO-3 → LUMO+2 (-0.16095)	π → π*
	Singlet		HOMO-2 → LUMO+1 (0.56541)	π → π*
	Singlet		HOMO → LUMO+3 (-0.34591)	Intramolecular charge transfer
15	Singlet	234.30 (0.1749)	HOMO-8 → LUMO (-0.24993)	π → π*
	Singlet		HOMO-5 → LUMO+1 (0.21392)	π → π*
	Singlet		HOMO-3 → LUMO+2 (-0.18836)	π → π*
	Singlet		HOMO-2 → LUMO+1 (0.20309)	π → π*
	Singlet		HOMO → LUMO+3 (0.53021)	Intramolecular charge transfer
16	Singlet	231.44 (0.0120)	HOMO-3 → LUMO1 (0.67996)	π → π*
	Singlet		HOMO-2 → LUMO+2 (0.10863)	π → π*
17	Singlet	227.15 (0.0047)	HOMO-9 → LUMO (0.60113)	σ → π*

	Singlet		HOMO-8 → LUMO (0.18673)	$\pi \rightarrow \pi^*$
	Singlet		HOMO-5 → LUMO+1 (0.25997)	$\pi \rightarrow \pi^*$
	Singlet		HOMO → LUMO+4 (-0.11729)	Intramolecular charge transfer
18	Singlet	227.01 (0.0022)	HOMO-1 → LUMO+2 (0.57715)	$n \rightarrow \pi^*$
	Singlet		HOMO → LUMO+4 (-0.38807)	Intramolecular charge transfer
19	Singlet	226.89 (0.0028)	HOMO-5 → LUMO+1 (0.14352)	$\pi \rightarrow \pi^*$
	Singlet		HOMO-1 → LUMO+2 (0.39796)	$n \rightarrow \pi^*$
	Singlet		HOMO → LUMO+4 (0.55330)	Intramolecular charge transfer
20	Singlet	224.29 (0.0911)	HOMO-9 → LUMO (-0.32566)	$\sigma \rightarrow \pi^*$
	Singlet		HOMO-8 → LUMO (0.11543)	$\pi \rightarrow \pi^*$
	Singlet		HOMO-5 → LUMO+1 (0.50403)	$\pi \rightarrow \pi^*$
	Singlet		HOMO-3 → LUMO+2 (-0.14264)	$\pi \rightarrow \pi^*$
	Singlet		HOMO → LUMO+1 (-0.17196)	Intramolecular charge transfer
	Singlet		HOMO-2 → LUMO+3 (-0.17676)	$\pi \rightarrow \pi^*$
	Singlet		HOMO-2 → LUMO+4 (-0.13757)	$\pi \rightarrow \pi^*$

^a Oscillator strength, ^b Orbital coefficient

1-(propylene-oxide)aminoanthraquinone (58)

#	State	Transition energy (nm)	Participating MO	Transition character
1	Singlet	495.98 (0.1536) ^a	HOMO → LUMO (0.70376) ^b	Intramolecular charge transfer
2	Singlet	411.06 (0.0001)	HOMO-1 → LUMO (-0.11031)	$n \rightarrow \pi^*$
	Singlet		HOMO-4 → LUMO+1 (-0.10167)	$n \rightarrow \pi^*$
	Singlet		HOMO-1 → LUMO (0.68612)	$n \rightarrow \pi^*$
3	Singlet	374.61 (0.0000)	HOMO-6 → LUMO (0.15178)	$n \rightarrow \pi^*$

Chapter 6. Appendix

	Singlet		HOMO-4 → LUMO (0.65884)	n → π*
	Singlet		HOMO-1 → LUMO (0.11022)	n → π*
	Singlet		HOMO-1 → LUMO+1 (-0.14864)	n → π*
4	Singlet	340.15 (0.0014)	HOMO-2 → LUMO (0.65851)	π → π*
	Singlet		HOMO → LUMO+1 (0.24253)	Intramolecular charge transfer
5	Singlet	323.87 (0.0152)	HOMO-3 → LUMO (0.46291)	π → π*
	Singlet		HOMO-2 → LUMO (-0.19470)	π → π*
	Singlet		HOMO → LUMO+1 (0.47970)	Intramolecular charge transfer
6	Singlet	319.76 (0.1547)	HOMO-3 → LUMO (0.50866)	π → π*
	Singlet		HOMO-2 → LUMO (0.14162)	π → π*
	Singlet		HOMO → LUMO+1 (-0.45082)	Intramolecular charge transfer
7	Singlet	291.35 (0.0011)	HOMO-6 → LUMO (0.68257)	n → π*
	Singlet		HOMO-4 → LUMO (-0.16115)	n → π*
8	Singlet	279.96 (0.1671)	HOMO-5 → LUMO (0.67769)	π → π*
	Singlet		HOMO-2 → LUMO+2 (-0.10307)	π → π*
9	Singlet	257.71 (0.0060)	HOMO → LUMO+2 (0.69272)	Intramolecular charge transfer
10	Singlet	266.46 (0.0000)	HOMO-4 → LUMO (0.14740)	n → π*
	Singlet		HOMO-1 → LUMO+1 (0.68482)	n → π*
11	Singlet	250.74 (0.0002)	HOMO-6 → LUMO+1 (0.13533)	n → π*
	Singlet		HOMO-4 → LUMO+1 (0.66881)	n → π*
	Singlet		HOMO-1 → LUMO (0.11290)	n → π*
12	Singlet	249.68 (0.0184)	HOMO-8 → LUMO (0.11925)	n → π*
	Singlet		HOMO-7 → LUMO (0.60408)	π → π*
	Singlet		HOMO-2 → LUMO+1 (0.21690)	π → π*

Chapter 6. Appendix

	Singlet		HOMO → LUMO+3 (0.18802)	Intramolecular charge transfer
13	Singlet	241.19 (0.5560)	HOMO-7 → LUMO (-0.10415)	$\pi \rightarrow \pi^*$
	Singlet		HOMO-3 → LUMO+2 (-0.16825)	$\pi \rightarrow \pi^*$
	Singlet		HOMO-2 → LUMO+1 (0.57612)	$\pi \rightarrow \pi^*$
	Singlet		HOMO → LUMO+3 (-0.32487)	Intramolecular charge transfer
14	Singlet	234.21 (0.1684)	HOMO-8 → LUMO (0.14000)	$n \rightarrow \pi^*$
	Singlet		HOMO-7 → LUMO (-0.24847)	$\pi \rightarrow \pi^*$
	Singlet		HOMO-5 → LUMO+1 (0.19732)	$\pi \rightarrow \pi^*$
	Singlet		HOMO-3 → LUMO+2 (-0.17839)	$\pi \rightarrow \pi^*$
	Singlet		HOMO-2 → LUMO+1 (0.18444)	$\pi \rightarrow \pi^*$
	Singlet		HOMO → LUMO+3 (0.53606)	Intramolecular charge transfer
15	Singlet	231.58 (0.0114)	HOMO-3 → LUMO (0.67992)	$\pi \rightarrow \pi^*$
	Singlet		HOMO-2 → LUMO+1 (0.10857)	$\pi \rightarrow \pi^*$
16	Singlet	229.42 (0.0035)	HOMO-8 → LUMO (0.63135)	$n \rightarrow \pi^*$
	Singlet		HOMO-7 → LUMO (-0.12032)	$\pi \rightarrow \pi^*$
	Singlet		HOMO-5 → LUMO+1 (-0.22624)	$\pi \rightarrow \pi^*$
	Singlet		HOMO-3 → LUMO+2 (0.10150)	$\pi \rightarrow \pi^*$
17	Singlet	226.81 (0.0011)	HOMO-1 → LUMO+2 (0.69981)	$n \rightarrow \pi^*$
18	Singlet	224.32 (0.1103)	HOMO-8 → LUMO (0.22779)	$n \rightarrow \pi^*$
	Singlet		HOMO-7 → LUMO (0.15116)	$\pi \rightarrow \pi^*$
	Singlet		HOMO-5 → LUMO+1 (0.55229)	$\pi \rightarrow \pi^*$
	Singlet		HOMO-3 → LUMO+2 (-0.15760)	$\pi \rightarrow \pi^*$
	Singlet		HOMO-2 → LUMO+1 (-0.18294)	$\pi \rightarrow \pi^*$
	Singlet		HOMO → LUMO+3 (-0.18025)	Intramolecular charge transfer
19	Singlet	219.70 (0.005)	HOMO-6 → LUMO+1 (0.68694)	$n \rightarrow \pi^*$

	Singlet		HOMO-4 → LUMO+1 (-0.14405)	$n \rightarrow \pi^*$
20	Singlet	214.13 (0.0001)	HOMO-9 → LUMO (0.21631)	$\sigma \rightarrow \pi^*$
	Singlet		HOMO-6 → LUMO+2 (0.12804)	$n \rightarrow \pi^*$
	Singlet		HOMO-4 → LUMO+2 (0.65221)	$n \rightarrow \pi^*$

^a Oscillator strength, ^b Orbital coefficient

6.2.3 Cartesian Coordinates

4-Piperidinyl-1,8-naphthalic anhydride (45b)

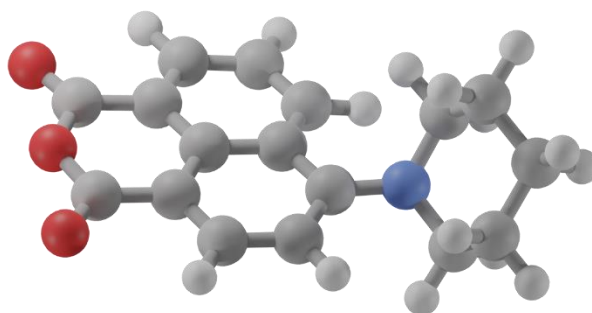


Figure 6.23: Calculated molecular structure of 4-Piperidinyl-1,8-naphthalic anhydride

```

O -3.15851 -2.97551 0.23354
C -2.85842 -1.80919 0.17764
C -3.76291 0.48653 0.28164
O -4.75782 1.14723 0.44069
C -1.52118 -1.26561 -0.05475
C -1.30888 0.13823 -0.10669
C -2.41429 1.02624 0.00971
C -2.24623 2.39543 -0.15185
C -0.97687 2.91133 -0.46561
C 0.11806 2.06527 -0.55414
C 0.00302 0.66823 -0.32884
C 1.13184 -0.24637 -0.40659
C 0.85434 -1.62687 -0.43336
C -0.43917 -2.12041 -0.25516
H -3.11559 3.04923 -0.06209
H -0.85449 3.98009 -0.65278
H 1.08354 2.48352 -0.83630

```

N 2.42471 0.22768 -0.49368
H 1.67271 -2.34044 -0.52145
H -0.61146 -3.19840 -0.23194
C 2.95209 1.26396 0.40831
C 3.48320 -0.55760 -1.13626
C 3.90723 0.66457 1.45321
H 2.12330 1.76625 0.91850
H 3.48527 2.02583 -0.19052
C 4.44716 -1.21059 -0.13844
H 4.05611 0.13991 -1.77634
H 3.02838 -1.29540 -1.80944
C 5.02973 -0.15198 0.80504
H 5.24751 -1.72754 -0.69313
H 3.91279 -1.97942 0.44641
H 5.68945 0.52377 0.23003
H 5.65963 -0.62264 1.57715
H 3.32519 0.02050 2.13581
H 4.32026 1.48542 2.06290
O -3.88215 -0.88315 0.35526

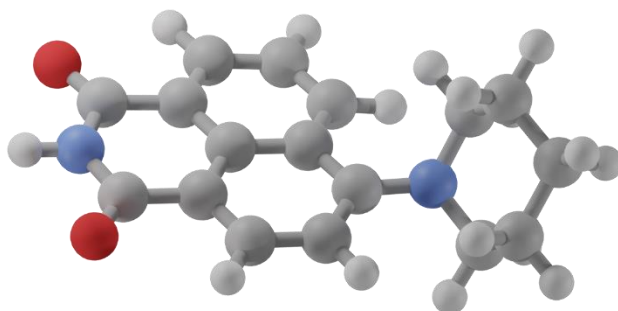


Figure 6.24: Calculated molecular structure of 4-Piperidinyl-1,8-naphthalimide

4-Piperidinyl-1,8-naphthalimide (54)

O -3.07311 -3.03974 0.22039
C -2.82360 -1.83957 0.16738
C -3.76644 0.47950 0.27895
O -4.76728 1.17069 0.43104
C -1.48923 -1.26736 -0.06851
C -1.29954 0.14244 -0.11272
C -2.41187 1.02454 0.01402
C -2.25098 2.39429 -0.13296
C -0.98534 2.92467 -0.44261
C 0.11459 2.08830 -0.54416
C 0.00692 0.68755 -0.33499
C 1.14491 -0.21101 -0.42285
C 0.89187 -1.59153 -0.45040
C -0.39852 -2.10342 -0.27342
H -3.12653 3.03725 -0.03469

H -0.87178 3.99597 -0.61729
H 1.07874 2.51068 -0.82384
N 2.43136 0.30149 -0.53300
H 1.71994 -2.29217 -0.54597
H -0.56051 -3.18235 -0.25506
C 2.95284 1.27035 0.45013
C 3.49758 -0.48379 -1.16817
C 3.84847 0.59263 1.49973
H 2.11587 1.77311 0.94661
H 3.53188 2.04150 -0.09132
C 4.41568 -1.20409 -0.17056
H 4.10648 0.22798 -1.75681
H 3.04621 -1.18113 -1.88613
C 4.98246 -0.20523 0.84628
H 5.22729 -1.70513 -0.72411
H 3.85120 -1.99213 0.35807
H 5.66910 0.49142 0.32950
H 5.57948 -0.72689 1.61178
H 3.22724 -0.07921 2.11887
H 4.25194 1.36858 2.17201
N -3.84931 -0.90627 0.34224
H -4.77671 -1.29120 0.51131

4-Piperidinyl-(N'-propylene-oxide)-1,8-naphthalimide (55)

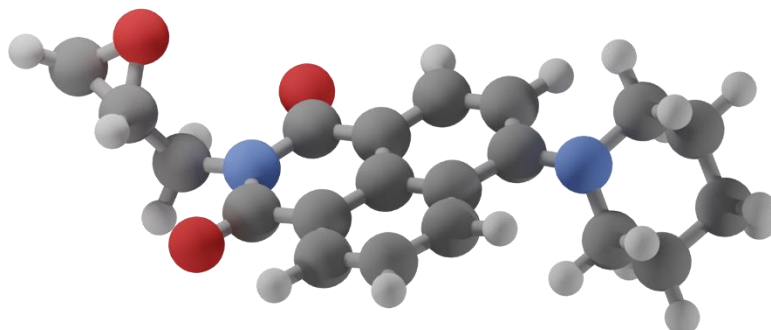


Figure 6.25: Calculated molecular structure of 4-Piperidinyl-1,8-naphthalimide.

O -2.3804863092 -2.3168472200 0.6172052548
C -1.9868436238 -1.1670734242 0.4481729499
N -2.8791728877 -0.0798889248 0.5827206494
C -4.2808363735 -0.3718208720 0.9299331096
C -5.2160980012 -0.2457633499 -0.2505531386
C -2.5296849444 1.2658021377 0.4287691959
O -3.3782425640 2.1428584213 0.5729416557
C -0.5918076434 -0.8344618629 0.1192469162
C -0.1705129993 0.5128444782 -0.0291209830
C -1.1197243569 1.5650516744 0.0830383769
C -0.7482534239 2.8807564135 -0.1551625898

C 0.5701818590 3.1787979814 -0.5447848667
C 1.5161418253 2.1702363355 -0.6368938485
C 1.1945937136 0.8202211803 -0.3359203096
C 2.1627207968 -0.2595509345 -0.4077609835
C 1.6825607600 -1.5764052349 -0.3290201214
C 0.3359009735 -1.8531397366 -0.0670591594
H -4.5902162722 0.3375122800 1.7102046969
H -4.3018143392 -1.3952096829 1.3176239643
H -1.5029976932 3.6626471772 -0.0650387116
H 0.8455941479 4.2060651368 -0.7897859236
H 2.5207487818 2.4142630025 -0.9794400716
N 3.5091934545 0.0204434589 -0.6047798935
H 2.3771540116 -2.4112596626 -0.4083120687
H 0.0005435614 -2.8863650886 0.0329884812
C 4.2332214634 0.9470146112 0.2864719460
C 4.3971525666 -0.9717590856 -1.2245655275
C 5.0551692960 0.1953655159 1.3458924679
H 3.5177532610 1.6145589592 0.7784691409
H 4.9045777182 1.5731827309 -0.3303301869
C 5.2326943637 -1.7723919196 -0.2153625262
H 5.0847470157 -0.4112253019 -1.8856210305
H 3.8009824128 -1.6270248026 -1.8732330661
C 6.0069335425 -0.8218968146 0.7067261737
H 5.9218342802 -2.4361294461 -0.7638262942
H 4.5729616768 -2.4199670195 0.3883243502
H 6.7734083634 -0.2849423365 0.1167849605
H 6.5462050706 -1.3882599351 1.4832903455
H 4.3627358229 -0.3216333902 2.0342823285
H 5.6149699734 0.9326697019 1.9458100060
C -6.3898492397 -1.1229904439 -0.3750956090
O -5.2252841577 -1.3349576718 -1.1887200371
H -7.2785319804 -0.7617506548 -0.9056193854
H -6.5729298426 -1.8892800316 0.3878014871
H -5.2577292453 0.7468185017 -0.7130821106

1-((3-chloro-2-hydroxypropyl)amino)anthraquinone (57)

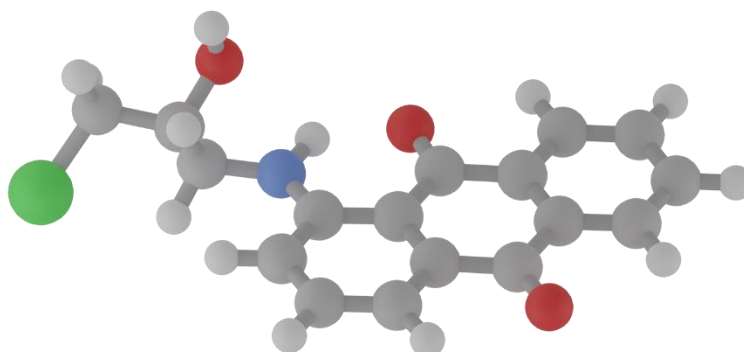


Figure 6.26: Calculated molecular structure of 1-((3-chloro-2-hydroxypropyl)amino)anthraquinone

C	-5.41371	-1.64296	-0.25472
C	-4.98516	-0.31746	-0.20549
C	-3.61738	-0.02178	-0.10802
C	-2.67358	-1.06532	-0.05878
C	-3.11373	-2.39641	-0.10826
C	-4.47501	-2.68373	-0.20606
C	-3.17548	1.39714	-0.05451
C	-1.20767	-0.78937	0.04570
C	-0.75687	0.60740	0.08581
C	-1.70684	1.66709	0.04940
C	-1.30685	2.99899	0.11156
H	-2.06730	3.77801	0.08064
C	0.05706	3.30481	0.22006
C	1.01174	2.30205	0.25540
C	0.64362	0.92916	0.17418
H	-6.47906	-1.87019	-0.33089
H	-5.69396	0.51058	-0.24071
H	-2.36878	-3.19130	-0.06891
H	-4.80966	-3.72257	-0.24483
H	0.37698	4.34744	0.28147
H	2.06331	2.57023	0.34866
O	-0.42370	-1.75214	0.10057
O	-3.98971	2.31580	-0.09434
N	1.58808	-0.04651	0.17176
H	1.22883	-1.00149	0.23269
C	3.00647	0.16388	0.36620
H	3.23720	0.44882	1.41506
H	3.37516	0.97864	-0.27537
C	3.75988	-1.12084	0.01396
H	3.58737	-1.35640	-1.04793
C	5.26525	-1.03008	0.26760
H	5.48736	-0.72671	1.30115
H	5.73457	-1.99896	0.06044

O 3.24495 -2.24310 0.72647
Cl 6.08154 0.19015 -0.81279
H 3.30257 -2.05304 1.67779

1-(propylene-oxide)amino)anthraquinone (58)

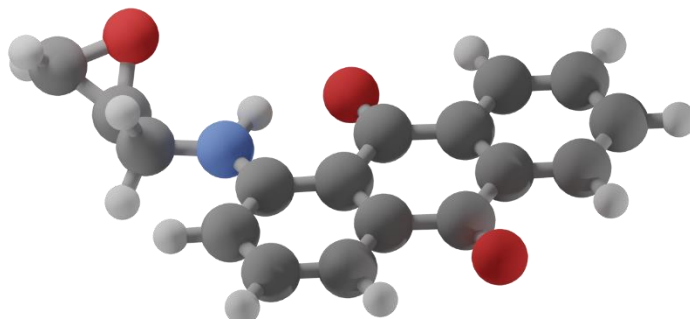


Figure 6.27: Calculated molecular structure of 1-(propylene-oxide)amino)anthraquinone (66).

C -4.63797700 -1.80159500 0.01522900
C -4.26037700 -0.45981700 0.02826100
C -2.90219400 -0.10943900 0.01330400
C -1.91653500 -1.11441600 -0.01469000
C -2.30538700 -2.46220900 -0.02672800
C -3.65751200 -2.80392900 -0.01215500
C -2.51471600 1.32615400 0.03009400
C -0.45962300 -0.77974600 -0.03248700
C -0.06328900 0.63392800 -0.02632100
C -1.05443600 1.65481400 0.01300700
C -0.70390500 3.00173200 0.03944500
H -1.49480400 3.74984200 0.06958100
C 0.65111200 3.36179200 0.03540500
C 1.64504400 2.39792600 -0.00439700
C 1.32589100 1.01145400 -0.05223400
H -5.69601900 -2.07145300 0.02674700
H -5.00215200 0.33930200 0.05053400
H -1.52828300 -3.22639400 -0.04763300
H -3.95225000 -3.85545300 -0.02202700
H 0.93289400 4.41661300 0.06923700
H 2.68915100 2.70817300 0.00580700
O 0.36437700 -1.71075200 -0.04756900
O -3.36545100 2.21153200 0.05688800
N 2.30294600 0.07119900 -0.12702900
H 1.97177500 -0.89088800 -0.03320000
C 3.72842800 0.33242000 -0.05735800
H 4.04001200 0.62128600 0.96446700
H 3.99806000 1.16221700 -0.73296000
C 4.48941900 -0.89695700 -0.48679700

H 4.30524100 -1.22396800 -1.51857700
 C 5.75386300 -1.28044000 0.15453100
 H 6.16027000 -0.65961500 0.96159200
 H 6.48972600 -1.85846900 -0.41556800
 O 4.53343600 -1.97323100 0.46749900

6.3 Chapter 4 Appendix

6.3.1 Small Scale AAQ Doped Polymer

Poly1

Table 6.7: GPC fit parameters for **AAQ-PhA-CHO1**.

Peak	a	b	c	d
Peak 1	1.057594	4.223285	0.0900723	2.08×10^{-5}
Peak 2	5.591981	4.500060	0.0527720	-0.02472538
Peak 3	0.2089189	4.634894	0.03814822	0.06021545

AAQ-PhA-CHO2

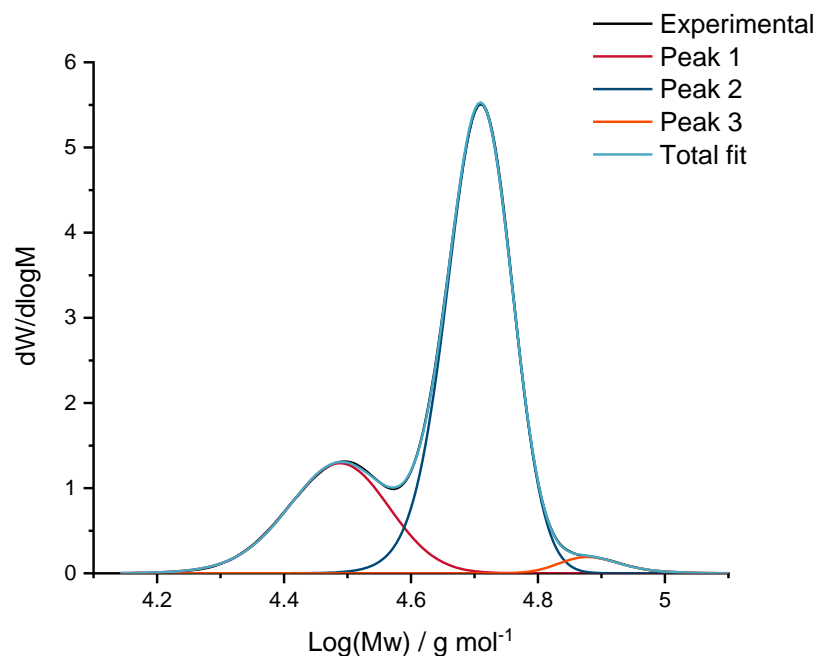


Figure 6.28: Experimental and fitted GPC data for **AAQ-PhA-CHO2**.

Table 6.8: GPC fit parameters for **AAQ-PhA-CHO2**

Peak	a	b	c	d
Peak 1	1.448867	4.521941	0.07107725	-0.04089061
Peak 2	6.191381	4.73197	0.04632069	-0.027001606
Peak 3	0.2438804	4.851283	0.03883703	0.03832512

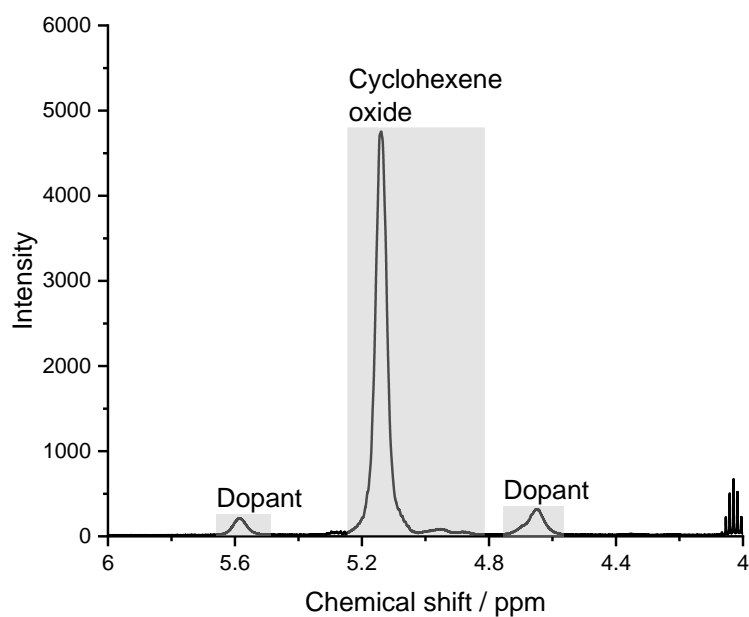
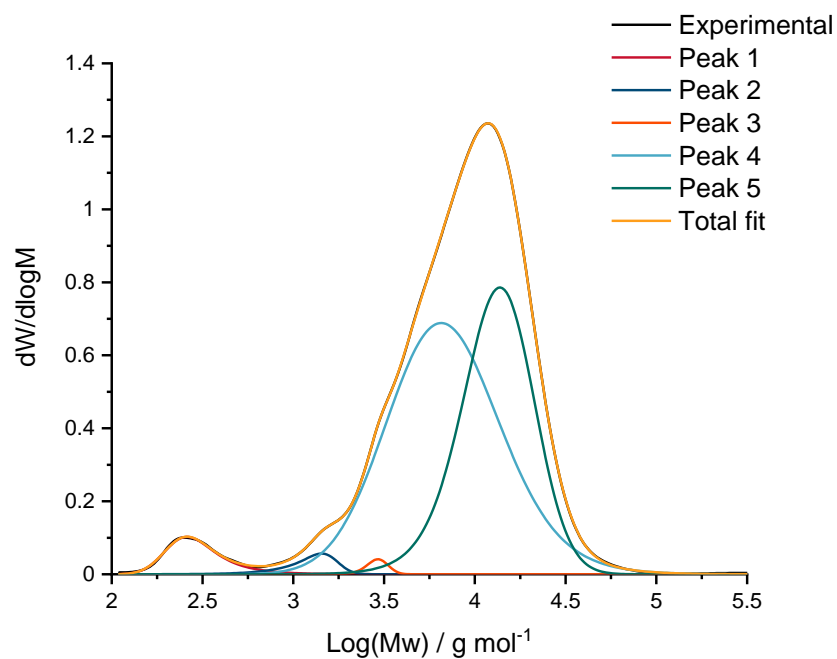


Figure 6.29: Ring opened epoxide regions

Nap-PhA

**Figure 6.30:** Experimental and fitted GPC data for **Nap-PhA**.**Table 6.9:** GPC fit parameters for **Nap-PhA**.

Peak	a	b	c	d
Peak 1	0.1503604	2.326195	0.1008734	0.1493777
Peak 2	0.1011934	3.227354	0.06620233	-0.1486543
Peak 3	0.0497262	3.49708	0.04927222	-0.04051218
Peak 4	0.7833745	3.674558	0.2765741	0.1732579
Peak 5	0.925571	4.235588	0.1703577	-0.1258461

6.3.2 Large Scale Polymer Synthesis

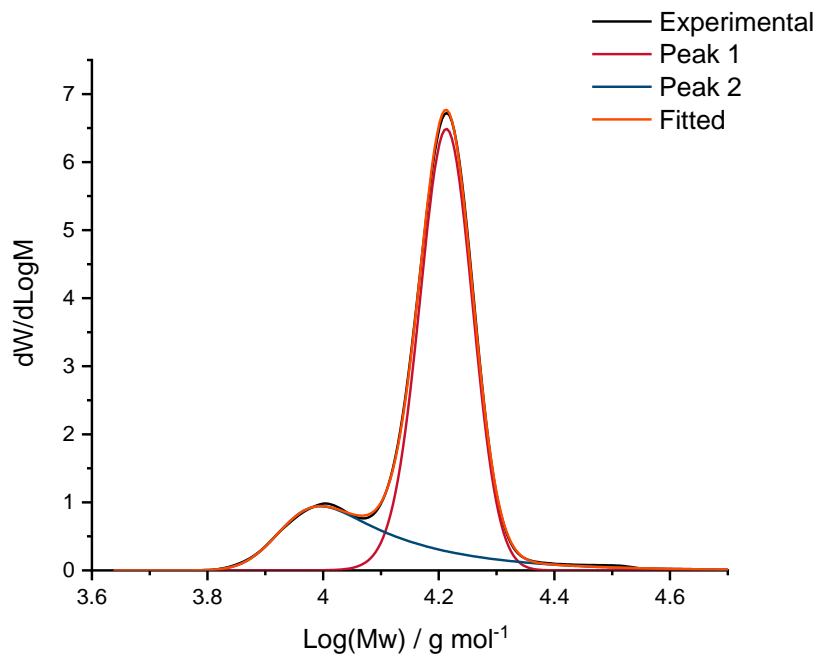


Figure 6.31: Experimental and fitted GPC data for PhA-CHO.

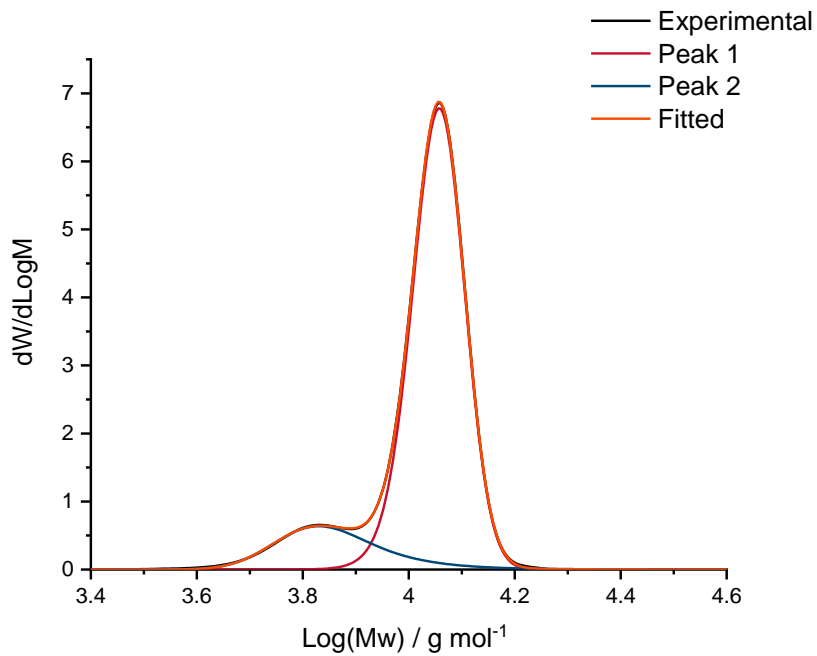
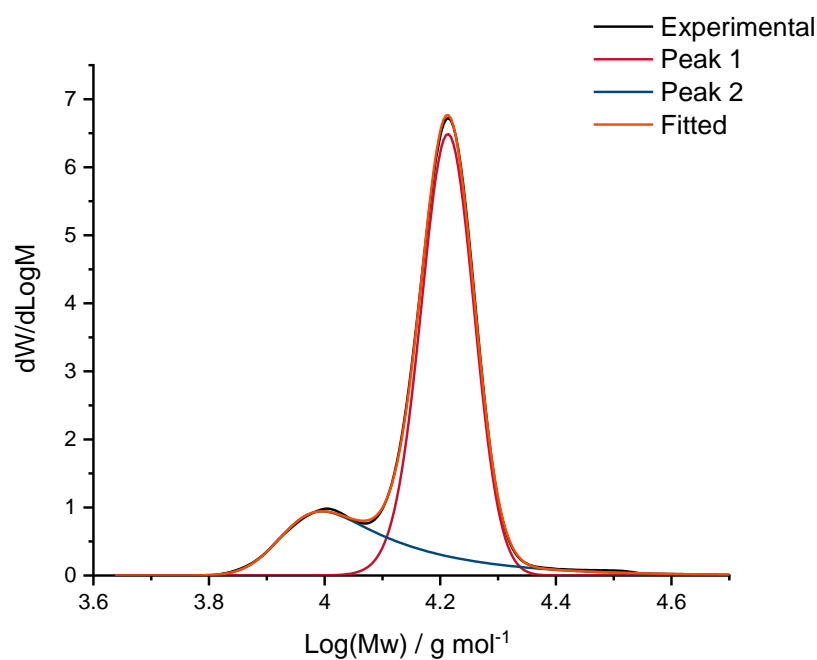


Figure 6.32: Experimental and fitted GPC data for AAQ-PhA-CHO.

Table 6.10: GPC fit parameters for large scale polymers

Polymer		a	b	c	d
PhA-CHO	Peak 1	5.2798	4.1254	0.0564	0.0299
	Peak 2	1.0038	3.8625	0.0997	0.0879
AAQ-PhA-CHO3	Peak 1	7.8633	4.0806	0.0441	-0.0289
	Peak 2	0.7232	3.8634	0.0703	-0.0420
Nap-PhA-CHO	Peak 1	6.9931	4.2297	0.0427	-0.0188
	Peak 2	1.9910	3.9330	0.0507	0.1544

**Figure 6.33:** Experimental and fitted GPC data for **Nap-PhA-CHO**.

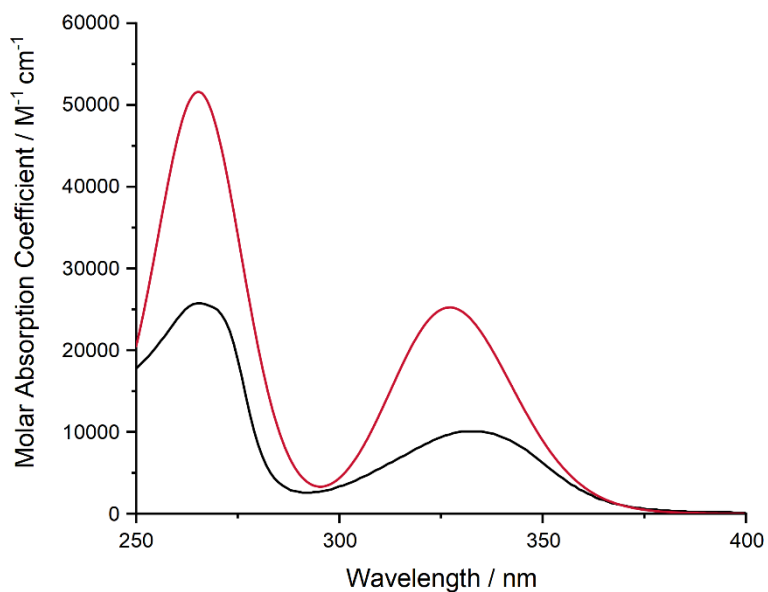


Figure 6.34: Experimental (black line) and simulated (red line, predicted ϵ) UV-Vis spectra of **36** in chloroform using TD-DFT with the B3LYP functional and cc-PVDZ basis set

6.3.3 Post-Polymerisation Modification

Table 6.11: GPC fit parameters for **ECH(38)-PhA**

Peak	a	b	c	d
Peak 1	0.4227	2.9946	0.0336	0.1019
Peak 2	0.1904	3.1270	0.0280	-0.0350
Peak 3	0.0435	3.2328	0.0204	-0.0149
Peak 4	0.2523	3.2965	0.0127	0.1823
Peak 5	0.2892	3.4153	0.1948	0.1948
Peak 6	2.2522	3.9696	0.1262	-0.3262
Peak 7	0.4713	4.0674	0.1000	0.0578

6.3.4 Polymer Degradation

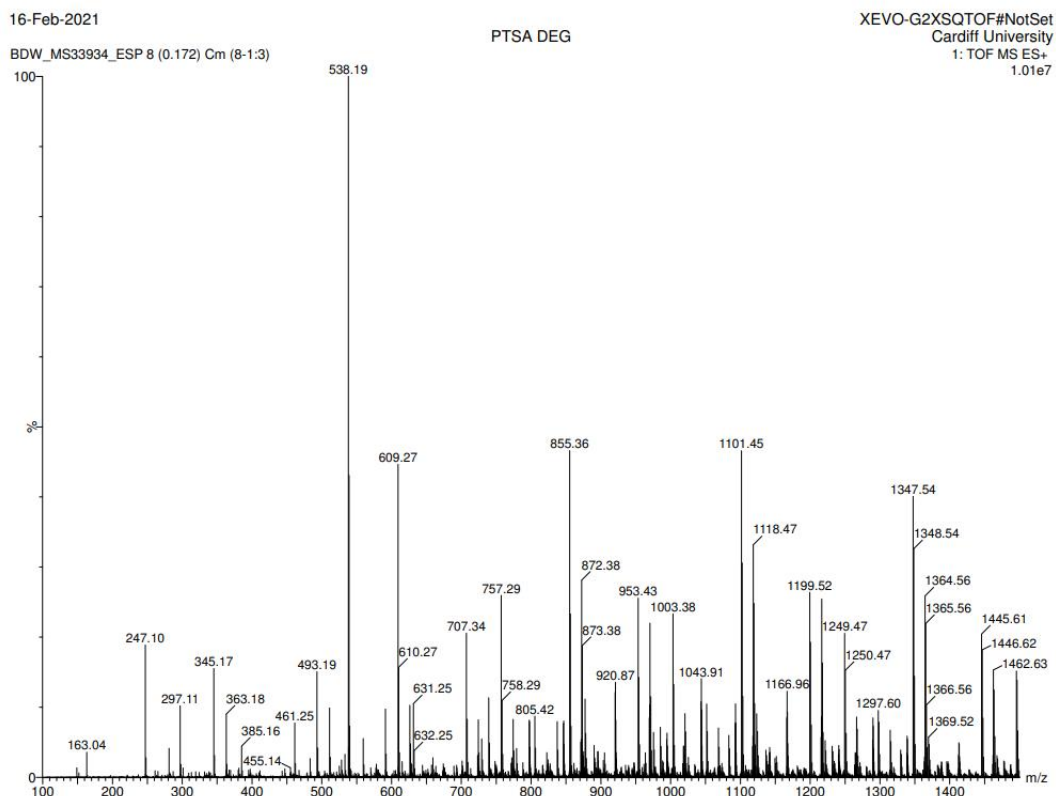


Figure 6.35: ESI mass spectrum for acidic hydrolysis of a polyester

^tBu-Salen (46)

#	State	Transition energy (nm)	Participating MO	Transition character
1	Singlet	328.03 (0.3202) ^a	HOMO-1 → LUMO+1 (-0.28843) ^b	π → π*
	Singlet		HOMO → LUMO (0.63375)	π → π*
2	Singlet	322.98 (0.0545)	HOMO-1 → LUMO (0.59911)	π → π*
	Singlet		HOMO → LUMO+1 (-0.33947)	π → π*
3	Singlet	305.34 (0.0027)	HOMO-1 → LUMO (0.35633)	π → π*
	Singlet		HOMO → LUMO+1 (0.60705)	π → π*
4	Singlet	303.86 (0.0062)	HOMO-1 → LUMO+1 (0.63324)	π → π*
	Singlet		HOMO → LUMO (0.30121)	π → π*

Chapter 6. Appendix

5	Singlet	267.51 (0.4856)	HOMO-5 → LUMO+1 (-0.21628)	n → π*
	Singlet		HOMO-4 → LUMO (0.27565)	n → π*
	Singlet		HOMO-2 → LUMO (0.58732)	π → π*
6	Singlet	264.75 (0.001)	HOMO-5 → LUMO (0.52570)	n → π*
	Singlet		HOMO-4 → LUMO+1 (-0.42841)	n → π*
	Singlet		HOMO-2 → LUMO+1 (-0.14613)	π → π*
7	Singlet	263.42 (0.2589)	HOMO-5 → LUMO+1 (-0.37575)	n → π*
	Singlet		HOMO-4 → LUMO (0.46486)	n → π*
	Singlet		HOMO-3 → LUMO+1 (0.14017)	π → π*
	Singlet		HOMO-2 → LUMO (-0.32062)	π → π*
8	Singlet	254.97 (0.0214)	HOMO-3 → LUMO (0.61587)	π → π*
	Singlet		HOMO-2 → LUMO+1 (-0.21713)	π → π*
	Singlet		HOMO-1 → LUMO+2 (-0.14815)	π → π*
	Singlet		HOMO → LUMO+3 (-0.16338)	π → π*
9	Singlet	253.46 (0.0052)	HOMO-5 → LUMO (0.13306)	n → π*
	Singlet		HOMO-3 → LUMO (0.26518)	π → π*
	Singlet		HOMO-2 → LUMO+1 (0.62005)	π → π*
10	Singlet	249.20 (0.1123)	HOMO-3 → LUMO+1 (0.65737)	π → π*
	Singlet		HOMO-2 → LUMO (0.17383)	π → π*
	Singlet		HOMO-1 → LUMO+3 (0.10011)	π → π*
	Singlet		HOMO → LUMO+2 (0.11105)	π → π*
11	Singlet	228.50 (0.0535)	HOMO-5 → LUMO+1 (0.53450)	n → π*
	Singlet		HOMO-4 → LUMO (0.42890)	n → π*
	Singlet		HOMO → LUMO+2 (0.11865)	π → π*
12	Singlet	228.36 (0.0001)	HOMO-5 → LUMO (0.44414)	n → π*
	Singlet		HOMO-4 → LUMO+1 (0.54570)	n → π*
13	Singlet	225.04 (0.5471)	HOMO-5 → LUMO+1 (-0.12565)	n → π*

Chapter 6. Appendix

	Singlet		HOMO-3 → LUMO+1 (-0.17452)	$\pi \rightarrow \pi^*$
	Singlet		HOMO-1 → LUMO+3 (0.30746)	$\pi \rightarrow \pi^*$
	Singlet		HOMO-1 → LUMO+5 (0.13578)	$\pi \rightarrow \pi^*$
	Singlet		HOMO → LUMO+2 (0.50908)	$\pi \rightarrow \pi^*$
	Singlet		HOMO → LUMO+4 (-0.13179)	$\pi \rightarrow \pi^*$
14	Singlet	223.94 (0.0945)	HOMO-3 → LUMO (0.15831)	$\pi \rightarrow \pi^*$
	Singlet		HOMO-2 → LUMO+1 (-0.16798)	$\pi \rightarrow \pi^*$
	Singlet		HOMO-2 → LUMO+3 (0.10369)	$\pi \rightarrow \pi^*$
	Singlet		HOMO-1 → LUMO+2 (0.26809)	$\pi \rightarrow \pi^*$
	Singlet		HOMO-1 → LUMO+4 (-0.16734)	$\pi \rightarrow \pi^*$
	Singlet		HOMO → LUMO+3 (0.52213)	$\pi \rightarrow \pi^*$
	Singlet		HOMO → LUMO+5 (0.15969)	$\pi \rightarrow \pi^*$
15	Singlet	220.07 (0.0354)	HOMO-1 → LUMO+2 (-0.10591)	$\pi \rightarrow \pi^*$
	Singlet		HOMO-1 → LUMO+3 (0.57465)	$\pi \rightarrow \pi^*$
	Singlet		HOMO → LUMO+2 (-0.39126)	$\pi \rightarrow \pi^*$
16	Singlet	220.00 (0.0029)	HOMO-1 → LUMO+2 (0.5848)	$\pi \rightarrow \pi^*$
	Singlet		HOMO-1 → LUMO+3 (0.10739)	$\pi \rightarrow \pi^*$
	Singlet		HOMO → LUMO+3 (-0.36957)	$\pi \rightarrow \pi^*$
17	Singlet	208.56 (0.5583)	HOMO-6 → LUMO (0.13895)	$\sigma \rightarrow \pi^*$
	Singlet		HOMO-3 → LUMO+3 (0.29408)	$\pi \rightarrow \pi^*$
	Singlet		HOMO-2 → LUMO+2 (0.36037)	$\pi \rightarrow \pi^*$
	Singlet		HOMO-1 → LUMO+3 (-0.12581)	$\pi \rightarrow \pi^*$
	Singlet		HOMO-1 → LUMO+5 (0.29325)	$\pi \rightarrow \pi^*$
	Singlet		HOMO → LUMO+2 (-0.16143)	$\pi \rightarrow \pi^*$
	Singlet		HOMO → LUMO+4 (-0.33053)	$\pi \rightarrow \pi^*$
18	Singlet	207.13 (0.0044)	HOMO-3 → LUMO+2 (0.29486)	$\pi \rightarrow \pi^*$
	Singlet		HOMO-2 → LUMO+3 (0.36377)	$\pi \rightarrow \pi^*$
	Singlet		HOMO-1 → LUMO+2 (-0.16665)	$\pi \rightarrow \pi^*$
	Singlet		HOMO-1 → LUMO+4 (-0.28427)	$\pi \rightarrow \pi^*$
	Singlet		HOMO → LUMO+3 (-0.18547)	$\pi \rightarrow \pi^*$
	Singlet		HOMO → LUMO+5 (0.30592)	$\pi \rightarrow \pi^*$

19	Singlet	202.16 (0.0002)	HOMO-11 → LUMO+1 (-0.14211)	$\sigma \rightarrow \pi^*$
	Singlet		HOMO-10 → LUMO (0.16058)	$\sigma \rightarrow \pi^*$
	Singlet		HOMO-8 → LUMO+1 (-0.39339)	$\sigma \rightarrow \pi^*$
	Singlet		HOMO-7 → LUMO (0.51203)	$\sigma \rightarrow \pi^*$
20	Singlet	202.07 (0.0003)	HOMO-11 → LUMO (0.17416)	$\sigma \rightarrow \pi^*$
	Singlet		HOMO-10 → LUMO+1 (-0.12455)	$\sigma \rightarrow \pi^*$
	Singlet		HOMO-8 → LUMO (0.50558)	$\sigma \rightarrow \pi^*$
	Singlet		HOMO-7 → LUMO+1 (-0.40269)	$\sigma \rightarrow \pi^*$

^a Oscillator strength, ^b Orbital coefficient

[Al(^tBu-Salen)Cl] (47)

#	State	Transition energy (nm)	Participating MO	Transition character
1	Singlet	399.29 (0.0180) ^a	HOMO → LUMO (0.70088) ^b	$\pi \rightarrow \pi^*$
2	Singlet	370.92 (0.0825)	HOMO-1 → LUMO (0.69989)	$\pi \rightarrow \pi^*$
3	Singlet	352.33 (0.0716)	HOMO → LUMO+1 (0.69735)	$\pi \rightarrow \pi^*$
4	Singlet	338.40 (0.0183)	HOMO-1 → LUMO+1 (0.69507)	$\pi \rightarrow \pi^*$
5	Singlet	296.28 (0.2664)	HOMO-4 → LUMO (0.31937)	$n \rightarrow \pi^*$
	Singlet		HOMO-2 → LUMO (0.60282)	$\pi \rightarrow \pi^*$
6	Singlet	289.60 (0.0869)	HOMO-5 → LUMO (0.10936)	$n \rightarrow \pi^*$
	Singlet		HOMO-5 → LUMO+1 (-0.11742)	$n \rightarrow \pi^*$
	Singlet		HOMO-4 → LUMO (0.52743)	$n \rightarrow \pi^*$
	Singlet		HOMO-3 → LUMO (-0.20988)	$\pi \rightarrow \pi^*$
	Singlet		HOMO-2 → LUMO (-0.34953)	$\pi \rightarrow \pi^*$

Chapter 6. Appendix

7	Singlet	282.00 (0.1368)	HOMO-4 → LUMO (0.19365)	$n \rightarrow \pi^*$
	Singlet		HOMO-3 → LUMO (0.63112)	$\pi \rightarrow \pi^*$
	Singlet		HOMO-2 → LUMO+1 (- 0.19532)	$\pi \rightarrow \pi^*$
8	Singlet	248.06 (0.0086)	HOMO-7 → LUMO (0.16720)	$n \rightarrow \pi^*$
	Singlet		HOMO-6 → LUMO (-0.14946)	$n \rightarrow \pi^*$
	Singlet		HOMO-5 → LUMO (-0.38869)	$n \rightarrow \pi^*$
	Singlet		HOMO-5 → LUMO+1 (- 0.11841)	$n \rightarrow \pi^*$
	Singlet		HOMO-4 → LUMO (0.15448)	$n \rightarrow \pi^*$
	Singlet		HOMO-4 → LUMO+1 (0.46111)	$n \rightarrow \pi^*$
	Singlet		HOMO-2 → LUMO+1 (0.12895)	$\pi \rightarrow \pi^*$
9	Singlet	266.05 (0.1982)	HOMO-4 → LUMO (0.12898)	$n \rightarrow \pi^*$
	Singlet		HOMO-3 → LUMO (0.14504)	$\pi \rightarrow \pi^*$
	Singlet		HOMO-3 → LUMO+1 (0.11792)	$\pi \rightarrow \pi^*$
	Singlet		HOMO-2 → LUMO+1 (0.63455)	$\pi \rightarrow \pi^*$
10	Singlet	264.37 (0.1570)	HOMO-3 → LUMO+1 (0.67728)	$\pi \rightarrow \pi^*$
	Singlet		HOMO-2 → LUMO+1 (- 0.10462)	$\pi \rightarrow \pi^*$
11	Singlet	257.68 (0.0057)	HOMO-6 → LUMO (-0.44044)	$n \rightarrow \pi^*$
	Singlet		HOMO-5 → LUMO (0.47594)	$n \rightarrow \pi^*$
	Singlet		HOMO-4 → LUMO+1 (0.23623)	$n \rightarrow \pi^*$
12	Singlet	253.28 (0.0090)	HOMO-6 → LUMO (0.24968)	$n \rightarrow \pi^*$
	Singlet		HOMO-6 → LUMO (0.50485)	$n \rightarrow \pi^*$
	Singlet		HOMO-5 → LUMO (0.25638)	$n \rightarrow \pi^*$

Chapter 6. Appendix

	Singlet		HOMO-4 → LUMO+1 (0.30305)	$n \rightarrow \pi^*$
13	Singlet	246.82 (0.0106)	HOMO-7 → LUMO (0.62813)	$n \rightarrow \pi^*$
	Singlet		HOMO-6 → LUMO (-0.10701)	$n \rightarrow \pi^*$
	Singlet		HOMO-5 → LUMO+1 (0.10712)	$n \rightarrow \pi^*$
	Singlet		HOMO-4 → LUMO+1 (- 0.26976)	$n \rightarrow \pi^*$
14	Singlet	244.02 (0.0092)	HOMO-5 → LUMO+1 (0.64107)	$n \rightarrow \pi^*$
	Singlet		HOMO-4 → LUMO (0.17026)	$n \rightarrow \pi^*$
	Singlet		HOMO-4 → LUMO+1 (0.19721)	$n \rightarrow \pi^*$
15	Singlet	238.62 (0.0081)	HOMO-6 → LUMO+1 (0.67225)	$n \rightarrow \pi^*$
	Singlet		HOMO-5 → LUMO+1 (- 0.11396)	$n \rightarrow \pi^*$
16	Singlet	237.62 (0.3512)	HOMO → LUMO+2 (0.65699)	$\pi \rightarrow \pi^*$
17	Singlet	233.46 (0.0026)	HOMO-7 → LUMO+1 (0.67732)	$n \rightarrow \pi^*$
	Singlet		HOMO-6 → LUMO+1 (0.10054)	$n \rightarrow \pi^*$
18	Singlet	231.37 (0.0808)	HOMO-1 → LUMO+4 (0.12912)	$\pi \rightarrow \pi^*$
	Singlet		HOMO → LUMO+3 (0.65082)	$\pi \rightarrow \pi^*$
	Singlet		HOMO → LUMO+5 (0.11749)	$\pi \rightarrow \pi^*$
19	Singlet	227.27 (0.0739)	HOMO-1 → LUMO+2 (0.66162)	$\pi \rightarrow \pi^*$
	Singlet		HOMO-1 → LUMO+4 (- 0.11888)	$\pi \rightarrow \pi^*$
20	Singlet	224.75 (0.0548)	HOMO-1 → LUMO+3 (0.63540)	$\pi \rightarrow \pi^*$
	Singlet		HOMO-1 → LUMO4 (-0.10150)	$\pi \rightarrow \pi^*$
	Singlet		HOMO → LUMO+2 (0.12103)	$\pi \rightarrow \pi^*$

Singlet	HOMO → LUMO+4 (0.13202)	$\pi \rightarrow \pi^*$
---------	-------------------------	-------------------------

^a Oscillator strength, ^b Orbital coefficient

6.3.5 Cartesian Coordinates

^tBu-Salen (36)

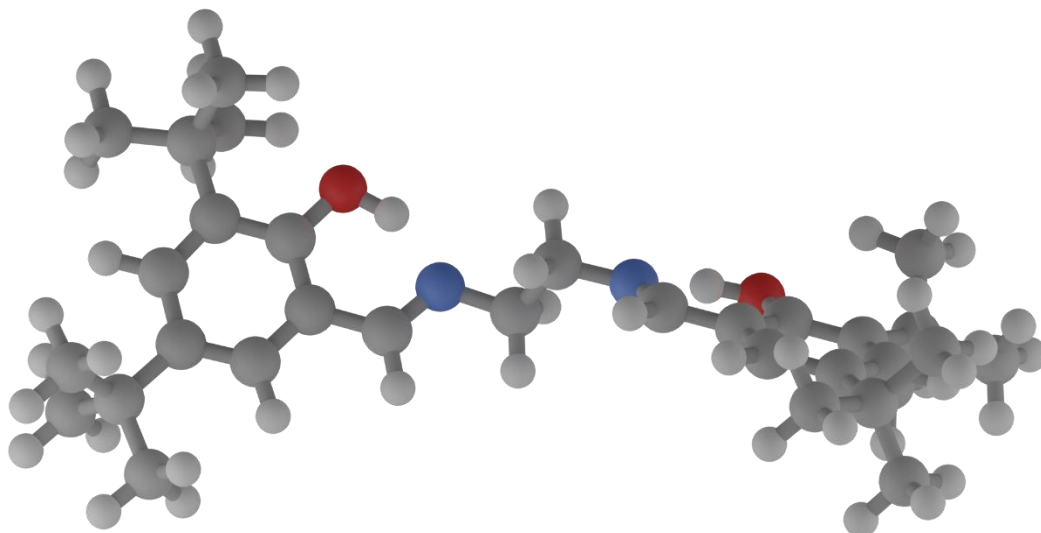


Figure 6.36: Calculated molecular structure of ^tBu-Salen (46).

```

C -0.41552 -0.64058 0.64737
H -0.18035 0.26172 1.24448
C 0.41535 -0.64014 -0.64696
H 0.18010 0.26248 -1.24353
H 0.12628 -1.52278 -1.24302
N -1.83189 -0.72917 0.34146
N 1.83174 -0.72867 -0.34109
C -2.62039 0.21797 0.71624
H -2.23247 1.09024 1.27469
C 2.62029 0.21848 -0.71577
H 2.23251 1.09075 -1.27433
C -4.05223 0.20537 0.44372
C -4.64845 -0.87697 -0.25714
C -4.84281 1.28531 0.88770
C -6.04760 -0.87152 -0.51066
C -6.21265 1.32503 0.65625
H -4.33812 2.09179 1.42141
C -6.77090 0.23011 -0.04316
H -7.84306 0.24770 -0.23053
C 4.05216 0.20562 -0.44347
C 4.84274 1.28557 -0.88749
C 4.64845 -0.87683 0.25729
C 6.21261 1.32515 -0.65624
H 4.33803 2.09215 -1.42104
C 6.04762 -0.87153 0.51050

```

C 6.77089 0.23008 0.04295
H 7.84309 0.24755 0.23015
O 3.88668 -1.90496 0.67884
O -3.88659 -1.90510 -0.67851
C -6.72959 -2.03196 -1.26870
C -7.11707 2.48306 1.11973
C 7.11705 2.48314 -1.11974
C 6.72965 -2.03210 1.26833
C -6.32214 3.57619 1.85668
H -5.54870 4.02561 1.21365
H -7.00285 4.38356 2.16969
H -5.83140 3.18686 2.76289
C -8.20003 1.94270 2.08234
H -8.85906 2.76088 2.41788
H -8.83369 1.18141 1.60126
H -7.74193 1.48534 2.97430
C -7.80193 3.12938 -0.10697
H -8.42326 2.40658 -0.65841
H -8.45732 3.95764 0.21048
H -7.05415 3.53480 -0.80779
C -6.53167 -3.35651 -0.49215
H -5.46827 -3.59768 -0.36796
H -6.99254 -3.29327 0.50752
H -7.01496 -4.18661 -1.03439
C -6.12830 -2.15827 -2.68972
H -5.04846 -2.35122 -2.65637
H -6.61268 -2.98833 -3.23105
H -6.29853 -1.23449 -3.26716
C -8.24621 -1.80898 -1.42563
H -8.76010 -1.74162 -0.45349
H -8.47589 -0.89812 -2.00119
H -8.68207 -2.66133 -1.97022
C 6.12868 -2.15846 2.68947
H 6.61310 -2.98863 3.23062
H 6.29912 -1.23471 3.26693
H 5.04882 -2.35128 2.65633
C 6.53148 -3.35660 0.49179
H 7.01485 -4.18677 1.03386
H 5.46804 -3.59768 0.36788
H 6.99206 -3.29331 -0.50802
C 8.24630 -1.80941 1.42504
H 8.76002 -1.74204 0.45281
H 8.47618 -0.89861 2.00060
H 8.68219 -2.66183 1.96950
C 8.19986 1.94275 -2.08250
H 8.83351 1.18137 -1.60152
H 7.74163 1.48547 -2.97443
H 8.85893 2.76089 -2.41808

C 7.80211 3.12932 0.10692
H 8.45752 3.95756 -0.21054
H 7.05444 3.53474 0.80787
H 8.42347 2.40645 0.65824
C 6.32214 3.57639 -1.85652
H 5.54878 4.02579 -1.21338
H 7.00288 4.38375 -2.16950
H 5.83132 3.18718 -2.76274
H 2.93918 -1.70058 0.39226
H -0.12632 -1.52354 1.24289
H -2.93911 -1.70075 -0.39176

[Al(tBu-Salen)Cl] (37)

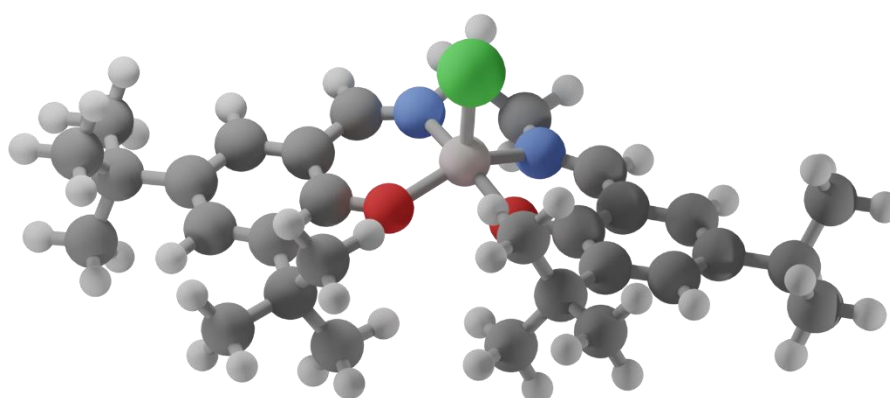


Figure 6.37: Calculated molecular structure of [Al(tBu-Salen)Cl] (47)

C 0.68086400 -3.93467000 0.19857600
H 1.35703500 -4.72835700 -0.15520400
H 0.36442800 -4.16995200 1.22858800
C -0.54895600 -3.80208400 -0.70312300
H -1.24858600 -4.64011500 -0.55933500
H -0.22911500 -3.79441300 -1.75975200
N 1.32190200 -2.62245900 0.19621400
N -1.18311000 -2.51225900 -0.39278600
C 2.60530400 -2.51178900 0.04968600
H 3.20506200 -3.43204200 -0.02558100
C -2.46513200 -2.38237600 -0.58271900
H -3.02429000 -3.26277700 -0.93472800
C 3.32505100 -1.27179900 -0.03852100
C 2.64853100 -0.01533200 -0.09834000
C 4.73775200 -1.34991300 -0.11920500
C 3.44017200 1.17026000 -0.25819900
C 5.51824900 -0.21530200 -0.24813100
H 5.18821700 -2.34241600 -0.07281100
C 4.82540800 1.01951500 -0.31609900
H 5.42591900 1.92074100 -0.42510400
C -3.23483900 -1.19142000 -0.37900600
C -4.63467600 -1.28872400 -0.56243700

C -2.61880700 0.05505300 -0.03321000
C -5.46774000 -0.19334300 -0.40299800
H -5.04256300 -2.26617700 -0.83225000
C -3.46468100 1.19950500 0.13159200
C -4.83872600 1.02593800 -0.05517700
H -5.47369300 1.89707200 0.07849700
O -1.31088700 0.14832000 0.10314100
O 1.32793900 0.06301000 -0.03756000
Al 0.00128500 -1.10918700 0.43893000
Cl -0.18184800 -1.32920700 2.65169100
C 2.78672800 2.56550400 -0.36686100
C 7.05568800 -0.24107100 -0.32507500
C -6.99180000 -0.32591000 -0.60001200
C -2.88324800 2.57913400 0.51104200
C 7.61172600 -1.67410000 -0.24373800
H 7.25083800 -2.30217000 -1.07389600
H 8.71140300 -1.64998300 -0.30081500
H 7.33981200 -2.16674500 0.70333400
C 7.64518200 0.57377000 0.84963500
H 8.74705400 0.57179700 0.80389000
H 7.31332300 1.62352500 0.82838700
H 7.34227800 0.14425600 1.81823300
C 7.51954200 0.38173600 -1.66241700
H 7.18653700 1.42610700 -1.76723800
H 8.62040600 0.37594600 -1.72729200
H 7.12380500 -0.18606700 -2.52016600
C 1.98123600 2.87499100 0.91710400
H 1.19178400 2.13428700 1.08980600
H 2.64597100 2.88635900 1.79687600
H 1.51205300 3.86996400 0.83639400
C 1.86370200 2.60812200 -1.60798100
H 1.07940800 1.84371400 -1.55076900
H 1.38072300 3.59635900 -1.68670500
H 2.44719400 2.44320200 -2.52928500
C 3.83081200 3.68758400 -0.53336200
H 4.51605400 3.75178200 0.32698000
H 4.43401800 3.56638000 -1.44735900
H 3.30882400 4.65435400 -0.61009300
C -2.14834800 2.48625100 1.86957500
H -1.72023200 3.46800700 2.13357100
H -2.84969400 2.19798800 2.67018600
H -1.33663900 1.74934900 1.84342500
C -1.90986700 3.05426500 -0.59268900
H -1.48330000 4.03551700 -0.32392800
H -1.08505400 2.34575200 -0.73146800
H -2.43900500 3.16889700 -1.55371300
C -3.97779200 3.65531800 0.65437100
H -4.53133600 3.81753200 -0.28442400

H -4.70420800 3.41027700 1.44570600
H -3.50589000 4.61253900 0.92673400
C -7.72904200 1.00729800 -0.37673100
H -7.58795500 1.39015900 0.64644100
H -7.39781300 1.78504100 -1.08306300
H -8.81011800 0.86135200 -0.52882000
C -7.55278700 -1.36021600 0.40329600
H -8.64193200 -1.47365300 0.27163300
H -7.09509100 -2.35249000 0.26635300
H -7.36515400 -1.04377800 1.44210100
C -7.28566800 -0.80275500 -2.04137100
H -6.81985100 -1.77809900 -2.25284900
H -8.37206200 -0.91121500 -2.19755500
H -6.90482900 -0.08011000 -2.78125300